MODELING AND ANALYSIS OF A LITHIUM-ION CONVECTION BATTERY

by

Weiran Gao

M. S. in Chemical Engineering Practice, Massachusetts Institute of Technology, 2022
M. S. in Chemical Engineering, Worcester Polytechnic Institute, 2018
B. S. in Chemical Engineering, Worcester Polytechnic Institute, 2017

Submitted to the Department of Chemical Engineering
in partial fulfillment of the requirements for the degree of

Doctor of Philosophy in Chemical Engineering

at the

MASSACHUSETTS INSTITUTE OF TECHNOLOGY

May 2024

Author ....
Department of Chemical Engineering
May 8th, 2024

Certified by ....
Fikile R. Brushett
Associate Professor of Chemical Engineering
Thesis Supervisor

Accepted by ....
Hadley D. Sikes
Willard Henry Dow Professor of Chemical Engineering
Graduate Officer

Modeling and Analysis of a Lithium-ion Convection Battery

by

Weiran Gao

Submitted to the Department of Chemical Engineering on 8 May 2024, in partial fulfillment of
the requirements for the degree of
Doctor of Philosophy in Chemical Engineering

Abstract:

Lithium-ion batteries (LIBs), crucial to modern portable electronics and increasingly significant in transportation and grid storage, represent the state-of-the-art in energy storage technology due to their high energy density, efficiency, and long cycle life. Despite declining costs and improving energy densities, driven by advancements in materials and manufacturing processes along with expanded market scale, current LIBs often struggle to meet the evolving demands of new applications. Current research predominantly focuses on material innovations, with less attention given to re-engineering cell architectures to address the technological challenges.

This thesis investigates the "convection battery" cell architecture, a novel approach involving circulating electrolyte through the porous electrodes and separator of a LIB cell to enhance mass and thermal transport. Compared to traditional LIBs, this architecture may enhance ion flux in electrodes, improve safety and maintenance, simplify system design, and ultimately reduce overall costs. Prior studies, including experimental work in our laboratory, have highlighted the benefits of electrolyte flow, yet a comprehensive engineering analysis on this aspect is lacking.

To bridge this gap, this thesis employs a combination of modeling and analytical techniques to systematically explore the potential advantages and opportunities enabled by the convection battery cell architecture. The first half of the thesis delves into the fundamental mechanisms of electrolyte convection in enhancing mass and thermal transport within a LIB cell, utilizing a convection battery sandwich cell layer model developed from the Li-ION SIMulation BAttery (LIONSIMBA) Toolbox. Through dimensional analysis, I identified conditions under which convection provides the most performance enhancement, alongside exploring the necessary flow rates and performance limitations.

In the latter half of the thesis, practical implementation aspects are examined, starting with the requisite additional electrolyte to achieve desired transport enhancements. A potential design for the convection battery system is proposed, and COMSOL-based convection battery cell stack models and a system design model were developed to aid the analyses. Through illustrating its utility in two distinct scenarios, I have endeavored to highlight the convection battery's unique value proposition and its potential to broaden the applicability of current LIB technologies. This thesis establishes a foundation for the convection battery technology, highlighting its potential to improve the performance of current LIB systems and to venture into novel application domains. To conclude the thesis, I discuss future research avenues and the design considerations essential for the advancement and realization of the convection battery technology.

Thesis Supervisor: Fikile R. Brushett
Title: Associate Professor of Chemical Engineering

Acknowledgements:

As I reflect on my PhD journey, which I embarked upon with a desire to fully realize my potential and to collaborate with inspiring minds, I can confidently say that this experience has exceeded my expectations. This achievement was made possible not only by the intellectual challenges and growth I encountered but also by the extraordinary individuals who supported me along the way.

First and foremost, I am deeply grateful to my research advisor, Prof. Fikile Brushett, who placed his trust in me to pursue this project in electrochemistry, a field I was unfamiliar with at the start. His willingness to invest time and provide continuous support has been a cornerstone of my PhD experience. From him, I learned not only the finer points of research communication but also how to envision the larger impact of our work. These skills will be invaluable in my future career.

I extend my thanks to my thesis committee members, Prof. Martin Bazant and Prof. Yet-Ming Chiang. Each committee meeting, though challenging, was instrumental in refining my thesis and enhancing my critical thinking. Their insightful feedback and encouragement pushed me to explore new depths in my research.

I must also acknowledge my former research advisor at Worcester Polytechnic Institute, Prof. Ronald Grimm. He was instrumental in shaping my early research skills, and his advice to explore Li-ion batteries was a guiding light as I considered the direction of my PhD research.

The support from the Brushett group has been indispensable. I am profoundly thankful for Dr. Javit Drake, Dr. Yasser Ashraf Gandomi, Dr. Lingping Kong, Dr. Madhu Majji, Dr. Michael Orella, Dr. McLain Leonard, Dr. Katharine Greco, Dr. Alexis Fenton, Dr. Kevin Tenny, Dr. Kara Rodby, Dr. Charles Wan, Dr. Bertrand Neyhouse, Dr. Lauren Clarke, Dr. Aditya Limaye, Alex Quinn, Nick Matteucci, Chris Mallia, Katelyn Ripley, Trent Weiss, Isabella Caruso, John Vergados, Anish Sukumar, Cindy Wong, Tom Goodwin, Arun Johnson, Katherine Stoll, and Ava Vargas. Working with such a group of intelligent and ambitious individuals, always ready to assist and support, has been truly inspiring. I am particularly indebted to Dr. Javit Drake, Trent Weiss, and Ava Vargas, with whom I have shared countless hours of fruitful and enjoyable collaboration. Their brilliant ideas and camaraderie have made this journey enjoyable. I am also grateful to my mentor, Mike, who dedicated much time to guide me through the initial phases of my work. My thanks also go to Dr. Thomas Carney, who began the experimental work which this thesis is built upon, and Katie, who taught me the experimental setups and passed on the knowledge.

My years at MIT were enriched by friendships that sustained me through challenges, both academic and personal. I am equally grateful for my college friends, who provided a refreshing escape and steadfast belief in my abilities, and my friends back in China, who ensured that home always felt welcoming.

My family, both in China and the US, and my in-laws, have been a constant source of support and nurturing, always prioritizing my happiness and well-being above all else. My mother, especially, has been a pillar of strength and resilience, teaching me to pursue what truly brings me joy, even if it means taking a step back.

Lastly, my deepest appreciation goes to my husband, Ben Drury. From being lab partners in college to partners in life, Ben has been my rock. His endless comfort during my most stressful days and his reminders of my worth and capabilities have been a source of strength. His love and support have been pivotal in my ability to complete this PhD.

Table of Contents:

Abstract: 3

Acknowledgements: 5

Table of Contents: 7

List of Figures: 13

List of Tables: 23

I. Introduction 25

1. Li-ion Batteries *26*

1.1. Technology overview 26

1.2. Li-ion battery chemistries 29

1.3. Growth of the Li-ion industry 35

1.4. Technology challenges and ongoing R&D activities 37

2. Convection-enhanced Li-ion Batteries *39*

2.1. Prior work in literature 40

2.2. Prior work in the Brushett Group 41

3. Thesis Scope and Outline *42*

4. Key Assumptions Underpinning the Thesis *44*

4.1. Flow-permeable electrode 46

4.2. Pressure drop and pumping loss 47

4.3. Uniform flow distribution 53

II. A Study on the Impact of Convection on Electrolyte Mass Transport 55

1. Introduction 55

2. Model Development 59

3. Model Analysis 68

4. Conclusions 77

5. List of Symbols 79

6. Appendix A: Electrolyte Conductivity Equation 80

7. Appendix B: Supplementary Figures 81

8. Appendix C: Supplementary Notes 84

8.1. Solid-phase diffusion model 84

8.2. Details of the concentration profiles 85

8.3. Impacts of flow direction 86

8.4. Pumping energy loss across single cell 87

8.5. Derivation of electrolyte transport equations 88

8.6. Derivation of dimensionless groups using timescales 90

8.7. Effects of solid-phase transport and kinetics 92

III. A Study on the Impact of Convection on Thermal Transport 94

1. Introduction 94

2. Model Development 99

3. Model Analysis 104

3.1. Base Case: Conditions of Significant Thermal and Mass Transport Limitations 104

3.2. Dimensionless Group Development 106

3.3. Diffusive Transport Limited Case 110

3.4. Thermal Transport Limited Case 112

3.5. Comparison Between Internal and External Cooling 114

3.6. On the Potential for Dynamic Thermal Regulation via Varying Electrolyte Flow Rate 118

4. Conclusions 119

5. List of Symbols 122

6. Appendix A: Equations used in the simulation 124

6.1. Heat source terms 124

6.2. Temperature-dependent values and properties 124

7. Appendix B: Supplementary Figures 126

8. Appendix C: Supplementary Notes 132

8.1. Pumping energy loss and energy gain across a single cell 132

8.2. Temperature change inside the tank 133

8.3. Impacts of flow direction 134

8.4. Derivation of $\overline{Q}_{total}$ for the dimensionless group calculation 136

8.5. Equivalent heat removal capabilities 139

IV. Transient Analyses on Mass and Thermal Transport 142

1. Introduction 142

2. Transient Electrolyte Mass Transport Analysis 142

2.1. Evolution of electrolyte concentration without electrolyte flow 143

2.2. Evolution of electrolyte concentration with electrolyte flow 148

3. Transient Thermal Transport Analysis 150

3.1. External cooling analysis 152

3.2. Internal cooling analysis 154

3.3. Comparison between external and internal cooling 155

4. Conclusions 156

5. List of Symbols 157

V. Extra Electrolyte Requirements 159

1. Introduction.. 159

2. Model Description 159

3. Results and Discussion 163

3.1. Extra electrolyte volume analysis 163

3.2. Extra electrolyte shape analysis 170

3.3. Practical design considerations 173

4. Conclusions.. 179

5. List of Symbols 180

6. Appendix: Tank concentration evolution 182

VI. System Design and Potential Applications 183

1. Introduction.. 183

2. A Conceptual Convection Battery System Design 184

3. Model Development 186

3.1. Thermal-electrochemical model 186

3.2. System design model 187

4. Potential Application Demonstrations.. 188

4.1. Fast charging.. 190

4.2. Stationary energy storage 198

5. Conclusions and Future Directions *202*

6. List of Symbols *204*

VII. Summary and Outlook **206**

VIII. References **210**

IX. Permissions **225**

List of Figures:

Figure I-1: Schematic of a Li-ion battery cell. Dashed and solid arrows show the directions of electron and lithium-ion transport during charging and discharging, respectively. 28

Figure I-2: Cost breakdown for various types of Li-ion cells.[12] NCA = lithium nickel cobalt aluminum oxide, NMC = lithium nickel manganese cobalt oxide, LFP = lithium iron phosphate. 31

Figure I-3: Historical increase in specific energy (a) and decrease in price with increased market size (b) of Li-ion battery cells.[17] 35

Figure I-4: Projected growth in Li-ion battery manufacturing capacity and demand worldwide from 2020 to 2030... 36

Figure I-5: The prior cell prototype in our lab. The cell uses ~5mm thick freestanding electrodes. 41

Figure I-6: Sensitivity analysis of the pressure drop calculation with the Kozeny-Carman equation. In the based case, the particle size (D_p) is 10 μm, the electrode hydraulic tortuosity (τ) is 2, the flow linear velocity (v_s) is 10 μm/s, and the electrode porosity (ε) is 0.4. 52

Figure II-1: Intercalation battery configurations with an (a) enclosed cell design as is typical in most modern devices or (b) novel flow-through design that attempts to improve the effective diffusivity of the electrolyte. The additional hardware required in (b) consists of an external storage tank and pump to provide forced convection through the porous intercalation materials and separators that compose the battery cell. 57

Figure II-2: The finite volume discretization and domain used for simulations of the convection battery in the LIONSIMBA+c model. The nodes are numbered from the left, starting at $x = \hat{x}_0$ for the left boundary of N = 1 to $x = \hat{x}_n$ for the right boundary of $N = n_p + n_s + n_n$. The diagram shown above is for the situation of flow from the negative electrode to the positive electrode such that the tank is located at a fictitious node N+1; however, if the flow were reversed, the tank would be located at a fictitious node 0. 62

Figure II-3: The effect of convective mass transfer on (a) the discharge polarization curve and (b) the concentration profile of electrolyte at t = 380 s. Note the location of positive and negative electrodes is opposite to that in **Figures II-1** and **II-2**. These data show the positive impact of increasing flow rate on cell performance by minimizing the instances of electrolyte salt depletion in the positive electrode. Further discussions of the concentration profiles and the impacts of flow direction can be found in Section 8.2 and Section 8.3. 68

Figure II-4: Accessed capacity enhancement by 0.01 m/s of flow compared to a cell without flow. The figure is generated from 5166 data sets with varying I_{app}, t_+, D, but same initial electrolyte concentration $c_{initial}$ = 1000 mol/m^3, and constant ohmic resistance, $\delta' = 3.89$ corresponding to a dimensional ohmic potential drop of 0.1 V. A different initial electrolyte concentration will result in similar trends with slight variations in values, as illustrated in **Figure II-9**. "*" indicates conditions used for **Figure II-3**. 74

Figure II-5: (a) Percentage of capacity accessed for convection cells with varying ξ values. The plot contains 29792 data sets with varying I_{app}, t_+, D, $c_{initial}$, v, and a constant δ' value of 3.89 (0.1 V dimensional ohmic drop). Results for $c_{initial}$ >1000 mol/m^3 are not included in the plot as they lead to slightly different behaviors at intermediate ξ values shown in **Figure II-10**. (b) Enlarged view of data for $\beta = 3$ and contours of Pe values. For a particular γ value, the percentage of capacity accessed increases with increasing Pe. 76

Figure II-6: (a) Percentage of capacity accessed during discharge for convection cells with v = 0.01 m/s (10^4 µm/s), as a function of δ' values ranging from 3.89 to 31.2, corresponding to dimensional ohmic drops ranging from 0.1 V to 0.8 V, respectively. The figure contains 560 data sets with varying I_{app}, t_+, D, and $c_{initial}$. Accessed capacity enhancement by 0.01 m/s of flow for data sets with $c_{initial} = 100$ mol/m^3 is shown in (b) for δ' = 3.89 and (c) for δ' = 31.2.................. 77

Figure II-7: Comparison between LIONSIMBA and LIONSIMBA+c model outputs at varying discharge rates with the same inputs and no flow.. 81

Figure II-8: Electrolyte conductivity as a function of salt concentration at T = 298.15 K used in the simulation with the conductivity maxima observed at 1 M.. 82

Figure II-9: Percentage of accessed capacity enhancement for selected β values with $c_{initial}$ from 0.1 M to 1.5 M, with δ' = 3.89.. 83

Figure II-10: Percentage of capacity accessed as function of ξ for selected β and γ values, with $c_{initial} = 1.5$ M and δ' = 3.89. 84

Figure II-11: Corresponding electrolyte concentration change in the tank as a function of time for **Figure II-3** in the main text.. 86

Figure II-12: (a) Cell voltage curves and (b) corresponding electrolyte concentration profiles for reverse flow direction compared to **Figure II-3** in the main text... 87

Figure III-1: Lithium-ion battery configurations with (a) an enclosed cell design as is typical of contemporary devices and (b) the proposed flow-through concept that attempts to improve mass and thermal transport through electrolyte convection. The additional hardware required in (b) consists of an external storage tank, pump, and tubing or pipes to provide forced convection through the porous intercalation materials and separator that compose the battery cell. Note that (b) is presented solely for the purpose of illustrating the underlying concept and the model setup. 98

Figure III-2: The effect of electrolyte convection on (a) the galvanostatic cell discharge (b) the concentration profile of electrolyte within the cell at t = 347 s, the end of discharge for the no flow case, and (c) the time-dependent trajectory of cell temperature. These results show the benefit of increasing flow rate on cell performance by minimizing the electrolyte concentration gradient while suppressing temperature rise. The corresponding heat generation data can be found in **Figure III-9**. Further discussions of the tank temperature change and the impacts of flow direction can be found in Section 8.2 and Section 8.3. 106

Figure III-3: Diffusive transport limited case (a) distributions of concentration and contributions to (b) reversible heat generation, (c) irreversible reaction heat generation, and (d) Joule heating. The figures are taken at t = 100 s, before complete electrolyte salt depletion occurs. The Joule heating in the current collectors is negligible and not shown. 112

Figure III-4: Thermal transport limited case temperature profile over time. The use of a large electrolyte diffusivity (D = normal value × 10^3) yields a uniform electrolyte concentration profile even in the absence of electrolyte flow (**Figure III-11**). Thus, the suppression of temperature gain by increasing flow rate is solely due to increased rates of heat removal and no effect on heat generation. 114

Figure III-5: Comparison of external cooling (left plots) and internal convective cooling (right plots) on three (3) key outputs: galvanostatic discharge curves (a, d), electrolyte concentration distributions (b, e) at 269 s, the end of the shortest discharge (h_{cell} = 12.9 W/(m^2K)), and transient temperature trajectories (c, f). Each curve on the left has a corresponding curve on the right of the same color with equal heat removal rate. Internal cooling shows improvements in these 3 key outputs with successive increasing flow rates. However, with external cooling, cell behavior shifts from thermal to mass transport limited ultimately leading to truncated discharge at the highest heat removal rate simulated. 117

Figure III-6: Demonstration of dynamic flow rate for thermal regulation. In reactive mode (a), convection is triggered by a safety temperature (e.g., thermal runaway protection); in proactive mode (b), convection is triggered by a change in current density (e.g., sudden acceleration in a BEV). 119

Figure III-7: Comparison between non-isothermal LIONSIMBA and LIONSIMBA+c model outputs: (a) discharge curves (b) temperature rise curves at varying discharge rates with the same inputs and no flow 126

Figure III-8: Flow rate-dependent temperature vs. position curves for the base case at 347 s, the end of discharge for the stagnant cell in Figure III-2(a). 127

Figure III-9: Heat generation by different sources as a function of the cell position at 347 s, the end of discharge for the stagnant cell, and the electrolyte flow rate for the conditions used in the base case: (a) Reversible heat generation, (b) irreversible reaction heat generation, (c) Joule heating, and (d) total heat generation. The Joule heating in the current collectors is negligible and not shown. 128

Figure III-10: Cell temperature as a function of time for the Diffusive Transport Limited Case for different electrolyte flow rates. 129

Figure III-11: Electrolyte concentration as a function of cell position for the Thermal Transport Limited Case. Across all flow rates considered, the electrolyte concentration remains constant across the cell, thus the curves directly overlay and are not visible. 130

Figure III-12: Heat generation by sources as a function of the cell position at 225 s (before complete electrolyte salt depletion occurs for the h_{cell} = 12.9 W/(m^2K) case), and the cell heat transfer coefficient or electrolyte flow rate for the conditions used in the Comparison Between Internal and External Cooling cases. Plots (a)-(d) show the reversible heat generation, irreversible reaction heat generation, Joule heating, and total heat generation for the external cooling conditions respectively; (e)-(h) show the same set of plots for the internal cooling conditions. The Joule heating in the current collectors is negligible and not shown. 132

Figure III-13: Flow rate dependent trade-off between energy gain and pumping loss for a convection cell under the conditions used for **Figure III-2** in the main text. 133

Figure III-14: Tank temperature change as a function of time at different flow rates for the base case. 134

Figure III-15: The effect of reverse electrolyte flow direction on (a) the discharge polarization curve (b) the concentration profile of electrolyte at t = 325 s (the end of the shortest discharge, v = 0.2 μm/s) and (c) the cell temperature rise compared to the zero-velocity base case in the main text. 135

Figure III-16: Heat generation by sources as a function of the cell position at 325 s (the end of the shortest discharge, v = 0.2 μm/s) and electrolyte flow rate for the reverse flow case: (a) reversible heat generation, (b) irreversible reaction heat generation, (c) Joule heating, and (d) total heat generation. The Joule heating in the current collectors is negligible and not shown.......... 136

Figure III-17: A relationship between v and h_{cell} that would yield the same heat removal capability for the cell considered in the section, Comparison Between Internal and External Cooling. The typical ranges of different external cooling methods are labeled for reference.[154] 140

Figure III-18: Discharge curve and temperature profile with artificial elimination of mass transport limitations and temperature dependence. The matching results validate heat transfer coefficient, h_{cell}, and velocity, v, values that cause equivalent external (a, b) and internal (c, d) heat removal rates. Comparison of these plots with **Figure III-5** in the main text shows the significant adverse effect of coupled mass transport on external cooling approaches that is overcome by internal convective cooling. 141

Figure IV-1: Comparison between simulated end-of-discharge electrolyte concentration results (solid lines) and the analytical steady-state solution shown in Eq. (IV-3) (dashed lines) for three different sets of conditions. 145

Figure IV-2: Electrolyte concentration evolution for conditions with small γ_M. 146

Figure IV-3: Electrolyte concentration evolution for conditions with small β_M and large γ_M. .. 147

Figure IV-4: Electrolyte concentration evolution for conditions with large β_M and γ_M. 148

Figure IV-5: Electrolyte concentration evolution for conditions with small ξ_M. 150

Figure IV-6: Schematic of the problem analyzed in this work 151

Figure IV-7: Impact of Bi on temperature distribution at (a) large Fo and (b) small Fo. 153

Figure IV-8: Impact of Pe on temperature distribution at (a) large Fo, (b) intermediate Fo, and (c) small Fo. 155

Figure IV-9: Comparative analysis of external vs. internal cooling effects on (a) cell maximum temperature and (b) cell maximum temperature difference.. 156

Figure V-1: (a) Accessed capacity enhancement under 5C isothermal discharge by electrolyte flow of varying flowrates compared to a cell without stagnant electrolyte as a function of extra-electrolyte-to-cell volume ratio (b) Cell electrolyte concentration overlay for extra-electrolyte-to-cell ratios of 0.005 (blue), 0.1 (red), and 100 (black) at electrolyte flowrates of 0.07 μm/s (long-dashed lines), 0.2 μm/s (short-dashed lines), and 10 μm/s (solid lines). The tank concentration evolution with time can be found in **Figure V-6**... 165

Figure V-2: (a) Accessed capacity enhancement under 5C discharge by electrolyte flow of varying flowrates compared to a cell without stagnant electrolyte as a function of extra-electrolyte-to-cell volume ratio. The cell is insulated (h_{cell} = 0 W/(m^2K)), and the well-mixed tank has a height/diameter ratio of 1.5 and an overall heat transfer coefficient (h_{tank}) of 100 W/(m^2K) (b) Minimum flow velocity required to keep cell temperature below the safety threshold before the completion of discharge, plotted against the extra-electrolyte-to-cell volume ratio. This is depicted for varying h_{tank} values under an insulated cell condition(h_{cell} = 0 W/(m^2K), indicated by solid lines), and for increasing h_{cell} values while keeping h_{tank} constant at 100 W/(m^2K) (indicated by dashed lines)... 167

Figure V-3: (a) Temperature profiles of cells with electrolyte recirculation pipes of varying length-to-diameter ratios, utilizing a fixed electrolyte volume at 30% of the cell's volume and a superficial velocity of 1.5 μm/s. The pipe has an overall heat transfer coefficient of 100 W/(m^2K). Dashed lines represent the temperature profiles under the well-mixed tank assumption with h_{tank} = 100 W/(m^2K), and the tank is matched in volume and surface area to the corresponding pipes. (b) Total pumping energy required for the cell and its recirculation pipes, plotted against varying pipe-to-cell volume ratios, with each line representing a different length-to-diameter ratio of the pipes. The energy increase enabled by electrolyte flow is 67 Wh/m^2. 171

Figure V-4: (a) Impact of extra electrolyte volume on the gravimetric energy density for a system designed to (a) solely utilize the mass transport benefit of electrolyte convection and (b) leverage both mass and thermal transport benefits of electrolyte flow. Note that the energy density value is based on the assumed system design in this work, and there are opportunities for improvement through system optimization. 176

Figure V-5: Total added cost of systems with electrolyte recirculation over a given lifetime. The pump is assumed to operate continuously over the associated lifespan at 50% efficiency. Solid lines represent the relative pump to added electrolyte costs of a given operating condition...... 178

Figure V-6: Concentration change within the tank under the conditions for **Figure V-1b**....... 182

Figure VI-1: (a) A baseline system design (no flow) based on CATL's Qilin battery pack. (b) A conceptual convection battery system design that aims to cause minimum disruption to the baseline system. 186

Figure VI-2: Schematic of the thermal-electrochemical model. 187

Figure VI-3: A sample Ragone plot comparing the convection battery system and a typical LIB system (no flow). 189

Figure VI-4: (a) Total charging time under isothermal conditions (298.15 K) of the cell without flow and with 10 μm/s flow. CC-CV charging protocol with 4.2V cutoff voltage is used. Note that the charging time values will vary depending cell design and ambient temperature, but the overall trends still hold. (b) The electrolyte flow reduces charging speed by enabling a more uniform electrolyte concentration. 192

Figure VI-5: The enhanced mass transport through 10 μm/s flow leads to (a) reduced lithium plating potential and (b) more uniform intercalation within the electrode. 193

Figure VI-6: (a) Temperature distribution at 142s within the cell undergoing CC (6C) – CV (4.2V) charge with external cooling (h_{cell} = 500 W/(m^2K), $T_{coolant}$ = 288.15 K). The cell is forced to stop due to the center reaching the safety cutoff temperature. (b) The maximum CC charging rates with external cooling to ensure the cell does not reach the safety cutoff temperature (blue), and the maximum temperature difference within the cell does no exceed 15K (black). Note that the coolant conditions are different, as the first case aims to maximize heat dissipation while the second case aims to minimize temperature difference. 194

Figure VI-7: Increasing electrolyte flowrate provides increasing thermal management benefits during fast charging. CC (6C) – CV (4.2V) is used, and the cell is charged from 10% to 80% capacity. 195

Figure VI-8: (a) Pumping power as a function of porosity calculated using the Kozeny-Carman equation. (b) The comparison of isothermal charging times of the two electrode designs without flow and with a 10 μm/s to eliminate mass transport limitations. 197

Figure VI-9: (a) Maximum 10s pulse discharge rate as a function of anode thickness for cells without flow and with 10 μm/s flow. (b) Maximum anode thickness that can be used to achieve full discharge of varying durations for cells without flow and with 10 μm/s flow. 201

List of Tables:

Table I-1: Classes of positive electrode materials for Li-ion batteries and the applications in which they are preferred.[11] LFP = the exemplar compound $LiFePO_4$, NCA = $Li(Ni,Co,Al)O_2$, LMO = $LiMn_2O_4$, LCO = $LiCoO_2$, and NMC = $Li(Ni, Mn Co)O_2$ (the nomenclature "NCM"is also used). Here, Y and N stand for "applicable" and "not applicable." 30

Table II-1: A subset of the critical parameters used in LIONSIMBA+c simulations that define the battery operation in the positive electrode, which is limiting under all conditions studied throughout this study. $^a\kappa_{eff}$ is calculated through the electrolyte concentration, c_e, temperature, T, as shown in Eq. (II-10).. 66

Table II-2: Other parameters used in modified LIONSIMBA. 66

Table II-3: Definitions of the dimensionless groups used throughout the remainder of this study to describe convection battery operation. 71

Table II-4: Energy gain and pumping loss by a convection cell with v = 10 μm/s.................... 88

Table II-5: Timescales and corresponding characteristic rates relevant to the electrolyte transport during convection battery operation. 91

Table II-6: Derivation of the dimensionless groups using timescales defined in **Table II-5**. 92

Table III-1: Simulation parameters used in this study. 104

Table III-2: Dimensionless groups quantifying the extent of bulk mass and thermal transport limitations. 109

Table III-3: Mass [M] and heat [H] transport dimensionless group values for the cases demonstrated in (a) Base Case (b) Diffusive Transport Limited Case and (c) Thermal Transport

Limited Case. The electrolyte properties at room temperature are used for the mass transport dimensionless group calculations. 110

Table V-1: Simulation parameters used in this study. 163

Table VI-1: Simulation parameters used in this section. 191

Table VI-2: The charging times and associated design and operating metrics at varying flowrates for a CC (6C) – CV (4.2V) 10%-80% charging session. For reference, the charging power of the system at 6C is 500 kW. * Includes an extra pump (0.5kg / 0.5L) for the electrolyte; ** Same pump as in the "no flow" system;*** A larger pump is used (adds 5kg / 2L); ****Assumes the heavy-duty pump is provided at the charging station. 196

Table VI-3: The charging performance and metrics of systems with two different electrode designs. The electrolyte flowrate is 320 μm/s, and the charging protocol is CC (6C) – CV (4.2V) with the cell from 10% to 80% capacity. 198

Table VI-4: Simulation parameters used in this section. 199

I. Introduction

A grand challenge of the 21st century will be the evolution of electrical power system to meet emerging energy demands while balancing environmental stewardship and cost-effectiveness. 82% of the total energy consumed in the United States is derived from fossil fuel sources (i.e., oil, coal, and natural gas) and dominated by electricity and transportation.[1] However, in the future, this dependence will not be feasible,[2] as rising population and continuing economic growth in the developing world are projected to double global energy consumption by 2050.[3] Moreover, the continued and increasing generation of anthropogenic carbon dioxide (CO_2) from fossil fuel combustion will likely have negative implications for the global climate.[4] Thus, in an effort to sustain increased societal power requirements and to decarbonize both the grid and transportation technology, low-cost, energy-dense power sources will be essential.

Electrochemical technologies, in particular lithium-ion (Li^+) batteries (LIBs), are among the key technologies to achieve a deep decarbonization through their emerging applications in transportation and in the electric grid. However, while the past decade has seen a steady decline in battery price and concomitant increase in energy density due to a combination of materials development, manufacturing advances, and market scale, current LIBs are still unable to meet the stringent performance, cost, and scale requirements of these emerging applications. As such, breakthroughs in the science and engineering of LIBs are needed to enable high-energy and high-power applications while maintaining low cost. This thesis aims to address the challenges facing the current LIB through the investigation of a novel LIB cell design, a so-called "convection battery". In this opening chapter, I commence with a comprehensive examination of the current state of LIB technology and its inherent challenges in Section 1. This is succeeded by Section 2, which presents an overview of the convection battery technology, setting the stage for the research presented in this thesis. Section 3 then outlines the thesis's framework, providing a logical flow of the topics and the research contributions to be discussed in the ensuing chapters. Finally, Section 4 discusses the assumptions underlying this thesis work.

1. Li-ion Batteries

1.1. Technology overview

Lithium-ion (Li-ion) batteries are a family of rechargeable batteries that utilize solid compounds at both the negative and positive electrodes as hosts for reversible lithium-ion storage. During discharge, lithium ions migrate internally from the negative electrode to intercalate into the positive electrode through a liquid electrolyte, while electrons simultaneously move in the same direction through an external circuit, powering the device to which the battery is connected. During charge, the process is reversed, with lithium ions migrating from the positive to the negative electrode, and electrons flowing through the external circuit, under voltage supplied by an external power source. The Li-ion battery is a relatively mature technology that has benefited from more than three decades of commercial development. Thanks to several factors—including the low atomic mass of lithium; the development of positive and negative electrodes that are capable of reversibly storing lithium ions at high mass and volume concentrations and with large differences in electrode potential (cell voltage); and the development of high conductivity electrolytes, supporting components, cell designs, and manufacturing methods—Li-ion batteries today offer energy and power densities that are superior to most other battery types. State-of-the-art Li-ion battery cells have a nominal voltage of 3.6–4.0 volts (V), a specific energy (or gravimetric energy density) between 100 and 250 watt-hours per kilogram (Wh/kg), and an energy density between 300 and 650 watt-hours per liter (Wh/L).[5,6] They have high roundtrip energy efficiency (85%–95%, depending on the rate of charge and discharge), low maintenance requirements, adequate cycle life for many applications (up to several thousand full charge/discharge cycles), and a low self-discharge rate. These merits have made Li-ion batteries the incumbent technology for a wide range of applications, from portable electronics and power tools to electric vehicles (EVs) and stationary energy storage systems.

A Li-ion cell contains several key components within its external housing (**Figure I-1**): a positive electrode, a negative electrode, aluminum and copper foil current collectors to which the positive and negative electrodes are respectively adhered, a liquid electrolyte, and a porous separator to electrically isolate the two electrodes from one another. The positive electrode (commonly referred to as the cathode, although this terminology is technically correct only during the discharge step) is typically a lithium transition-metal oxide such as lithium cobalt oxide (LCO), lithium manganese oxide (LMO), lithium nickel-manganese-cobalt oxide (NCM or NMC), or lithium iron phosphate (LFP). The electrode also contains electrochemically inactive materials that improve electrical and structural characteristics, typically conductive carbon powders and a polymeric binder. The mixture of active and inactive materials is coated on an aluminum foil current collector, which, in turn, is connected to the external electrical terminals of the cell. The negative electrode (or anode during discharge) is typically a graphite-based material, with higher-specific-energy Li-ion battery cells now incorporating silicon in varying amounts. These active materials are also mixed with conductivity enhancers and binders and subsequently coated on a copper current collector. To a large extent, the choice of compounds for positive and negative electrodes defines battery performance and favored applications of different types of Li-ion battery cells. The liquid electrolyte enables the movement of lithium ions between the two electrodes during charge and discharge; it consists of a lithium salt (e.g., lithium hexafluorophosphate, $LiPF_6$) dissolved in an organic solvent, which is most commonly composed of a blend of alkyl and cyclic carbonates (e.g., ethylene carbonate, propylene carbonate, ethyl methyl carbonate, etc.). Various chemical additives in the electrolyte are used to improve the performance, lifetime, and safety of the cell. The liquid electrolyte can also be infused into a polymer, forming a gel electrolyte; Li-ion batteries that use this type of electrolyte are typically called lithium-polymer (or Li-poly) batteries.[7] In addition to gel electrolytes, fully solid polymer electrolytes have been used—albeit in batteries produced at relatively low volumes; today, inorganic compounds (ceramics) are being widely studied as possible successors to liquid electrolytes.[8] Solid-state batteries using either organic or inorganic electrolytes have potential advantages in safety and energy density compared to liquid electrolyte systems, but lag in commercial maturity.

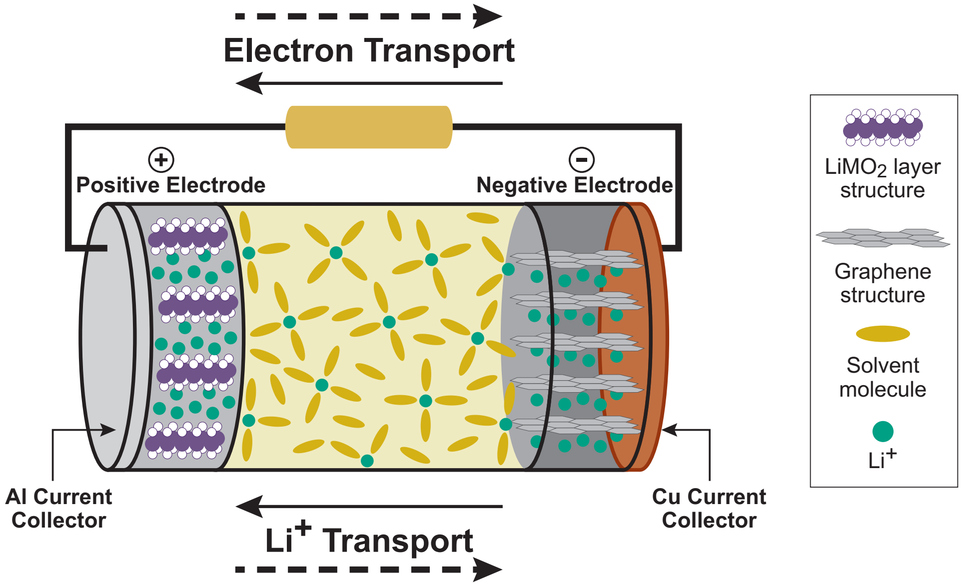

Figure I-1: *Schematic of a Li-ion battery cell. Dashed and solid arrows show the directions of electron and lithium-ion transport during charging and discharging, respectively.*

Li-ion cells are manufactured in a wide range of sizes and in two basic forms: cylinders and rectangular prisms. Cylindrical cells are typically contained in a metal can, while prismatic cells may be contained in a metal can or in a sealed bag made from a multilayered polymer sheet, forming a so-called pouch cell. Individual Li-ion cells, for which the nominal cell voltage is determined by the specific combination of positive and negative electrode materials, can be directly used in small-scale applications such as cell phones. To deliver the increased capacity and operating voltage required for larger-scale applications, multiple cells are interconnected in various series and parallel configurations to form battery modules and packs. Applications that require a large number of interconnected Li-ion cells, such as EVs and grid-scale energy storage systems, also require several additional subsystems to ensure proper and safe operation. These subsystems include thermal management systems that help maintain a proper cell temperature range and battery management systems (BMSs) that electronically monitor and control the operating state of the cells and battery pack. For grid storage applications, additional electronics in the form of inverters and transformers are used to connect the storage systems to each other and to the grid; in addition, supervisory controls are used to monitor the entire system and provide an interface between the BMS and the grid.[9,10]

1.2. Li-ion battery chemistries

1.2.1. Positive electrodes

A variety of positive electrode compounds are used in Li-ion batteries depending on the desired combination of energy density, power density, lifetime, safety, and cost. **Table I-1** shows today's most common positive electrode families and their corresponding applications. The positive electrode active material is generally the most expensive single component in the cell, representing 30%–50% of the total material cost, as shown in **Figure I-2**, which breaks down material costs for Li-ion cells of several types.

Table I-1: *Classes of positive electrode materials for Li-ion batteries and the applications in which they are preferred.*[11] *LFP = the exemplar compound $LiFePO_4$, NCA = $Li(Ni,Co,Al)O_2$, LMO = $LiMn_2O_4$, LCO = $LiCoO_2$, and NMC = $Li(Ni, Mn Co)O_2$ (the nomenclature "NCM"is also used). Here, Y and N stand for "applicable" and "not applicable."*

Type	Consumer Electronics	Power Tools	Light Duty Vehicles	Cars	Commercial Vehicles	Buses	Grid/Energy Storage Systems
LFP	Y	Y	Y	Y	Y	Y	Y
NCA	Y	N	Y	Y	N	N	Y
LMO	Y	Y	Y	Y	N	N	Y
LCO	Y	N	N	N	N	N	N
NMC	Y	Y	Y	Y	Y	Y	Y

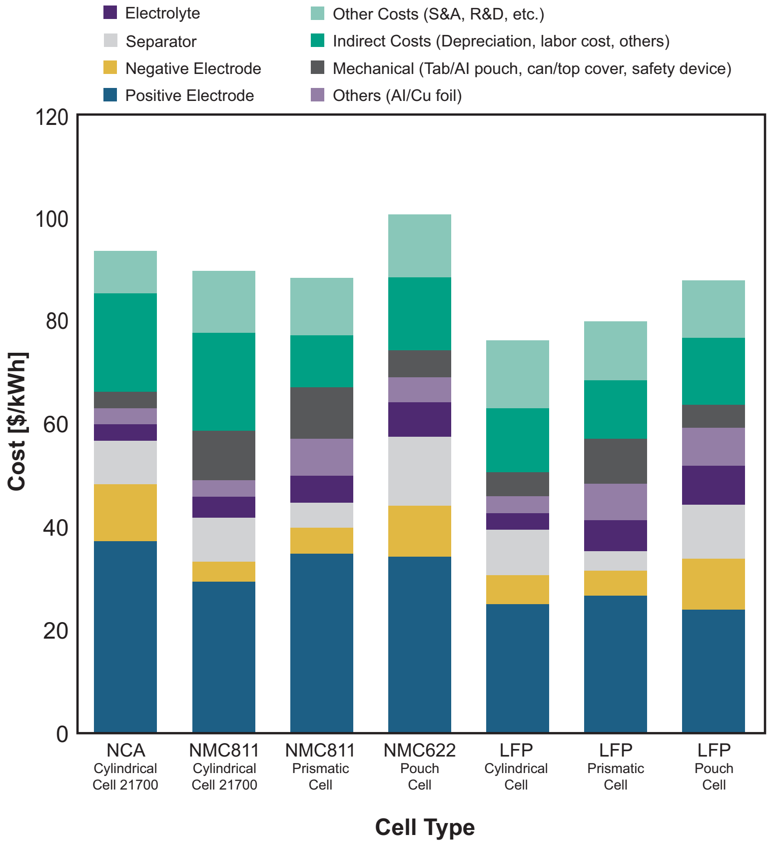

Figure I-2: *Cost breakdown for various types of Li-ion cells.*[12] *NCA = lithium nickel cobalt aluminum oxide, NMC = lithium nickel manganese cobalt oxide, LFP = lithium iron phosphate.*

The first commercially successful Li-ion batteries, launched by Sony Corporation of Japan in 1991,[13] used lithium cobalt oxide (LCO) as the positive electrode material. When paired with a graphite negative electrode, these batteries produced a cell voltage of about 3.8 V,[14] considerably exceeding the voltage of aqueous chemistries and necessitating the use of non-aqueous electrolytes. The main drawbacks of LCO are its relative instability against thermal abuse (thermal runaway is initiated at temperatures as low as 150°C),[6] its relatively short life (500–1000 cycles), and the high cost of cobalt. While LCO-based Li-ion batteries continue to be widely used in portable electronic devices due to their attractive specific energy, this type of battery is unlikely to see use in grid storage applications given the existence of subsequently developed Li-ion alternatives.

Several structural analogs to LCO positive electrodes have been commercialized that partly or completely substitute nickel, manganese, and aluminum for cobalt. These analogs are motivated by the desire to achieve lower cost, greater resource availability, and/or improved safety, while retaining high specific energy. Lithium nickel cobalt aluminum oxide (NCA)-based cells have been developed with comparable specific energy to LCO-based cells (200–250 Wh/kg, for cells designed for a life of 1000–2000 cycles) while using lower-cost metals (typically 85% nickel and 15% aluminum;[5,15] NCA has been the primary Li-ion positive electrode chemistry used in Tesla EVs. Lithium nickel-manganese-cobalt-oxide (NMC) is a family of positive electrodes in which the relative amounts of the three transition metals vary from a ratio of 1:1:1 to a ratio of 8:1:1 in standard formulations (the relative proportions are indicated by the nomenclature, such as "NMC-111" and "NMC-811"). Higher nickel content provides higher voltage and specific energy, but at the expense of poorer thermal stability and cycle life. Nonetheless, by fine-tuning material composition, synthesis methods, and electrolyte composition, NMC-622 and NMC-811 chemistries have been successfully commercialized for EV applications. Thus, the development pathway for this family of positive electrodes has led from a starting point of 100% cobalt in LCO to only 10% cobalt in NMC-811, and NMC positive electrodes with even lower cobalt content are imminent. While multiple advances helped increase the specific energy of commercial Li-ion cells from an upper bound of about 100 Wh/kg in 1991 to approximately 260 Wh/kg today (**Figure I-3a**), the systematic development of the LCO-NCA-NMC class of positive electrodes has played an especially important role.

Two classes of Li-ion positive electrodes have the potential to achieve even lower cost per stored energy than high-nickel NMCs: lithium manganese oxide (LMO) and lithium iron phosphate (LFP). However, both have lower specific energy than the NMC family of positive electrodes.

Lithium manganese oxide was the first of the two to reach commercial production, around 1996.[16] Compared to LCO positive electrodes, LMO positive electrodes (when used with graphite negative electrodes) have a similar operating voltage of about 3.9 V, but their lower practical specific capacities[15] result in a lower specific energy at the cell level of 100–140 Wh/kg.[6] For grid applications, the main limitation of LMO positive electrodes is that they are subject to a mode of chemical degradation related to the dissolution of manganese and its migration to the negative electrode. This type of degradation, which is exacerbated at temperatures above about 50°C,[14] limits the life of LMO positive electrodes to 1000–1500 cycles.[6] However, LMO batteries have been used in power tools, electric bicycles, and medical devices; in addition, LMO has been blended with NMC positive electrodes to improve power density and reduce cost. There are several possible avenues to mitigate the elevated temperature dissolution issue (e.g., positive electrode particle coatings, electrolyte composition design, ion-blocking membranes), which, if successful, could make LMO-containing Li-ion batteries an attractive low-cost option for grid storage.

LFP was first commercialized in the early 2000s. Among commercial positive electrodes, it is the most chemically stable, it does not contain resource-limited elements, and it is capable of lasting several tens of thousands of cycles. LFP-graphite cells using nanoscale powders are among the highest power density Li-ion cells available. LFP has the lowest cell voltage of commercialized Li-ion chemistries—about 3.5 V when used with a graphite negative electrode—which contributes to its stability. This feature, along with a moderate specific capacity, results in a cell-level specific energy of 90–140 Wh/kg.[6] The lower specific energy has limited the use of LFP positive electrode in some applications—for example, EVs with long driving range—but the combination of power, safety, lifetime, and cost they offer has led to use in a broad range of small and large commercial applications ranging from power tools to residential and grid-scale energy storage applications. LFP positive electrodes are also increasingly used in batteries for passenger EVs where maximizing driving range is not a priority (e.g., buses). They represent perhaps the most attractive low-cost Li-ion positive electrode option available today for stationary storage systems.

1.2.2. Negative electrodes

The original development of the Li-ion battery was enabled by carbon-based negative electrodes and graphitic carbon continues to be the most widely used anode material today. However, two alternative negative electrodes have made inroads into commercial products. Lithium titanate spinel is a metal oxide negative electrode that provides high power and exceptionally good cycle life but at the expense of a smaller cell voltage (of about 2.5 V when used with typical Li-ion positive electrodes) and a concomitant reduction in energy density. The cost of chemicals per unit stored energy is high for Li-ion batteries using this type of negative electrode; as a result, it is limited to applications that require high power and high cycling frequency. A second alternative to carbon is silicon-based negative electrodes, which are attractive for high energy density applications given that the specific capacity of silicon, at greater than 3,000 milliampere-hours per gram (mAh/g), is nearly ten times that of graphite (372 mAh/g). In practice, the capacity of silicon anodes must be constrained to lower values to obtain adequate cycle life for most applications. Currently, silicon (commonly in the form of micro or nano particles) is added to graphite-based negative electrodes in small amounts to achieve a combined specific capacity of 400–500 mAh/g. A current trajectory of development is toward negative electrodes with higher silicon concentrations for use in high-energy-density Li-ion battery applications such as EVs. Over time, silicon-based negative electrodes may find use in Li-ion batteries for grid storage.

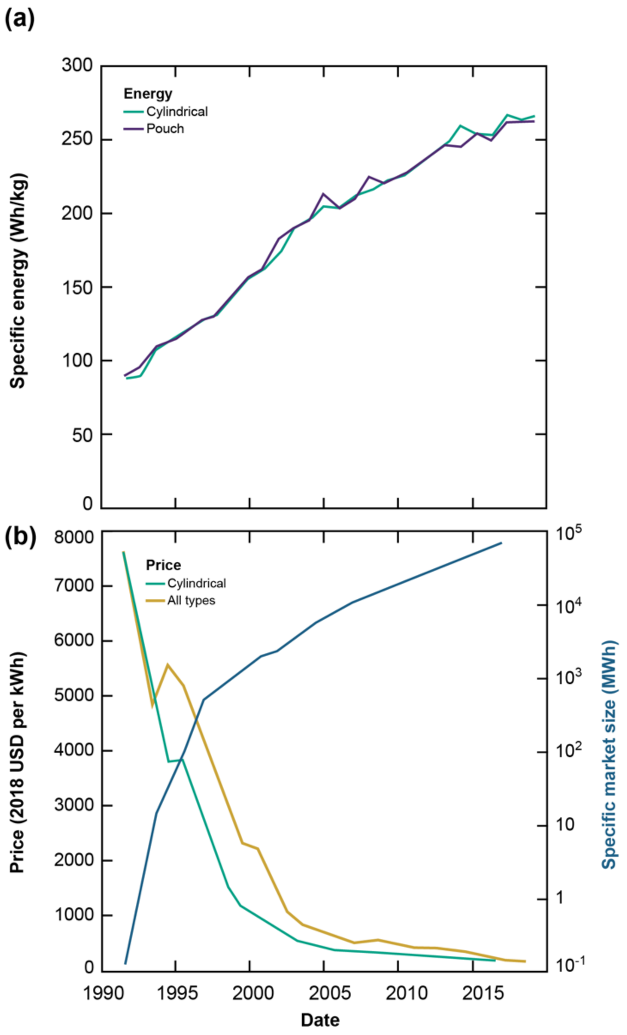

Figure I-3: *Historical increase in specific energy (a) and decrease in price with increased market size (b) of Li-ion battery cells.*[17]

1.3. Growth of the Li-ion industry

Applications of Li-ion batteries were mainly concentrated in portable electronic devices from the inception of this technology in 1991 through the mid-2000s.[18,19] Thereafter, applications in power tools and motor vehicles took hold, such that Li-ion has become the dominant battery architecture across each of those markets today. As of 2016, electronic devices accounted for about 35% of the Li-ion battery market, cars and buses accounted for 50% (mostly in China), and industrial and energy storage systems (e.g., grid storage, uninterruptible power supplies) accounted for 5%; the remainder of the market (10%) was for other uses such as medical devices, power tools, and e-bikes.[19] Since 2016, growth has been primarily driven by the hybrid and all-electric vehicle markets, electric buses, and industrial applications.[20] Since 1995, the size of the Li-ion market, as measured by total storage capacity, has grown by a factor of about one thousand (**Figure I-3b**), reaching approximately 100 gigawatt-hours (GWh) of annual production (globally) in 2019.

Concurrently, prices for Li-ion batteries have dropped 97% since 1991 (**Figure I-3b**). Between 2010 and 2019, Li-ion prices fell by about 85%.[21] Despite declining prices, total market size in dollar terms increased from about $9 billion in 2008[18] to $37 billion in 2019; the market is projected to reach $129 billion by 2027.[22] Multiple projections signal enormous growth in Li-ion manufacturing capacity between now and 2030, driven mainly by growth in the EV market. From about 500 GWh worldwide today, the upper bound of projected manufacturing capacity in 2030 is about 2,500 GWh worldwide, as summarized in **Figure I-4**.

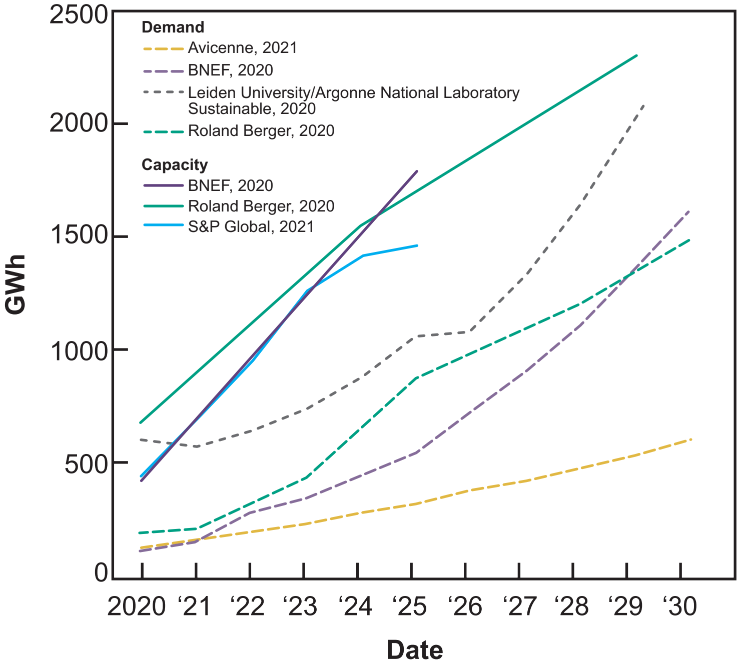

Figure I-4: *Projected growth in Li-ion battery manufacturing capacity and demand worldwide from 2020 to 2030.*

1.4. Technology challenges and ongoing R&D activities

Despite the many advantages that LIB offers, some issues and challenges remain for the broader market penetration of the technology. The first and arguably the biggest challenge is related to safety. While generally a safe technology under normal conditions (i.e. no defects, no damage, no abuse, etc.), LIB failures can lead to catastrophic consequences such as fire and explosion due to the energy-dense materials and the flammable solvent used inside the cell. This is particularly an issue under more extreme conditions, such as applications that are more accident-prone (EVs), require high power input/output (EVs, electric aviation), and need to be applied at large scale (stationary storage systems). Because of the potential safety issue, transportation of LIB has already been regulated,[23] and it might be reasonable to expect storage and installation regulations of large LIB systems in the future should they become largely deployed.

Another challenge is regarding the rate capability for emerging applications. For example, range anxiety stemming from the protracted recharge times, especially in cold weather,[24] is a significant hurdle to their widespread adoption.[25] To mitigate these customer concerns, the US Advanced Battery Consortium has instituted a 2023 goal for EV batteries to achieve 80% pack recharge within 15 minutes.[26] Currently, this can only be accomplished with less energy-dense, more expensive cells using thin electrodes. Similarly, LIB-powered electric aircraft are, at present, hindered by a combined requirement of high specific energies capable of accommodating long-duration flight and high-power takeoff and landing.[27] State-of-the-art LIBs have specific energies of ~250 Wh/kg and a maximum discharge rate of ca. 3C, far below the requisite values for electrified flight.[28]

Besides the aforementioned performance-level issues, cost is also a challenge that hinders the technology's penetration into a larger application space. Although the price of LIB cell has gone down significantly during the past decade, it is still considered too high to be cost-competitive for stationary applications. While LIB cost reduction has been largely driven by the increasing demand for EV and the corresponding manufacturing capacity expansion, there still remains many opportunities to reduce cost through technology advancement. For example, most of today's LIB cell designs are optimized for EVs which focus on high energy and power densities, some requirements that are not so relevant to stationary applications. It is possible that the optimal cell design for stationary applications could have a different, and potentially lower cost than the EV batteries, but such an innovation is unlikely to occur until there is a large demand in the stationary application space. Nevertheless, as the technology becomes more mature and the manufacturing capacity continues to expand, LIB price will likely keep decreasing, eventually approaching the cost of the chemicals that make up the cell. In other words, material cost sets the floor on the battery cost. In general, battery chemistries that contain earth-abundant elements such as LFP are more favorable in terms of cost reduction in the long term.

Intensive research efforts have been put into LIB technology to improve energy and power densities, extend lifetime, reduce cost, and meanwhile maintaining safety. A majority of the ongoing research focuses on material innovation, altering the existing battery materials or developing new materials to enhance the battery performance. The properties of the individual components that make up a LIB cell play important roles in determining the battery performance, and thus material innovation could be an effective way towards LIB technology enhancement. For the cathode, current research focus is on high-capacity and high-energy materials to boost energy and power densities. The advanced cathode materials tend to have decreased cobalt content, and increased manganese and nickel contents, which also benefits the cost.[29,30] For the anode, materials that enable higher energy density and increased cycle life are highly sought after. Of the emerging materials, titanate-based materials demonstrate potential for stationary storage systems due to their superior stability that enables long cycle life.[29,31] Besides the electrodes, some material-focused research efforts are also devoted to other components in the LIB cell, such as electrolytes with improved stability and transport properties, innovative separator materials that enhance battery safety, etc.

Besides material innovation, battery performance and safety can also be enhanced through better design and engineering at multiple scales. At the cell level, some of the ongoing research includes optimizing the electrode microstructure and thickness to enhance ionic and electronic transport properties; altering the capacity balancing of the two electrodes (N/P ratio) to reduce degradation; investigating different cell geometrical designs to enhance cell heat dissipation capabilities. At the module and pack levels, researchers have been exploring different heating and cooling system designs and control strategies to maintain the battery at optimal operating temperature;[32] the design of advanced Battery Management Systems to effectively monitor and balance the individual cells in a large storage system has also attracted some attention.[9,33]

2. Convection-enhanced Li-ion Batteries

Developing new battery cell architectures offer a promising route to advancing performance, building upon, and potentially outpacing, traditional material-based innovations. Recent advancements, including BYD's blade battery,[34] CATL’s Qilin battery,[35] and Tesla’s 4680 battery,[36] have attempted to address energy and power density needs by adopting larger cell sizes and minimizing redundant “non-energy-storing” pack components. While these improvements increase energy content and reduce bills of material, challenges persist. Key amongst these are the difficulties in managing heat dissipation, a problem that becomes increasingly pronounced with larger cell and pack sizes.[37] Additionally, these cell-to-pack innovations do not effectively address the high-rate charging and discharging limitations inherent in current LIB cell designs. In this thesis, I investigate an alternative LIB cell design, the “lithium-ion convection battery”, which aims to address the fundamental limitations of current LIB cell designs, and streamlines cell-to-pack integration by removing unnecessary components. In this configuration, electrolyte is circulated through the cell, passing through the porous solid electrodes and separator, to overcome mass and heat transfer limitations.

2.1. Prior work in literature

The convection battery concept was arguably first proposed and demonstrated in the peer-reviewed literature by Suppes and coworkers.[38] The initial study used an aqueous Zn/MnO_2 chemistry in a packed bed configuration, and the authors reported that electrolyte convection enables the use of a larger separator distance, which can potentially be used to improve the safety of batteries with metal electrodes (e.g. reduced dendrite formation and associated shorting).[38] The authors also showed that arresting electrolyte flow during cell discharge increases voltage losses. In follow-up work, the same authors described a non-aqueous $LiFePO_4$/graphite chemistry in a packed bed configuration with 6 mm electrodes.[39] In this second study, they showed that convection can enable a greater fraction of the theoretical capacity to be accessed but, this increase was from 9% (without flow) to 25% (with flow) ,which is significantly less than what is routinely achieved in coin cell configurations.[39] Beyond this experimental work, theoretical analyses were pursued to understand how bulk flow reduced concentration gradients within the cell.[40,41] Specifically, Suppes and co-workers developed a one-dimensional model which illustrated that, if high enough (here, 118 μm/s), electrolyte superficial velocity can flatten the ion concentration profile across the cell and increase limiting current.[40] Additionally, the model confirmed that convection lowers cell overpotential, consequently improving voltaic efficiency.

2.2. Prior work in the Brushett Group

Inspired by this prior work, our research group began exploring convection batteries in 2016 initially developing a prototype cell to assess practical feasibility (**Figure I-5)**. The cell was constructed with ~5 mm thick, freestanding, pressed-pellet electrodes based on an aqueous Prussian blue analogue chemistry and featured rapid redox kinetics, inexpensive constituent elements, and simple synthesis.[42] The specific model chemistry considered was the following (with 1 M NaCl used as the electrolyte):

$$Cu^{II}Na[Fe^{III}(CN)_6] + Na^+ + e^- \longrightarrow Cu^{II}Na_2[Fe^{II}(CN)_6] \qquad \text{E = 0.98 V vs. SHE}$$

$$Fe^{III}Na[Fe^{II}(CN)_6] + Na^+ + e^- \longrightarrow Fe^{II}Na_2[Fe^{II}(CN)_6] \qquad \text{E = 0.41 V vs. SHE}$$

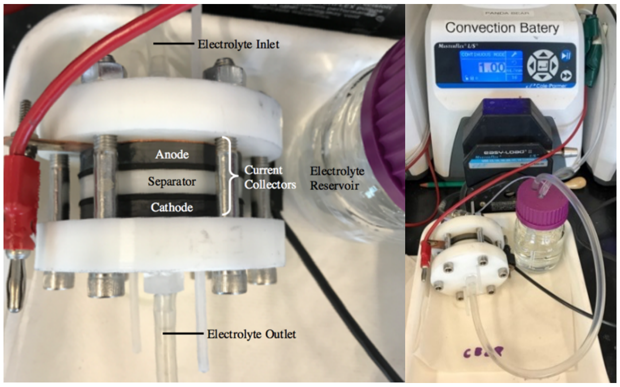

Figure I-5: *The prior cell prototype in our lab. The cell uses ~5mm thick freestanding electrodes.*

Using a constant volume flowrate of 1 mL/min, the prototype cell demonstrated stable coulombic (99%), voltaic (74%), and energy (74%) efficiencies, for over 1500 charge/discharge cycles at a C/2.5 rate, corresponding to stable cycling over 10 months. A ca. 25% increase in capacity is observed for cycles with flow turned on, which confirms that convection can help enhance performance. While generally successful, it was challenging to systematically optimize the prototype by varying experimental conditions. The effectiveness of flow has a complex dependence on a combination of electrode properties, electrolyte composition, and cell operating conditions, such that sometimes flow enabled capacity enhancement and other times it did not. Additionally, the prototype cell design enabled access of ca. 60% of the theoretical capacity, which is significantly higher than prior convection battery work, but still lags behind conventional coin cell configuration. Finally, while useful as a model redox chemistry, the Prussian blue analogues do not afford a high cell voltage (0.57 V) limiting both energy and power density.

3. Thesis Scope and Outline

In the quest to optimize cell performance, our exploration leads us to several pivotal areas of inquiry. From a fundamental standpoint, we are drawn to questions such as: (1) What benefits can electrolyte convection offer in enhancing cell performance? (2) Under which conditions are these benefits maximized? (3) What level of flow is necessary to realize these enhancements? Beyond fundamental aspects, we must also delve into engineering considerations to evaluate the practical feasibility of implementing this approach. Key questions in this regard include: (1) How much additional electrolyte is required to achieve the anticipated benefits? (2) How does the pumping loss weigh against the energy gains? (3) What are the potential applications for the convection battery concept?

This thesis is propelled by the quest to answer these questions, utilizing simulation tools to shed light on these critical issues and offer actionable insights in the realm of Li-ion battery chemistry. The focus on Li-ion chemistry is due to its predominant role in contemporary battery applications and the availability of comprehensive modeling tools for its study. It is important to clarify that the objective of this thesis is not to finalize an optimized system; rather, the aim is to assess the viability of the convection battery approach and its potential worthiness for further experimental investigation. The selection of Li-ion chemistry and the specific cell and system designs employed in this work serve solely to facilitate this exploration and to address the pertinent questions identified earlier. Consequently, the designs and models presented herein should be regarded as initial, conceptual frameworks, which are likely to evolve significantly towards a fully realized engineered solution. This work is, at its core, an exploratory endeavor meant to lay the groundwork for future innovation and experimentation.

This thesis unfolds over several chapters, each addressing a unique facet of the Li-ion convection cell, beginning with the fundamental inquiries in **Chapters II** through **IV**. In **Chapter II**, I explore how electrolyte convection can enhance mass transport within the electrolyte. I introduce the LIONSIMBA+c model, an extension of the existing Li-ION SIMulation BAttery (LIONSIMBA) Toolbox,[43] adapted to perform isothermal simulations for the sandwich cell layer of a Li-ion convection battery. Through dimensional analysis, I pinpoint conditions under which convection provides the most performance enhancement and address critical considerations such as the required flow rate and the limits of performance improvement through electrolyte flow. **Chapter III** shifts the focus to the impact of electrolyte convection on thermal transport. I further refine the LIONSIMBA+c model to conduct non-isothermal simulations, examining how convection influences cell temperature regulation. This chapter contrasts the efficacy of internal cooling, achieved via electrolyte flow, with traditional external thermal management strategies. **Chapter IV** complements the findings of the preceding chapters by applying analytical methods to investigate the transient behaviors of electrolyte concentration and cell temperature. It also examines the temperature distribution across multiple layers of the sandwich cell configuration utilized in the LIONSIMBA+c simulations, providing a holistic view of the concentration and thermal dynamics within the convection-enhanced LIB cell.

The latter half of the thesis, starting with **Chapter V**, examines practical considerations of implementing a convection battery system. It discusses the additional electrolyte requirements for achieving the previously outlined mass and thermal transport benefits. A COMSOL-based model of the convection battery sandwich cell layer is developed to simulate various Li-ion chemistries. This model includes a 1D representation of the electrolyte recirculation loop, offering a more realistic analysis of electrolyte dynamics within the loop compared to a simplified storage tank model. **Chapter VI** synthesizes the accumulated knowledge, proposing a potential design for the convection battery system and its applications. This chapter introduces a system design model and a COMSOL-based 2D simulation capable of depicting the temperature dynamics within a large stack of sandwich cell layers, showcasing the practical applicability of the convection battery concept. In the concluding **Chapter VII**, I reflect on the future research avenues and the design considerations essential for the advancement and realization of the convection battery technology.

4. Key Assumptions Underpinning the Thesis

Throughout this thesis, the model and analyses are predicated based on several foundational assumptions critical for the framework of the investigation, which include:

(1) *The porous electrodes are permeable to flow while remaining mechanical integrity under flowrates at least up to 10 μm/s.*

(2) *The Kozeny-Carman equation provides a reasonable approximation of the pressure drop and associated pumping energy through the electrodes.*

(3) *The flow can be uniformly distributed across the entire electrode area.*

While a Li-ion convection cell in the configuration considered in this thesis has not been explicitly demonstrated in existing literature, there is a confluence of related knowledge in literature and unpublished work from our laboratory that supports the plausibility of these assumptions. First, initial prototypes of the convection battery, both from the literature and our lab as discussed in

Section 2, provide a foundational proof that electrolyte convection can flow perpendicularly through battery electrodes to enhance cell performance. Although these prototypes differ in electrode configuration, fabrication method, and battery chemistry from the system considered in this thesis, they highlight the practicality of the core concepts. Additionally, the development of systems containing flow-through porous electrodes has a long history,[44] and one recent advancement includes electrochemical flow reactors for lithium extraction from natural brines, which may offer valuable insights for convection battery design.[45–47] These reactors employ electrodes made from $LiMn_2O_4$ coated on petroleum coke particles[48] or carbon cloth[46,49], and are designed in either flow-by or flow-through configurations. The pressure drop measured in the flow-through cells[46] is comparable to the predictions made by the Kozeny-Carman equation for the convection battery cell in this work. Moreover, technologies like redox flow batteries and flow-through capacitive deionization systems, which bear resemblance to the convection battery, have seen significant technological progress. Insights from these systems, such as strategies used to uniformly distribute fluid flow, could be instrumental in the development of the convection battery system. Second, the current landscape of lithium-ion batteries (LIBs) predominantly features electrodes that are not permeable to flow, primarily due to the solid current collectors that support the electrode coating. However, our lab is developing alternative LIB electrode fabrication techniques that promise to circumvent this limitation. Specifically, we are exploring a modification of the conventional LIB electrode fabrication method to coat electrode material on a flow-permeable current collector. Furthermore, our lab's experience with non-solvent induced phase separation (NIPS) for developing redox flow battery electrodes offers a nuanced approach to controlling electrode microstructure for optimal flow dynamics. These innovative strategies, alongside other potential fabrication techniques, could offer a promising path for the convection battery development. Lastly, the envisaged flow rate in this thesis, particularly to harness the mass transport benefits discussed, can be as low as approximately μm/s. At such low flow rates, the associated pressure drop is expected to be minimal, and it is unlikely that the mechanical stability of the electrode will be compromised. The intricate trade-offs and challenges associated with higher flow rates to achieve thermal transport benefits in a large battery system are examined in **Chapter VI**. The subsequent sections delve into more detailed discussions on each of the three assumptions mentioned above.

4.1. Flow-permeable electrode

To facilitate electrolyte flow through the electrodes, conventional current collectors used in current LIBs, which are impermeable, must be replaced with alternative designs. Potential replacements include perforated or mesh current collectors, which are not only commercially available but have also been successfully employed in various electrochemical systems.[50,51] Leveraging such flow-permeable current collectors, our lab has adeptly fabricated LIB electrodes with cohesive coatings using the traditional slurry-casting method. Subsequent flow break-through experiments on these electrodes demonstrated their permeability to the testing fluid (water) while affirming their structural integrity post-experimentation. These preliminary findings are indicative of the potential to develop flow-permeable LIB electrodes that can withstand operational demands.

While the perpendicular flow of electrolyte through the electrodes is not achievable with conventional LIBs due to the impermeable nature of the current collectors, studies have shown that electrolyte flow parallel to the electrode does occur during the operation of LIB cylindrical cells.[52–54] This flow is driven by the net volume change in the electrodes during charging and discharging cycles, compelling the electrolyte to move in and out. This effect is particularly pronounced in silicon-containing anodes. The widespread commercial availability and reliable performance of LIB cylindrical cells, with their respectable cycle lives, indicate that such electrolyte flow does not adversely affect cell functionality. Furthermore, when considering flow in the perpendicular direction as in the convection battery, it is conceivable that the separators could provide an additional safeguard against material leaching, thereby maintaining the integrity of the electrode.

4.2. Pressure drop and pumping loss

In evaluating the viability of the convection battery concept, it is essential to weigh the energy gains against the potential drawbacks of pressure drop and pumping loss. Excessive pumping energy, when compared to the gained energy, can render the concept inefficient. This is particularly pertinent given the novelty of the flow-through Li-ion electrode configuration examined in this study, which lacks precedent in existing literature and, consequently, empirical data on pressure drops. To bridge this gap, we utilize the Kozeny-Carman equation, a widely recognized method for estimating pressure drops and pumping losses. In this section, we explore the foundational assumptions of the Kozeny-Carman equation, evaluate its applicability to the convection battery system, and conduct a sensitivity analysis. This analysis aims to reveal the impact of any discrepancies between theoretical assumptions and the actual behavior of the convection battery on our pressure drop estimates.

Kozeny-Carman equation derivation and relevant assumptions

The Kozeny-Carman equation is a useful framework for analyzing the pressure drop in porous media during creeping flow (i.e. Re << 1). In the context of the convection battery, we consider flow rates up to 1000 μm/s, leading to a maximum Reynolds number of:

$$Re_p = \frac{v_s d_p \rho}{(1-\varepsilon)\,\mu} = \frac{1000\,\mu m/s * 10\,\mu m * 1.25\,kg/cm^3}{(1-0.4) * 0.05\,P} * \left(\frac{1\,cm}{10^4\,\mu m}\right)^2 = 4.2 * 10^{-3} \ll 1 \qquad \text{(I-1)}$$

Where the electrolyte is assumed to be LP30 in which the viscosity and density is well tabulated in the literature.[55] This calculation suggests that the Kozeny-Carman equation applies to the convection battery across the entire range of flow rates examined.

The Kozeny-Carman equation is derived from the framework that creeping flow through a porous medium can be approximated by Hagen-Poiseuille flow through a bundle of tortuous channels of some homogeneous mean effective path length L_{eff}. This results in the well-known form of the equation:

$$\frac{\Delta P}{L_0} = v_s \frac{K\mu}{\phi_s^2 D_p^2} \frac{(1-\varepsilon)^2}{\varepsilon^3} \tag{I-2}$$

Where L_0 is the total length, v_s is the superficial velocity, K is a dimensionless constant, μ is the fluid viscosity, ε is the porosity, and Φ_s is the sphericity of the particles with diameter D_p. The explicit derivations can be found in Carman's original paper or alternative texts.[56,57] In particular, note that this equation is semi-empirical in nature, in that the dimensionless constant K is typically defined to be 180 based on fitting of experimental data across a wide regime of porosities, media, and fluid velocities as was carried out by Forchheimer.[58][*] Further, there are several explicit assumptions made in deriving this equation that could be challenged by realistic systems. Therefore, in order to appropriately apply this equation for calculation of pressure drop in flowing the electrolyte through the porous electrode, we carefully consider these assumptions:

(1) Channels in porous media have a hydraulic tortuosity of $\tau_{hyd} = \sqrt{2}$. This assumption was put forth because the streamlines in the experiments conducted in the work analyzed by Carman were

---

[*] Note that on occasion it is defined to be 150, but this is likely to be simplification from the Ergun equation[59] rather than explicit fitting for creeping flow, and therefore likely less accurate.

angled at 45° from the mean flow direction such that the effective path length was longer than the bulk media by this factor. However, this factor was wrapped into the dimensionless constant K by Carman, likely because the tortuosities in such setups did not substantially vary. In practice it is of interest to instead rewrite the equation in a general form as many practical systems are likely to have tortuosities different from those observed by Carman:

$$\frac{\Delta P}{L_0} = v_s \frac{K' \mu \tau_{hyd}^2}{\phi_s^2 D_p^2} \frac{(1-\varepsilon)^2}{\varepsilon^3} \tag{I-3}$$

Where K' is the new dimensionless constant not incorporating the tortuosity. It is noteworthy that the tortuosity is squared—this is because the tortuosity must be applied twice: once to correct for the difference in path lengths, and a second time in correcting for the difference in channel and superficial velocities.[60] In battery electrodes, porosities have been commonly found to vary between 1 and 5[61]—those with tortuosity greater than $\sqrt{2}$ would be underestimated by the commonly utilized Kozeny-Carman.

(2) Particles that are spherical do not touch. If particles were to touch, this would modify their accessible surface area which directly correlates to pressure drop via induced viscous drag. In real cases, it is likely that particles are not perfectly spherical and, therefore, overlap to some extent. Deviations from Kozeny-Carman for non-spherical particles are well documented in the literature, in which the resulting K value can vary by as much as a factor of two. Still, we note that this analysis was limited to well-defined shapes such as cylinders and plates, and not irregular shapes such as quadrilobes which tend to have greater deviations.

(3) Particle sizes are uniform. For spherical particles of uniform size, the Kozeny-Carman equation holds very well over a large range of sizes. However, it has been documented that for porous media composed of a mixture of spheres of size ratio 5:1 or greater in near equal proportions, the pressure

drop can deviate substantially from that calculated using Kozeny-Carman, even when accounting for the mean particle diameter via a Sauter diameter.[57]

Use of Kozeny-Carman in related fields

The Kozeny-Carman has found utility in many fields including packed bed catalysis, electrochemical flow-through separations for water treatment, and electrochemical storage. Although this framework has not been validated for flow through slurry-cast electrodes, we hold that its deployment and experimental validation in similar systems warrants its use. We highlight two instances of this in the literature as key examples.

As mentioned, the Kozeny-Carman equation has been utilized in packed bed reactors (PBRs), especially in three phase systems in which there is a mixed gas-liquid feed. In one instance, a gas-liquid feed comprised primarily of dimethyl acetamide (DMAc) was fed into a PBR with a 4.6 mm diameter, not too dissimilar to that utilized in the LIB literature.[62] This reactor was structured to have a 2 cm long calming chamber at the inlet composed of 75 μm diameter glass beads—only slightly larger than secondary particles in common metal-oxide cathodes—to enhance fluid dispersion at the inlet. This chamber had a porosity of 0.36, again similar to electrodes manufactured for LIBs. The catalyst bed was packed above the calming chamber with particles on the order of 200 μm at a porosity of 0.73. Based on the volumetric flow rates tabulated, the fluid was flowed between approximately 1000-2500 μm/s, similar or slightly higher than the expected operating window for the convection battery.

In evaluating pressure drops across the entire bed, it was found that the calming chamber dominated. Further, while at the lower flow rates the Kozeny-Carman equation underpredicted the experimental pressure drop by approximately a factor of 3, it perfectly matched the values at higher flow rates. However, it was noted in the discussion that there were system instabilities in maintaining the pressures due to the complexity of the multiphase hydrodynamics, which may contribute to the deviation of the Kozeny-Carman equation at the lower flow rates—experimentally, the values found here tended to have larger experimental error.

In the LIB field, Kozeny-Carman has been utilized in assessing mechanical failures under loading.[63] Specifically, it has been employed to describe electrode permeability in stress models. It was found that when the analytical solution derived from the Kozeny-Carman framework was fitted to experimental data it yielded a nearly perfect correlation, with particle sizes nearly identical to that of the secondary particles. It should be noted that when numerical results with certain assumptions relaxed were used to fit the experimental data, the fit using the primary rather than the secondary particle size yielded the best results; however, it is possible that other inherent assumptions not accounted for in the model may have led to the deviation, for which altering the particle size enabled an improved fit. It is also possible that the primary particle size enabled improved fitting because placing the electrode under mechanical stress similar to that in calendar led to deformation and cracking of the secondary particles into its primary particle components. This process has been well-documented in the literature, where additional calendaring can facilitate improved total surface area as a result of secondary particle fracturing, and may not adequately represent convection battery.[64]

The collective evidence from the literature supports the adoption of the Kozeny-Carman framework for our system-level analysis. We are currently conducting experiments to further validate these theoretical estimations.

Sensitivity analysis with the Kozeny-Carman equation

Building on the preceding discussion, the Kozeny-Carman equation is utilized in this thesis work to elucidate the interplay between pressure drop, pumping power, and performance of the convection battery concept. We adopt a conventional dimensionless constant K of 180, reflecting a hydraulic tortuosity of $\sqrt{2}$, and use the average size of the secondary particles with a sphericity of 1 that align with their typical shape. A sensitivity analysis, illustrated in **Figure I-6**, assesses the potential variances in pressure drop should the practical conditions diverge from these theoretical assumptions. The baseline parameters for this analysis include particle size (D_p) of 10 μm, hydraulic tortuosity (τ) of $\sqrt{2}$, linear flow velocity (v_s) of 10 μm/s, and an electrode porosity (ε) of 0.4.

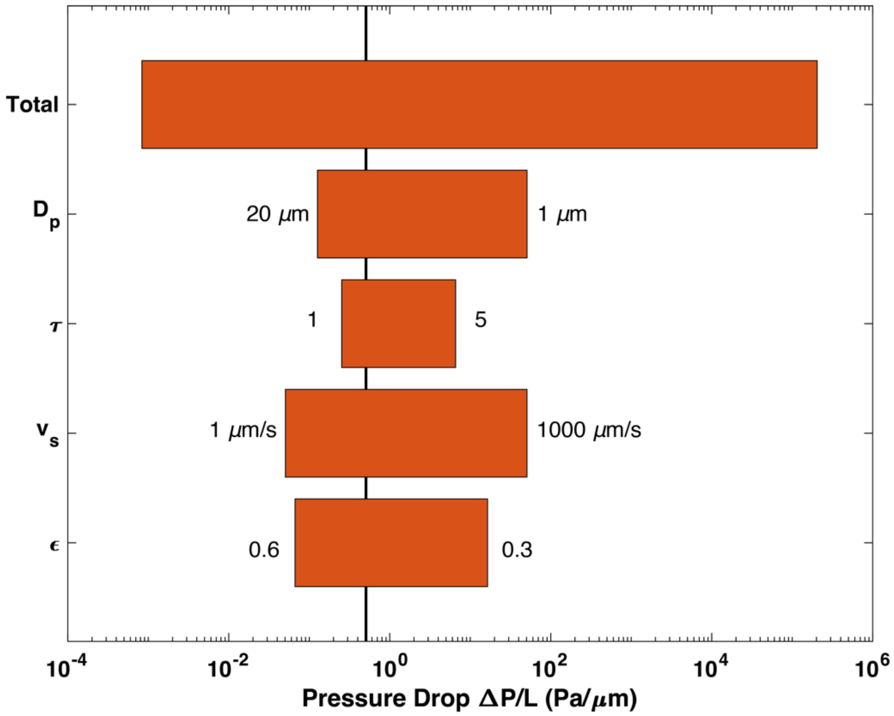

Figure I-6: *Sensitivity analysis of the pressure drop calculation with the Kozeny-Carman equation. In the based case, the particle size (D_p) is 10 μm, the electrode hydraulic tortuosity (τ) is $\sqrt{2}$, the flow linear velocity (v_s) is 10 μm/s, and the electrode porosity (ε) is 0.4.*

It should be noted that the electrode microstructure (electrode porosity and tortuosity) is a factor that can be controlled with the appropriate fabrication techniques. As previously stated, our research group is working on developing an Li-ion fabrication electrode using the NIPS method, which is capable of fine tuning the electrode microstructure for the desired flow dynamics. Prior work from our research group with NIPS-fabricated electrodes has demonstrated flow permeabilities of at least 10 Darcys for porosities between 0.5 and 0.8.[65] Additionally, Palagonia et al. have developed a flow-through reactor design for lithium brine extraction that is similar to the Li-ion convection battery configuration discussed in this thesis.[46] This design uses porous $LiMn_2O_4$ and $KNi[Fe(CN)_6]$ electrodes, hand-painted onto 250 μm-thick carbon cloths using a slurry composition similar to that for LIB electrodes. Experimental data shows that a cell with two electrodes and a separator, covering a 1.1 cm^2 area, exhibits a hydraulic resistance of 130 mbar min/mL. Assuming a separator thickness of 20 μm, this configuration results in a pressure drop of 4.6×10^{-4} Pa/μm at a flow rate of 10 μm/s, substantially lower than the values predicted in **Figure I-6**. Based on these findings, we anticipate that it is feasible to produce Li-ion electrodes for the convection battery that exhibit favorable flow permeability, even at lower porosities than these prior demonstrations. Furthermore, the development of fabrication techniques aimed at reducing tortuosity presents additional opportunities to decrease pumping losses.[66,67]

4.3. Uniform flow distribution

In this thesis, the efficacy of the convection battery is predicted based on the assumption that the electrolyte flow is uniformly distributed within the cell. While the demonstration of uniform flow is challenging in the absence of a comprehensive cell prototype, the concept of flow distribution is not novel and finds relevance across various fields. This inter-disciplinary relevance suggests that principles and strategies for achieving uniform flow in other systems could be adapted for the convection battery. For example, redox flow batteries, which also necessitate even flow distribution over extensive electrode areas, could provide valuable insights into potential solutions, such as different flow field designs.[68–70] Drawing from such analogies, we posit that the convection battery can achieve a similarly uniform flow with thoughtful engineering and design interventions.

To facilitate the even spread of electrolyte from the inlet throughout the cross-sectional area of the cell, several approaches are under consideration. One such strategy involves the integration of a flow or microfluidic distributor[71–73] at the inlet, which could uniformly direct the flow into the cell. Alternatively, employing multiple inlet ports could serve to evenly distribute the electrolyte across the cell. Further ensuring uniform flow within the cell, the design of perforated current collectors warrants careful consideration. The orifices in these collectors could be meticulously designed to double as flow distributors, thereby aiding in the uniform distribution of electrolyte flow. Moreover, the use of mesh current collectors, albeit necessitating novel electrode fabrication techniques, presents another viable avenue for achieving uniform flow. The electrode microstructure itself offers additional opportunities for promoting uniform flow distribution. For instance, the NIPS method could be employed to create electrodes with tailored anisotropic permeability, thereby enhancing flow distribution across the electrode surface.

II. A Study on the Impact of Convection on Electrolyte Mass Transport

1. Introduction

Ubiquitous in portable electronics and emergent in transportation and stationary applications, lithium (Li)-ion batteries arguably represent the state-of-the-art in electrochemical energy storage technology owing to their energy density, roundtrip efficiency, and cycle life.[6,74] While the past decade has seen a steady decline in battery price and concomitant increase in energy density due to a combination of materials development, manufacturing advances, and market scale,[75,76] current Li-ion batteries are challenged by the often incongruous requirements of emerging applications.[25,27] Of particular note is the need for rechargeable batteries with both high power and high energy density at a reasonable cost.[77] In the current cell format, sustained high power is frequently limited by diffusive transport losses, which necessitate the use of thin electrodes and separators.[25,78–80] This, in turn, leads to inactive components occupying a substantial fraction of the battery weight and volume, leading to higher subsequent energy storage costs.[81]

Most current research efforts focus on achieving performance improvements through material innovations including electrolyte formulations with reduced viscosity, increased conductivity, and high Li^+ transference numbers;[82–84] charge-storage materials with surface coatings or structuring to enhance intercalation rates;[85,86] cell chemistries with higher energy density due to increased capacity and/or voltage;[87–89] and electrode microstructures with reduced tortuosity and increased pore connectivity.[66,90,91] In contrast, few have contemplated cell engineering as a means of unlocking new pathways to performance and cost targets.[92–94] One potentially promising approach is the convection battery, in which electrolyte is circulated through the device to overcome mass transport limitations (**Figure II-1b**).[38–40,95] Forced convection enables a more uniform electrolyte concentration throughout the cell, in principle allowing for the use of thicker electrodes or operation at high currents while maintaining high accessed capacity.[39] Compared to the traditional sealed cell configuration (**Figure II-1a**), the convection format can offer several advantages including (1) electrodes with an increased and controllable ion flux, (2) improved safety and maintenance, (3) simplified manufacturing, and, ultimately, (4) reduced system costs.[39] Suppes and co-workers demonstrated proof-of-concept convection cells, in a packed bed configuration, for both aqueous (Zn-MnO_2) and non-aqueous (C-$LiFePO_4$) chemistries.[38,39] Notably, for the C-$LiFePO_4$ cell, which contained 6-mm-thick particle-bed-type electrodes, the authors observed an increase in accessed capacity from 10% to 25% for cells with stagnant and flowing electrolyte, respectively.[39] While these seminal experimental studies established that convection could improve cell performance, the prototype cell capacities were low, suggesting there are limits to this approach. To explain the impact of convection, Suppes and co-workers developed a simple electrolyte transport model that showed increasing superficial velocity reduced spatial concentration gradients within the cell thereby increasing the limiting current density and energy efficiency.[40] These findings were further supported by theoretical analysis of electrolyte transport through a porous separator by Kim and Monroe.[41] While these works serve an important role in demonstrating convection-enhanced intercalation batteries, the results are limited to just several cases of cell size, flow velocity, and operating current.

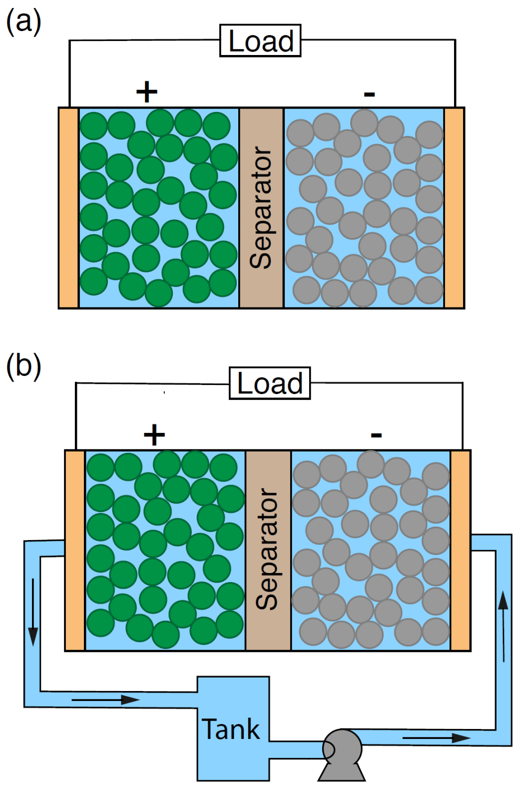

Figure II-1: *Intercalation battery configurations with an (a) enclosed cell design as is typical in most modern devices or (b) novel flow-through design that attempts to improve the effective diffusivity of the electrolyte. The additional hardware required in (b) consists of an external storage tank and pump to provide forced convection through the porous intercalation materials and separators that compose the battery cell.*

The past literature leaves key unanswered questions about the potential benefits of convection batteries in terms of ranges of geometric, physical, and operating parameters. It is critical to understand (1) the combinations of parameters that yield enhancement in convection battery performance relative to closed cells with no convection, (2) the upper limits to any enhancement, and (3) the transition behavior and output between these upper limits and corresponding closed cell cases. The intertwined nature of relationships between cell thickness, electrolyte flow rate, transport properties, and operating current and the resultant polarization, power output, and accessed capacity of the cell are unclear. Furthermore, there is no prior substantial body of results to understanding these relationships. To this end, we refine a Li-ion electrochemical model, perform a systematic study using a range of parameters, and present comprehensive representations of cell performance as a function of these parameters. In doing so, we describe the key scaling relationships and introduce dimensionless groups that describe the conditional efficacy of convection batteries.

Despite a paucity of convection battery models beyond the works described above, there is a rich history of mathematical modeling in Li-ion batteries.[96–98] Arguably the most widely-used approach is the porous-electrode theory based pseudo-two-dimensional (P2D) model originally developed by Newman and co-workers.[99] The model describes thermodynamics, electrochemistry, and transport phenomena in the cell via a set of tightly coupled partial differential-algebraic equations (PDAEs) with variations in cell length (x), active material particle radius (r), and time (t). This model has since been reformulated using different numerical techniques and implemented in programs such as DUALFOIL,[100] COMSOL,[101] and Battery Design Studio.[102] More recently, Braatz and co-workers translated this model to MATLAB to increase usability, and have since termed their updated model the Li-ION SIMulation BAttery Toolbox (LIONSIMBA).[43] Here, we leverage and extend this pre-existing framework to describe convection in Li-ion cells.

In this work, we seek to provide more comprehensive insight into the impact of convection on the cell-level performance of Li-ion batteries. Specifically, we modify the LIONSIMBA software to incorporate a convection term in the Nernst-Planck equation, amend the boundary conditions to allow for electrolyte flow into and out of the cell, and introduce an electrolyte tank. The new open-source package, LIONSIMBA+c, is first validated against the original software and then used to generate more than 50,000 battery discharge curves as a function of cell dimensions, electrode, electrolyte, and separator properties, as well as electrochemical and fluid dynamic operating conditions. Through dimensional analysis, this simulation-based data set can be described compactly through relative scales of dimensionless groups, which both reveal cell-level performance trade-offs and indicate regions where convection is an effective means of boosting performance. While we focus only on cell-level performance enhancement and do not include discussion on system-level designs and trade-offs, we anticipate that the insights provided by this study will inform future cell engineering campaigns and may inspire further investigation of convection-enhanced energy storage systems.

2. *Model Development*

As discussed in the Introduction, LIONSIMBA has been previously validated against COMSOL MultiPhysics commercial software[103] and Newman's Fortran DUALFOIL[100] simulations to demonstrate the accuracy of its predictions to Li-ion battery operation.[43] LIONSIMBA uses a P2D model[44,99] to generate a set of PDAEs by assuming that the cell is perfectly mixed radially, but may contain spatial temperature, concentration, or potential gradients in the axial dimension. The set of PDAEs is subsequently reformulated into ordinary differential-algebraic equations (DAEs) using finite volume method (FVM) by partitioning the spatial domain into discrete volumes or cells, each with constant properties due to the assumption of being perfectly mixed, and approximating the fluxes through the surfaces of these cells and the rate of generation within in terms of the volume averages. Through the FVM formulation, as opposed to a finite difference solution, boundary conditions involving a specified external flux may be treated exactly, rather than as an approximation. This system of equations is solved numerically using the IDA solver produced by Lawrence Livermore National Laboratory, which uses a variable-order, variable-coefficient backwards differentiation formula.[104] To enable the desired extensions to LIONSIMBA, we needed to make the changes described in greater detail in the following paragraphs: (1) introduce the convection term to the Nernst-Planck equation, (2) modify the boundary conditions to the cell to account for forced convection at the boundaries, (3) gauge the conservation of anions within the external tank, and (4) calculate the electrode active area as a function of its porosity.

The convective flux term of the Nernst-Planck equation originally excluded from LIONSIMBA is necessary to model electrolyte forced through the intercalation cell by an external pump. Although the heat transfer equations were also modified to account for electrolyte flow, for the remainder of this work we assume isothermal operation to limit our focus to the connection between mass transfer and cell performance. The effects of heat-transfer and the possibility for the use of convection to limit thermal excursions are beyond the scope of this initial study, but will be contemplated in future work. Eq. (II-1) shows the modified species conservation equation which includes the convective transport term (See Section 8.5 for detailed derivation).

$$\varepsilon_i \frac{\partial c_e(x,t)}{\partial t} = \frac{\partial}{\partial x}[D_{\text{eff},i} \frac{\partial c_e(x,t)}{\partial x}] - v \frac{\partial c_e(x,t)}{\partial x} + \begin{cases} a_i(1-t_+) j(x,t) & \text{if} \quad i \in \{p,n\} \\ 0 & \text{if} \quad i \in \{s\} \end{cases} \tag{II-1}$$

Here ε_i is the fractional porosity of domain *i*, where $i \in \{p, s, n\}$ indicates the positive electrode (*p*), separator (*s*), or negative electrode (*n*) respectively, $c_e(x,t)$ is the anion concentration, which is equivalent to the cation concentration via the assumption of bulk electroneutrality, at position *x* and time *t*, $D_{\text{eff},i}$ is the effective diffusion coefficient, *v* is electrolyte superficial velocity through the cell, which is constant by the assumption of constant fluid density within the cell, a_i is the total particle surface area per unit volume of the electrode, t_+ is the Li^+ transference number, and $j(x,t)$ is the ionic flux averaged over the interfacial area between the matrix and the pore solution. To avoid undue complication to the analyses, we neglect axial dispersion due to velocity variation in transverse directions. Based on estimations using Sherwood et al. for porous media flow,[105] this neglect is reasonable at the typical low velocities used in the model. For the fraction of high velocity cases, convection in the primary flow direction already dominates transport and causes spatial uniformity in concentration. Hence, we expect that axial dispersion from convective spreading only slightly enhances performance beyond the results of the present study. Another acceptable model approximation is the theory of dilute solutions rather than concentrated solutions. Although dilute solution treatment overlooks some effects, such as, slight variations in density and velocity, importantly, the approach is particularly appropriate for major objectives of the work. In the identified upper limits of convection cell performance at high flow rates, concentrations remain relatively uniform and near inlet values. Then, to explain conditional convection cell performance enhancement, dilute solution theory enables the model to capture the trends and competition of transport modes.

The boundary conditions can be treated in a similar fashion to the original LIONSIMBA model, such that there is no diffusive flux entering or exiting the cell domain, but, due to forced electrolyte motion, convective fluxes now traverse these boundaries. This can be rationalized by considering a convection battery cell connected to the external tank with tubes that have cross-sectional area significantly smaller than that of the cell, the joints of which are thus dominated by strong convection and the diffusive fluxes are negligible in comparison. The cell boundaries specified by Eq. (II-2), as visualized in **Figure II-2**, result in a zero-derivative at the positions $x = \hat{x}_0 = 0$ and $x = \hat{x}_n = \Sigma L_i$, where ΣL_i is the total thickness of the electrodes and separator.

$$\left.\frac{\partial c_e(x,t)}{\partial x}\right|_{x=\hat{x}_0,\hat{x}_n} = 0 \tag{II-2}$$

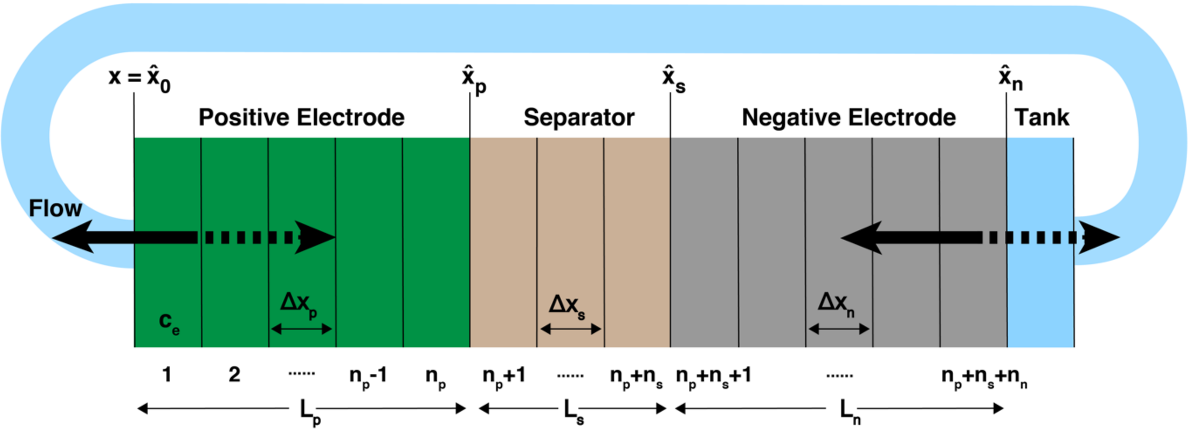

Figure II-2: *The finite volume discretization and domain used for simulations of the convection battery in the LIONSIMBA+c model. The nodes are numbered from the left, starting at* $x = \hat{x}_0$ *for the left boundary of* $N = 1$ *to* $x = \hat{x}_n$ *for the right boundary of* $N = n_p + n_s + n_n$*. The diagram shown above is for the situation of flow from the negative electrode to the positive electrode such that the tank is located at a fictitious node* $N+1$*; however, if the flow were reversed, the tank would be located at a fictitious node 0.*

In addition to requiring the inclusion of the convection term, an open system with forced convection from an external holding tank with complete recycling requires a conservation equation on this feed material. By assuming the tank is well mixed, it can be treated as a fictitious node external to the battery cell components. When electrolyte flows from the negative electrode to the positive electrode, a material balance on the tank gives Eq. (II-3).

$$V_{\text{tank}} \frac{dc_{\text{tank}}(t)}{dt} = A_{\text{tube}} v_{\text{tube}} [c_{e,1}(t) - c_{\text{tank}}(t)] \qquad \text{(II-3)}$$

While the superficial electrolyte velocity in the tubes entering and exiting the tank, v_{tube}, is unknown, at steady state and by assuming constant fluid density, the continuity equation simplifies to $A_{\text{tube}} v_{\text{tube}} = A_{\text{cell}} v$, where A_{cell} and A_{tube} are the cross-sectional areas of the battery cell and the tube, respectively. Using this relationship, the unknown tank velocity can be substituted for known values, resulting in Eq. (II-4), which we use as the modeled conservation equation for anion concentration in the tank, c_{tank}, while simultaneously solving for all other concentrations within the battery pack.

$$\frac{dc_{\text{tank}}(t)}{dt} = \frac{A_{\text{cell}}}{V_{\text{tank}}} v[c_{e,1}(t) - c_{\text{tank}}(t)] \tag{II-4}$$

Lastly, whereas the original LIONSIMBA model allowed independent selection of the spherical radius of solid particles, R_p, electrode porosity, ε, and volumetric surface area, a, in reality these parameters will be interdependent, in accordance with Eq. (II-5). As such, we include this relationship in our updated model, to better reflect the physical limitations that are inherent to solid materials.

$$a = \frac{3}{R_p}(1 - \varepsilon - \varepsilon_{\text{filler}}) \tag{II-5}$$

Additionally, while the original LIONSIMBA modeled solid electrolyte conductivity in isothermal operation,[106] it contained relationships for liquid electrolyte conductivity in the non-isothermal case, which we adapted for LIONSIMBA+c by fixing the temperature (Eq. (II-10)). Although dilute solution theory would predict correlation between the diffusivity, transference number, and conductivity,[107] in this work we treat these as independent parameters to provide a broad understanding of the device design space without limiting model applicability in concentrated solution conditions or alternate electrolytes.

Given the analytical modifications to the original n_p, n_s, and n_n control volumes in the positive electrode, separator, and negative electrode, respectively, the finite volume equations for interior points can be determined by assuming that each node is perfectly back-mixed, resulting in the set of equations shown in Eq. (II-6).

$$\varepsilon_i \frac{\mathrm{d}c_{e,k}(t)}{\mathrm{d}t} = D_{\mathrm{eff},k+\frac{1}{2}} \frac{[c_{e,k+1}(t) - c_{e,k}(t)]}{\Delta x_i^{2}} - D_{\mathrm{eff},k-\frac{1}{2}} \frac{[c_{e,k}(t) - c_{e,k-1}(t)]}{\Delta x_i^{2}} + v \frac{[c_{e,k+1}(t) - c_{e,k}(t)]}{\Delta x_i} + \begin{cases} a_i(1-t_+)j_k(t) & \text{if} \quad i \in \{p,n\} \\ 0 & \text{if} \quad i \in \{s\} \end{cases} \tag{II-6}$$

We discretize the convection term using upwind differencing scheme due to its stability and robust convergence behavior, and its accuracy is adequate for the purpose of this study.[108] Throughout this study, we assume that the electrolyte flows from the Li$^+$-generating electrode (negative during discharge; solid arrow in **Figure II-2**) to the Li$^+$-consuming electrode (positive during discharge) as this minimizes electrolyte salt depletion at low flowrates (Section 8.3**)**. In these equations, Δx_i is the width of each node in domain *i*, and *k* the index of the node being considered. The boundary conditions given by Eq. (II-2) can similarly be discretized by considering anion conservation within nodes 1 and *N* assuming perfect mixing, resulting in Eq. (II-7) and (II-8) respectively, where $N = n_p + n_s + n_n$.

$$\varepsilon_p \frac{dc_{e,1}(t)}{dt} = D_{\mathrm{eff},1.5} \frac{[c_{e,2}(t) - c_{e,1}(t)]}{\Delta x_p^{2}} + v \frac{[c_{e,2}(t) - c_{e,1}(t)]}{\Delta x_p} + a_p(1-t_+)j_1(t) \tag{II-7}$$

$$\varepsilon_n \frac{dc_{e,N}(t)}{dt} = -D_{\mathrm{eff},N-0.5} \frac{[c_{e,N}(t) - c_{e,N-1}(t)]}{\Delta x_n^{2}} + v \frac{[c_{\mathrm{tank}}(t) - c_{e,N}(t)]}{\Delta x_n} + a_n(1-t_+)j_N(t) \tag{II-8}$$

To ensure that the aforementioned changes made for LIONSIMBA+c did not generate unexpected deviations from the original model, we compare simulated discharge curves using both LIONSIMBA and LIONSIMBA+c with stagnant electrolyte at different C rates, defined as the applied current density normalized by areal capacity. **Figure II-7** shows no difference between the model outputs, indicating that the modifications did not introduce artificial changes to the expected behavior.

While the previous sections describe the modifications made to the LIONSIMBA toolkit to create LIONSIMBA+c, the task of effectively sampling the battery operating space to elucidate the regimes in which forced convection may be used to improve battery performance remains daunting given the number of possible engineering variables. To this end, for early investigation not shown, we leverage Monte Carlo methods which generate a random battery system with unique electrolyte properties and subsequently examine the impacts of stochastically selected applied current densities and forced flow velocities within the battery. For the plots shown, we used dimensionless group values to generate simulation conditions that uniformly cover the entire space and then back calculate the electrolyte properties, applied current density, and forced flow velocity. **Table II-1** shows the critical parameter value ranges used for this sampling procedure, and the base parameter values selected for any un-sampled values, while **Table II-2** contains extraneous parameter values needed to repeat these simulations which are not relevant to further discussion. As we sought to understand the sensitivity of battery performance to electrolyte transport, we performed a number of galvanostatic simulations in LIONSIMBA+c using the original LIONSIMBA operating state of charge (SoC) range of 85.51% to 0.9% with a lower cutoff voltage of 2.5 V. In each simulation, we used a cell cross-sectional area of 1 cm^2 and tank volume of 50 mL, where the tank contains electrolyte identical to that initially in the cell. We selected the higher-order polynomial approximation method provided by the original LIONSIMBA as the solid-phase diffusion model (Section 8.1) for all our simulations. In total, we generated ca. 50,000 data sets with distinct combinations of cell parameters and operating conditions, with each simulation costing ca. 30 s of wall time.

Table II-1: *A subset of the critical parameters used in LIONSIMBA+c simulations that define the battery operation in the positive electrode, which is limiting under all conditions studied throughout this study.* $^{a}\kappa_{eff}$ *is calculated through the electrolyte concentration,* c_e*, temperature, T, as shown in Eq. (II-10).*

Symbol	Unit	Value
b	-	2.5
c_{initial}	[mol/m^3]	100 – 1500
D	[m^2/s]	10^{-13} – 10^{-6}
D_{eff}	[m^2/s]	$D\varepsilon^b$
F	[C/mol]	96487
I_{app}	[A/m^2]	10 – 300
L	[m]	8×10^{-5}
Q_{A}	[C/m^2]	96073
R	[J/mol/K]	8.314
T	[K]	298.15
t_+	-	0 – 1
v	[m/s]	0 – 0.01
ε	-	0.4
$\varepsilon_{\mathrm{filler}}$	-	0.025
σ	[S/m]	100
σ_{eff}	[S/m]	$\sigma(1-\varepsilon-\varepsilon_{\mathrm{filler}})$
κ_{eff}	[S/m]	varies with $c_{\mathrm{e}}^{\mathrm{a}}$
t_{dis}	[s]	Q/I_{app}

Table II-2: *Other parameters used in modified LIONSIMBA.*

	Units	Positive Electrode	Separator	Negative Electrode
	-	$\mathrm{Li_\theta CoO_2}$	-	$\mathrm{Li_\theta C_6}$
a	m^2/m^3	862500	-	851100
b	-	2.5	2.5	2.5
$c_{\mathrm{s}}^{\mathrm{max}}$	mol/m^3	51554	-	30555
D^s	m^2/s	1×10^{-14}	-	3.9×10^{-14}
k	m$^{2.5}$/(mol$^{0.5}$s)	2.334×10^{-11}	-	5.031×10^{-11}
L	m	8×10^{-5}	4×10^{-5}	8×10^{-5}
n	-	100	100	100
R_p	m	2×10^{-6}	-	2×10^{-6}
ε	-	0.4	0.4	0.4
$\varepsilon_{\mathrm{filler}}$	-	0.025	-	0.0326
$\Theta_{100\%}$	-	0.4955	-	0.8551
$\Theta_{0\%}$	-	0.9917	-	0.0066
σ	[S/m]	100	-	100

To illustrate the potential effectiveness of convection-aided intercalation battery operation, we select a cell shown to access 60% of its theoretical capacity with a stagnant electrolyte (**Figure II-3a**). By introducing a flowing electrolyte with superficial velocities of 0.04 μm/s and 0.07 μm/s, 83% and 98% of the theoretical capacity could be accessed, respectively, as the electrolyte mass transfer limitations originally occurring within the cell were eliminated. While increasing electrolyte flow rate beyond this point does not impact the accessed capacity, it results in greater power- and energy-density as a higher cell voltage is maintained across the discharge profile. **Figure II-3b** suggests these performance benefits are caused by a smoothing of the concentration profile, and are in qualitative agreement with prior models on this topic,[40] while any discrepancies are attributable to differences in cell parameters and operating conditions. Critically, the cell with a stagnant electrolyte experiences salt depletion in the positive electrode, causing the cell voltage to rapidly approach the cutoff voltage, whereas flowing electrolyte can be used to delay or altogether eliminate salt depletion. However, even when the flowing electrolyte can completely eliminate liquid-phase mass transfer resistances, an inability to access the theoretical capacity would suggest additional battery losses including ohmics, kinetics, or solid-phase mass transfer which cannot be rectified by improved liquid-phase transport (*vide infra*). Beyond enabling higher accessible capacities, more uniform concentration profiles lead to reduced concentration and activation overpotentials, and increased electrolyte conductivity (**Figure II-8**), thus the greater power- and energy-density. However, the performance benefits achieved by increasing electrolyte flowrate are anticipated to plateau, resulting in optimal flowrates selected to balance the improvements in electrochemical performance with the increased pumping losses needed to support electrolyte flow. Despite the hypothetical existence of such optima, for the conditions assessed here, the pumping losses through the cell constituted at most 0.006% of the energy gain on a per cell basis (Section 8.4) and consequently will not be considered further. Pumping loss in components external to the cell require system design and are beyond the scope of the current work. Through this illustration, we are able to rationalize improvements in cell performance by a flattening concentration profile; however, as **Figure II-3** is an extremely limited view of the overall parameter space, further simulations are needed to understand the broader trends.

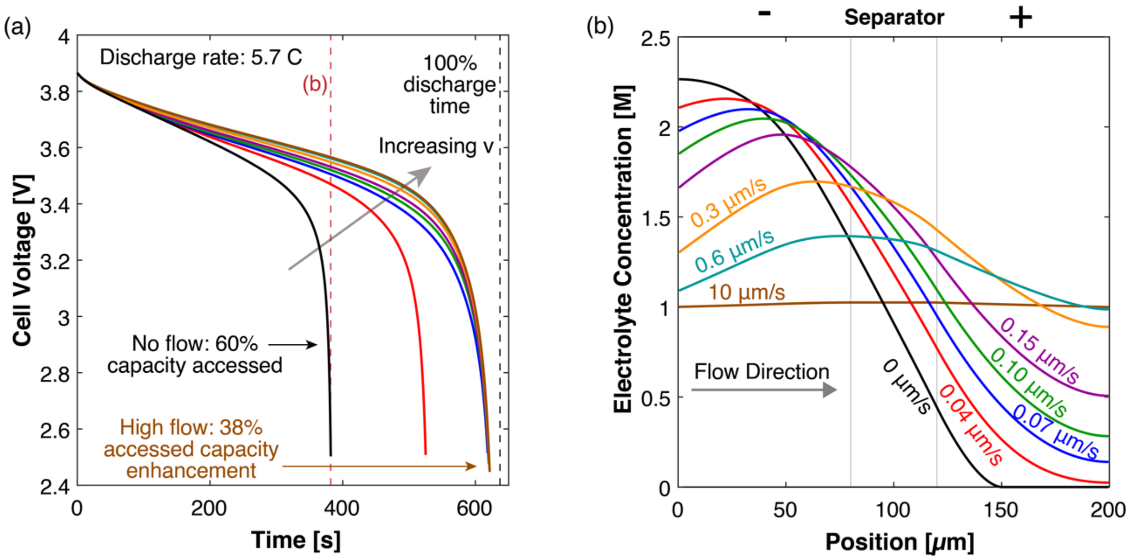

Figure II-3: *The effect of convective mass transfer on (a) the discharge polarization curve and (b) the concentration profile of electrolyte at t = 380 s. Note the location of positive and negative electrodes is opposite to that in* ***Figures II-1*** *and* ***II-2****. These data show the positive impact of increasing flow rate on cell performance by minimizing the instances of electrolyte salt depletion in the positive electrode. Further discussions of the concentration profiles and the impacts of flow direction can be found in Section 8.2 and Section 8.3.*

3. Model Analysis

The development of LIONSIMBA+c enables assessment of cell performance via the simulation of individual discharge curves as a function of electrolyte properties and flow rate, electrode properties and dimensions, and applied current. With many adjustable and often interdependent system parameters, cell performance can be exhaustively characterized by full parametric sweeps (**Table II-1**) over multiple conditions as discussed above. The use of simulations, as opposed to experiments, enables the rapid identification of performance sensitivities, the evaluation of parameter-dependent tradeoffs, and the estimation of property sets required to achieve performance targets. However, compact and meaningful representation of cell performance as a function of individual variables is challenging as these outputs are based on coupled reaction and transport processes whose relative importance varies with different scales. Combining physical quantities into dimensionless groups can provide insight on the relative importance of different physical processes within the battery and, in turn, a large number of simulation results can be collapsed into a lower dimensional space. Here, we first report the derivation of relevant dimensionless groups, followed by data analyses using these dimensionless groups.

Because our focus is on the impact of convection on the electrolyte-phase transport during battery operation, it is natural to begin deriving relevant dimensionless groups from electrolyte transport equations. The anion conservation equation, Eq. (II-1), equates the time rate of change of anion concentration to the divergence of the total anion flux. By electing to non-dimensionalize this equation (Section 8.5) through the thickness of the positive electrode, L, the full discharge time, t_{dis}, applied current density, I_{app}, and the initial concentration, c_{initial}, the order of magnitude of the resulting terms will be entirely defined by the coefficient groupings as shown in Eq. (II-9).

$$\frac{c_{\mathrm{initial}}\varepsilon_i L}{t_{\mathrm{dis}}}\frac{\partial \tilde{c}_e}{\partial \tilde{t}} = -\frac{\partial}{\partial \tilde{x}}\left(-\frac{D_{\mathrm{eff}} c_{\mathrm{initial}}}{L}\frac{\partial \tilde{c}_e}{\partial \tilde{x}} + v c_{\mathrm{initial}}\tilde{c}_e - \frac{1-t_+}{F} I_{\mathrm{app}}\tilde{i}_2 \right) \qquad \text{(II-9)}$$

Based on this dimensionless form of the transport equation, several scales become immediately apparent: (1) electrolyte accumulation/depletion, $c_{\mathrm{initial}}\varepsilon_i L t_{\mathrm{dis}}^{-1}$; (2) diffusion flux, $D_{\mathrm{eff}} c_{\mathrm{initial}} L^{-1}$; (3) convective flux, $v c_{\mathrm{initial}}$; (4) electromigrative flux, $(1-t_+) I_{\mathrm{app}} F^{-1}$. Comparing the relative magnitudes of these fluxes, as shown in **Table II-3**, gives insight into the dominant transport phenomena and its relative importance on cell performance in the battery. In comparing the transport phenomena in an enclosed system, the diffusive and electromigrative fluxes, as determined by the dimensionless parameter γ, need to balance to prevent electrolyte salt depletion. A large value of γ indicates an increased likelihood for Li salt depletion in the cathode due to insufficient diffusive transport into the cathode. To include the effects of convection in our analysis, we introduce ξ, which is a measure of electromigrative flux compared to the sum of the diffusive and convective fluxes, such that in the absence of convection, $\xi = \gamma$. In the same manner, large values of ξ would indicate that the combined diffusive-convective fluxes are slower than the electromigrative flux removing ions from the cathode. Finally, any electrolyte initially present can be used to buffer against electrolyte salt depletion in the cathode, as measured by β, the ratio of electromigration to average flux required for electrolyte salt depletion. Importantly, the exact values of these parameters will change between the positive electrode, negative electrode, and separator. In this work, the dimensionless analyses presented are based on the positive electrode values, as, under the specific conditions contemplated, this is the most likely source of performance limitations. Note that the set of dimensionless quantities discussed above can also be derived using time constants as demonstrated in Section 8.6.

Table II-3: *Definitions of the dimensionless groups used throughout the remainder of this study to describe convection battery operation.*

Dimensionless group	**Expression**	**Meaning**
γ	$\dfrac{I_{\text{app}}(1-t_+)L}{FD_{\text{eff}}c_{\text{initial}}}$	$\dfrac{\text{migration}}{\text{diffusion}}$
ξ	$\dfrac{I_{\text{app}}(1-t_+)}{\dfrac{FD_{\text{eff}}c_{\text{initial}}}{L}+Fvc_{\text{initial}}}=\dfrac{\gamma}{1+Pe}$	$\dfrac{\text{migration}}{\text{diffusion + convection}}$
Pe	$\dfrac{Lv}{D_{\text{eff}}}$	$\dfrac{\text{convection}}{\text{diffusion}}$
β	$\dfrac{I_{\text{app}}t_{\text{dis}}(1-t_+)}{Fc_{\text{initial}}\varepsilon L}=\dfrac{Q_A(1-t_+)}{Fc_{\text{initial}}\varepsilon L}$	$\dfrac{\text{migration}}{\text{flux causing electrolyte salt depletion}}$
δ'	$\dfrac{FI_{\text{app}}L}{RT}(\dfrac{1}{\kappa_{\text{eff}}}+\dfrac{1}{\sigma_{\text{eff}}})$	Dimensionless ohmic potential drop

In addition to electrolyte transport limitations, electronic and ionic resistances, solid-phase transport, and kinetics may contribute to lower cell voltages or accessed capacity, and we identified ohmic losses to have the most dominant impacts on our own simulation results. As such, we include an additional dimensionless group, δ', to characterize the ohmic losses of a cell, similar to that defined by Newman and co-workers.[107] For this particular value, the electrolyte conductivity, κ_{eff}, is calculated through Eq. (II-10) using the initial electrolyte concentration in the cell as opposed to the spatiotemporally varying concentration. While the solid-phase transport and kinetics may also limit cell performance, we focus our analysis on electrolyte phase transport limitations, as these other effects constitute minor contributions to performance under the conditions studied (Section 8.7).

In this paper, simulations are performed with a wide range of input parameter values to identify overarching trends in convection cell performance. While all input parameter values used are grounded in realm of physical possibility, not all combinations may be practically achievable based on current material sets. Even in such cases, the observations made provide guidance for future research opportunities. Additionally, while this study uses a $LiCoO_2$/graphite redox chemistry, the qualitative understandings of the dimensionless groups gained from this work should be applicable to other battery chemistries. LIONSIMBA can readily be applied to different chemistries and cell formats provided requisite property values are available, and we encourage interested readers to adapt the simulations and analyses to their needs.

For the remainder of this work, we demonstrate the utility of these dimensionless groups through their ability to predict qualitative model behavior to enhance the field's understanding of the critical points for convective mass transfer used to improve battery performance. In all cases, we rely on the accessed capacity of charge stored within the battery as the metric of performance, although there are additional performance benefits to convection, because reducing inaccessible capacity is the first step towards improving overall energy density. To begin answering the question of the value of convective transport in an electrochemical cell, we examine a subset of the data of varying both γ and β. Under identical values of γ and β, we compare the capacity accessed in a cell containing a stagnant electrolyte versus a cell with a very high electrolyte velocity of 0.01 m/s (10^4 μm/s). Note in **Figure II-3**, a velocity of just 10 μm/s yielded relatively uniform concentration and transport-optimized performance. We define the difference between the stagnant and 0.01-m/s capacities as the accessed capacity enhancement, where a positive value indicates that a greater capacity is available when the electrolyte is flowing. The data contained in **Figure II-4** show the regions where a flowing electrolyte can greatly improve the accessible capacity only existing in areas where both γ and β are large. Although quantitative differences exist for different initial electrolyte concentrations due to changing kinetic and solid-phase transport resistances, **Figure II-9** shows the same qualitative trend as observed here. These trends can be rationalized by returning to the definitions of the dimensionless groups γ and β, where γ is the ratio of electromigration to diffusion, and β is the ratio of electromigration to the total flux that would cause electrolyte salt depletion. From these definitions, a cell with small γ has diffusion within the cell capable of balancing electromigration in the opposite direction, making electrolyte salt depletion highly unlikely. In practice, a small γ is the result of a thin electrode, an electrolyte with high diffusivity or large Li^+ transference number, or a low discharge rate. Similarly, with a small value of β in the cathode, the initial amount of salt in the electrolyte is more than can be depleted by the electromigration of ions. For cells with low electrode porosity, small Li^+ transference number, or high specific capacity active materials, both γ and β values are large, suggesting the accessed capacity for these cells can be significantly enhanced by including convective transport as a means of balancing electrolyte mass transfer.

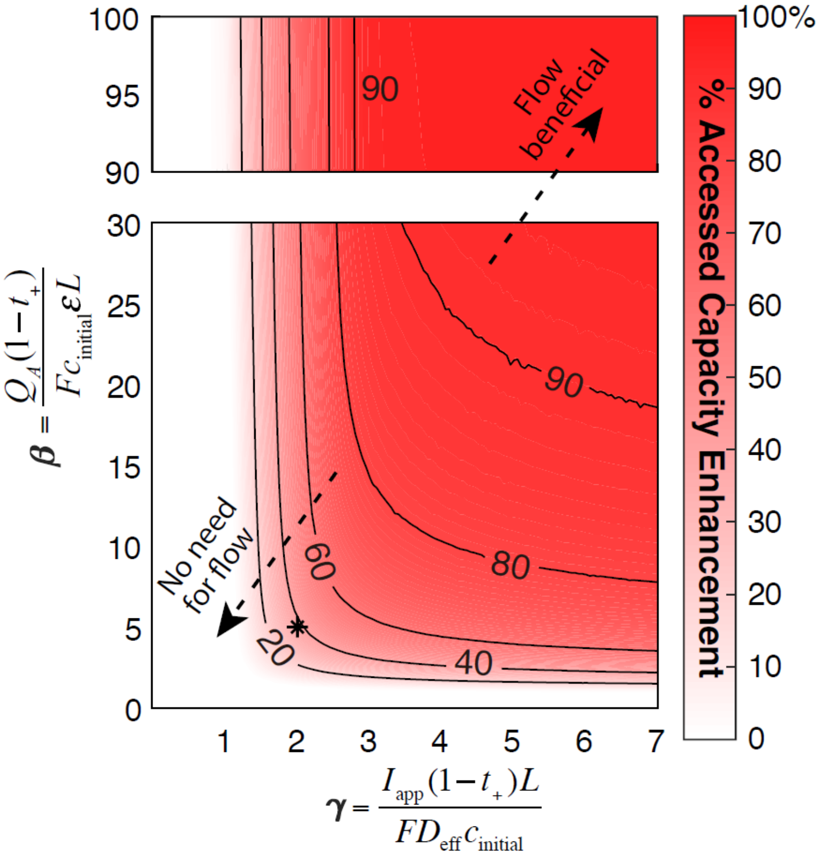

Figure II-4: *Accessed capacity enhancement by 0.01 m/s of flow compared to a cell without flow. The figure is generated from 5166 data sets with varying* I_{app}, t_+, *D, but same initial electrolyte concentration* $c_{initial}$ = *1000 mol/m*^{3}*, and constant ohmic resistance,* δ' = *3.89 corresponding to a dimensional ohmic potential drop of 0.1 V. A different initial electrolyte concentration will result in similar trends with slight variations in values, as illustrated in* ***Figure II-9****. "*" indicates conditions used for* ***Figure II-3****.*

Building on the analysis showing capacity enhancement with extremely high velocity, further analysis can help us to understand the degree to which intermediate flow rates and parameter combinations enable the convection cell to approach the theoretical maximum enhancement. As before, we select a subset of all collected data, choosing varying β, as indicated by different discrete colors, γ, as indicated by the saturation color bar, and ξ, as plotted on the abscissa in **Figure II-5**, to demonstrate any underlying patterns in these parameters' impact on cell performance. In addition to confirming the observations made in **Figure II-4**, this further analysis shows the clear existence of performance transition regimes where $1 \lesssim \xi \lesssim 3$. In this range, electromigration flux roughly balances diffusion and convection fluxes combined. Interestingly, the transition region narrows with increasing β. This observation can be explained by a greater vulnerability to transport limitations with higher β due to decreased initial amount of salt to buffer any transport imbalance between electromigation versus diffusion and convection. By comparing these first two analyses (**Figures II-4** and **II-5**), there is clear analogy between ξ and γ as both parameters represent the ratios of fluxes in opposite directions within the intercalation cell. Interestingly, however, in **Figure II-5**, there is a broadening of the curves of each color that we otherwise expect to be individual traces collapsing all Pe values, with only β and ξ determining the behavior of cells with flowing electrolyte. Instead, the data presented suggests that the diffusional flux scale, $D_{\text{eff}}c_{\text{initial}}L^{-1}$, and convective flux scale, vc_{initial}, of the same magnitude do not counterbalance electromigration equally. A suspected cause is that the scales used to derive the dimensionless numbers are only estimates based on initial conditions and do not capture the dynamic behavior of the cell. When operated at intermediate ξ values, a concentration gradient develops during cell operation, resulting in different magnitudes of diffusion and convection terms in Eq. (II-1) due to their different dependence on the concentration gradient. This hypothesis is further supported by the diminution of the broadening at low ξ values when the concentration gradient becomes more uniform.

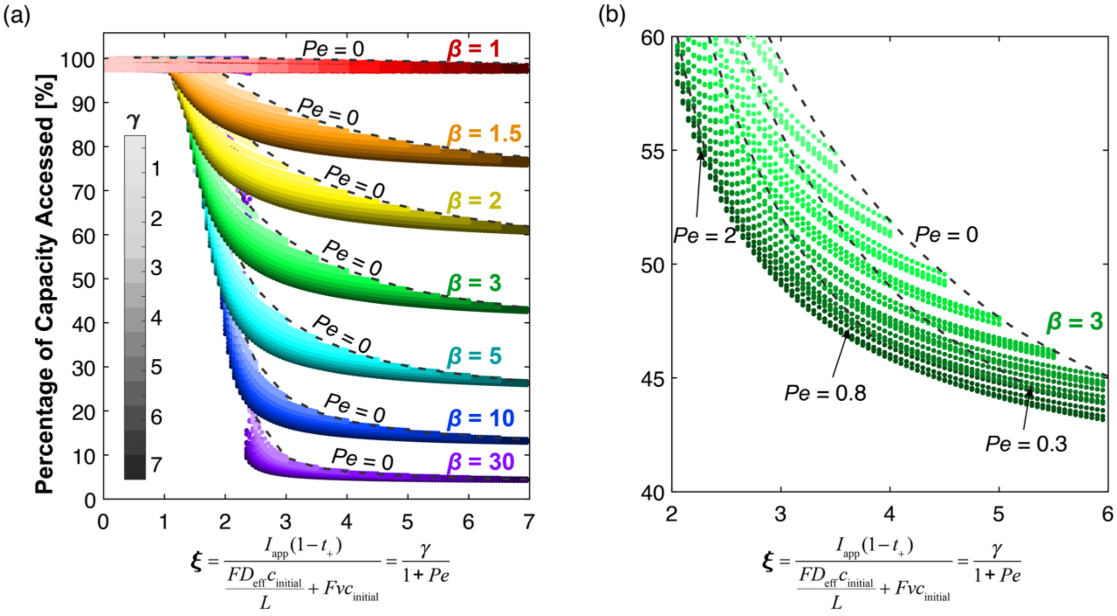

Figure II-5: *(a) Percentage of capacity accessed for convection cells with varying ξ values. The plot contains 29792 data sets with varying I_{app}, t_+, D, $c_{initial}$, v, and a constant δ' value of 3.89 (0.1 V dimensional ohmic drop). Results for $c_{initial}$ >1000 mol/m^3 are not included in the plot as they lead to slightly different behaviors at intermediate ξ values shown in* ***Figure II-10****. (b) Enlarged view of data for β = 3 and contours of Pe values. For a particular γ value, the percentage of capacity accessed increases with increasing Pe.*

Lastly, LIONSIMBA+c can be used to understand the impact of improved transport on non-transport resistances within the cell, such as low electrolyte conductivity or sluggish kinetics. For this study, we focus on the impacts of ohmic losses as shown in **Figure II-6**, but an analogous approach could be used to better understand the possible improvements in other areas of cell-design. With increasing ohmic resistance, the accessed capacity decreases monotonically from ca. 97% at $\delta' = 3.89$ to ca. 54% at $\delta' = 31.2$, despite including $v = 0.01$ m/s electrolyte flow to eliminate any sources of mass-transfer losses. Again, we see some spread in these data as individual simulations will have unique kinetic and solid-phase transport resistances, but the variance decreases with increasing *δ'* as fewer parameter combinations achieve the desired value. As previously discussed, by reducing the electrolyte salt concentration gradient, a convection cell offers opportunities for reduced concentration and activation overpotentials, and potentially improved electrolyte conductivity compared to a stagnant cell. **Figures II-6b** and **II-6c** compare the accessed capacity enhancement by convection for cells with low ohmic resistance (δ' = 3.89) and high ohmic resistance (δ' = 31.2). Both figures demonstrate the same qualitative trends seen in **Figure II-4** but differ in the upper limit for enhancement, as discussed earlier. As such, while introducing convection can overcome cell limitations caused by diffusional resistances, this approach is not a panacea for limited accessed capacity.

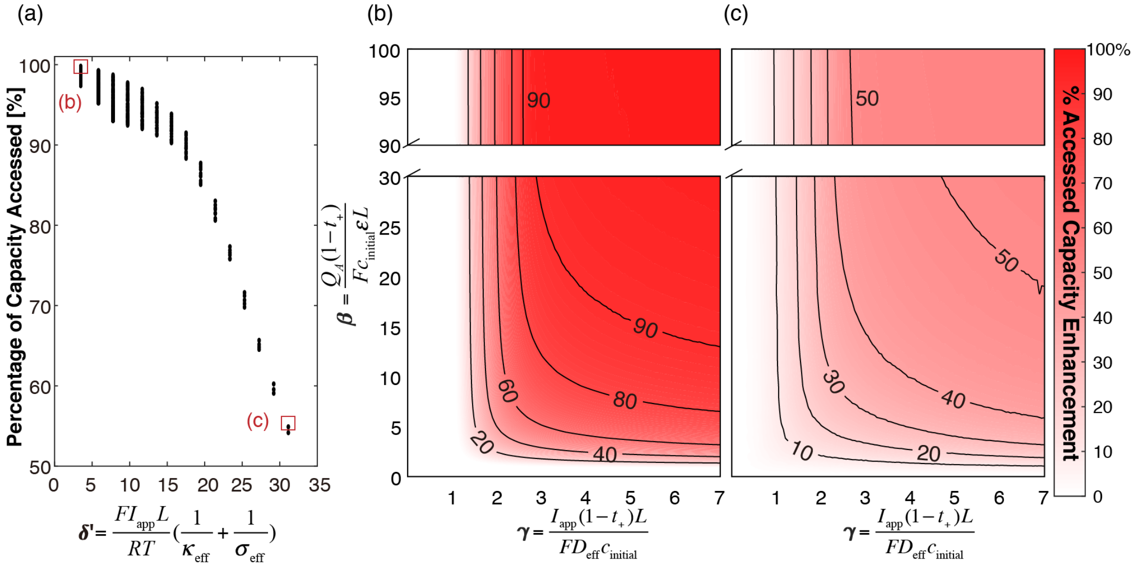

Figure II-6: *(a) Percentage of capacity accessed during discharge for convection cells with v = 0.01 m/s (10^4 μm/s), as a function of δ' values ranging from 3.89 to 31.2, corresponding to dimensional ohmic drops ranging from 0.1 V to 0.8 V, respectively. The figure contains 560 data sets with varying* I_{app}, t_+, *D, and* $c_{initial}$. *Accessed capacity enhancement by 0.01 m/s of flow for data sets with* $c_{initial}$ *= 100 mol/m*^{3} *is shown in (b) for δ' = 3.89 and (c) for δ' = 31.2.*

4. Conclusions

The avoidance of electrolyte mass transfer limits in intercalation-based battery chemistries would enable significant enhancements in accessible capacity and overall battery performance for a number of important applications. As such, we modified the open-source LIONSIMBA model of enclosed Li-ion batteries to incorporate electrolyte flow and, subsequently, simulated the impact of convection on isothermal cell performance over a broad range of conditions. For a cell operated under electrolyte transport limited conditions, such as high C-rate or low electrolyte diffusivity, electrolyte flow minimizes concentration gradients across the cell thereby preventing electrolyte salt depletion that adversely affects kinetic, ohmic, and transport resistances and, if uncontrolled, can result in hazardous conditions within the battery. This, in turn, can enable an expanded operating envelope for intercalation batteries by increasing the accessible capacity but the effectiveness of this approach is dependent upon electrode properties, electrolyte composition, cell dimensions, and operating conditions. With the extension and description of physically meaningful dimensionless groups, we collapse >10 physical parameters and thousands of cell discharge simulation results into insightful comprehensive plots, **Figures II-4** to **II-6**. These plots quantitatively address the critical questions of when convection is needed, how much is needed, and what is the upper bound of enhancement when convection is used. To summarize our key findings, convection is most helpful for a cell with large γ and β values, which has high transport resistance from diffusion and there is limited salt in the electrolyte solution to compensate. Practical conditions with large γ and β include high applied current density, low electrode porosity, low Li^+ transference number, and active materials with high specific capacity. The dimensionless group, ξ, represents the ratio of electromigrative flux to the sum of diffusion and convective fluxes, and can help determine whether flowrate is high enough to access full capacity. The group δ' can help determine ohmic resistance, which is one of the factors that can limit the maximum percentage of capacity that a convection cell can access if the resistance is large. If significant, kinetic and solid-phase transport effects may also limit convection cell performance, and their impacts can be analyzed using a similar approach as demonstrated in this work for ohmic resistance.

Our simulation work suggests that compared to an enclosed cell, a convection cell provides opportunities for a range of operating conditions and electrode design parameters. With the same or similar dimensionless plots presented here, the practitioner can readily calculate dimensionless group values for a cell and application of interest to estimate any benefit of flow. This approach could potentially lead to applications leveraging rate capability, such as fast charging, and enable high energy density by increasing electrode thickness. By eliminating electrolyte salt depletion, convection could improve cell safety under extreme conditions. The understanding of transport under isothermal conditions in this work lays the foundation to include convective heat transfer and to explore the anticipated benefit of thermal regulation in future modeling and experimentation.

ACKNOWLEDGEMENTS FOR THIS WORK

The authors gratefully acknowledge funding from the MIT Deshpande Center. MJO gratefully acknowledges the National Science Foundation Graduate Research Fellowships Program under Grant No. 1122374. Any opinions, findings, and conclusions or recommendations expressed in this material are those of the authors and do not necessarily reflect the views of the National Science Foundation. TJC gratefully acknowledges the National Defense Science and Engineering Graduate (NDSEG) Fellowship awarded by DoD, Air Force Office of Scientific Research. Finally, the authors thank Dr. Robert Darling (RTRC) for his helpful suggestions.

5. *List of Symbols*

Symbol	**Description**
a	Particle surface area to volume
A_{cell}	Cell cross-sectional area
A_{tube}	Tube cross-sectional area
b	Bruggeman's coefficient
$c_e(x,t)$	Anion concentration in the electrolyte

c_{initial}	Initial electrolyte concentration
$c_{\text{tank}}(t)$	Tank concentration
$c_{\text{s,max}}$	Maximum solid-phase concentration
D_{bulk}	Electrolyte diffusivity of a free solution
D_{eff}	Effective electrolyte diffusivity
D_{s}	Solid-phase diffusivity
F	Faraday constant
I_{app}	Applied current density
$j(x,t)$	Ionic flux
k	Reaction rate constant
L	Thickness
n	Number of control volumes used
Q_A	Areal capacity
R	Gas constant
R_p	Particle radius
T	Absolute temperature
t_{dis}	Time to completely charge or discharge battery at I_{app}
t_+	Li^+ transference number
v	Superficial velocity in the cell
v_{tube}	Superficial velocity in the tube
V_{tank}	Tank volume
ε	Porosity
$\varepsilon_{\text{filler}}$	Filler fraction
$\Theta_{100\%}$	Stoichiometry at 100% SoC
$\Theta_{0\%}$	Stoichiometry at 0% SoC
κ_{eff}	Effective electrolyte conductivity
σ	Solid-phase conductivity
σ_{eff}	Effective solid-phase conductivity

6. *Appendix A: Electrolyte Conductivity Equation*

For both models, we used Eq. (II-10) to calculate the effective electrolyte conductivity equation at $T = 298.15$ K.[109]

$$\kappa_{\text{eff}} = \varepsilon^{\text{brugg}} \times 10^{-4} \times c_e(x,t) \times \left(\begin{array}{c} -10.5 + 0.668 \times 10^{-3} \cdot c_e(x,t) + 0.494 \times 10^{-6} \cdot c_e{}^2(x,t) + \\ (0.074 - 1.78 \times 10^{-5} \cdot c_e(x,t) - 8.86 \times 10^{-10} \cdot c_e{}^2(x,t)) \cdot T + \\ (-6.96 \times 10^{-5} + 2.8 \times 10^{-8} \cdot c_e(x,t)) \cdot T^2 \end{array} \right)^2 \tag{II-10}$$

7. *Appendix B: Supplementary Figures*

Figure II-7 compares discharge curves at varying C-rates for the original LIONSIMBA and LIONSIMBA+c with $v = 0$ m/s. The identical outputs suggest no artifacts were introduced to the original model during the modifications.

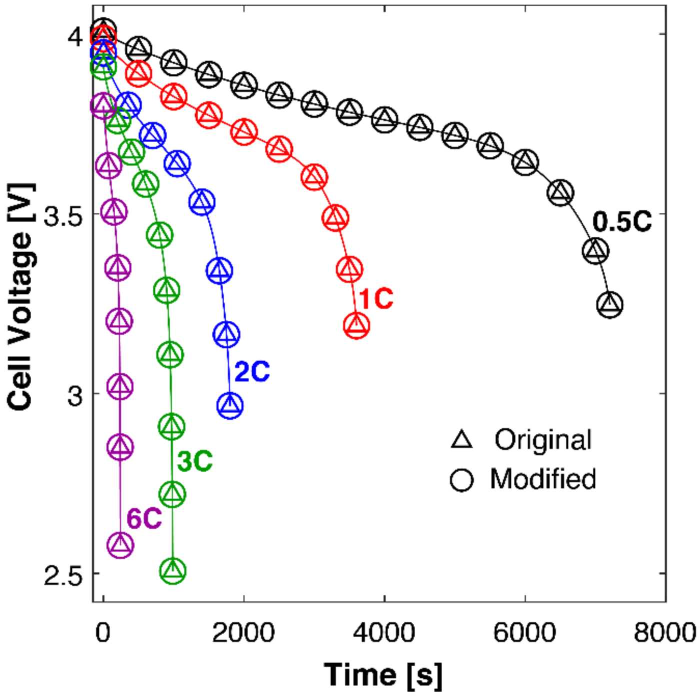

Figure II-7: *Comparison between LIONSIMBA and LIONSIMBA+c model outputs at varying discharge rates with the same inputs and no flow.*

Figure II-8 shows the conductivity of the electrolyte, $LiPF_6$ in PC/EC/DMC, as a function of $LiPF_6$ concentration at T = 298.15 K used in the simulation.[109] The curve is generated by least-square fits of experimental measurements to Eq. (II-11).[109] The plot is a non-monotonic concave down curve, with maxima at 1 M electrolyte concentration. By maintaining the electrolyte concentration closer to the initial concentration of 1 M, a convection cell can help reduce electrolyte-phase ohmic resistance, thus minimize ohmic potential drop.

$$\sqrt{\frac{\kappa(c,T)}{c}} = \sum_{i=0}^{n}\sum_{j=0}^{k}\kappa_{ij}c^{i}T^{j} \tag{II-11}$$

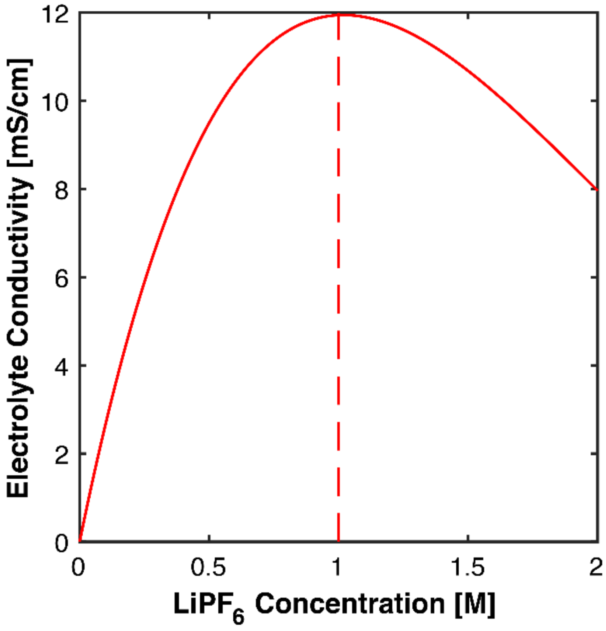

Figure II-8: *Electrolyte conductivity as a function of salt concentration at T = 298.15 K used in the simulation with the conductivity maxima observed at 1 M.*

Figure II-9 shows the enhancement, as a percentage, in accessed capacity by convection for selected β values with initial concentration, c_{initial}, varying from 0.1 M to 1.5 M. All the conditions have a δ' value of 3.89. Different c_{initial} values show the same trend with slight variation in absolute values. This variation is a result of different kinetic and solid-phase diffusion resistances for different c_{initial} and I_{app} combinations. The 1 M and 0.1 M curves within the different β values are precisely the data in **Figure II-4** and **Figure II-6b** respectively.

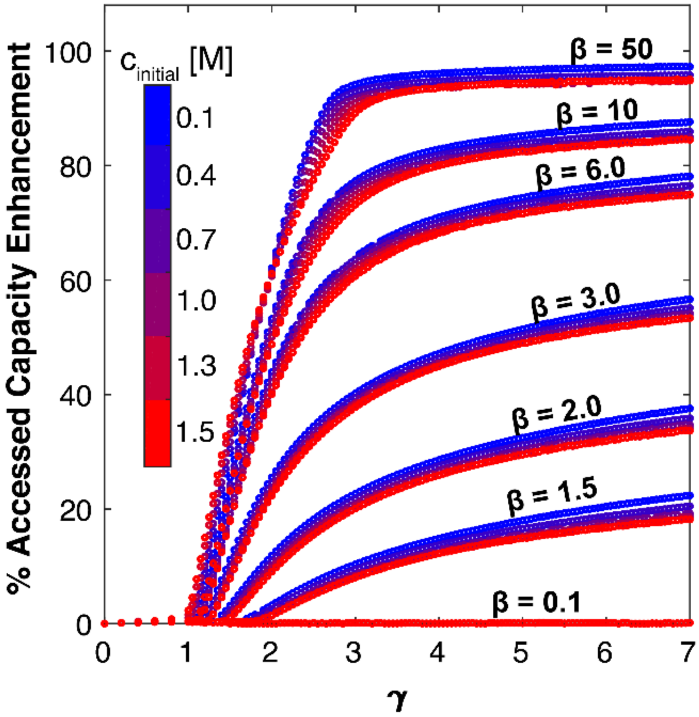

Figure II-9: *Percentage of accessed capacity enhancement for selected β values with $c_{initial}$ from 0.1 M to 1.5 M, with $\delta' = 3.89$.*

Figure II-10 shows the percentage of capacity accessed as a function of ξ for selected β and γ values, with $c_{\mathrm{initial}} = 1.5$ M and $\delta' = 3.89$. The figure shows similar trends as in **Figure II-5a** in the main text, with the exception of the transitional region of $1 < \xi < 3$ that now demonstrates complex behavior as a result of the non-monotonic electrolyte conductivity change with concentration, as shown in **Figure II-8**. Specifically, there is a concentration buildup at intermediate flowrates as explained in Section 8.2. When $c_{\mathrm{initial}} > 1$ M, this concentration buildup leads to lower average electrolyte conductivity in the cell, thus larger ohmic drops and decreased accessed capacity.

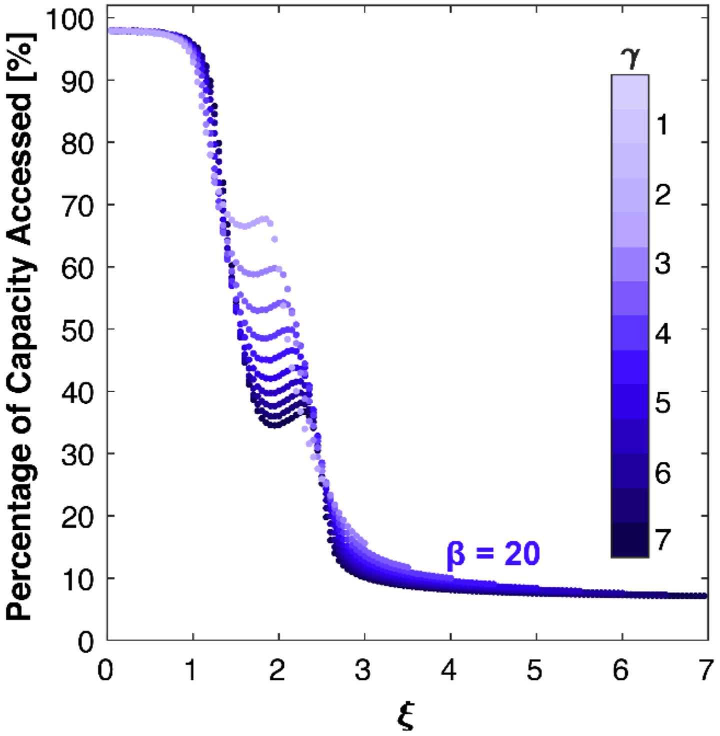

Figure II-10: *Percentage of capacity accessed as function of ξ for selected β and γ values, with* $c_{initial}$ *= 1.5 M and δ' = 3.89.*

8. Appendix C: Supplementary Notes

8.1. Solid-phase diffusion model

LIONSIMBA offers three choices of solid-phase diffusion model, including (1) a two-parameter polynomial approximation,[110] (2) a higher-order polynomial approximation,[110] and (3) Fick's law. The first two models are approximations of Fick's law without significant loss of accuracy. Detailed comparisons between the three models can be found in Ref. 3. In this study, we elect to use the higher-order polynomial approximation model for all the simulations. This choice is based on the high discharge rates used, up to 10 C, for which the higher-order polynomial approximation demonstrated higher accuracy than the two-parameter polynomial approximation.[111] We also observe that the higher-order polynomial approximation shows better convergence than the two-parameter polynomial approximation for our applications. While the higher-order polynomial approximation is less accurate than the full Fick's law model at high C-rates (RMSE = 1.9% at 10 C), we find this reduction in accuracy is acceptable for our application, especially when the savings in computational time, ca. 60% at low C-rates and ca. 40% at high C-rates, are considered.[111]

The equations for the higher-order polynomial approximation are shown below. In the equations, $c_s^{\text{avg}}(x,t)$ is the solid-phase average concentration, $j(x,t)$ is the ionic flux, R_p is the active material particle radius, D_{eff}^s is the effective solid phase diffusivity, $q(x,t)$ is the volume-averaged concentration flux, and $c_s^*(x,t)$ is the solid-phase surface concentration.

$$\frac{\partial c_s^{\text{avg}}(x,t)}{\partial t} = -3\frac{j(x,t)}{R_p}$$

$$\frac{\partial q(x,t)}{\partial t} = -30\frac{D_{\text{eff}}^s}{R_p^{\,2}}q(x,t) - \frac{45}{2}\frac{j(x,t)}{R_p^{\,2}}$$

$$c_s^*(x,t) - c_s^{\text{avg}}(x,t) = -\frac{j(x,t)R_p}{35D_{\text{eff}}^s} + 8R_p q(x,t)$$

8.2. Details of the concentration profiles

A close inspection of the concentration profiles in **Figure II-3b** in the main text leads to additional intriguing findings. Without flow, the amount of lithium ion accumulation in the negative electrode equals the amount of Li^+ depletion in the positive electrode, and the average concentration is the initial electrolyte concentration. However, this is not necessarily the case in a convection cell. During discharge of a convection cell with the flow direction in **Figure II-3** in the main text, the electrolyte exits the positive electrode to the tank, and enters from the tank to the negative electrode. When the electrolyte concentration exiting the cell is lower than that entering the cell, there is a net accumulation of electrolyte concentration in the cell, and a net depletion in the tank.

The electrolyte concentrations in the cell and the tank average volumetrically to the initial electrolyte concentration. **Figure II-3b** demonstrates this feature in cells with superficial velocities between 0.04 and 0.6 μm/s. **Figure II-11** shows the tank concentration change with time. Because of a high tank volume/ cell area ratio used in our simulation, the change in tank concentration is insignificant. Though not explored in this publication, the ability to accumulate salt in the cell may have utility in further applications, such as enabling the use of a lower electrolyte concentration while still maintaining a relatively small ohmic resistance.

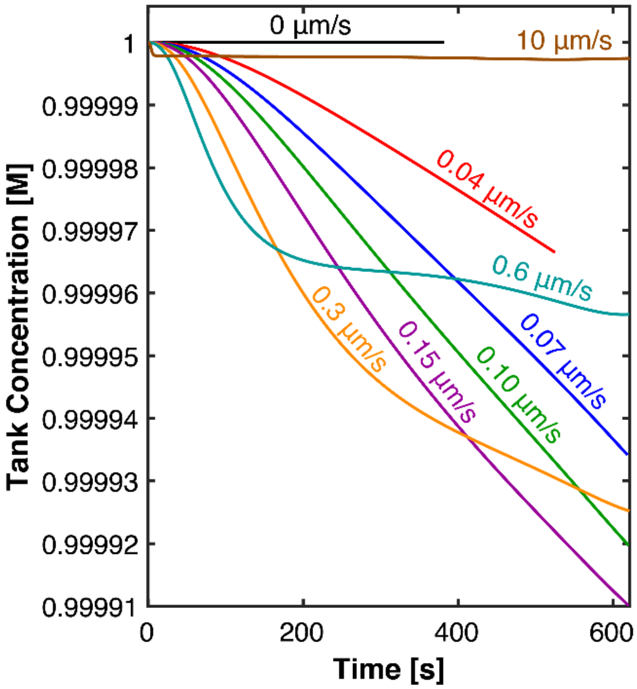

Figure II-11: *Corresponding electrolyte concentration change in the tank as a function of time for* ***Figure II-3*** *in the main text.*

8.3. Impacts of flow direction

Figure II-12 shows the cell voltage curves and corresponding electrolyte concentration profiles with same conditions but reverse flow direction compared to **Figure II-3** in the main text. The trends are similar to what we discussed for **Figure II-3**, except the impacts of flow on cell performance appear to be less significant at low flow velocities as electrolyte salt depletion persists. At $v = 10$ μm/s when the electrolyte concentration approaches $c_{\text{initial}} = 1$ M everywhere, both flow directions have the same effects on cell performance. These observations also agree with previous literature findings.[40] This suggests that flow should be in the direction from the Li^+ generating electrode to the Li^+ consuming electrode for maximal effectiveness at low flowrates.

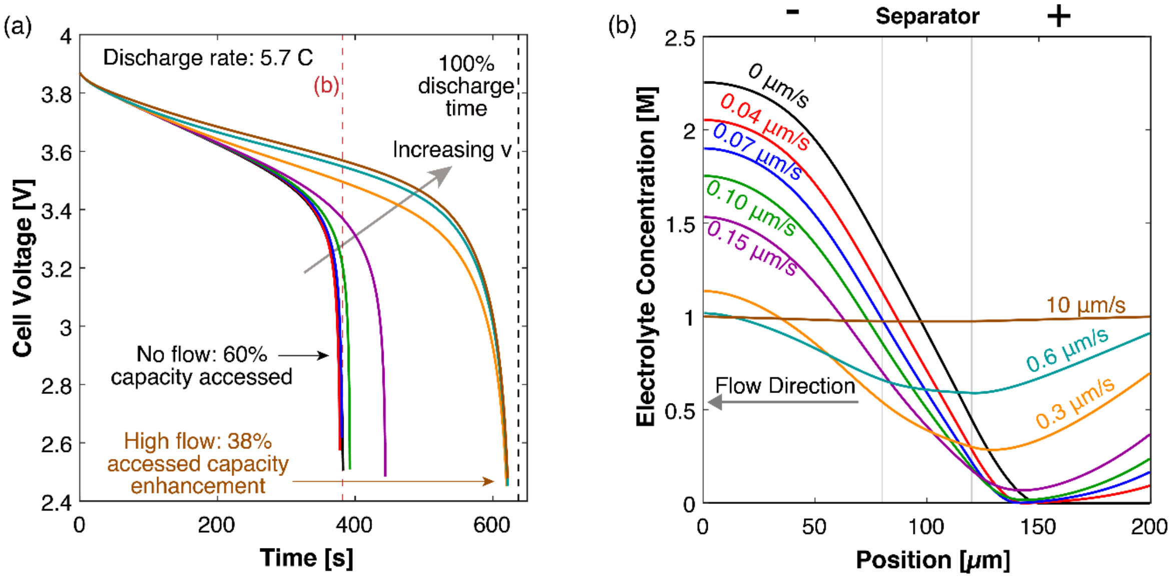

Figure II-12: *(a) Cell voltage curves and (b) corresponding electrolyte concentration profiles for reverse flow direction compared to* ***Figure II-3*** *in the main text.*

8.4. Pumping energy loss across single cell

The pressure drop through the cell is estimated using Kozeny-Carman Equation:

$$\frac{\Delta p}{L} = v \frac{180\mu}{\Phi_s^{\,2} D_p^{\,2}} \frac{(1-\varepsilon)^2}{\varepsilon^3} \qquad \text{(II-12)}$$

where Δp is the pressure drop, L is the cell total length, v is the superficial velocity, μ is the electrolyte viscosity, ε is the porosity, and Φ_s is the sphericity of the particles with diameter D_p.

The energy required for pumping flowrate Q through a cell with cross-sectional area A during discharge time t_d is estimated with Eq. (II-13):

$$W_\mathrm{pump} = Q\Delta p t_\mathrm{d} = Av^2 \frac{180\mu}{\Phi_s{}^2 D_p{}^2} \frac{(1-\varepsilon)^2}{\varepsilon^3} L t_\mathrm{d} \tag{II-13}$$

The cell used in **Figure II-3** in the main text has $L = 200$ µm, $\varepsilon = 0.4$, and the active materials are assumed to be spheres with $\Phi_s = 1$ and $D_p = 4 \times 10^{-6}$ m. Assuming the electrolyte has a viscosity of 10 cP, **Table II-4** shows energy gain for one cell, $E_\mathrm{cell\_gain}$, and pumping loss for one cell, $E_\mathrm{cell\_loss}$, per unit area of the cell with $v = 10$ µm/s compared to the cell without flow.

Table II-4: *Energy gain and pumping loss by a convection cell with v = 10 µm/s.*

	Discharge time [s]	Cell areal energy density [Wh/m^2]	Required pumping energy for one cell [Wh/m^2]
$v = 0$ µm/s	382	57.6	0
$v = 10$ µm/s	622	92.9	0.0022
		$E_\mathrm{cell\_gain} = 35.3$	$E_\mathrm{cell\_loss} = 0.0022$

Beyond the single cell considered here, one can analyze the system level trade-off with and without pumping. Such an analysis calls for a thorough analysis of pumping losses throughout the cell stack, manifolds, pumping equipment, and tank which fall beyond the scope of this study.

8.5. Derivation of electrolyte transport equations

For a binary univalent electrolyte, $c_e = c_+ = c_-$, $z_+ = 1$, $z_- = -1$. In a porous electrode, the superficial flux densities of anions and cations are given by Eq. (II-14) and (II-15), respectively, where u_i is the effective ionic mobility, D_i is the effective ionic diffusion coefficient, and Φ_2 is the potential in the pore-filling electrolyte:

$$\mathbf{N}_- = -D_- \nabla c_e + v c_e + u_- F c_e \nabla \Phi_2 \qquad \text{(II-14)}$$

$$\mathbf{N}_+ = -D_+ \nabla c_e + v c_e - u_+ F c_e \nabla \Phi_2 \qquad \text{(II-15)}$$

Eq. (II-16) gives the superficial current density $\mathbf{i}_2$ in the pore phase for the binary electrolyte:

$$\mathbf{i}_2 = F(\mathbf{N}_+ - \mathbf{N}_-) = -F(D_+ - D_-)\nabla c_e - F^2 \nabla \Phi_2 (u_+ c_e + u_- c_e) \qquad \text{(II-16)}$$

Substituting Eq. (II-16) into Eq. (II-14) yields:

$$\mathbf{N}_- = -D_{\text{eff}} \nabla c_e + v c_e - \frac{1-t_+}{F}\mathbf{i}_2 \qquad \text{(II-17)}$$

where the effective electrolyte diffusion coefficient $D_{\text{eff}} = \frac{2D_+ D_-}{D_+ + D_-}$, and the Li$^+$ transference number $t_+ = \frac{u_+}{u_+ + u_-}$.

A material balance on the anionic species using Eq. (II-17) gives Eq. (II-18), which is the form used for Eq. (II-9).

$$\varepsilon \frac{\partial c_e}{\partial t} = -\frac{\partial \mathbf{N}_-}{\partial x} = -\frac{\partial}{\partial x}(-D_{\text{eff}} \frac{\partial c_e}{\partial x} + v c_e - \frac{1-t_+}{F}\mathbf{i}_2) = \frac{\partial}{\partial x}(D_{\text{eff}} \frac{\partial c_e}{\partial x}) - v\frac{\partial c_e}{\partial x} + \frac{1-t_+}{F}\frac{\partial \mathbf{i}_2}{\partial x} \qquad \text{(II-18)}$$

Only Li$^+$ species in the electrolyte undergoes reaction, and Faraday's law relates $\mathbf{i}_2$ to j, the Li$^+$ ionic flux from the solid phases to the pore solution:

$$\frac{\partial \mathbf{i}_2}{\partial x} = aFj \qquad \text{(II-19)}$$

Combining Eq. (II-18) and (II-19) gives the governing equation in the form of Eq. (II-1):

$$\varepsilon \frac{\partial c_e}{\partial t} = \frac{\partial}{\partial x}\left(D_{\text{eff}} \frac{\partial c_e}{\partial x}\right) - v \frac{\partial c_e}{\partial x} + a(1-t_+) j \qquad \text{(II-20)}$$

8.6. Derivation of dimensionless groups using timescales

In the main text, we derive and discuss the dimensionless groups in **Table II-3** in the context of fluxes, as this provides a straightforward comparison between the magnitude of different physical processes. Alternatively, the dimensionless groups can be derived using timescale analysis, an approach that is also used in literature.[112–114] To identify the relevant timescales, the non-dimensionalized equation Eq. (II-9) can be rewritten as:

$$\frac{1}{t_{\text{dis}}} \frac{\partial \tilde{c}_e}{\partial \tilde{t}} = -\frac{\partial}{\partial \tilde{x}}\left(-\frac{D_i}{L^2} \frac{\partial \tilde{c}_e}{\partial \tilde{x}} + \frac{v_{\text{por},i}}{L} \tilde{c}_e - \frac{1-t_+}{F c_{\text{initial}} \varepsilon_i L} I_{\text{app}} \tilde{i}_2\right) \qquad \text{(II-21)}$$

Where D_i is the ionic diffusivity in the electrode corrected only for the tortuosity, and relates to the effective diffusivity D_{eff} by $D_{\text{eff}} = \varepsilon_i D_i$; $v_{\text{por},i}$ is the electrolyte phase velocity in the porous electrode, and relates to the superficial velocity v by $v = \varepsilon_i v_{\text{por},i}$. The equation yields several time scales summarized in **Table II-5**, which are also compared to their counterparts expressed in rates.

Table II-5: *Timescales and corresponding characteristic rates relevant to the electrolyte transport during convection battery operation.*

Phenomenon	**Characteristic Timescale**	**Characteristic Rate (mol / time*cell area)**	**Meaning**	**Implication: Discharge ends due to…**
Discharge	$t_{\mathrm{dis}} = \frac{Q_A}{I_{\mathrm{app}}}$	$\frac{I_{app}}{F}$	Timescale to: • deplete Li in anode or fill cathode solid at applied current •use full theoretical capacity	Exhaustion of theoretical capacity if t_{dis} small
Electrolyte Diffusion	$t_{\mathrm{diff}} = \frac{L^2}{D_i}$	$\frac{D_{eff} c_{initial}}{L}$	Timescale for diffusion: •across electrode or separator, •to revive cathode from Li^+ depletion	Diffusion unable to prevent Li^+ depletion if t_e large
Convection	$t_{\mathrm{convec}} = \frac{L}{v_{\mathrm{por},i}}$	$v\, c_{initial}$	•Flow residence timescale •Timescale needed for convection to revive cathode from Li^+ depletion	Convection unable to prevent Li^+ depletion if t_c large
Migration	$t_{\mathrm{depletion}} = \frac{F c_{\mathrm{initial}} \varepsilon_i L}{(1-t_+) I_{\mathrm{app}}}$	$\frac{I_{app}(1-t_+)}{F}$	Timescale of electrolyte Li^+ salt: •depletion in cathode •excess in anode	Li^+ salt depletion in cathode and excess in anode if t_m small

Similar forms of diffusion and migration timescales have also been defined in prior literature.[114] Using these timescales, the dimensionless groups in **Table II-3** can be derived as:

Table II-6: *Derivation of the dimensionless groups using timescales defined in* ***Table II-5****.*

Dimensionless group	Definition	Expression
γ	$\dfrac{t_{\text{diff}}}{t_{\text{depletion}}}$	$\dfrac{I_{\text{app}}(1-t_+)L}{FD_{\text{eff}}c_{\text{initial}}}$
ξ	$\dfrac{\dfrac{1}{\dfrac{1}{t_{\text{diff}}}+\dfrac{1}{t_{\text{convec}}}}}{t_{\text{depletion}}}$	$\dfrac{I_{\text{app}}(1-t_+)}{\dfrac{FD_{\text{eff}}c_{\text{initial}}}{L}+Fvc_{\text{initial}}}=\dfrac{\gamma}{1+Pe}$
Pe	$\dfrac{t_{\text{diff}}}{t_{\text{convec}}}$	$\dfrac{Lv}{D_{\text{eff}}}$
β	$\dfrac{t_{\text{dis}}}{t_{\text{depletion}}}$	$\dfrac{I_{\text{app}}t_{\text{dis}}(1-t_+)}{Fc_{\text{initial}}\varepsilon L}=\dfrac{Q_A(1-t_+)}{Fc_{\text{initial}}\varepsilon L}$

8.7. Effects of solid-phase transport and kinetics

Effect of solid-phase transport

The effect of solid-phase diffusion can be evaluated using the solid diffusion timescale (t_s) derived in Eq. **Error! Reference source not found.**. A similar expression has also been reported by Jiang et al.[114] In this study, the particle radius R_p and solid-phase diffusivity D^s are constants, hence the solid-phase diffusion timescale in the positive electrode has a constant value of 133.3 s.

$$t_s = \frac{\text{amount of Li in solid}}{\text{solid diffusion rate}} = \frac{c_s^* \times \left(\frac{4}{3} \pi R_p^3 \right)}{\left(\frac{D^s c_s^*}{R_p} \right) \times \left(4\pi R_p^2 \right)} = \frac{R_p^2}{3D^s} \tag{II-22}$$

Comparison with the timescales defined in **Table II-5** can help estimate the magnitude of solid-phase diffusion resistance. Firstly, the discharge timescale (t_{dis}) used in this study ranges from 320 s to over 2000 s, which is significantly larger than t_s, suggesting fast solid-phase diffusion during the discharge process. Secondly, for the cases in this study the electrolyte diffusion timescale ($t_{\text{depletion}}$) is in general relatively large. For example, the condition used in **Figure II-3** has $t_{\text{depletion}}$ of 256 s, and thus solid-phase transport is not a major limitation in comparison.

Effect of kinetics

We define a dimensional kinetics potential drop ($V_{kinetics}$) in Eq. **Error! Reference source not found.**, which is derived from v^2 defined by Newman and co-workers,[107] and δ' defined in this work.

$$V_{kinetics} = \frac{RTI_{\text{app}}}{F^2 aLk\sqrt{c_{\text{initial}}(c_s^{\max} - c_{s,\text{initial}}^*)c_{s,\text{initial}}^*}} \tag{II-23}$$

For the conditions used in **Figure II-3**, $V_{kinetics}$ is 0.031 V and 0.027 V in positive and negative electrodes, respectively, which are both small compared to the dimensional ohmic drop of 0.1 V. This holds true for all the sets of conditions used in this study.

III. A Study on the Impact of Convection on Thermal Transport

1. Introduction

Lithium-ion (Li^+) batteries (LIBs) are expected to play an important role in global decarbonization through their ubiquity in portable electronics and emergence in transportation and on the electric grid.[115,116] Over the last few decades, LIB prices have steadily decreased while energy density has increased due to a combination of material development, manufacturing improvements, and market scale.[17,76] However, current embodiments are still unable to meet the demanding performance, cost, and scale requirements of many new applications.[27,117] A notable challenge is thermal management, as for today's LIBs, typical operating temperatures between 15 °C and 40 °C are required to ensure optimal cell and battery performance, durability, and safety.[118] At elevated temperatures, accelerated solid-electrolyte interphase growth and component degradation can lead to capacity/power fade,[117,119] and, in the most extreme cases, thermal runaway and hazardous releases. At low temperatures, sluggish electrolyte transport and electrode reaction kinetics facilitate lithium plating and subsequent lithium dendritic growth on the negative electrode.[120,121] In addition, non-uniform temperature distribution leads to reaction maldistribution within the electrodes of individual cells and electrical imbalance between cells within the modules and packs, both of which reduce battery performance and cycle life.[121–123]

To mitigate the adverse impacts of temperature, the battery thermal management system (BTMS) has become an essential component of the battery pack. Most current BTMS utilize an external strategy, where heat is exchanged through the exterior surfaces or tabs of the battery cells. Categorized by the heat transfer media (HTM), some common BTMS include air-, liquid-, and phase-change-materials (PCMs)-based approaches, each possessing benefits and limitations.[124,125] An air-based BTMS has merits, such as, simple structure, low cost, low weight, easy maintenance, and no leakage concern, but is challenged by high-rate charge/discharge applications due to the low heat capacity and thermal conductivity of air.[126,127] Comparatively, a liquid-based BTMS has greater thermal conductivity and heat capacity, leading to better heat transfer efficiency and compactness, and is hence a popular choice for space-constrained applications, such as, battery electric vehicles (BEVs).[119,128,129] Among liquid-based systems, indirect methods that adopt water-glycol mixtures, nanofluids, or liquid metals as the HTM have been widely investigated.[119,124] While such solutions are relatively easy to implement, they rely on heat transfer auxiliaries such as cooling tubes or plates that add weight and complexity to the battery pack. Further, the additional heat resistance and confined contact area with the cell surfaces limits heat transfer efficiency.[124] Direct liquid systems that use a dielectric HTM, such as mineral oil, to contact the cells are emerging because, as compared to the aforementioned indirect methods, they enable simpler design, smaller footprints, and greater heat transfer rates.[130,131] However, the HTM suitable for these systems can be expensive as well as viscous and/or dense, leading to significant cost, power consumption, and added weight.[130] In recent years, PCM-based BTMSs have received considerable attention.[132,133] The PCM absorbs or releases a large amount of latent heat during phase transitions, resulting in a relatively constant temperature for the battery. However, most PCMs have poor thermal conductivities, which lead to low material utilization.[132] There is also a risk for thermal runaway in the case of complete melting, especially under harsh conditions, such as, high charge/discharge rates and high ambient temperature.[134]

In contrast to external thermal management approaches, there has been limited focus on methods of internal thermal management that regulate temperature from within the battery cell. Internal thermal management is most commonly used in battery preheating strategies, which leverage the heat generated inside cells when applying a current at low temperatures due to high resistance.[135,136] Over the past decade, only a few systems that utilize internal means of device cooling have been proposed. Bandhauer et al. developed a passive cooling approach for prismatic cells that used an internal evaporator with micro-channels integrated in a thick current collector.[137] A subset of the same authors then demonstrated through simulations that even though the pack volume increased due to the engineered current collector, the pack-level volumetric energy density for both charge and discharge was still greater than for a similar pack with external liquid cooling.[138] Mohammadian et al. proposed another internal cooling approach for prismatic cells in which liquid electrolyte served as a coolant, flowing through rectangular micro-channels embedded in the electrodes.[139] The authors showed that internal cooling not only effectively decreases the maximum temperature inside the cell, but enables a five-fold improvement in the temperature uniformity within the cell as compared to external liquid cooling at the same pumping power.[139] For cylindrical formats, several studies have contemplated a through-hole in the core of the cell to form an axial fluidic channel for liquid or gas coolants, or to embed a heat pipe or a thermally-conducting metal rod.[140–142] Such a configuration enables rapid heat dissipation especially in the center of the cell albeit with a minor reduction in cell capacity and energy density.

Despite the different configurations, all of the aforementioned internal and external cooling methods for LIBs have inherent shortcomings in thermal management due to their collective reliance on heat exchange with macroscopic surfaces. There is limited heat transfer area within the battery typically, and the introduction of new area inside a cell, for example, via pipes, channels, or rods mentioned above, leads to a loss of internal volume. High heat removal rates therefore require large amounts of cooling fluid, high flow rates, and/or significant pumping or fan power relative to overall battery system size and output. Additional disadvantages are spatial nonuniformity within a cell or pack, especially as battery size increases. Further, there is no access to the interior of electrodes and thus no benefit to transport to and from electrode material surfaces.

As an alternative approach, electrolyte can be directly circulated through the porous electrodes and separator of the electrochemical cell (**Figure III-1b**). A similar configuration was proposed for lead-acid batteries by Choi and Yao in 1979, who showed through simulation that electrolyte circulation can effectively maintain the cell temperature at a desired setpoint while providing a uniform temperature field.[143] For LIBs, such a cell configuration was proposed by Gordon and Suppes in 2013 as an approach to overcome electrolyte diffusion limitations, and is termed the convection battery.[40] Several subsequent reports have studied the benefits of incorporating forced electrolyte convection on mass transport via experiment and modeling.[39–41,144] Specifically, the circulating electrolyte reduces concentration gradients across the cell, thereby preventing salt depletion that adversely affects kinetic, ohmic, and transport resistances. This, in turn, leads to improvements in accessible capacity as well as energy and power density, especially under conditions of electrolyte mass transport limitations, such as high C-rate, thick electrodes, or low electrolyte diffusivity.[144] While an effective means of enhancing mass transport, forced electrolyte convection can also support battery thermal management, as it introduces convective heat transfer to the cell. Thus far, the impact of electrolyte convection on thermal regulation for LIBs has not been well-described. Initial investigation of thermal effects can be difficult to pursue experimentally, as it requires precise control and measurement of the heat fluxes; computationally, non-isothermal modeling provides a path to exploration given that the simultaneous impact of convection on electrolyte heat and mass transport may lead to further synergistic effects.

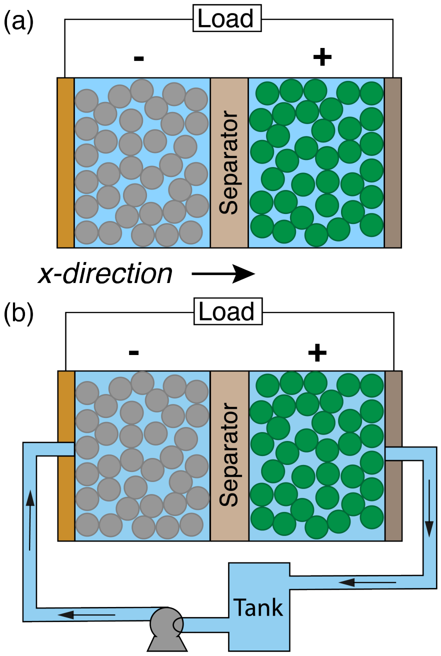

Figure III-1: *Lithium-ion battery configurations with (a) an enclosed cell design as is typical of contemporary devices and (b) the proposed flow-through concept that attempts to improve mass and thermal transport through electrolyte convection. The additional hardware required in (b) consists of an external storage tank, pump, and tubing or pipes to provide forced convection through the porous intercalation materials and separator that compose the battery cell. Note that (b) is presented solely for the purpose of illustrating the underlying concept and the model setup.*

Here, we aim to investigate the effect of a circulating electrolyte stream on thermal management through 1D modeling of a single LIB cell. Building upon prior work that employs isothermal modeling and dimensional analysis to elucidate the impact of electrolyte convection on mass transport,[144] we expand to temperature varying conditions to illustrate the impact of electrolyte convection on simultaneous mass and thermal transport. We first describe the model development including incorporation of a convective term into the governing cell heat balance equation, the modification of thermal boundary conditions at the current collectors, and the introduction of heat exchange equations between the electrolyte tank and the surrounding environment. We subsequently illustrate through three distinct case studies that electrolyte flow can suppress temperature rise in LIB cells that operate at high rates through a combination of reduced heat generation and increased heat removal. Accordingly, we derive dimensionless groups to describe key thermal transport processes that, along with their mass transport analogues,[144] describe conditions under which electrolyte convection can improve thermal management and the extent of these potential benefits. Lastly, we highlight the capability of electrolyte convection to dynamically regulate cell temperature through varying flow rate, which offers consideration of greater flexibility and responsiveness in thermal management.

2. *Model Development*

In our previous work,[144] we developed a convection cell model, LIONSIMBA+c, by extending the Li-ION SIMulation BAttery Toolbox (LIONSIMBA),[111] a pseudo two-dimensional (P2D) representation that has been validated against COMSOL MultiPhysics commercial software[103] and Newman's Fortran DUALFOIL.[100] By introducing a convection term to the governing electrolyte mass transport equation and including a continuity equation to describe the electrolyte tank, we were able to investigate the impact of electrolyte flow on cell performance as a function of component geometries, electrolyte properties, and cell operating conditions. The detailed descriptions of the modifications made, the governing equations, as well as the discretized approaches can be found in our prior open-access publication.[144] Here, we expand the capabilities of LIONSIMBA+c to enable the study of thermal processes within a convection cell. Specifically, we (1) introduced a convection term into the governing heat balance equation within the electrodes and separator; (2) amended the boundary conditions to account for the flowing electrolyte at the inlet and outlet of the cell; (3) adjusted the heat transport equation at both current collectors to account for the cell design change due to the addition of electrolyte tubing; and (4) incorporated energy conservation equations to track the electrolyte temperature within the external tank under a range of assumptions about its heat exchange mode with the surrounding environment including isothermal, adiabatic, ambient cooling, and constant heat flux input/output.

The original LIONSIMBA software package, developed by Torchio et al.,[111] considers both isothermal and non-isothermal cell operation. For non-isothermal operation, the model adopts a general thermal treatment derived by Gu and Wang[145] to simulate the temperature change within a LIB cell. Similar to the description of electrolyte mass transport, the thermal model assumes that the cell temperature is radially uniform but that spatial temperature gradients can exist in the axial direction (x-direction in **Figure III-1**). An assumption underlying this approach is that the lateral walls of the cell are well-insulated, and heat exchange with the environment only occurs through the current collectors at either end of the cell (axial). It is also assumed that the different phases within the cell are in local thermal equilibrium, that is $T_{\text{liquid}}(x,t) = T_{\text{solid}}(x,t) = T(x,t)$. In LIONSIMBA+c, a convective term is introduced into the local heat balance within the electrodes and separator, as shown in Eq. (III-1).

$$\rho_i C_{p,i} \frac{\partial T(x,t)}{\partial t} = \frac{\partial}{\partial x}[\lambda_i \frac{\partial T(x,t)}{\partial x}] - \rho_e C_{p,e} v \frac{\partial T(x,t)}{\partial x} + \begin{cases} Q_{\text{ohm}} + Q_{\text{rxn}} + Q_{\text{rev}} & \text{if } i \in \{p,n\} \\ Q_{\text{ohm}} & \text{if } i \in \{s\} \end{cases} \tag{III-1}$$

Here, ρ_i, $C_{p,i}$, and λ_i are the density, heat capacity, and thermal conductivity of domain *i,* where $i \in \{p, s, n\}$ indicates the positive electrode (*p*), separator (*s*), or negative electrode (*n*), respectively, $T(x,t)$ is the temperature at position *x* and time *t*, ρ_e is the electrolyte density, $C_{p,e}$ is the electrolyte heat capacity, and *v* is the superficial electrolyte velocity, which is assumed to be constant throughout the cell. While many possible sources of heat generation exist in a LIB cell,[146] the model considers three major contributors: (1) Q_{ohm}, the heat generation from ohmic resistance (Joule heating); (2) Q_{rxn}, the irreversible reaction heat generation due to activation overpotential; (3) Q_{rev}, the reversible reaction heat generation due to entropy change. The expressions for these heat generation sources are refined based on the work by Srinivasan and Wang,[147] and provided in Section 6. The current collectors exchange heat with the surrounding environment, yielding the same boundary conditions as the original model:

$$-\lambda_{cu}\left.\frac{\partial T(x,t)}{\partial x}\right|_{x=0}=h_{\mathrm{cell}}\left(T_{ambient}-T(x,t)\right) \tag{III-2}$$

$$-\lambda_{al}\left.\frac{\partial T(x,t)}{\partial x}\right|_{x=L}=h_{\mathrm{cell}}\left(T(x,t)-T_{ambient}\right) \tag{III-3}$$

Here, λ_{cu} and λ_{al} are the thermal conductivities of the negative copper (*cu*) and positive aluminum (*al*) current collectors, respectively, h_{cell} is the convective heat transfer coefficient of the cell, and $T_{ambient}$ is the temperature of the ambient environment external to and surrounding the cell, which is assumed to be constant at 298 K in this study. As shown in **Figure III-1b**, the convection cell configuration contemplated in this study assumes that the electrolyte flow enters and exits the electrochemical cell through tubes located at the center of the current collectors. For simplicity, we assume that, upon entering the cell, the flow is immediately uniformly distributed in the radial direction (cross-sectional plane perpendicular to the x-direction in **Figure III-1**), and that this uniformity is maintained until the exit (i.e., we do not consider any entrance or exit effects). We also assume the tubing between the cell and the tank is well-insulated and does not exchange heat with the surrounding environment or the current collectors. At the cell inlet and outlet, Danckwerts boundary conditions are implemented:

$$\begin{aligned}A_{\mathrm{cell}}\mathrm{N}_{inlet}&=\left.\left[-(A_{\mathrm{cell}}-A_{\mathrm{tube}})\lambda_{i,flow^{in}}\frac{\partial T(x,t)}{\partial x}+A_{\mathrm{cell}}\rho_e C_{p,e}vT(x,t)\right]\right|_{flow^{in}}\\&=\left.\left[-A_{\mathrm{cell}}\lambda_{i,flow^{out}}\frac{\partial T(x,t)}{\partial x}+A_{\mathrm{cell}}\rho_e C_{p,e}vT(x,t)\right]\right|_{flow^{out}}\end{aligned} \tag{III-4}$$

$$\begin{aligned}A_{\mathrm{cell}}\mathrm{N}_{outlet}&=\left.\left[-(A_{\mathrm{cell}}-A_{\mathrm{tube}})\lambda_{i,flow^{out}}\frac{\partial T(x,t)}{\partial x}+A_{\mathrm{cell}}\rho_e C_{p,e}vT(x,t)\right]\right|_{flow^{out}}\\&=\left.\left[-(A_{\mathrm{cell}}-A_{\mathrm{tube}})\lambda_{i,flow^{in}}\frac{\partial T(x,t)}{\partial x}+A_{\mathrm{cell}}\rho_e C_{p,e}vT(x,t)\right]\right|_{flow^{in}}\end{aligned} \tag{III-5}$$

In Eq. (III-4) and (III-5), A_{cell} and A_{tube} are the cross-sectional areas of the cell and the tube, respectively. The addition of the inlet/outlet tubes at the center of the current collectors necessitates modification of the heat transfer equation to account for the continuity in the output current:

$$\rho_i C_{p,i}\frac{\partial T(x,t)}{\partial t}=\frac{\partial}{\partial x}[\lambda_i\frac{\partial T(x,t)}{\partial x}]+\frac{\left(\frac{A_{\text{cell}}}{A_{\text{c.c.}}}I_{app}(t)\right)^2}{\sigma_i}\quad i\in\{al,cu\} \tag{III-6}$$

Here, $A_{\text{c.c.}}$ is the current collector cross-sectional area where $A_{\text{c.c.}}+A_{\text{tube}} = A_{\text{cell}}$, I_{app} is the applied current density, and σ_i is the electrical conductivity of the current collectors. Note that variable current operation (I_{app} as a function of time) is possible with LIONSIMBA+c, but is not pursued here. The temperature change inside the external electrolyte tank can be described as follows:

$$V_{\text{tank}}\rho_e C_{p,e}\frac{dT_{\text{tank}}(t)}{dt}=\begin{cases} 0 & \text{Isothermal} \\ A_{cell}\rho_e C_{p,e}v[T_{in}(t)-T_{\text{tank}}(t)]+\begin{cases} 0 & \text{Adiabatic} \\ A_{\text{tank}}h_{\text{tank}}\left(T_{ambient}-T_{\text{tank}}(t)\right) & \text{Ambient Cooling} \\ A_{\text{tank}}q & \text{Constant Input}\end{cases} \end{cases} \tag{III-7}$$

We assume that the tank is well-mixed with a volume V_{tank} and a total surface area A_{tank}. Four different heat exchange conditions between the tank and the surrounding environment are considered in the model: (1) Isothermal, where the tank remains at its initial temperature at all times; (2) adiabatic, where the tank does not exchange heat with its surroundings, and any temperature change is only due to the electrolyte flowing into and out of the tank; (3) ambient cooling, where the surface of the tank exchanges heat with its surroundings via convective cooling, and h_{tank} is the convective heat transfer coefficient of the tank; and (4) constant input, where there is constant heat flux q into (q is positive) or out of (q is negative) the tank through its surface. The discretization of the thermal governing equations follows the approach described in prior work,[144] which uses the finite volume method (FVM) to partition the spatial domain into discrete volumes, while the convection term is treated with the upwind differencing scheme. Upon the aforementioned modifications, we compare simulated discharge curves using both LIONSIMBA and LIONSIMBA+c under non-isothermal conditions and with stagnant electrolyte ($v = 0\ \mu\text{m/s}$). As shown in **Figure III-7**, there is no difference between the model outputs across a range of C-rates, indicating that the modifications did not introduce artificial changes to the expected behavior.

The parameters used for the simulations performed in this study are shown in **Table III-1**. While this modeling framework can support the investigation of a wide range of component parameters and operating conditions, for clarity and tractability, we elect to study cell behavior under the following conditions. For all cell components, the literature-reported experimental values of ρ_i, $C_{p,i}$, and λ_i are used.[148] Temperature-dependent physicochemical properties (e.g., electrolyte diffusion coefficient) are described using the relationships implemented in the original LIONSIMBA package,[111] which are shown in Section 6. All the simulations were performed for galvanostatic operation, with a state of charge (SoC) range of 85.51% to 0.9%, a lower voltage limit of 2.5 V, and an upper temperature limits of 52 °C (325 K) based on the typical operating conditions and safety cutoffs for LIBs.[149] For the subsequent simulations, we used a cell cross-sectional area of 1 cm^2 and an adiabatic tank with a volume of 50 mL. The use of 1 cm^2 is convenient for normalization and does not reflect a fundamental limitation of the model. Specifically, the findings described herein scale to cells of various areas subject to cross-sectional uniformity. The tube cross-sectional area is assumed to be 10% of the cell cross-sectional area, that is, $\frac{A_{\text{tube}}}{A_{\text{cell}}} = 1 - \frac{A_{\text{c.c.}}}{A_{\text{cell}}} = 0.1$. While LIONSIMBA+c makes it possible to specify distinct initial electrolyte concentrations and temperatures in the cell and tank, this work assumes the same initial electrolyte concentration of 1 M and same initial temperature of 25 °C (298 K) throughout the domain.

Table III-1: *Simulation parameters used in this study.*

	Units	**Positive CC**	**Positive Electrode**	**Separator**	**Negative Electrode**	**Negative CC**
	-	Al	$Li_\theta CoO_2$	-	$Li_\theta C_6$	Cu
a	m^2/m^3	-	862500	-	851100	-
$brugg$	-	-	2.5	2.5	2.5	-
C_p	J/kg/K	903	1269	1978	1437	385
$C_{p,e}$	2055 J/kg/K					
c_{initial}	mol/m^3	-	1000	1000	1000	-
$c_s^{\max}$	mol/m^3	-	51554	-	30555	-
D_i^s	m^2/s	-	1×10^{-14}	-	3.9×10^{-14}	-
$E_a^{D_i^s}$	J/mol	-	5000	-	5000	-
$E_a^{k_i}$	J/mol	-	5000	-	5000	-
F	96487 C/mol	-	-	-	-	-
I_{app}	$150\ A/m^2$					
k_i	$m^{2.5}/(mol^{0.5}s)$	-	2.334×10^{-11}	-	5.031×10^{-11}	-
L	m	1×10^{-5}	8×10^{-5}	4×10^{-5}	8×10^{-5}	1×10^{-5}
n	-	12	100	50	100	12
R	8.314 J/mol/K	-	-	-	-	-
R_p	m	-	2×10^{-6}	-	2×10^{-6}	-
t_+	0.37					
ε	-	-	0.4	0.4	0.4	-
$\varepsilon_{\mathrm{filler}}$	-	-	0.025	-	0.0326	-
$\Theta_{100\%}$	-	-	0.4955	-	0.8551	-
$\Theta_{0\%}$	-	-	0.9917	-	0.0066	-
λ	W/m/K	238	1.58	0.33	1.04	398
ρ	kg/m^3	2702	2329	1009	1347	8933
ρ_e	$1130\ kg/m^3$					
σ	S/m	3.55×10^{7}	100	-	100	5.96×10^{7}

3. Model Analysis

3.1. Base Case: Conditions of Significant Thermal and Mass Transport Limitations

To illustrate how the consideration of the thermal effects impacts convection cell performance, we begin by repeating a base case analysis described in our prior work,[144] where the galvanostatic discharge of a single LIB cell with a stagnant electrolyte (v = 0 μm/s) was simulated at 5.7 C (150 A/m^2 for a 26 Ah/m^2 cell) and at isothermal conditions. Here, as shown in **Figure III-2**, we perform the same simulation, but relaxing the isothermal assumption and allowing the cell temperature to vary freely. A small cell convective heat transfer coefficient (h_{cell} = 0.5 W/(m^{2}K)) is used to represent any background heat exchange between the cell and its surroundings. The discharge curve, **Figure III-2a**, shows that the accessible capacity without flow is just 54% of theoretical capacity. A large electrolyte concentration gradient develops across the cell during discharge due to the competing effects of diffusion and electromigration (**Figure III-2b**). However, with the inclusion of thermal processes, complete electrolyte salt depletion in the positive electrode is not realized by the end of the discharge, indicating that electrolyte mass transport limitation is not the sole cause of the abbreviated runtime. Rather, in the absence of electrolyte flow, the cell temperature increases rapidly upon discharge and reaches the cutoff (safety) temperature prior to electrolyte depletion (**Figure III-2c**). The rate of temperature rise can be slowed by convective flow, and for the single cell considered here, a superficial electrolyte velocity of 0.7 μm/s prevents the cell from hitting the cutoff temperature during discharge. For perspective, this flowrate for the single cell corresponds to a residence time of ~290s. Greater velocities further suppress cell temperature rise, and gradually reduce the electrolyte concentration gradient as well (**Figure III-2b**). Note that while the model simulates the cell temperature as a function of axial position, the temperature is uniform across the cell due to its thinness (**Figure III-8**). Thus, the temperature shown in **Figure III-2c** represents both the average cell temperature and the temperature at all positions and in all phases within the cell. Overall, **Figure III-2** shows that the introduction of electrolyte flow simultaneously enhances mass and heat transport, both driving electrolyte concentration uniformity and mitigating cell temperature rise. It is noteworthy that, for the single cell analyzed in this study, overcoming the mass and thermal limitations requires electrolyte convection at similar scales, on the order of 1-10 μm/s, for a near-uniform electrolyte concentration profile (**Figure III-2b**) and a temperature trajectory close to the initial cell temperature (**Figure III-2c**). In a battery format of greater thickness, such as, multiple layers of the same single cell, the flow rate required to eliminate mass transport limitation would remain in the same order of magnitude as that for the single cell. However, a larger flow rate would be necessary to overcome thermal limitations. Nevertheless, for the scope of the current study, the corresponding pressure drop and resultant pumping losses across a single cell follow the estimates described in our previous study[144] and remain negligible compared to the energy gain on a per cell basis (Section 8.1).

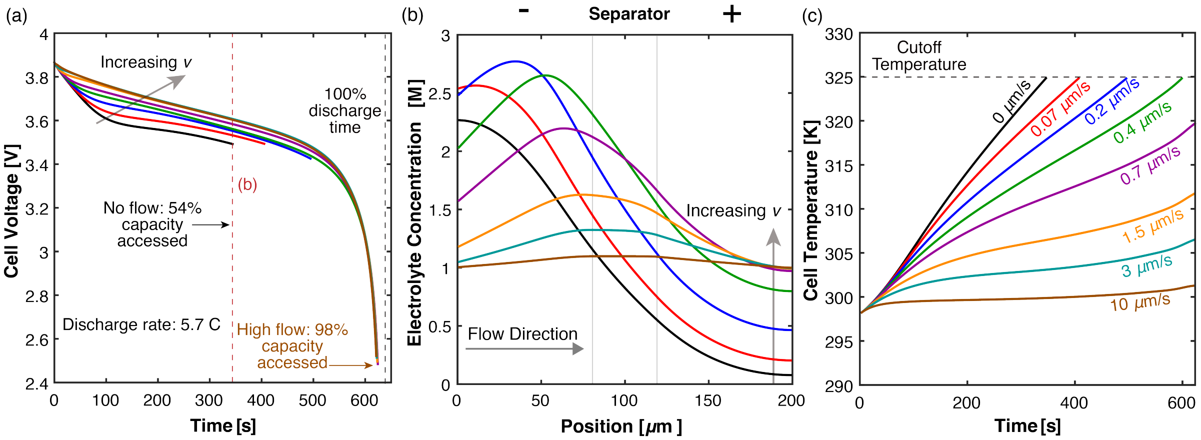

Figure III-2: *The effect of electrolyte convection on (a) the galvanostatic cell discharge (b) the concentration profile of electrolyte within the cell at t = 347 s, the end of discharge for the no flow case, and (c) the time-dependent trajectory of cell temperature. These results show the benefit of increasing flow rate on cell performance by minimizing the electrolyte concentration gradient while suppressing temperature rise. The corresponding heat generation data can be found in* ***Figure III-9****. Further discussions of the tank temperature change and the impacts of flow direction can be found in Section 8.2 and Section 8.3.*

3.2. Dimensionless Group Development

Having demonstrated the case of benefit to runtime with both heat and mass transport effects, we present a generalized analysis of cell and component dimensions, component properties, and operational parameters where convection may prove advantageous. Compact and meaningful representation of cell performance as a function of individual cell properties and operating conditions can be challenging as it often requires comprehensive parametric sweeps. Alternatively, combining the relevant physical parameters into dimensionless groups can provide insight on how the relative scales of different physical processes influence performance. For the single convection cell considered in this study, the temperature profile across the cell remains uniform, hence we limit our focus to dimensionless groups that describe the average cell temperature rise. To derive the dimensionless groups, we examine the overall cell heat balance equation:[*]

$$\overline{\rho}\,\overline{C}_p A_{\text{cell}} L_{\text{cell}} \frac{\mathrm{d}T_{\text{cell}}}{\mathrm{d}t} = \overline{Q}_{\text{total}} A_{\text{cell}} L_{\text{cell}} - A_{\text{cell}} \rho_e C_{p,e} v\left(T_{\text{cell}} - T_{\text{tank}}\right) - 2A_{\text{c.c.}} h_{\text{cell}}\left(T_{\text{cell}} - T_{ambient}\right) \quad \text{(III-8)}$$

Next, we identify appropriate scales for the terms in Eq. (III-8). Applied current density and areal capacity provide a timescale of discharge, $t_{\text{dis}} = \frac{Q_A}{I_{\text{app}}}$. Then, by approximating the cell temperature change from its initial temperature, T_{init}, at $t = 0$, to a safety cutoff temperature, T_{max}, at $t = t_{\text{dis}}$, and the tank temperature with its initial temperature, $T_{\text{tank, init}}$, several useful quantities emerge: (1) the magnitude of ambient heat exchange rate of the cell, $2A_{\text{c.c.}} h_{\text{cell}}\left(T_{\text{max}} - T_{ambient}\right)$– in this case, the cell exchanges heat with the surrounding environment through the current collectors at either end of the device only; (2) the magnitude of convective heat exchange rate with the tank, $A_{\text{cell}} \rho_e C_{p,e} v(T_{\text{max}} - T_{\text{tank,init}})$; (3) average heat generation rate, $\overline{Q}_{total} A_{\text{cell}} L_{\text{cell}}$; and (4) Average heat storage rate, $\frac{\overline{\rho}\overline{C}_p A_{\text{cell}} L_{\text{cell}} (T_{\text{max}} - T_{\text{init}})}{t_{\text{dis}}}$. The average volumetric heat generation rate, $\overline{Q}_{total}$, can be estimated

---

[*] Cell thermal energy accumulates or depletes from internal heat generation and net fluxes at the boundaries – convection from the tank and ambient heat exchange. Mathematically, this emerges from integration of the local heat balance, Eq. (III-1), and substitutions from the subsequent equations.

using the cell parameters and operating conditions, as detailed in Section 8.4; the multiplicative product of the average density, $\bar{\rho}$, and the average heat capacity, $\bar{C}_p$, can be calculated by averaging the ρC_p products of each cell component weighted by their respective thicknesses. Comparing these quantities yields the list of dimensionless groups that can be used to evaluate the average cell temperature gain (shown in **Table III-2**), which are subsequently denoted with the subscript H. To prevent any temperature rise, the heat removal rate from the cell must balance the heat generation rate within the cell. That is, the ratio of heat generation to heat removal must be small. In the case of an enclosed device (e.g., a conventional LIB cell) where heat removal relies on ambient heat exchange alone, this ratio is captured by the dimensionless parameter, γ_H. A large γ_H value indicates that the heat removal rate is insufficient, which, in turn, leads to temperature increases during charge or discharge. In the case of a convection cell, the electrolyte flow provides an additional mode of heat removal, and ξ_H represents the ratio of the heat generation to the sum of heat removal via ambient cooling and electrolyte convection. In the absence of convection, $\gamma_H = \xi_H$. Similar to γ_H, a large ξ_H value indicates insufficient combined heat removal as compared to heat generation. Finally, the inherent buffering ability of the cell against heat generation is captured by β_H, where a large value indicates the cell is more prone to temperature increase for a given amount of heat generation. The dimensionless groups for mass transport, derived in our prior work,[144] are also included in **Table III-2** for reference and comparison, and are subsequently denoted with the subscript M. These groups are analogous to those used to describe heat transport. Specifically, γ_M compares the electromigrative and diffusive fluxes, where a large value of this parameter indicates an increased likelihood for electrolyte salt depletion in the positive electrode during discharge due to insufficient diffusive transport. ξ_M compares the electromigrative flux to the sum of diffusive and convective fluxes, where large values of this variable indicates that the combination of diffusive and convective fluxes are slower than the electromigrative flux that removes anions from the cathode. β_{M} measures the buffering ability of the cell against electrolyte salt depletion, and a large value of this quantity indicates that the initial amount of salt in the electrolyte is insufficient compared to the depletion by the electromigration of the anions.

Table III-2: *Dimensionless groups quantifying the extent of bulk mass and thermal transport limitations.*

Dimensionless group	**Meaning**	**Mass Transport [M]**	**Heat Transfer [H] ($\bar{T}_{cell}$ vs. t)**
γ	Inherent transport ability	$\frac{I_{\mathrm{app}}(1-t_{+})L}{FD_{\mathrm{eff}}c_{\mathrm{initial}}}$	$\frac{\bar{Q}_{total}L_{\mathrm{cell}}}{2\frac{A_{\mathrm{c.c.}}}{A_{\mathrm{cell}}}h_{\mathrm{cell}}\left(T_{\max}-T_{ambient}\right)}$
ξ	Transport ability with convection	$\frac{I_{\mathrm{app}}(1-t_{+})}{\frac{FD_{\mathrm{eff}}c_{\mathrm{initial}}}{L}+Fvc_{\mathrm{initial}}}$	$\frac{\bar{Q}_{total}L_{\mathrm{cell}}}{2\frac{A_{\mathrm{c.c.}}}{A_{\mathrm{cell}}}h_{\mathrm{cell}}\left(T_{\max}-T_{ambient}\right)+\rho_{e}C_{p,e}v\left(T_{\max}-T_{\mathrm{tank,init}}\right)}$
β	Buffering ability	$\frac{I_{\mathrm{app}}t_{\mathrm{dis}}(1-t_{+})}{Fc_{\mathrm{initial}}\varepsilon L}$	$\frac{\bar{Q}_{total}t_{\mathrm{dis}}}{\bar{\rho}\bar{C}_{p}\left(T_{\max}-T_{\mathrm{init}}\right)}$

The corresponding dimensionless group values of the *Base Case* are shown in **Table III-3, column (a)**. The large values for all the four dimensionless groups indicate that, under these conditions and in the absence of convection, the inherent mass and thermal transport properties are insufficient to support the high discharge rate of 5.7 C in a cell of these dimensions. This deficiency explains the large electrolyte concentration gradient and rapid temperature increase shown in **Figures III-2b** and **c**, respectively.

Table III-3: *Mass [M] and heat [H] transport dimensionless group values for the cases demonstrated in (a) Base Case (b) Diffusive Transport Limited Case and (c) Thermal Transport Limited Case. The electrolyte properties at room temperature are used for the mass transport dimensionless group calculations.*

	(a) Base Case	**(b) Diffusive Transport Limited**	**(c) Thermal Transport Limited**
γ_M	2.4	2.4	2.4×10^{-3}
β_M	19.6	19.6	19.6
γ_H	3.0	3.0×10^{-3}	2.1
β_H	3.6	3.6	2.5

While the *Base Case* demonstrates that the introduction of electrolyte convection enables simultaneous enhancement of mass and heat transport, further investigation is needed to decouple and elucidate the impact of convection on each process. This can be achieved by contemplating two extensions of the *Base Case*: (1) *Diffusive Transport Limited Case*, where without convection, the cell has adequate heat transfer capabilities but the same poor mass transport properties and conditions used in the *Base Case*, and (2) *Thermal Transport Limited Case*, where the mass transport in the cell without convection is sufficiently facile, but the heat transfer rates are restricting. The following sections discuss the findings from these two alternative cases.

3.3. Diffusive Transport Limited Case

In the first scenario, to focus on a diffusion limited case, we consider a cell with a convective heat transfer coefficient (h_{cell} = 500 W/(m^{2}K)) large enough to facilitate thermal transport to the point that the increase in cell temperature during discharge is negligible (**Figure III-10**), while all other conditions remain identical to the *Base Case*. The corresponding dimensionless group values are shown in **Table III-3, column (b)**. The heat transfer coefficient value chosen here is representative of an indirect liquid cooling system.[150] This case corresponds to a cell with external heat removal capability sufficient to maintain near-isothermal operation (e.g., a highly effective thermal regulation system), which approaches the isothermal base case described in our prior work.[144] In the absence of an elevated average cell temperature, which increases diffusion rates, electrolyte mass transport presents significant limitations, but this can be alleviated by increasing electrolyte convection (or decreasing ξ_M value) as shown in **Figure III-3a**. Enhanced electrolyte mass transport rates also positively impact the thermal regulation of the cell. As shown in **Figure III-3b**, reduced electrolyte concentration gradients facilitate more uniform reversible heat generation, suggesting improved reaction homogeneity particularly within the Li-ion-consuming electrode (here, the positive electrode). Importantly, this observation implies that electrolyte convection may help mitigate reaction maldistribution that limits power output and capacity utilization of thick electrodes in energy-dense cells.[78] Furthermore, electrolyte convection can reduce irreversible reaction heat generation in the positive electrode and overall Joule heating as shown in **Figures III-3c** and **III-3d**, respectively. As convection enables higher electrolyte concentration in the positive electrode facilitating the charge transfer reaction, the activation overpotential required to sustain a desired current output is reduced thus lowering irreversible reaction heat generation. Moreover, a uniform ~1 M electrolyte concentration across the cell decreases Joule heating by lowering ohmic losses (high ionic conductivity). Collectively, these results demonstrate that electrolyte flow can enable greater spatial uniformity in heat generation as well as reduce overall heat generation within a cell. In this case, the average volumetric heat generation rate ($\bar{Q}_{total}$) is halved at $10\,\mu$m/s as compared to stagnant operation. As previously mentioned, the cell temperature gain is determined by both the rate of heat generation and the rate of heat removal. It is this ability to decrease heat generation via electrolyte flow that differentiates the convection approach from other external and internal thermal regulation methods that are solely designed to enhance heat removal rates. The reduction in heat generation through convection appears unique amongst reported BTMS and relaxes the requirement for heat removal capability in the first place.

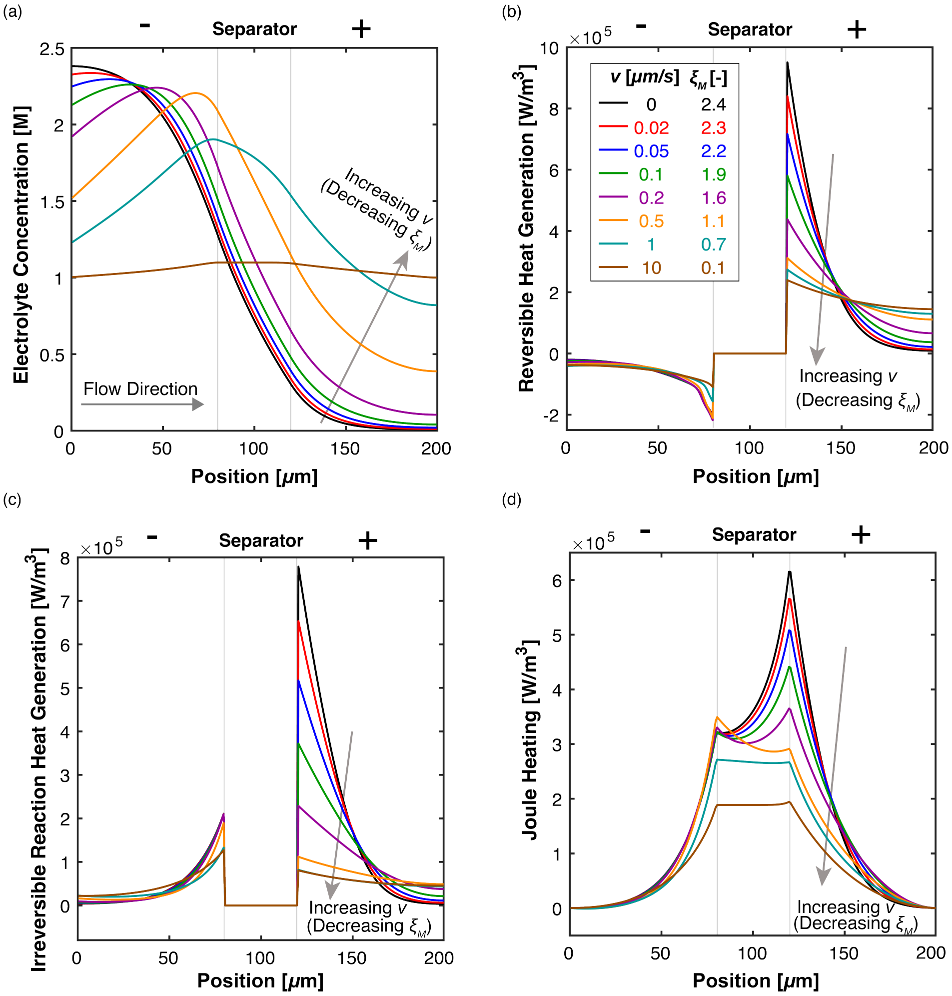

Figure III-3: *Diffusive transport limited case (a) distributions of concentration and contributions to (b) reversible heat generation, (c) irreversible reaction heat generation, and (d) Joule heating. The figures are taken at t = 100 s, before complete electrolyte salt depletion occurs. The Joule heating in the current collectors is negligible and not shown.*

3.4. Thermal Transport Limited Case

In the second scenario, we consider a cell without mass transfer limitations by invoking a very large electrolyte diffusivity (*D = normal value* × *10^3*) with all other conditions the same as the *Base Case*. While, to the best of our knowledge, such diffusive rates are infeasible in practical electrolytes, the simulated conditions are instructive as they enable isolation of the effects of electrolyte convection on heat transfer. The corresponding dimensionless group values are shown in **Table III-3, column (c)**. The γ_H and β_H values are both slightly lower than *Base Case* values as the augmented diffusivity leads to more uniform electrolyte concentration across the cell, reducing the activation overpotential and thus diminishing the heat generation rate, $\bar{Q}_{total}$. This result is analogous to increasing the electrolyte flow rate in the previous case. This effect is clearly observable in **Figure III-4**, where even without electrolyte flow, the cell can discharge for a longer time as compared to its counterpart in **Figure III-2c**. With the introduction of electrolyte flow, the temperature rise is further suppressed, and when $\xi_H \lesssim 1$, the cell can be fully discharged, accessing almost all of the available charge storage capacity, without hitting the upper threshold. Thus, **Figure III-4** evinces the second effect of electrolyte flow on thermal management, namely that bulk flow can remove heat from the cell to prevent temperature increase (i.e., boosting the heat removal capability of the cell). Additionally, consistent with physical intuition, a transition value of $\xi_H \lesssim 1$ means that the heat generation rate $\lesssim$ the heat removal rate. As a heuristic, the amount of flow required to prevent the cell from hitting the cutoff temperature can be estimated from $\xi_H = 1$, and the remaining parameters defining this dimensionless group in **Table III-2**. Note that although a single cell (~200 μm) is demonstrated in this study, ξ_H is also applicable to a larger battery format, which suggests that the flowrate needed to suppress average temperature rise roughly scales with the system dimension in the direction of flow. Also note that while convection can effectively prevent the cell temperature gain, it may be desirable for the cell to operate at a set temperature above or below the ambient conditions.[151,152] This may be to promote favorable reaction kinetics and/or mass transport characteristics, to heat a device in cold climes, or to cool a device subjected to excessive heat due to local weather conditions or proximity to an external heat source. A non-ambient target temperature can be achieved by regulating the flow rate and/or introducing electrolyte pre- conditioned at a different inlet temperature.

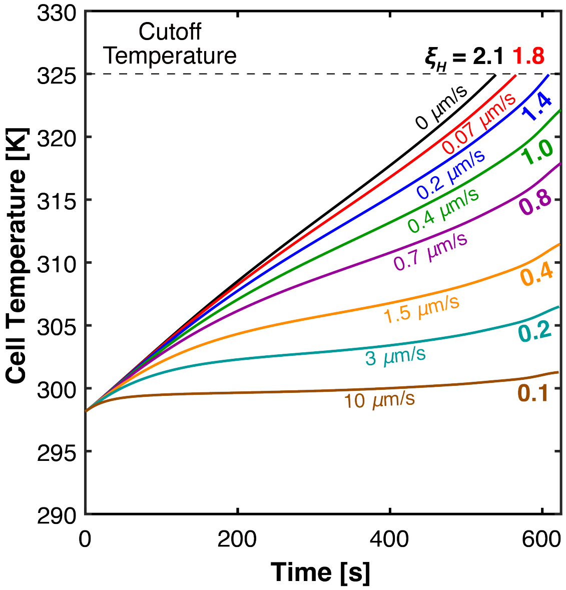

Figure III-4: *Thermal transport limited case temperature profile over time. The use of a large electrolyte diffusivity (D = normal value × 10^3) yields a uniform electrolyte concentration profile even in the absence of electrolyte flow (**Figure III-11**). Thus, the suppression of temperature gain by increasing flow rate is solely due to increased rates of heat removal and no effect on heat generation.*

3.5. Comparison Between Internal and External Cooling

The analyses above illustrate the unique advantages that a flowing electrolyte offers through simultaneous improvement of mass and heat transport with one of the two limitations significantly relaxed. Now we directly compare the impact of convection (hereafter referred to as “internal cooling”) and the typical external thermal management methods (hereafter referred to as “external cooling”) on temperature regulation and cell performance, with no upfront relaxation of any transport limitation. We use the same cell configuration and discharge conditions as in the *Base Case*. For external cooling, the cell exchanges heat with the surrounding environment through the axial ends (i.e., the current collectors), with a total representative heat exchange rate of $2A_{\text{cell}}h_{\text{cell}}\left(T_{\max}-T_{ambient}\right)$. For internal cooling, electrolyte flows through the cell in the direction shown in **Figure III-1b** (from the negative electrode to the positive electrode) and exchanges heat with the tank at a representative heat exchange rate, $A_{\text{cell}}\rho_e C_{p,e}v(T_{\max}-T_{\text{tank}})$. Equivalent heat removal rates are anticipated for the external and internal modes when the two heat exchange rates are equal, as is shown in Section 8.5. However, as **Figure III-5** demonstrates, an "equivalent" set of v and h_{cell} values yields the same heat removal capability yet different impact on cell temperature regulation and thus performance. With external cooling, the first increments in h_{cell} value help extend the cell runtime (**Figure III-5a**) by inhibiting temperature rise (**Figure III-5c**) and prolonging or avoiding the 325 K cutoff. However, without internal convection, mass transfer relies upon temperature-dependent diffusion alone, and further increases in h_{cell} values have an adverse effect on mass transfer. A lower average cell temperature results in slower electrolyte mass transport (**Figure III-5b**) leading to lower cell operating voltage (reduced power density), and even shortens the cell runtime as electrolyte salt depletion increases at higher h_{cell} values. Hence, for external cooling, increasing heat removal capability (i.e., increasing h_{cell}) improves thermal transport but compromises mass transport; if the cell has a large electrolyte mass transport resistance (i.e., large γ_M and β_M values*)*, such as the case shown in **Figure III-5**, increasing h_{cell} values will ultimately cause the cell to transition from thermal-transport-limited behavior to diffusive-transport-limited behavior. This compromise is in contrast with the internal cooling, where increasing heat removal capability (i.e., increasing v) results in simultaneous heat and mass transport enhancement, as shown in **Figures III-5d**, **III-5e**, and **III-5f**, ensuring that neither bulk transport mode hinders cell performance at sufficient v.

The contrasting impact of the two cooling strategies on electrolyte mass transport has further implications on their efficacy. As discussed in the *Diffusive Transport Limited Case,* improved electrolyte mass transport, such as, with internal cooling, leads to diminished heat generation rates due to reduced overpotential losses. Conversely, heat removal with external cooling decreases electrolyte mass transport and therefore increases heat generation as shown in **Figure III-12**. Consequently, internal cooling suppresses cell temperature rise more effectively than external cooling even with the same heat removal capability, as observed by comparing **Figures III-5c** with **III-5f**. This implies that compared to external cooling, the heat removal capability required of internal cooling is lowered due to the reduced amount of heat generation. This finding further supports the argument that through enhanced electrolyte mass transport, the internal cooling method offers unique advantages over external cooling methods by both removing heat (heat transfer) *and* reducing heat generation (mass transfer), resulting in greater effectiveness.

The comparison between internal and external cooling discussed here is not limited to a single cell of ~200 μm thickness but is also applicable to larger systems, such as, multiple cell layers. However, in these cases, the effect of temperature gradient becomes significant and should be considered for the design with both cooling strategies. Regarding the internal cooling strategy, the temperature gradient is mainly present in the direction of flow and is closely related to the system design/configuration and resultant flow path, which are beyond the scope of this initial work. Nevertheless, the temperature gradient can be significantly reduced or become negligible at high flow rates. As such, the findings presented here represent the full potential of electrolyte flow (i.e., the performance of an optimized system) and provide a basis for future work on system development.

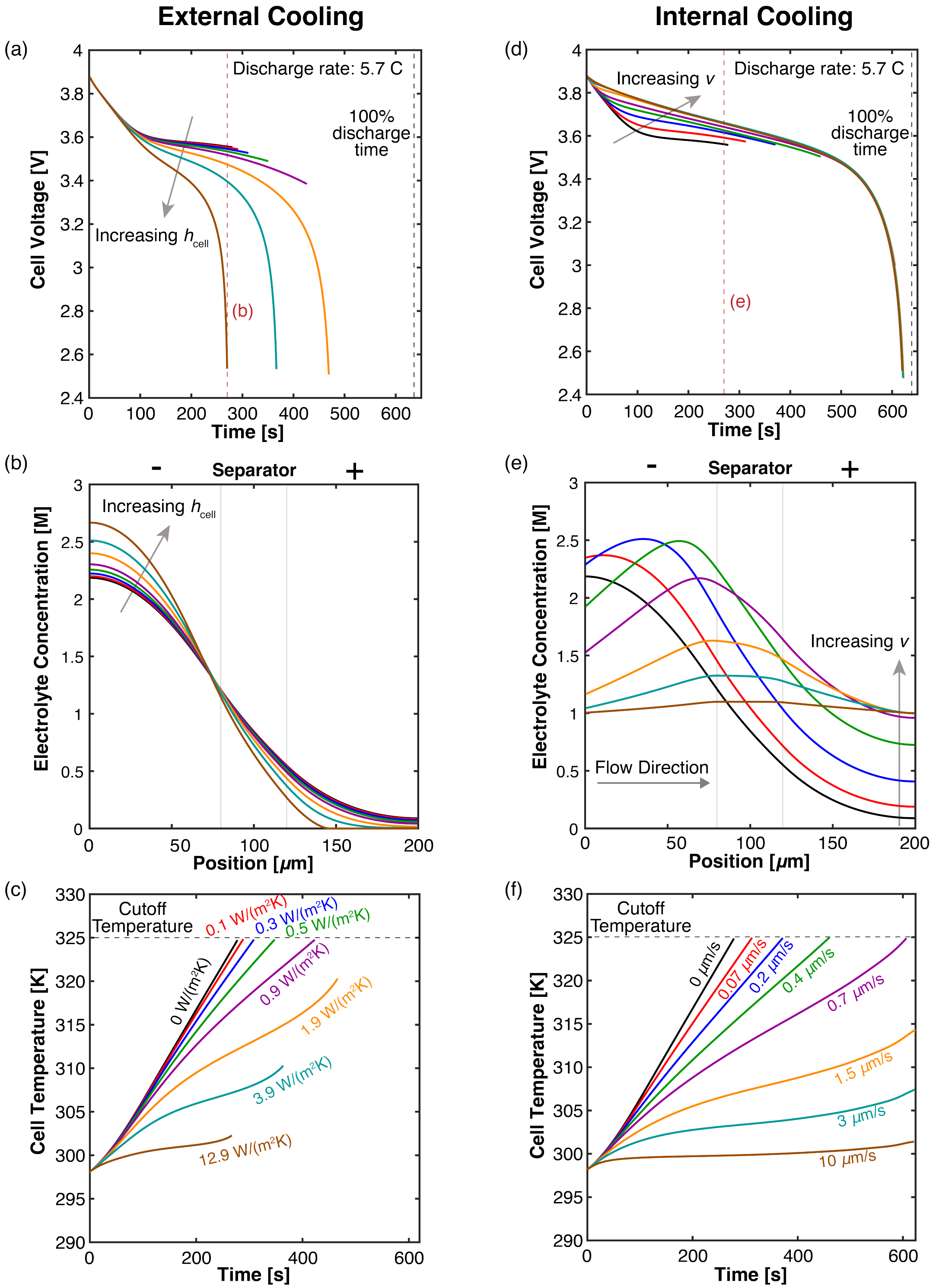

Figure III-5: *Comparison of external cooling (left plots) and internal convective cooling (right plots) on three (3) key outputs: galvanostatic discharge curves (a, d), electrolyte concentration distributions (b, e) at 269 s, the end of the shortest discharge ($h_{cell} = 12.9$ W/(m^2K)), and transient temperature trajectories (c, f). Each curve on the left has a corresponding curve on the right of the same color with equal heat removal rate. Internal cooling shows improvements in these 3 key outputs with successive increasing flow rates.*

However, with external cooling, cell behavior shifts from thermal to mass transport limited ultimately leading to truncated discharge at the highest heat removal rate simulated.

3.6. On the Potential for Dynamic Thermal Regulation via Varying Electrolyte Flow Rate

The ability to modulate electrolyte flow rate during convection cell operation offers new opportunities to dynamically regulate the cell performance. While many different and specific scenarios could be considered, we contemplate two general approaches in **Figure III-6**. In the first scenario, as shown in **Figure III-6a**, we illustrate a reactive approach where electrolyte convection is triggered by a cell safety temperature (in this example 325 K), and a sufficient flow rate (that satisfies $\xi_H \lesssim 1$) suppresses the temperature rise almost instantaneously. In practice, this scenario may correspond to urgent rescue situations, such as, thermal runaway protection. Interestingly, the higher flow rates (0.7-10 μm/s) have convex temperature profiles, where the temperature drops immediately upon the introduction of flow, but, given sufficient time, gradually increases again. This is because as the cell temperature reduces, the heat removal rate decreases to the point where it is less than the heat generation rate and the cell temperature begins to increase again. In a second scenario, we show a proactive approach where the flow rate is changed based on operating conditions. As shown in **Figure III-6b**, electrolyte convection is simultaneously introduced when there is a change in C-rate. This corresponds to a situation where a rapid change in battery power is required during operation, such as, a sudden acceleration in a BEV. The ξ_H values calculated for this scenario are based on 5.7 C and a cutoff temperature of 325 K, so a flow rate that suffices $\xi_H \lesssim 1$ suggests that the cell will not reach the cutoff temperature of 325 K. If minimum temperature rise is desired, a smaller cutoff temperature (e.g., 300 K) could be used to calculate the corresponding flow rate that yields $\xi_H = 1$.

Importantly, variable "on-demand" convection instead of continuous flow allows the system to forgo convection when not needed, such as, for low current charge or discharge, for intentional self-heating, or for pumping energy savings. Reactive mode (**Figure III-6a**) can tune the use of flow to critical situations only, but precise effectiveness of this mode may rely on accurate temperature measurements of the cells within a battery pack. The proactive use of flow coordinated with a significant increase in heat generation, for example, in **Figure III-6b**, can prevent temperature escalation in advance or when difficult to reliably measure. However, proactive scenario can call for flow prematurely or when unnecessary, such as, if high heat generation operation is aborted.

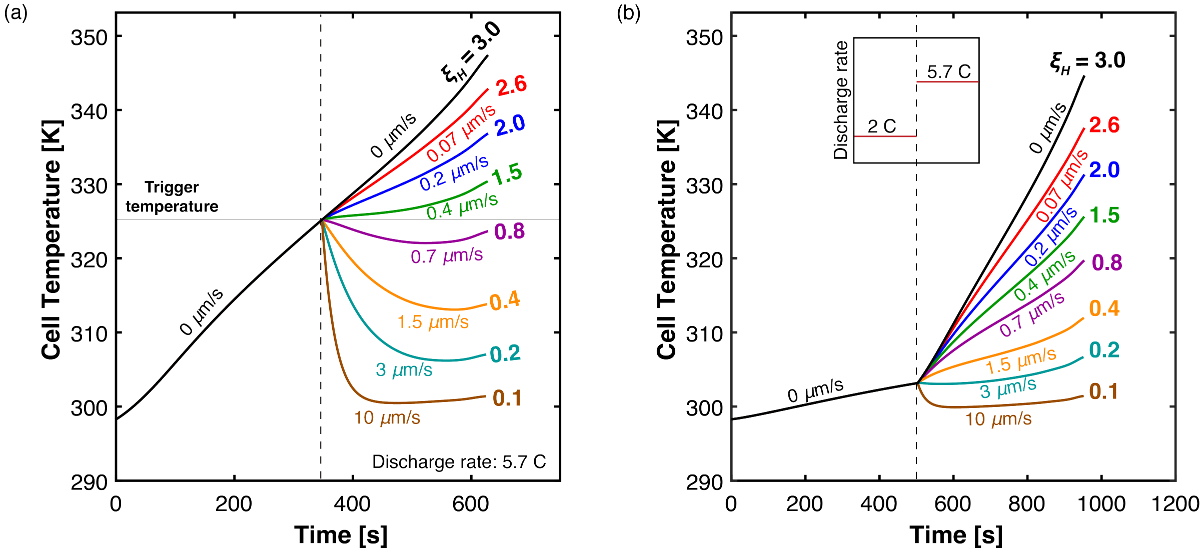

Figure III-6: *Demonstration of dynamic flow rate for thermal regulation. In reactive mode (a), convection is triggered by a safety temperature (e.g., thermal runaway protection); in proactive mode (b), convection is triggered by a change in current density (e.g., sudden acceleration in a BEV).*

4. Conclusions

Effective thermal management remains key to enabling emerging applications of LIBs, particularly those that require high power input and output (such as, BEV fast charging, electric aviation), or need large battery formats (e.g., stationary storage systems). In this work, we investigated a unique internal cooling strategy, where the electrolyte is directly circulated through the porous electrodes and separator of a LIB cell. We expanded upon our prior isothermal model, LIONSIMBA+c, to incorporate convective heat transfer mode. Through the modeling and analysis of a single LIB cell (~200 μm), we illustrated the impact of electrolyte flow on thermal management, which lays a foundation for the consideration of larger, practical systems. To summarize our findings, we showed that the electrolyte flow can effectively suppress temperature rise in a single LIB cell operating at high rates, and elucidated its dual effects on thermal management: (1) Electrolyte flow ***reduces heat generation rate*** through the elimination of the electrolyte concentration gradient, and through the resulting decreases in activation, ohmic, and concentration overpotentials. (2) The bulk electrolyte flow ***enhances heat removal rate*** by directly carrying the generated heat out of the cell. To aid interpretation and understanding between the balance of heat generation, heat storage, and heat removal, we derived three dimensionless groups, β_H, γ_H, and ξ_H, that characterize the simulation results, which parallel our prior list of dimensionless groups for mass transport processes.[144] In summary, electrolyte convection is most beneficial to introduce to cells with insufficient heat capacity and heat removal relative to heat generation, which is represented by large β_H and γ_H values. The dimensionless group, ξ_H, compares the heat generation rate to the total heat removal rate including electrolyte convection, and can help determine the flow needed to prevent the cell from reaching the safety cutoff temperature. The temperature rise of a cell can be curbed through the balance of heat generation by heat removal, as represented by $\xi_H \lesssim 1$. It should be emphasized that the dimensionless groups developed in this study are not restricted to single cells. The group, ξ_H, for instance, scales with thickness and can provide estimates for larger energy storage devices composed of multiple cell layers as well.

Electrolyte convection has favorable effects on cell transport behavior that differ from existing approaches. Cooling strategies to date focus nearly exclusively on improving heat removal, which can lead to increased heat generation rates due to reduced mass transport at lower temperatures. In some cases, this sacrifice of transport properties shifts the cell from thermal-transport-limited to mass-transport-limited regimes. In contrast, the cooling strategy proposed here offers synergistic enhancement of heat and mass transport, which results in more effective thermal management, as it not only improves heat removal capability, but also reduces heat generation in the first place. This method also offers opportunities for dynamic temperature regulation through readily adjustable electrolyte flow rate and temperature. One application of particular interest is the cell operation at a slightly elevated but stable temperature for improved kinetic and transport properties without compromising safety.

While this work focuses on the scale of a single cell (~200 μm thickness, 1 cm^2 area), we expect the reduction in heat generation and improved heat removal with electrolyte convection would play a signification role in larger embodiments (such as, thick electrodes, greater area cells, and multi-cell configurations). The dimensionless groups on thermal and mass transport derived in this and prior work[144] can be used to guide the design of convection battery prototypes. Nevertheless, transforming this concept in a scaled prototype requires considerations beyond those discussed here. As ξ_H suggests, the flowrate needed to suppress the temperature rise roughly scales with the system dimension in the direction of flow. For the single cell studied here, pumping loss is negligible, but thus may change for a larger system that relies solely on electrolyte flow for heat removal. Furthermore, when the flow path is longer, the temperature gradient can become significant at intermediate flow rates. The design of the electrolyte storage tank is also crucial, as a bigger tank may increase heat removal efficacy but at the expense of system energy density.

Such factors and tradeoffs should be carefully evaluated in future work on system design and optimization. In addition, the cost and availability of technology innovation and additional hardware to enable fluidic distribution across high aspect ratio flow through porous electrodes, as well as the potential benefits in terms of improved performance and cost savings, should be carefully considered. It is worth noting that, compared to external liquid-based BTMS, this concept presents an opportunity to explore a simplified balance of plant that could include the elimination of external cooling pipes and plates, which warrants further investigation. Future research should incorporate both technical and economic analyses to ensure the practicality and scalability of this concept in real-world applications.

ACKNOWLEDGEMENTS FOR THIS WORK

The authors gratefully acknowledge funding from ExxonMobil through the MIT Energy Initiative. W.G. gratefully acknowledges the MathWorks Engineering Fellowship through the MIT Department of Chemical Engineering. J.D. gratefully acknowledges the MIT MLK Visiting Professor and Scholars Program. The authors also thank Trent Weiss of the Brushett Group for insightful discussions. Interested researchers can contact the authors for additional information about the model used in this study and to address inquiries related to the underlying code.

5. *List of Symbols*

Symbol	**Description**
a	Particle surface area to volume
$A_{\text{c.c.}}$	Current collector cross-sectional area
A_{cell}	Cell cross-sectional area
A_{tank}	Tank total heat transfer surface area
A_{tube}	Tube cross-sectional area
$brugg$	Bruggeman's coefficient
C_p	Heat capacity
$\bar{C}_p$	Average cell heat capacity
$C_{p,e}$	Electrolyte heat capacity
$c_e(x,t)$	Anion concentration in the electrolyte

c_{initial}	Initial electrolyte concentration
$c_{\mathrm{tank}}(t)$	Tank concentration
$c_s^*(x,t)$	Solid-phase surface concentration
$c_s{}^{\mathrm{max}}$	Maximum solid-phase concentration
D	Electrolyte diffusivity
D_{eff}	Effective electrolyte diffusivity
$D_{\mathrm{eff},i}^{s}$	Effective solid-phase diffusivity
D_i^s	Solid-phase diffusivity
$E_a^{D_i^s}$	Solid-phase diffusion temperature dependent activation energy
$E_a^{k_i}$	Reaction rate constant temperature dependent activation energy
F	Faraday constant
h_{cell}	Cell convective heat transfer coefficient
h_{tank}	Tank convective heat transfer coefficient
I_{app}	Applied current density
$j(x,t)$	Ionic flux
$\mathbf{k}_{eff,i}$	Effective reaction rate constant
k_i	Reaction rate constant
L	Thickness
L_{cell}	Total cell thickness
n	Number of control volumes used
Q_A	Areal capacity
Q_{ohm}	Volumetric ohmic heat source term
Q_{rev}	Volumetric reversible reaction heat source term
Q_{rxn}	Volumetric irreversible reaction heat source term
$\bar{Q}_{total}$	Average volumetric heat generation rate
q	Tank input/output heat flux
R	Gas constant
R_p	Particle radius
$T_{ambient}$	Ambient temperature
T_{max}	Safety cutoff temperature
T_{ref}	Reference temperature
T_{tank}	Tank temperature
$T_{\mathrm{tank,init}}$	Tank initial temperature
$T(x,t)$	Cell temperature
t_{dis}	Time to completely charge or discharge battery at I_{app}
t_+	Li^+ transference number
U	Open circuit potential
V_{tank}	Tank volume
v	Superficial velocity in the cell
v_{tube}	Superficial velocity in the tube
ε	Porosity
$\varepsilon_{\mathrm{filler}}$	Filler fraction
η	Surface overpotential
$\Theta_{100\%}$	Stoichiometry at 100% SoC
$\Theta_{0\%}$	Stoichiometry at 0% SoC
κ_{eff}	Effective electrolyte conductivity

λ	Thermal conductivity
ρ	Density
$\bar{\rho}$	Average cell density
ρ_e	Electrolyte density
σ	Solid-phase conductivity
σ_{eff}	Effective solid-phase conductivity
Φ_e	Electrolyte potential
Φ_s	Solid potential

6. *Appendix A: Equations used in the simulation*

6.1. Heat source terms

$$Q_{\text{ohm}} = \begin{cases} \sigma_{\text{eff},i}\left(\dfrac{\partial \Phi_s(x,t)}{\partial x}\right)^2 + \kappa_{\text{eff},i}\left(\dfrac{\partial \Phi_e(x,t)}{\partial x}\right)^2 - \dfrac{2\kappa_{\text{eff},i}RT(x,t)}{F}(1-t_+)\dfrac{\partial \ln c_e(x,t)}{\partial x}\dfrac{\partial \Phi_e(x,t)}{\partial x} & \text{if} \quad i \in \{p,n\} \\ \kappa_{\text{eff},i}\left(\dfrac{\partial \Phi_e(x,t)}{\partial x}\right)^2 - \dfrac{2\kappa_{\text{eff},i}RT(x,t)}{F}(1-t_+)\dfrac{\partial \ln c_e(x,t)}{\partial x}\dfrac{\partial \Phi_e(x,t)}{\partial x} & \text{if} \quad i \in \{s\} \end{cases}$$

where $\sigma_{\text{eff},i} = \sigma_i\left(1-\varepsilon_i-\varepsilon_{\text{filler,i}}\right)$

$Q_{\text{rxn}} = Fa_i j(x,t)\eta_i(x,t)$ where $\eta_i(x,t) = \Phi_s(x,t) - \Phi_e(x,t) - U_i$, $\quad i \in \{p,n\}$

$$Q_{\text{rev}} = Fa_i j(x,t)T(x,t)\left.\frac{\partial U_i}{\partial T}\right|_{T_{ref}}, \; i \in \{p,n\}$$

6.2. Temperature-dependent values and properties

Open circuit potential

$$U_p = U_{p,ref} + (T(x,t)-T_{ref})\left.\frac{\partial U_p}{\partial T}\right|_{T_{ref}}$$

$$U_n = U_{n,ref} + (T(x,t)-T_{ref})\left.\frac{\partial U_n}{\partial T}\right|_{T_{ref}}$$

$$\left.\frac{\partial U_p}{\partial T}\right|_{T_{ref}} = -0.001\left(\frac{0.199521039-0.9283738822\theta_p+1.3645506890000003\theta_p^{\,2}-0.6115448939999998\theta_p^{\,3}}{1-5.6614798869999997\theta_p+11.476361191\theta_p^{\,2}-9.824312135999998\theta_p^{\,3}+3.048755063\theta_p^{\,4}}\right)$$

$$\left.\frac{\partial U_n}{\partial T}\right|_{T_{ref}} = 0.001\left(\frac{\begin{gathered}0.005269056+3.2992657709\theta_n-91.793257798\theta_n^{\,2}+1004.911008\theta_n^{\,3}-5812.278127\theta_n^{\,4}+\\ 19329.7549\theta_n^{\,5}-37147.8947\theta_n^{\,6}+38379.18127\theta_n^{\,7}-16515.053308\theta_n^{\,8}\end{gathered}}{\begin{gathered}1-48.09287227\theta_n+1017.234804\theta_n^{\,2}-10481.80419\theta_n^{\,3}+59431.3\theta_n^{\,4}-\\ 195881.6488\theta_n^{\,5}+374577.3152\theta_n^{\,6}-385821.1607\theta_n^{\,7}+165705.8597\theta_n^{\,8}\end{gathered}}\right)$$

$$U_{p,ref} = \frac{-4.656+88.669\theta_p^{\,2}-401.119\theta_p^{\,4}+342.909\theta_p^{\,6}-462.471\theta_p^{\,8}+433.434\theta_p^{\,10}}{-1+18.933\theta_p^{\,2}-79.532\theta_p^{\,4}+37.311\theta_p^{\,6}-73.083\theta_p^{\,8}+95.96\theta_p^{\,10}}$$

Where $\theta_p = \dfrac{c_{s,p}^{*}(x,t)}{c_{s,p}^{\max}}$

$$U_{n,ref} = 0.7222+0.1387\theta_n+0.029\theta_n^{\,0.5}-\frac{0.0172}{\theta_n}+\frac{0.0019}{\theta_n^{\,1.5}}+0.2808e^{0.9-15\theta_n}-0.7984e^{0.4465\theta_n-0.4108}$$

Where $\theta_n = \dfrac{c_{s,n}^{*}(x,t)}{c_{s,n}^{\max}}$

Effective electrolyte diffusion coefficient

$$D_{\mathrm{eff},i} = \varepsilon_i^{brugg,i}\times 10^{-4}\times 10^{-4.43-\frac{54}{T(x,t)-229-5\times 10^{-3}c_e(x,t)}-0.22\times 10^{-3}c_e(x,t)}$$

Effective electrolyte conductivity

$$\kappa_{\mathrm{eff},i} = \varepsilon_i^{brugg,i}\times 10^{-4}\times c_e(x,t)\times\left(\begin{gathered}-10.5+0.668\times 10^{-3}\cdot c_e(x,t)+0.494\times 10^{-6}\cdot c_e^{\,2}(x,t)+\\ (0.074-1.78\times 10^{-5}\cdot c_e(x,t)-8.86\times 10^{-10}\cdot c_e^{\,2}(x,t))\cdot T(x,t)+\\ (-6.96\times 10^{-5}+2.8\times 10^{-8}\cdot c_e(x,t))\cdot T^2(x,t)\end{gathered}\right)^2$$

Effective reaction rate

$$\mathbf{k}_{\text{eff,i}} = k_i e^{-\frac{E_a^{k_i}}{R}\left(\frac{1}{T(x,t)} - \frac{1}{T_{ref}}\right)}$$

Effective solid-phase diffusion coefficient

$$D^s_{\text{eff},i} = D^s_i e^{-\frac{E_a^{D_i^s}}{R}\left(\frac{1}{T(x,t)} - \frac{1}{T_{ref}}\right)}$$

7. Appendix B: Supplementary Figures

Figure III-7 compares discharge and temperature rise curves at varying C-rates for the original LIONSIMBA[111] and LIONSIMBA+c with $v = 0$ μm/s. The identical outputs suggest no artifacts were introduced to the original model during the modifications.

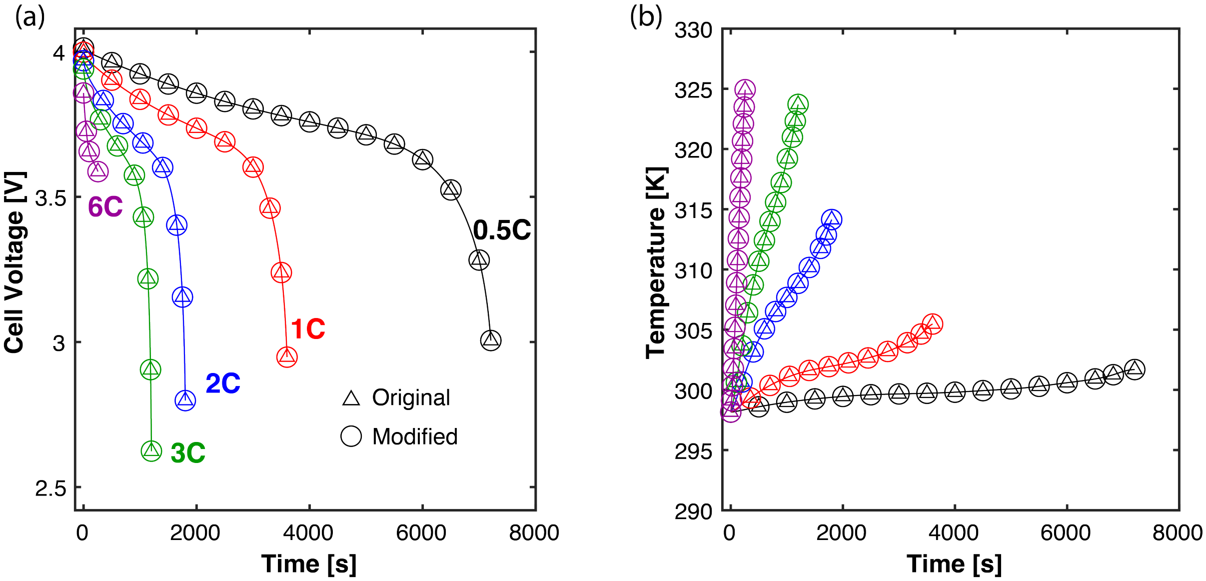

Figure III-7: *Comparison between non-isothermal LIONSIMBA and LIONSIMBA+c model outputs: (a) discharge curves (b) temperature rise curves at varying discharge rates with the same inputs and no flow.*

Figure III-8 shows the temperature vs. cell position for the *base case* at 347 s, which corresponds to the end of discharge for the stationary cell in **Figure III-2a**. Due to the thinness of the cell used for this study, the temperature distribution is uniform across the cell as expected with $Bi = \frac{hL}{\lambda} << 1$. This uniformity allows representation of the cell temperature with a single value rather than as a function of position.

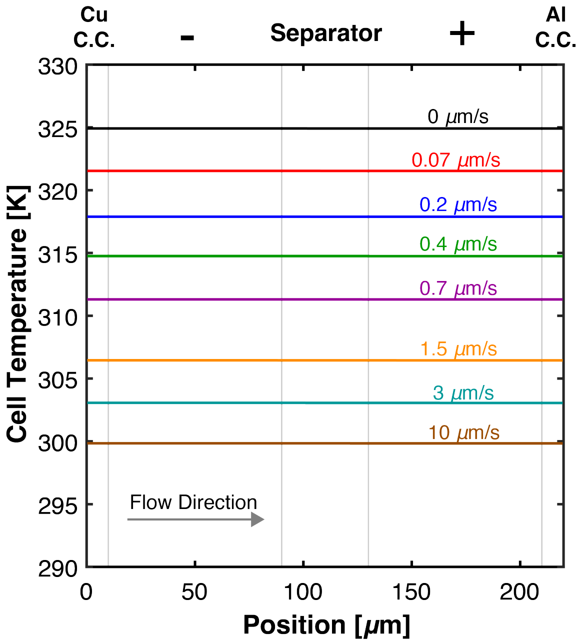

Figure III-8: *Flow rate-dependent temperature vs. position curves for the base case at 347 s, the end of discharge for the stagnant cell in Figure III-2(a).*

Figure III-9 shows the heat generation by sources, as well as the total heat generation for the *base case* at 347 s (end of discharge for the stationary cell in **Figure III-2a**). With the increasing electrolyte flow rate, the heat generation reduces in magnitude and becomes more uniform across the cell.

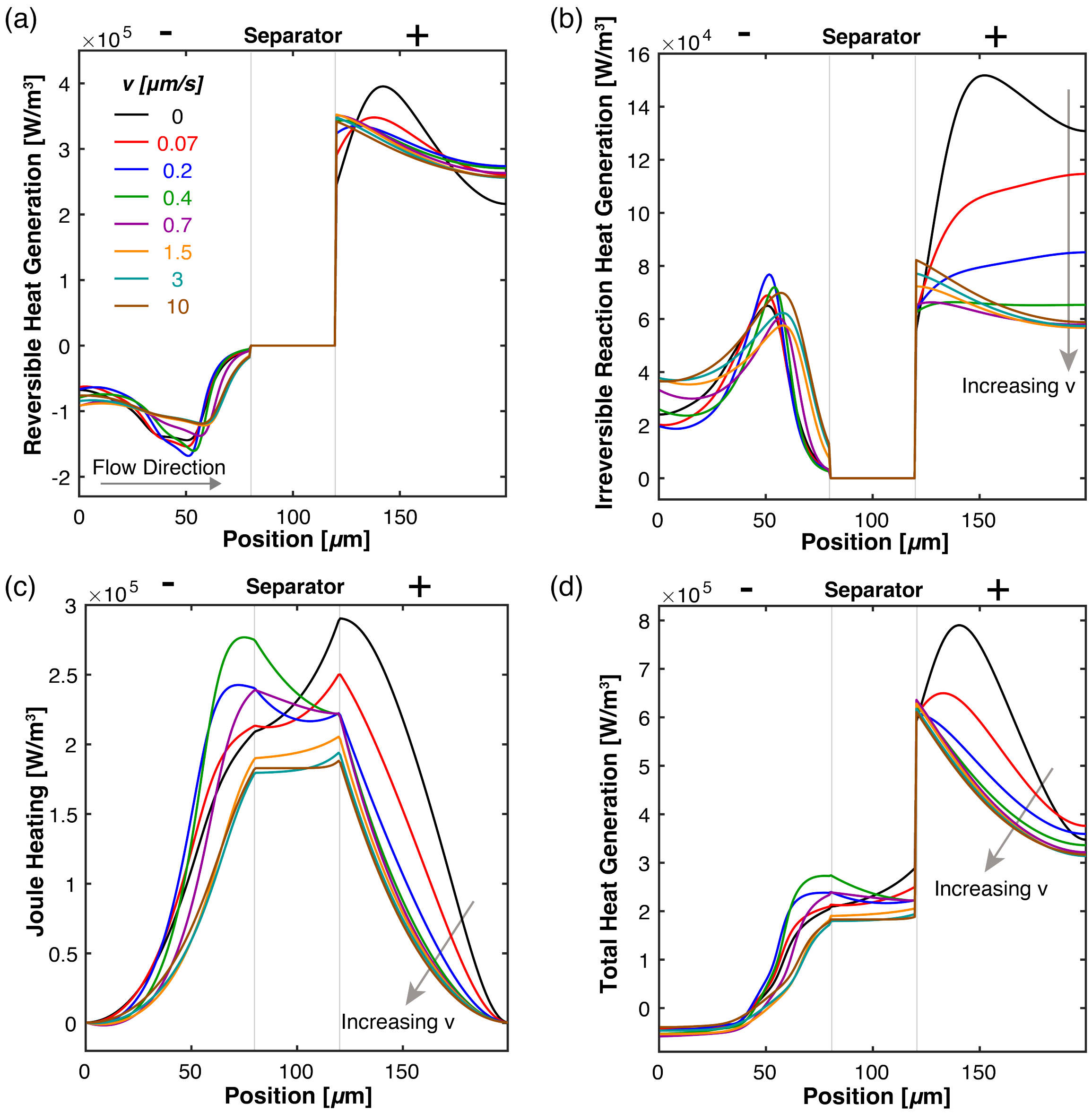

Figure III-9: *Heat generation by different sources as a function of the cell position at 347 s, the end of discharge for the stagnant cell, and the electrolyte flow rate for the conditions used in the base case: (a) Reversible heat generation, (b) irreversible reaction heat generation, (c) Joule heating, and (d) total heat generation. The Joule heating in the current collectors is negligible and not shown.*

Figure III-10 shows the cell temperature as a function of time at different electrolyte flow rates for the *Diffusive Transport Limited Case.* The negligible temperature rise confirms that the use of a large heat transfer coefficient (h_{cell} = 500 W/(m^{2}K)) effectively eliminates thermal transport limitations as intended. Thus, this case focuses on the impact of electrolyte convection on mass transport, and the subsequent influence on heat generation rate shown in **Figure III-9**.

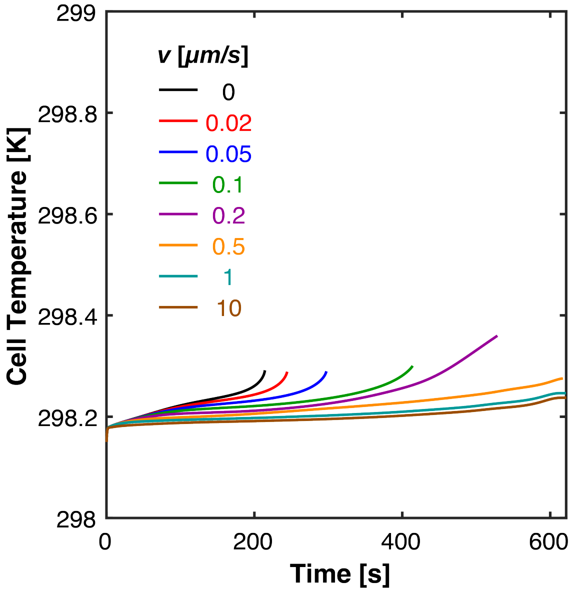

Figure III-10: *Cell temperature as a function of time for the Diffusive Transport Limited Case for different electrolyte flow rates.*

Figure III-11 shows the electrolyte concentration as a function of position in the cell at different electrolyte flow rates for the *Thermal Transport Limited Case*. The uniform concentration confirms that the use of a large diffusion coefficient ($D = normal\ value \times 10^3$) effectively eliminates mass transfer limitations as intended. Thus, this case focuses on the impact of electrolyte convection on thermal transport.

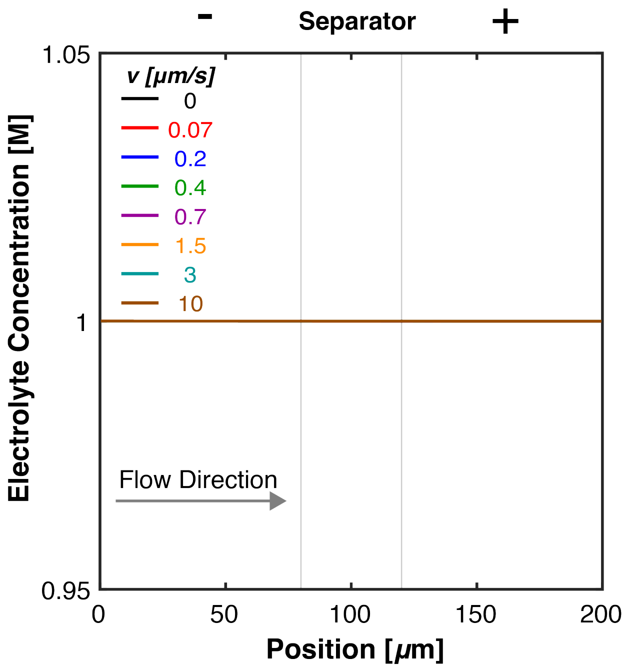

Figure III-11: *Electrolyte concentration as a function of cell position for the Thermal Transport Limited Case. Across all flow rates considered, the electrolyte concentration remains constant across the cell, thus the curves directly overlay and are not visible.*

Figure III-12 shows the heat generation by sources, as well as the total heat generation at 225 s (before complete electrolyte salt depletion for the h_{cell} = 12.9 W/(m^{2}K) case) for the cases shown in *Comparison Between Internal and External Cooling*. For external cooling, the heat generation rate increases with increasing h_{cell} due to slower mass transport at lower temperatures. For internal cooling, the heat generation rate decreases with increasing v as mass transport improves as discussed in *Diffusive Transport Limited Case*.

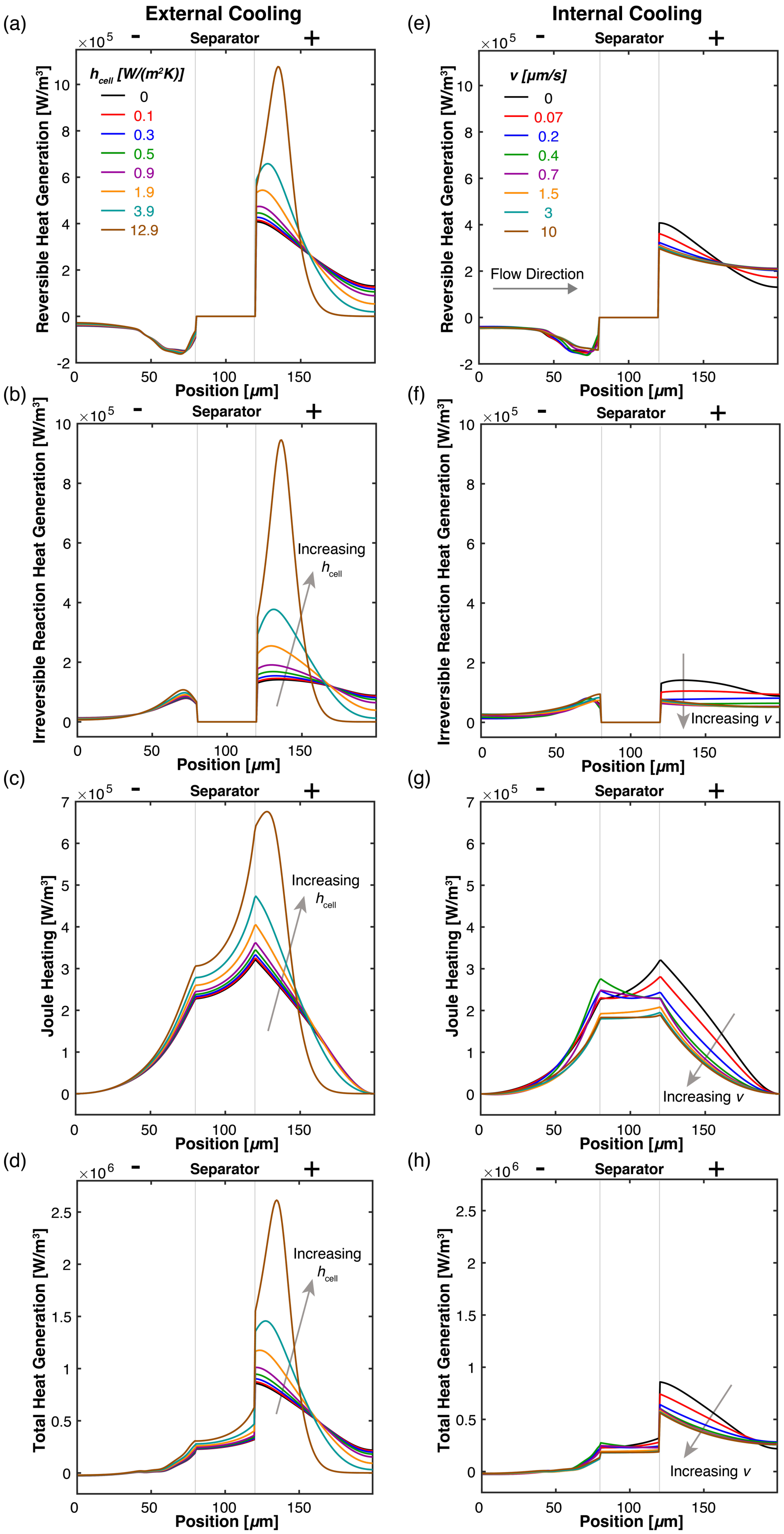
External Cooling
Internal Cooling
(a)
(b)
(c)
(d)
(e)
(f)
(g)
(h)
-
Separator
+
×10^5
×10^6
h_{cell} [W/(m²K)]
0
0.1
0.3
0.5
0.9
1.9
3.9
12.9
v [μm/s]
0
0.07
0.2
0.4
0.7
1.5
3
10
Flow Direction
Increasing h_{cell}
Increasing v
Reversible Heat Generation [W/m³]
Irreversible Reaction Heat Generation [W/m³]
Joule Heating [W/m³]
Total Heat Generation [W/m³]
Position [μm]
0
50
100
150

Figure III-12: *Heat generation by sources as a function of the cell position at 225 s (before complete electrolyte salt depletion occurs for the* $h_{cell} = 12.9$ *W/(m*^{2}*K) case), and the cell heat transfer coefficient or electrolyte flow rate for the conditions used in the Comparison Between Internal and External Cooling cases. Plots (a)-(d) show the reversible heat generation, irreversible reaction heat generation, Joule heating, and total heat generation for the external cooling conditions respectively; (e)-(h) show the same set of plots for the internal cooling conditions. The Joule heating in the current collectors is negligible and not shown.*

8. *Appendix C: Supplementary Notes*

8.1. Pumping energy loss and energy gain across a single cell

The pressure drop through the cell is estimated using Kozeny-Carman equation[153]:

$$\frac{|\Delta p|}{L_{\text{cell}}} = v \frac{180\mu}{\Phi_s^2 D_p^2} \frac{(1-\varepsilon)^2}{\varepsilon^3} \tag{III-9}$$

where Δp [Pa] is the pressure drop, L_{cell} [m] is the cell total length, v [m/s] is the superficial velocity, μ [cP] is the electrolyte viscosity, ε [-] is the porosity, and Φ_s [-] is the sphericity of the particles with diameter D_p [m]. The energy required to maintain a pumping flow rate Q [m^3/s] through a cell with cross-sectional area A [m^2] during discharge time t_{d} [s] is estimated with Eq. (III-10):

$$E_{\text{pump}} = Q|\Delta p| t_{\text{d}} = A v^2 \frac{180\mu}{\Phi_s^2 D_p^2} \frac{(1-\varepsilon)^2}{\varepsilon^3} L_{\text{cell}} t_{\text{d}} \tag{III-10}$$

The cell used in **Figure III-2** in the main text has $L_{\text{cell}} = 2 \times 10^{-4}$ m, $\varepsilon = 0.4$, and the active materials are assumed to be spheres with $\Phi_s = 1$ and $D_p = 4 \times 10^{-6}$ m. Assuming the electrolyte has a viscosity of 10 cP, a flow rate of 10 μm/s results in a pressure drop of approximately 1000 Pa across the two electrodes and the separator in a single cell. This suggests that the pressure the hardware needs to withstand is relatively low. **Figure III-13** shows energy gain and pumping loss per unit area of a single cell as functions of the superficial velocity compared to the cell without flow that has an areal energy density of 52 Wh/m^2. A flow rate above 0.5 μm/s nearly doubles the cell energy output and incurs 4 orders of magnitude smaller pumping energy loss. Note that the electrolyte viscosity will decrease with higher temperature,[83] which is not considered here, making the analysis a conservative estimate. Also note that this calculation is performed for flow within a single cell. A thorough analysis of fluid dynamics throughout the cell stack, manifolding, pumping equipment, and tank would be necessary to understand this trade-off at the system-level.

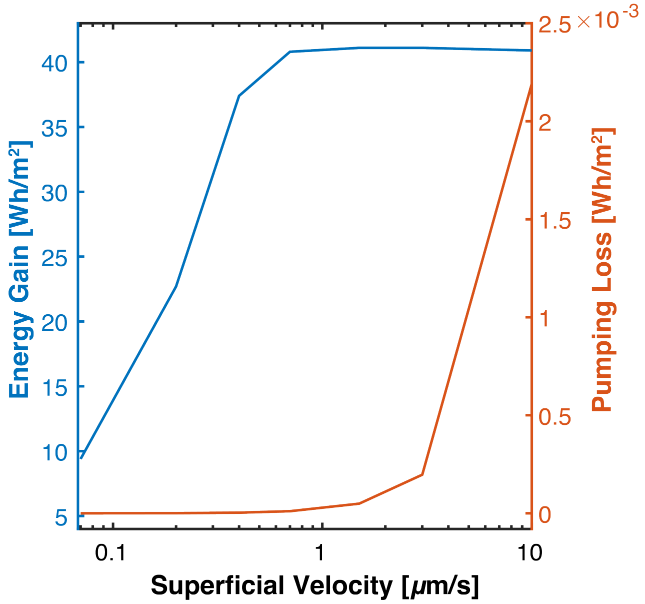

Figure III-13: *Flow rate dependent trade-off between energy gain and pumping loss for a convection cell under the conditions used for* ***Figure III-2*** *in the main text.*

8.2. Temperature change inside the tank

Figure III-14 shows the temperature change inside the external electrolyte storage tank as a function of time at different flow rates used for the *base case*. While the tank is operating adiabatically (*i.e.,* there is no heat exchange of the tank with the ambient environment), the temperature remains virtually unchanged at all flow rates. This consistency is because the tank used in this study has a large volume compared to the single cell size. In this case, the heat exchange mode of the tank with the environment has no impact on the cell operation. In practice, a smaller tank-to-cell volume ratio will likely be used to achieve greater system-level energy and power density, and some cooling capacity of the tank will likely be required for effective thermal management. The optimal design of the tank-to-cell volume ratio and the tank heat exchange mode is beyond the scope of this initial study.

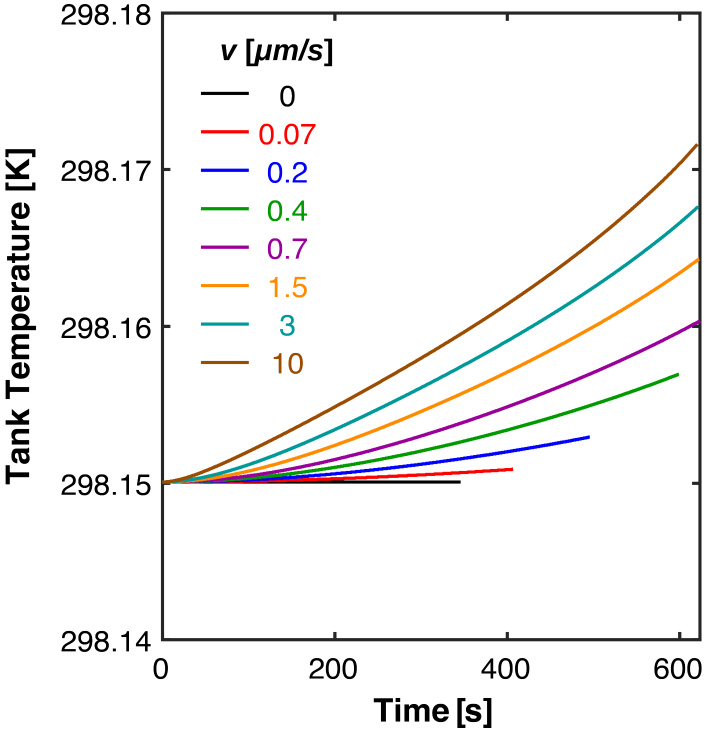

Figure III-14: Tank temperature change as a function of time at different flow rates for the base case.

8.3. Impacts of flow direction

Figure III-15 shows the cell voltage curves, the corresponding electrolyte concentration profiles, and the cell temperature profiles under the same conditions as the *base case* but with flow direction reversed. The trends are similar to what was discussed for the *base case*, except the impacts of flow on cell performance and temperature regulation appear to be less significant, or even adverse at low flow rates. This effect can be more clearly observed in **Figure III-16**, which shows the heat generation by sources and the total heat generation at 325 s (the end of the shortest discharge,

$v = 0.2$ μm/s). At low flow velocities ($v < 1.5$ μm/s), the total heat generation rate at most locations inside the cell is actually higher than the case without electrolyte flow due to lower electrolyte concentration. This is in contrast with the *base case*, where the heat generation rate at most locations inside the cell monotonically decreases with increasing flow rate as shown in **Figure III-9**. These results suggest that flow should be introduced in the direction from the Li$^+$-generating electrode to the Li$^+$-consuming electrode for maximal effectiveness at low flow rates.

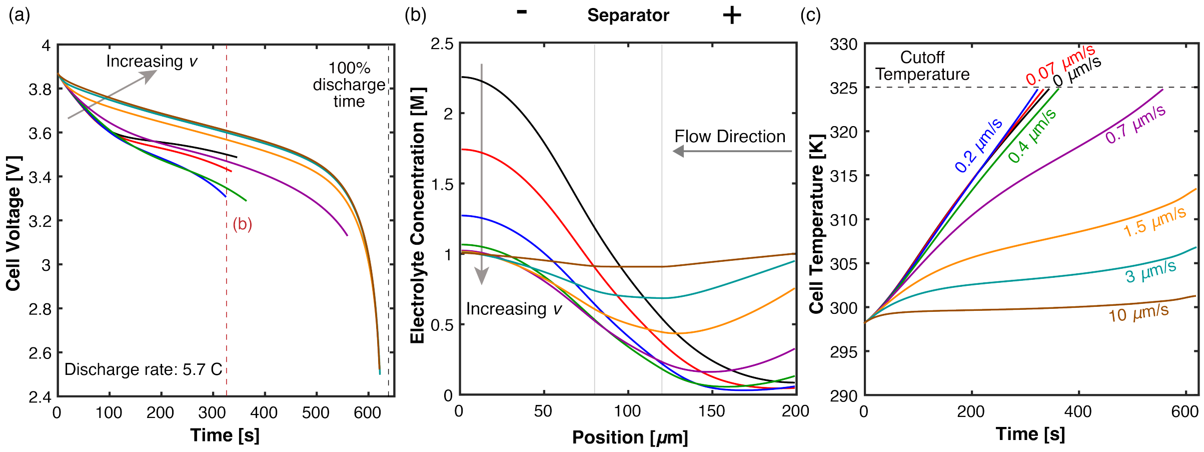

Figure III-15: *The effect of reverse electrolyte flow direction on (a) the discharge polarization curve (b) the concentration profile of electrolyte at t = 325 s (the end of the shortest discharge, v = 0.2 μm/s) and (c) the cell temperature rise compared to the zero-velocity base case in the main text.*

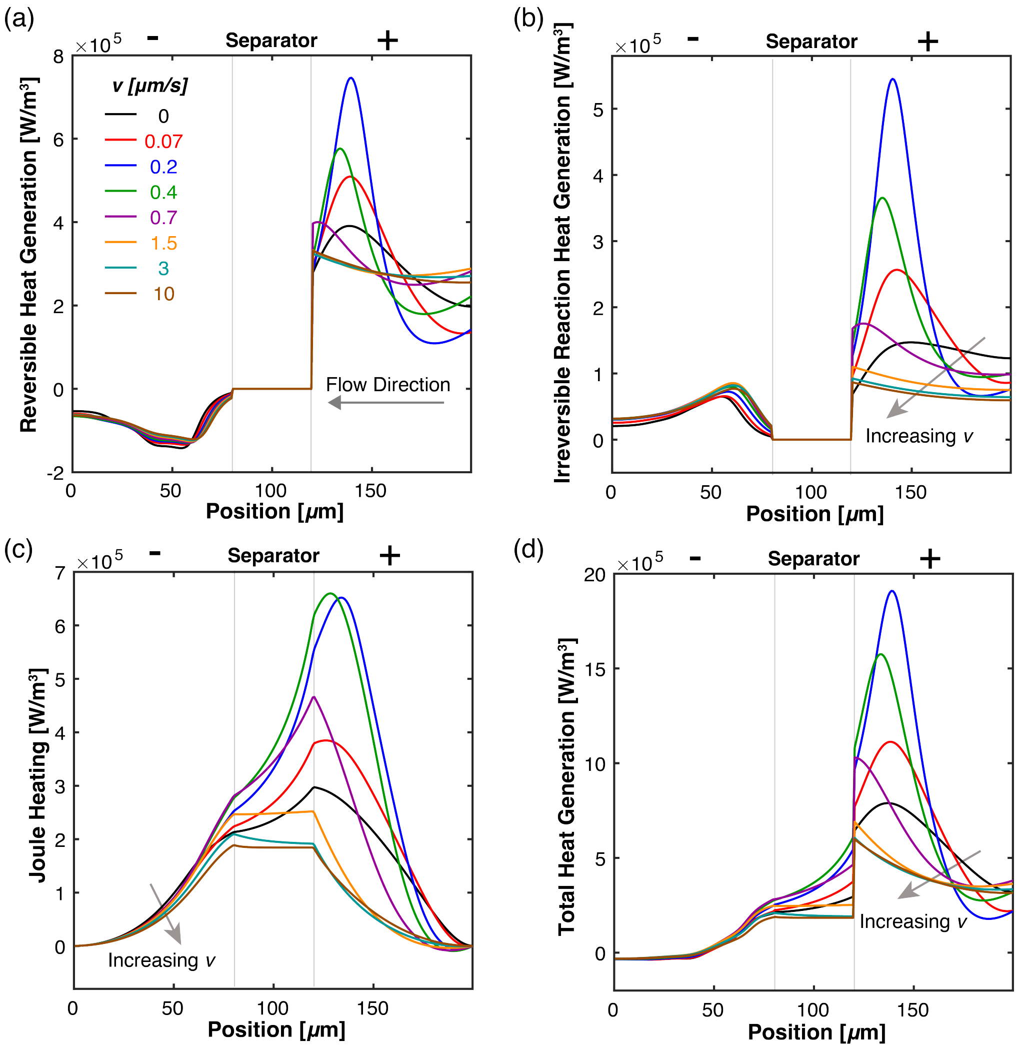

Figure III-16: *Heat generation by sources as a function of the cell position at 325 s (the end of the shortest discharge, v = 0.2 μm/s) and electrolyte flow rate for the reverse flow case: (a) reversible heat generation, (b) irreversible reaction heat generation, (c) Joule heating, and (d) total heat generation. The Joule heating in the current collectors is negligible and not shown.*

8.4. Derivation of $\bar{Q}_{total}$ for the dimensionless group calculation

The average volumetric heat generation rate, $\bar{Q}_{total}$ [W/m^3], used for calculating the dimensionless group values in **Table III-2** of the main text is estimated using the following equation:

$$\bar{Q}_{total}L_{\text{cell}}=I_{\text{app}}\left(\eta_{ohmic}+\eta_{conc}+\eta_{act}+T\frac{\partial U}{\partial T}\right) \qquad \text{(III-11)}$$

In Eq. (III-11), L_{cell} [m] is the total thickness of the two electrodes and the separator, and I_{app} [A/m^2] is the applied current density. The equation considers heat generation from four sources: the ohmic overpotential η_{ohmic} [V], the concentration overpotential η_{conc} [V], the activation overpotential η_{act} [V], and the reversible reaction heat due to entropy change as characterized by the last term within the parentheses on the right-hand side of the equation.

A representative electrolyte concentration change (Δc_e [mol/m^3]) at the end of discharge is estimated by the relative contributions of electromigration, diffusion, and convection fluxes:

$$\Delta c_e = \left(\frac{(1 - t_+) I_{\text{app}}}{F \varepsilon L} - \frac{D_{\text{eff}} c_{\text{initial}}}{\varepsilon L^2} - \frac{v c_{\text{initial}}}{\varepsilon L} \right) t_d \tag{III-12}$$

Here L [m] is the electrode thickness, and t_d [s] is either the time to complete discharge or the time for Δc_e to equal the initial concentration c_{initial}, whichever occurs first (i.e., Δc_e cannot exceed c_{initial}). Additionally, Δc_e is set to 0 if it is calculated to be a negative value, as a reverse concentration gradient where the concentration in the positive electrode is greater than that in the negative electrode during discharge is physically impossible. The electrolyte concentration in the separator at the end of discharge is estimated to be the initial concentration, c_{initial}. The representative electrolyte concentrations at the end of discharge in the negative electrode ($c_{e,n}$) and positive electrode ($c_{e,p}$) are evaluated as:

$$c_{e,n} = c_{\text{initial}} + \Delta c_e \tag{III-13}$$

$$c_{e,p} = c_{\text{initial}} - \Delta c_e \tag{III-14}$$

The ohmic overpotential, η_{ohmic}, in Eq. (III-11) is estimated individually for the two electrodes and the separator by:

$$\eta_{ohmic} = I_{\text{app}} L \left(\frac{1}{\kappa_{\text{eff}}} + \frac{1}{\sigma_{\text{eff}}} \right) \tag{III-15}$$

In Eq. (III-15), L [m] is the thickness of each section; κ_{eff} [S/m] is the effective electrolyte conductivity, and is evaluated at room temperature with $\frac{c_{e,n} + c_{\text{initial}}}{2}$, c_{initial}, and $\frac{c_{e,p} + c_{\text{initial}}}{2}$ to represent the average concentration in the negative electrode, the separator, and the positive electrode, respectively; σ_{eff} [S/m] is the effective solid-phase conductivity, and is considered for the electrodes only. The concentration overpotential, η_{conc}, in Eq. (III-11) is calculated with Eq. (III-16) at room temperature ($T = 298$ K).

$$\eta_{conc} = \frac{(1 - t_{+})RT}{F} \ln\left(\frac{c_{e,n}}{c_{e,p}}\right) \tag{III-16}$$

In Eq. (III-16), t_{+} [-] is the Li^{+} transference number, R is the universal gas constant [8.314 J/(mol K)], F is the Faraday constant [96485 C/mol]. The activation overpotential, η_{act}, in Eq. (III-11) can be evaluated for each electrode using:

$$\eta_{act} = \frac{RTI_{\mathrm{app}}}{F^{2}aLk\sqrt{c_{\mathrm{initial}}(c_{s}^{\max} - c_{s,\mathrm{initial}}^{*})\,c_{s,\mathrm{initial}}^{*}}} \tag{III-17}$$

In Eq. (III-17), a [m^2/m^3] is the particle surface area per unit volume, k [$m^{2.5}/(mol^{0.5}s)$] is the reaction rate constant, c_s^{max} [mol/m^3] is the maximum solid-phase concentration, and $c_{s,\mathrm{initial}}^{*}$ [mol/m^3] is the initial solid-phase surface concentration.

For the last term in Eq. (III-11), a representative value of 2.4×10^{-4} V/K is selected to estimate $\frac{\partial U}{\partial T}$ based on the correlations in Section 6, and the whole term is evaluated at room temperature ($T = 298$ K).

Note that this approach provides an estimated $\overline{Q}_{total}$ for the dimensionless group calculation, which can subsequently be used to guide cell design. Because the estimation of $\overline{Q}_{total}$ relies only on information that can be easily obtained prior to cell operation (e.g., cell and electrolyte properties, operating conditions), the dynamic changes that occur during discharge cannot be fully captured. While generally in good agreement with the actual $\overline{Q}_{total}$ values determined from simulations, the estimated $\overline{Q}_{total}$ values may deviate from the actual values, albeit within an order of magnitude, under certain extreme conditions. As an example, this approach tends to underestimate $\overline{Q}_{total}$ for cells with very large electrolyte mass transport resistance (e.g., high C-rate operation, low electrolyte diffusivity), as the large amount of Joule heating resulting from electrolyte salt depletion near the end of discharge is not considered in the calculation.

8.5. Equivalent heat removal capabilities

The total representative heat exchange rate for the cell considered in *Comparison Between Internal and External Cooling* is $2A_{\text{cell}}h_{\text{cell}}\left(T_{max} - T_{ambient}\right)$ for external cooling, and $A_{\text{cell}}\rho_e C_{p,e} v\left(T_{max} - T_{\text{tank}}\right)$ for internal cooling. Assuming the tank remains at ambient temperature due to its large size compared to the cell, comparing these two quantities yields $\frac{External\ Cooling}{Internal\ Cooling} = 2\frac{h_{\text{cell}}}{\rho_e C_{p,e} v}$, where h_{cell} is the external convective heat transfer coefficient, and ρ_e, $C_{p,e}$, and v are the density, heat capacity, and superficial velocity of the electrolyte, respectively. Note $\frac{h}{\rho_e C_{p,e} v}$ is also the expression for the Stanton number (*St*), but it is used differently in this context as *St* considers two different cooling fluids as opposed to a single fluid. The prefactor in the expression is determined by the cooling methods and the cell form factor. A value of 2 appears in this case to account for the two cooling surfaces of the external cooling method – the current collectors at either end of the cell. Equivalent heat removal capability, but generally unequal heat generation, should be expected for external and internal cooling methods when the expression has a value of 1. As ρ_e and $C_{p,e}$ are known electrolyte properties, a relationship between v and h_{cell} that yields equivalent heat removal capability can be determined as shown in **Figure III-17**.

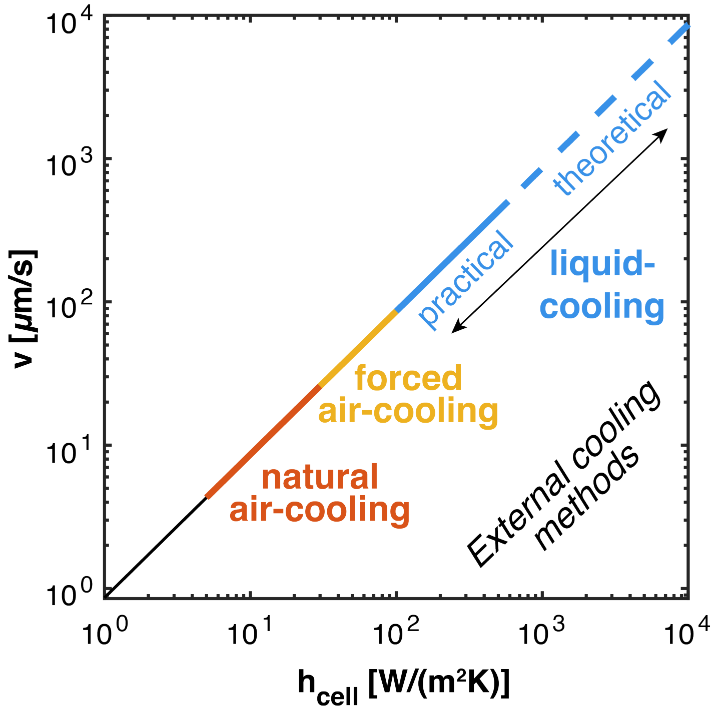

Figure III-17: *A relationship between v and h_{cell} that would yield the same heat removal capability for the cell considered in the section, Comparison Between Internal and External Cooling. The typical ranges of different external cooling methods are labeled for reference.*[154]

To validate this relationship, a set of v and the corresponding h_{cell} values based on **Figure III-17** are used to simulate the performance of a single cell, as shown in **Figure III-18**. As we only compare the heat removal capability of the two cooling methods, an artificially high diffusivity (D = *normal value* × 10^3) is used to eliminate the convolution of mass transport enhancement by convection. As **Figure III-18** shows, the sets of v and h_{cell} values indeed yield the same performance, suggesting they result in the equivalent heat removal capability. Also note that the exact same cell performance shown in **Figure III-18** can only be observed when the cell is thin (*i.e.*, temperature is uniform across the cell); if there were a temperature gradient within the cell, the internal and external cooling methods would have different impacts on the cell performance even if they would yield the same heat removal capability. The detailed discussion on this effect is beyond the scope of the present study.

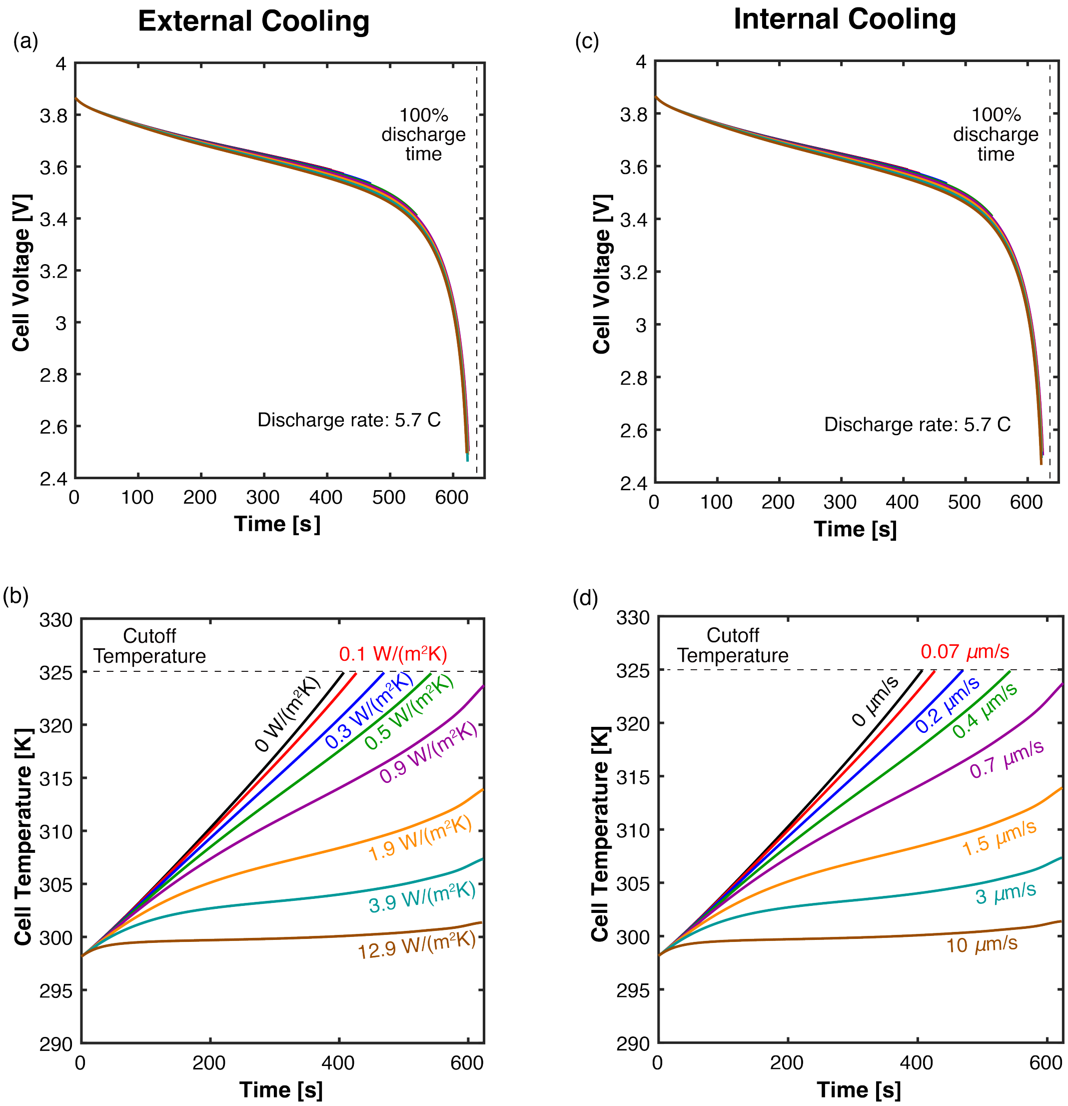

Figure III-18: *Discharge curve and temperature profile with artificial elimination of mass transport limitations and temperature dependence. The matching results validate heat transfer coefficient,* h_{cell}*, and velocity, v, values that cause equivalent external (a, b) and internal (c, d) heat removal rates. Comparison of these plots with* ***Figure III-5*** *in the main text shows the significant adverse effect of coupled mass transport on external cooling approaches that is overcome by internal convective cooling.*

IV. Transient Analyses on Mass and Thermal Transport

1. Introduction

In **Chapters II** and **III**, we analyzed mass and thermal transport to explore the design space and operational parameters of cells where electrolyte convection is advantageous. These studies primarily focused on end-of-discharge states following a complete discharge cycle. Building on this, the present chapter expands the investigation to include transient behaviors—specifically, the evolution of concentration and temperature profiles over time. This exploration is crucial for understanding the potential benefits of convection in applications requiring short-duration, pulsed charge/discharge cycles, such as electric vehicle acceleration. It also helps assess the practicality of intermittent electrolyte flow strategies aimed at reducing pumping demands and improving system responsiveness.

Furthermore, the previous thermal transport analysis was confined to a single cell layer with uniform temperature due to its thin geometry. However, in larger-scale systems, such as multi-layer cells (e.g., prismatic and cylindrical) or battery packs, significant temperature gradients are expected. This chapter, therefore, expands our exploration to these larger configurations, using analytical methods to investigate the development of transient temperature profiles across greater length scales. Finally, it presents a comparative analysis of internal and external thermal management approaches in their effectiveness at regulating temperature at these expanded length scales.

2. Transient Electrolyte Mass Transport Analysis

In **Chapter II**, the impact of electrolyte on mass transport in cells undergoing continuous full discharges is discussed, and regions where electrolyte flow will lead to significant performance enhancement are identified through simulations. This section aims to discuss the impact of electrolyte flow on mass transport by analytically examining the electrolyte mass transport governing equation, and provides some insights into the transient development of electrolyte concentration, which will help answer questions such as at what time does electrolyte salt depletion occur.

The non-dimensionalized form of the electrolyte mass transport governing equation (Eq. (II-1) **in Chapter II**) is given by:

$$\left(\frac{1}{t_{\text{dis}}}\right)\cdot\frac{\partial\tilde{c}_e}{\partial\tilde{t}}=-\frac{\partial}{\partial\tilde{x}}\left[-\left(\frac{D_{\text{eff},p}}{\varepsilon_p L_p{}^2}\right)\cdot\frac{\partial\tilde{c}_e}{\partial\tilde{x}}+\left(\frac{v}{\varepsilon_p L_p}\right)\cdot\tilde{c}_e-\frac{I_{\text{app}}\left(1-t_+\right)}{c_{\text{initial}}\varepsilon_p L_p F}\cdot\tilde{i}_2\right] \tag{IV-1}$$

A list of timescales becomes apparent from this equation, as shown in **Table II-5** in **Chapter II**. Using these timescales, a list of dimensionless groups can be derived as shown in **Table II-6** in **Chapter II**, which are used to analyze the impact of electrolyte flow on cell performance as discussed in **Chapter II**. To analyze the transient evolution of electrolyte concentration profiles, one additional dimensionless group, $Fo=\frac{t_{\text{dis}}}{t_{\text{diff}}}=\frac{t_{\text{dis}}D_{\text{eff},p}}{\varepsilon_p L_p{}^2}$, is added to the list. This dimensionless group compares the discharge timescale to the diffusion timescale. A large *Fo* value suggests a long discharge process compared to the diffusion process, which is an indicator that the electrolyte concentration has reached a pseudo-steady state by the end of discharge.

2.1. Evolution of electrolyte concentration without electrolyte flow

As discussed in **Chapter II**, there are three distinct regions revealed by **Figure II-4**: (1) small $\gamma_M=\frac{t_{\text{diff}}}{t_{\text{depletion}}}=\frac{I_{\text{app}}\left(1-t_+\right)L_p}{FD_{\text{eff},p}c_{\text{initial}}}$, in which region electrolyte salt depletion will not occur as diffusion rate is sufficient compared to electrolyte migration rate; (2) small

$\beta_M = \frac{t_{\mathrm{dis}}}{t_{\mathrm{depletion}}} = \frac{I_{\mathrm{app}}\left(1-t_+\right)t_{\mathrm{dis}}}{Fc_{\mathrm{initial}}\varepsilon_p L_p}$, in which region electrolyte salt depletion will not occur as there is sufficient initial electrolyte to buffer against electrolyte salt depletion; (3) large γ_M *and* β_M, in which region electrolyte salt depletion will occur due to a combination of insufficient diffusion rate and initial electrolyte concentration. The development of electrolyte concentration for conditions in each of the three regions will be examined in the next sections.

2.1.1. Electrolyte concentration development for conditions with small γ_M

The observation that electrolyte salt depletion will not occur when γ_M is small can be justified by examining the steady-state solution of the electrolyte mass transport governing equation. Assuming uniform reaction distribution, **Equation II-1** for the positive electrode (*p*) without the convection term can be written as:

$$\varepsilon_p \frac{\partial c_e(x,t)}{\partial t} = D_{\mathrm{eff},p}\frac{\partial^2 c_e(x,t)}{\partial x^2} + \frac{\left(1-t_+\right)I_{\mathrm{app}}}{FL_p} \tag{IV-2}$$

With the boundary conditions $K\left(c_{\mathrm{bulk}}-c\right) = -D_{\mathrm{eff},p}\frac{\partial c}{\partial x}$ where $K = \frac{2D_{\mathrm{eff},s}}{L_s}$ at the separator/positive electrode interface, and $-D_{\mathrm{eff},p}\frac{\partial c}{\partial x} = 0$ at the positive electrode/current collector interface, the steady-state solution can be written as:

$$c = c_{\mathrm{bulk}} - \frac{\left(1-t_+\right)I_{\mathrm{app}}}{2D_{\mathrm{eff},p}FL_p}\left(x-L_p\right)^2 + \frac{\left(1-t_+\right)I_{\mathrm{app}}}{2D_{\mathrm{eff},p}FL_p}L_p^{\,2} + \frac{\left(1-t_+\right)I_{\mathrm{app}}}{K\cdot F} \tag{IV-3}$$

Figure IV-1 shows the validation of this equation against simulation results. For the conditions used in **Chapter II**, $K = \frac{2D_{\mathrm{eff},s}}{L_s} = \frac{4D_{\mathrm{eff},p}}{L_p}$, and $c_{\mathrm{bulk}} = c_{\mathrm{initial}}$, the steady-state concentration is $\left(1-\frac{\gamma_M}{4}\right)c_{\mathrm{initial}}$ at the separator/positive electrode interface, and $\left(1-\frac{3}{4}\gamma_M\right)c_{\mathrm{initial}}$ at the positive electrode/current collector interface, which represents the minimum electrolyte concentration ($c_{ss,min}$) inside the cell. Hence, to avoid electrolyte salt depletion at the steady state, the equation $c_{ss,min} = \left(1 - \frac{3}{4}\gamma_M\right) c_{\text{initial}} \geq 0$ needs to be satisfied, which requires that $\gamma_M = \frac{t_{\text{diff}}}{t_{\text{depletion}}} \leq \frac{4}{3}$. This validates the observation in **Chapter II** that electrolyte salt depletion will not occur if $\gamma_M < \sim 1$.

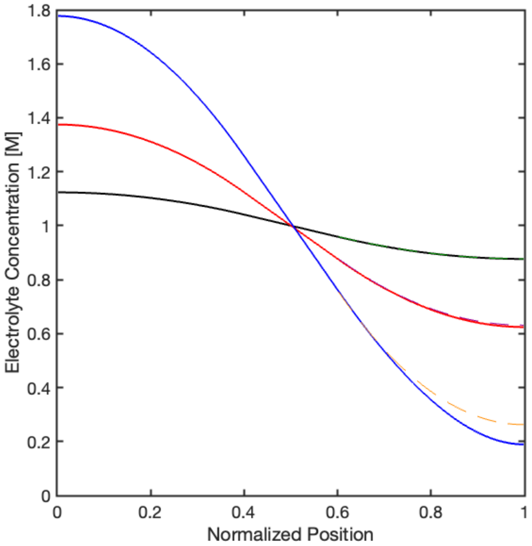

Figure IV-1: *Comparison between simulated end-of-discharge electrolyte concentration results (solid lines) and the analytical steady-state solution shown in Eq. (IV-3) (dashed lines) for three different sets of conditions.*

Figure IV-2 shows the typical transient concentration development trends for conditions with small γ_M. Most concentration change occurs within the timescale $t_{\text{diff}} = \frac{\varepsilon_p L_p^2}{D_{\text{eff},p}}$, and $Fo = \frac{t_{\text{dis}}}{t_{\text{diff}}}$ can thus be used to inform whether the steady-state solution is a good approximation for the end-of-discharge electrolyte concentration profile for a given discharge period t_{dis}.

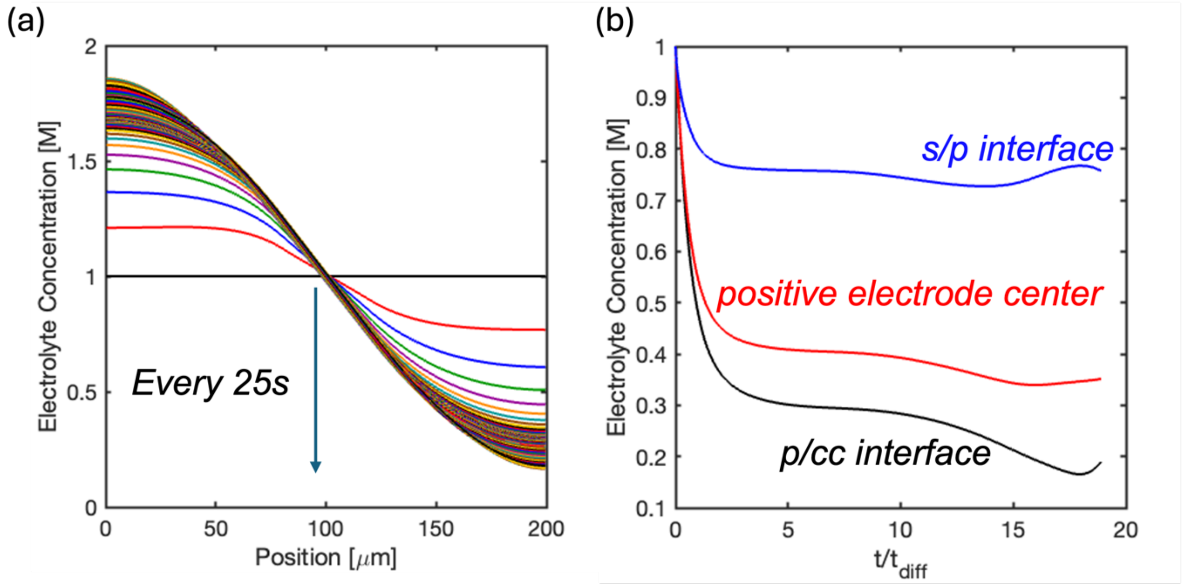

Figure IV-2: *Electrolyte concentration evolution for conditions with small* $\gamma_{M.}$

2.1.2. *Electrolyte concentration development for conditions with small* β_M

The observation that electrolyte salt depletion will not occur when γ_M is small can be justified by examining the electrolyte concentration change with consumption only. Assuming uniform reaction distribution, the electrolyte concentration governing equation without diffusion in the positive electrode can be written as:

$$\varepsilon_p \frac{\partial c_e(x,t)}{\partial t} = \frac{\left(1-t_+\right) I_{\text{app}}}{FL_p} \tag{IV-4}$$

With the initial condition $c|_{t=0} = c_{\text{initial}}$, the electrolyte concentration at time t is:

$$c = c_{\text{initial}} - \frac{|I_{\text{app}}|\left(1-t_+\right)}{\varepsilon_p L_p F} t \tag{IV-5}$$

The time at which electrolyte concentration is 0, $t_{\text{depletion}}$, is thus $t_{\text{depletion}} = \frac{c_{\text{initial}} \varepsilon_p L_p F}{I_{\text{app}}\left(1 - t_+\right)}$. As such, electrolyte salt depletion will not occur if the discharge timescale (t_{dis}) is smaller than $t_{\text{depletion}}$, i.e., $\beta_M = \frac{t_{\text{dis}}}{t_{\text{depletion}}} = \frac{I_{\text{app}}\left(1 - t_+\right) t_{\text{dis}}}{F c_{\text{initial}} \varepsilon_p L_p} < 1$.

For conditions with small β_M and γ_M, the electrolyte concentration evolution follows that discussed in Section 2.1.1. For conditions with small β_M and large γ_M, the discharge completes before t_{diff}, and the pseudo-steady state will not occur by end of discharge. In this case, the electrolyte concentration development typically follows the patterns in **Figure IV-3**, where the majority of the electrolyte concentration can be approximated with $c = c_{\text{initial}} - \frac{\left|I_{\text{app}}\right|\left(1 - t_+\right)}{\varepsilon_p L_p F} t$. Note that under these conditions, the electrolyte concentration profile is strongly affected by reaction distribution inside the electrode.

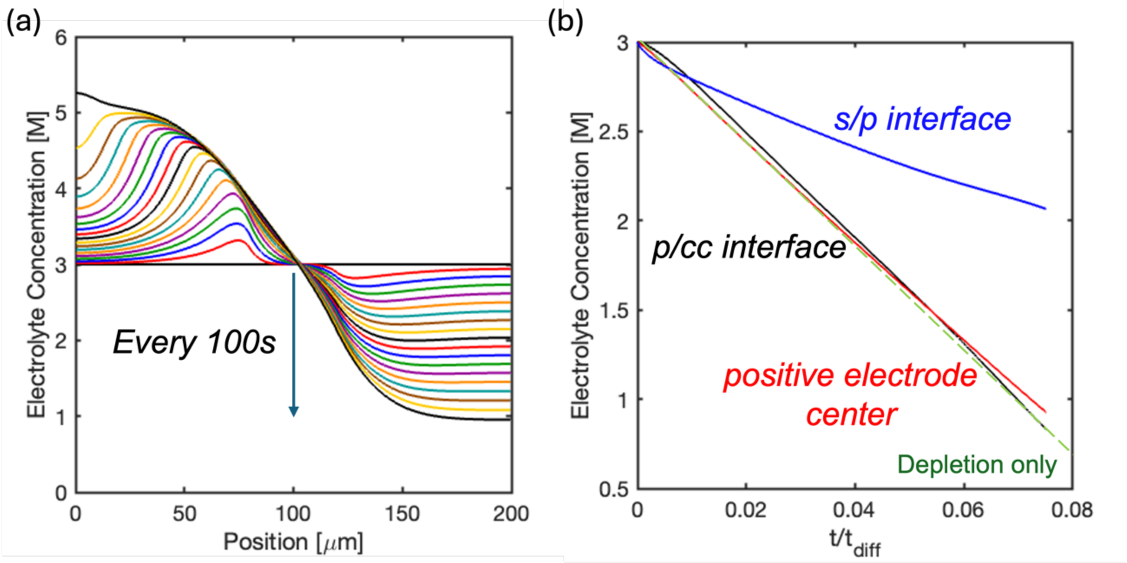

Figure IV-3: *Electrolyte concentration evolution for conditions with small β_M and large γ_M.*

2.1.3. Electrolyte concentration development for conditions with large γ_M and β_M

For conditions with both large γ_M and β_M values, the electrolyte salt depletion will occur, as the steady-state solution will lead to a negative concentration in the lithium-depleting electrode, and the depletion timescale is smaller than the discharge timescale. The electrolyte concentration generally evolves following **Figure IV-4**. Simulation data suggest that the electrolyte salt depletion occurs around $t=\dfrac{t_{\text{dis}}}{\beta_M\left(1-\dfrac{1}{\gamma_M}\right)}$, which converges to $\dfrac{t_{\text{dis}}}{\beta_M}$ at large γ_M, and increased electrolyte diffusivity will lead to a smaller γ_M and delay electrolyte salt depletion.

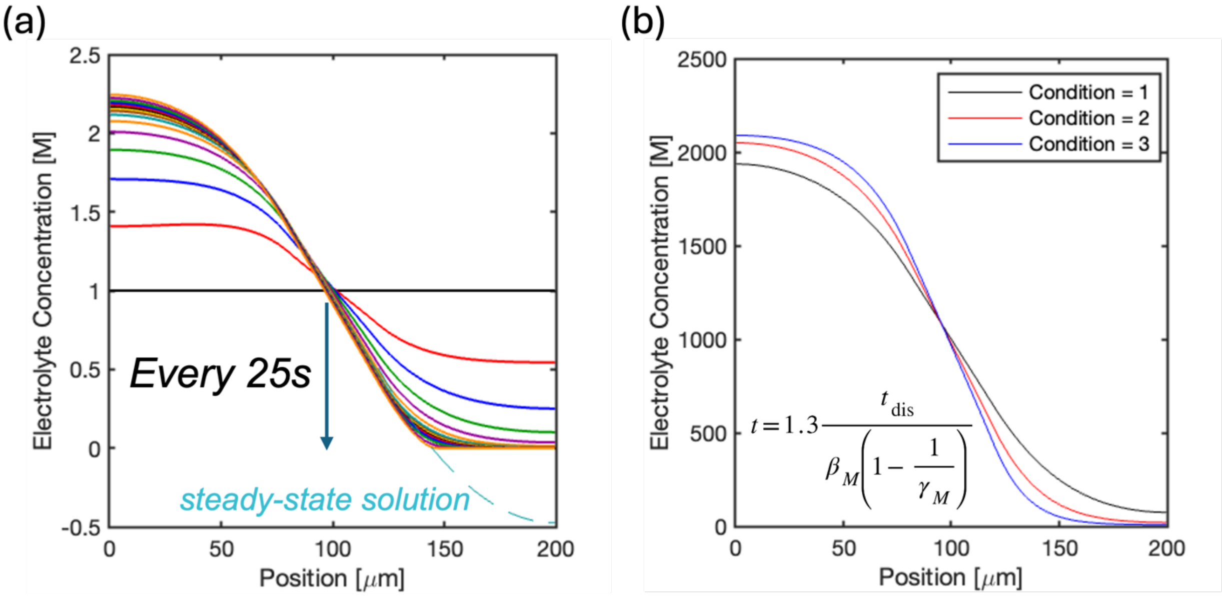

Figure IV-4: *Electrolyte concentration evolution for conditions with large β_M and γ_M.*

2.2. Evolution of electrolyte concentration with electrolyte flow

In **Chapter II**, it is observed that a flowrate is sufficient to eliminate electrolyte mass transport limitation when it satisfies $\xi_M=\dfrac{t_{\text{combined}}}{t_{\text{depletion}}}=\dfrac{I_{\text{app}}\left(1-t_+\right)}{\dfrac{FD_{\text{eff},p}c_{\text{initial}}}{L_p}+Fvc_{\text{initial}}}=\dfrac{\gamma_M}{1+Pe}<\sim 1$, where

$t_{\text{combined}} = \dfrac{1}{\dfrac{1}{t_{\text{diff}}} + \dfrac{1}{t_{\text{convec}}}}$. Similar to the case with small γ_M, this observation can be justified by examining the electrolyte concentration steady-state solution with flow. Assuming uniform reaction distribution, Eq. (II-1) for the positive electrode (*p*) with the convection term can be written as:

$$\varepsilon_p \frac{\partial c_e(x,t)}{\partial t} = D_{\text{eff},p} \frac{\partial^2 c_e(x,t)}{\partial x^2} - v \frac{\partial c_e}{\partial x} + \frac{\left(1 - t_+\right) I_{\text{app}}}{F L_p} \tag{IV-6}$$

The boundary condition at the separator/positive electrode interface can be approximated with $K\left(c_{\text{bulk}} - c\right) + v\left(c_{\text{bulk}} - c\right) = -D_{\text{eff},p} \frac{\partial c}{\partial x}$ where $K = \frac{2D_{\text{eff},s}}{L_s}$, and c_{bulk} is the concentration in the middle of the separator. At the positive electrode/current collector interface, the boundary condition is $-D_{\text{eff},p} \frac{\partial c}{\partial x} = 0$. At steady state, the concentration difference between the two boundaries of the positive electrode is $\left[\frac{1}{Pe} - \frac{1}{Pe^2}\left(1 - e^{-Pe}\right)\right] \cdot \gamma_M \cdot c_{\text{initial}}$, which is approximately $\frac{\gamma_M}{Pe} \cdot c_{\text{initial}}$. This suggests that a small γ_M (high diffusivity) or large *Pe* (high convection) helps reduce electrolyte concentration gradient, confirming the observations in **Chapter II**. Additionally, to ensure the lowest steady-state concentration within the cell (i.e., the concentration at the positive electrode/current collector interface) is above zero, the flowrate needs to satisfy $\xi_M \leq \frac{c_{\text{bulk}}}{c_{\text{initial}}} \sim 1$, corresponding to the findings in **Chapter II**.

The electrolyte concentration evolution with sufficient flowrate (i.e., small ξ_M) is shown in **Figure IV-5**, where $t_{\text{combined}} = \dfrac{1}{\dfrac{1}{t_{\text{diff}}} + \dfrac{1}{t_{\text{convec}}}}$ effectively serves the same role as t_{diff} in the case of no electrolyte flow. In this case, most concentration change occurs within t_{combined}, and

$\frac{\beta_M}{\xi_M} = \frac{t_{\text{dis}}}{t_{\text{combined}}}$ can be utilized to determine if the steady-state solution accurately approximates the electrolyte concentration profile at the end of the discharge period for a specified duration t_{dis}.

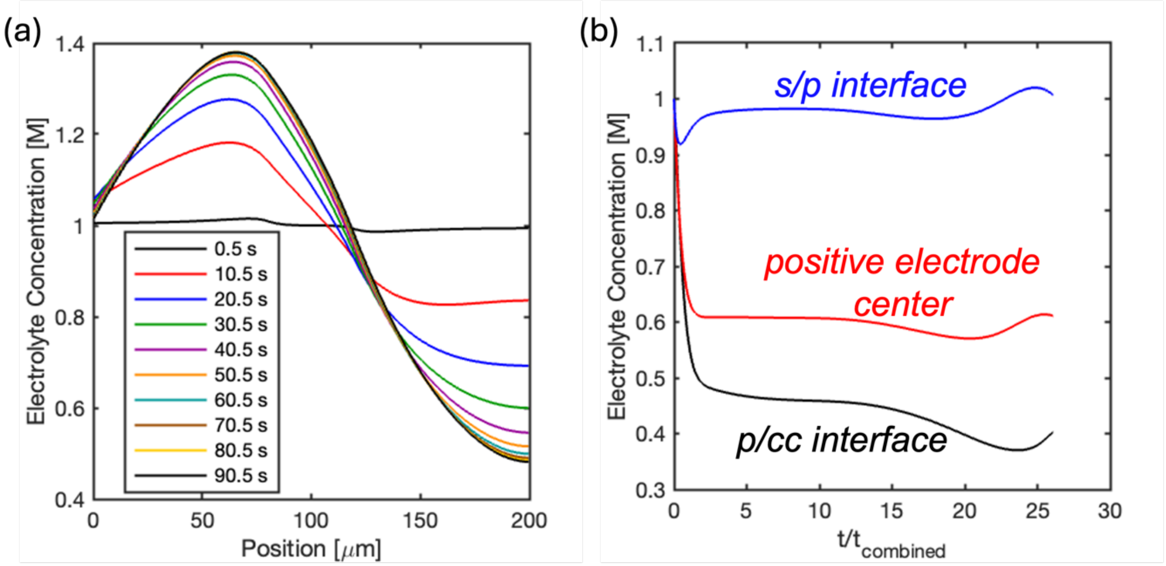

Figure IV-5: *Electrolyte concentration evolution for conditions with small* ξ_M.

3. *Transient Thermal Transport Analysis*

In **Chapter III**, a single sandwich cell layer consisting of two electrodes and a separator was examined, and the temperature distribution within the layer is uniform due to its thinness. However, a typical LIB cell is composed of numerous sandwich cell layers, leading to a much greater thickness ranging from several millimeters for a pouch cell to tens of millimeters for a prismatic or cylindrical cell. At this larger length scale, temperature gradient will likely develop, which is undesirable since it can lead to inhomogeneous degradation within the cell.[121,155] In this section, I compare temperature evolutions and distributions within the cell cooled externally via ambient heat transfer and internally via electrolyte convection. **Figure IV-6** shows the schematic of the problem analyzed in this section, where the domain represents a LIB cell consisting of multiple sandwich layers with a total thickness of L and a cross-sectional area A. The cell is assumed to have uniform thermal conductivity λ, heat capacity C_p, and uniform density ρ. For external cooling, the cell is cooled from both ends by a cooling fluid at temperature T_a with a heat transfer coefficient h. For internal cooling, the electrolyte with an inlet temperature T_{inlet} flows through the cell with a surficial velocity v. The top and bottom of the cell are assumed to be insulated, leading to a 1D problem with the temperature variations in the horizontal direction. To simplify the analysis, the heat generation rate Q within the cell is assumed to be constant and uniform. This approach is broadly justifiable, as simulation data indicate that variations in heat generation during battery operation are relatively minor (less than 30%). However, treating the heat generation as uniform might overestimate the internal temperature gradient of the cell. In reality, the sandwich layers located in the cooler regions of the cell could cause an increase in heat generation due to reduced kinetics and transport properties, which would in turn diminish the temperature gradient. Despite these potential overestimations, this simplified analysis provides a foundational insight into the temperature dynamics of cells under various cooling strategies, both external and internal.

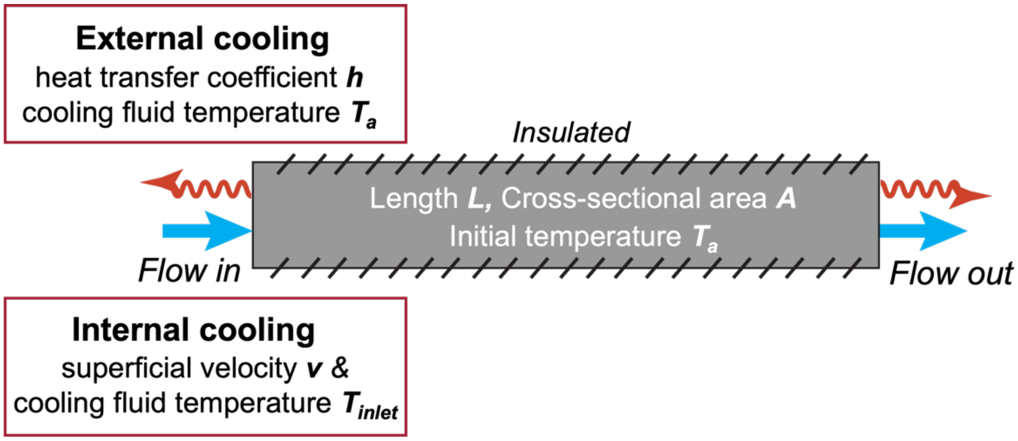

Figure IV-6: *Schematic of the problem analyzed in this work.*

The thermal transport governing equation in the cell is shown in Equation III-1 in **Chapter III**, which can be non-dimensionalized as:

$$\frac{1}{Fo}\frac{\partial \theta}{\partial \tilde{t}} = \frac{\partial^2 \theta}{\partial \tilde{x}^2} - Pe\frac{\partial \theta}{\partial \tilde{x}} + 1 \tag{IV-7}$$

In this equation, the non-dimensionalized parameters are $\theta = \frac{\left(T - T_a\right)\lambda}{QL^2}$ where T_a is the ambient temperature; $\tilde{t} = \frac{t}{t_{dis}}$; and $\tilde{x} = \frac{x}{L}$. The dimensionless group $Fo = \frac{t_{dis}}{t_{cond}}$ where $t_{cond} = \frac{L^2}{\alpha} = \frac{L^2}{\frac{\lambda}{\rho C_p}}$ compares the discharge time with the thermal conduction time, and $Pe = \frac{Lv}{\alpha_e} = \frac{Lv}{\frac{\lambda}{\rho_e C_{p,e}}}$ compares the thermal conduction time with the convection time. For the cell considered in **Figure IV-6,** if $T_{inlet} = T_a$, the left (inlet) boundary condition is $Pe \cdot \theta - Bi \cdot \theta = \frac{\partial \theta}{\partial \tilde{x}}$ where $Bi = \frac{hL}{\lambda}$ compares ambient heat transfer to thermal conduction, and the right (outlet) boundary condition is $- Bi \cdot \theta = \frac{\partial \theta}{\partial \tilde{x}}$.

3.1. External cooling analysis

For the cell with external cooling only, Eq. (IV-7) can be simplified as:

$$\frac{1}{Fo}\frac{\partial \theta}{\partial \tilde{t}} = \frac{\partial^2 \theta}{\partial \tilde{x}^2} + 1 \tag{IV-8}$$

With boundary conditions $- Bi \cdot \theta = \frac{\partial \theta}{\partial \tilde{x}}$ at both sides, the steady-state solution is:

$$\theta = -\frac{(\tilde{x} - 0.5)^2}{2} + \frac{1}{2Bi} + \frac{1}{8} \tag{IV-9}$$

The dimensionless temperatures at the center and surface of the cell are $\theta_{center} = \frac{1}{2Bi} + \frac{1}{8}$ and $\theta_{surface} = \frac{1}{2Bi}$, respectively, leading to a dimensional maximum cell temperature of $T_{center} = \frac{QL^2}{8\lambda} + \frac{QL}{2h} + T_a$, and a dimensional maximum temperature difference of

$\left(T_{center}-T_{surface}\right)_{max}=\frac{QL^2}{8\lambda}$. This suggests that at steady state, the temperature gradient within the cell will become more significant with large amount of heat generation, large cell thickness, or small thermal conductivity, and increased external cooling will only help control the cell maximum temperature rather than the temperature gradient. Similar to the mass transport, whether the steady-state solution is a good approximation of the end-of-discharge temperature profile is dependent on the dimensionless group Fo. Simulation data suggest that steady-state solution is approached when $Fo>\frac{4}{Bi}+1$. **Figure IV-7** shows the impact of Bi on cell temperature distribution under large Fo, corresponding to long discharge time duration (or low C rate), and small Fo, corresponding to short discharge time duration (or high C rate). For a particular cell with long discharge duration, an increased Bi (i.e., increased h) will only lead to reduced maximum temperature as opposed to temperature gradient as discussed previously. At short duration, an increased Bi may lead to a larger temperature gradient, as the cell surface temperature gets controlled while the cell center undergoes adiabatic temperature rise.

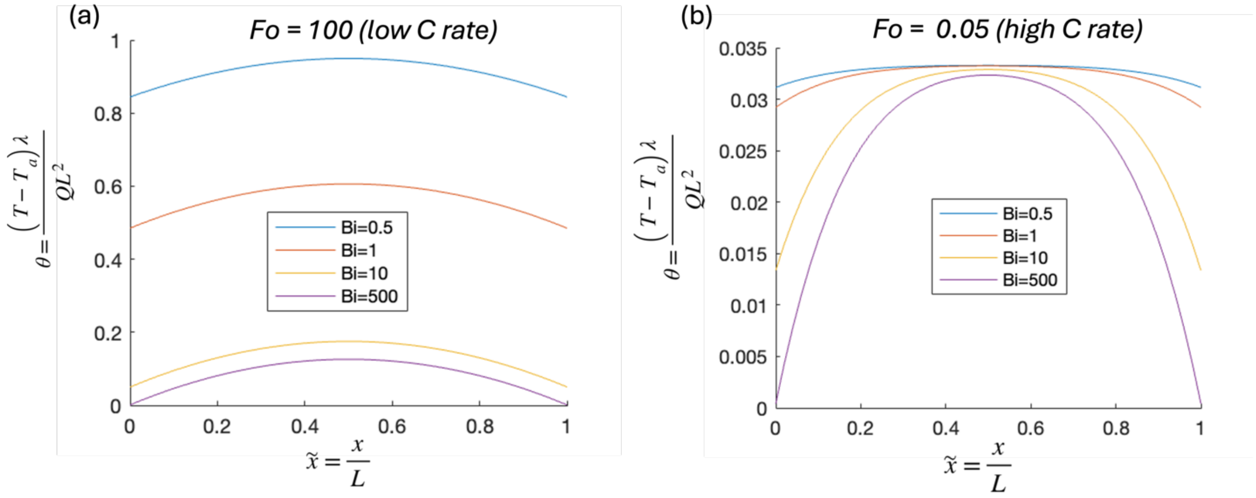

Figure IV-7: *Impact of Bi on temperature distribution at (a) large Fo and (b) small Fo.*

3.2. Internal cooling analysis

For the cell with internal cooling only, Eq. (IV-7) has boundary conditions of $Pe \cdot \theta = \frac{\partial \theta}{\partial \tilde{x}}$ and $\frac{\partial \theta}{\partial \tilde{x}} = 0$ at the left and right cell end, respectively. The steady-state solution is:

$$\theta = \frac{1}{Pe^2}\left(1 - e^{Pe(\tilde{x}-1)}\right) + \frac{\tilde{x}}{Pe} \tag{IV-10}$$

The dimensionless temperatures at the inlet and outlet of the cell are $\theta_{inlet} = \frac{1}{Pe^2}\left(1 - e^{-Pe}\right)$ and $\theta_{outlet} = \frac{1}{Pe}$, respectively. The maximum temperature difference within the cell, $\theta_{outlet} - \theta_{inlet} = \frac{1}{Pe} - \frac{1}{Pe^2}\left(1 - e^{-Pe}\right)$, decreases with increasing *Pe*, and can be approximated with $\frac{1}{Pe}$ at large *Pe* (*Pe* > 20). This leads to a dimensional maximum temperature of $\frac{QL}{\rho_e C_{p,e} v} + T_a$, and a maximum temperature difference of $\frac{QL}{\rho_e C_{p,e} v}$. This suggests that at steady state, a high flowrate can lead to both a reduction in the maximum temperature and the temperature gradient. For internal cooling, simulation data suggest that the steady-state solution is a good approximation of the end-of-discharge temperature profile when $Fo > \frac{8}{Pe}$. This strong dependence on *Pe* introduces complexity into its effect on the cell during transient phases, as seen in **Figure IV-8**. For a particular cell, a high flow rate (i.e., large *Pe*) at long discharge duration (i.e., large *Fo*) will lead to reduced maximum cell temperature and temperature gradient, as discussed with the steady-state solution. At intermediate *Fo*, increasing flowrate will still result in a lower maximum temperature, but the temperature gradient may first increase before a decrease, as the temperature profile develops faster with increasing *Pe*. At very small *Fo*, similar to the external cooling external cooling, an increased *Fo* may lead to a larger temperature gradient, as the inlet temperature gets controlled while the outlet temperature follows adiabatic temperature rise. This analysis indicates that determining the optimal flow rate for minimizing temperature gradients should be contingent upon the specific condition of the cell and the intended operating modes.

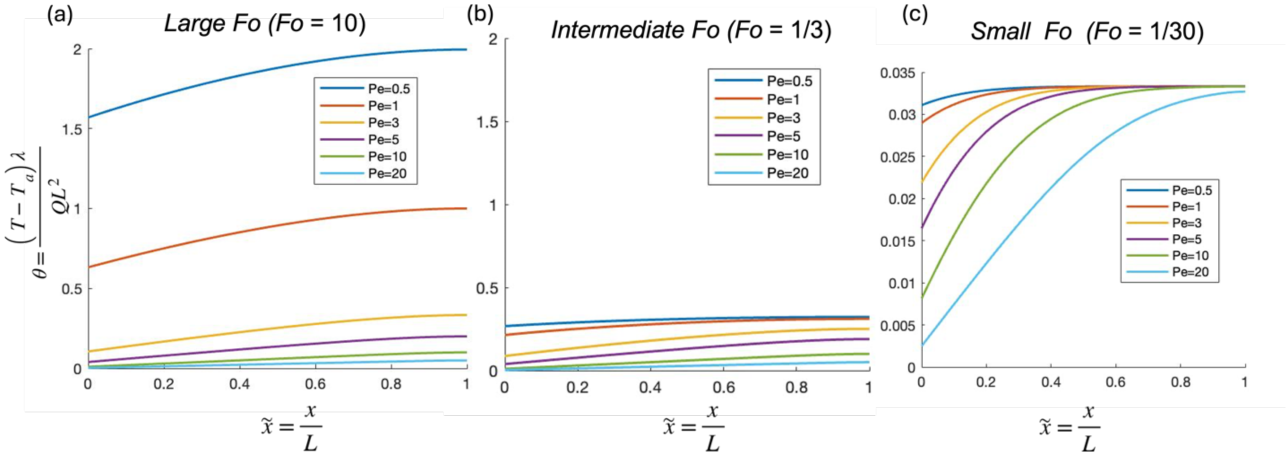

Figure IV-8: *Impact of Pe on temperature distribution at (a) large Fo, (b) intermediate Fo, and (c) small Fo.*

3.3. Comparison between external and internal cooling

While both external and internal cooling methods can help control the cell temperature, their impact on the cell temperature distribution is different. External cooling has limited control over the maximum temperature difference within the cell, and in some cases, increased external cooling can lead to a temperature variation within the cell. In contrary, internal cooling has direct control over the cell temperature distribution, and in theory, the temperature gradient can always be minimized with a sufficiently high flowrate (the practical impact of high flow on the cell is discussed in **Chapter VI)**. The difference between the two approaches can be explained using field synergy principle, which indicates that improving synergy for the velocity and temperature gradient/heat flow fields can markedly enhance heat transfer with less increased flow resistance.[156] **Figure IV-9** illustrates the comparative effectiveness of external vs. internal cooling in managing peak cell temperatures and temperature disparities, highlighting conditions under which one approach outperforms the other. Note that in the region where external cooling leads to a smaller temperature variation, it results in a higher peak cell temperature. As demonstrated in the figure, internal cooling with a large *Pe* is generally preferred, as it leads to effective thermal regulation with a minimized temperature gradient. However, choosing a high flow rate necessitates weighing the trade-offs, including higher pumping power and greater degradation risks, as elaborated in **Chapter VI**.

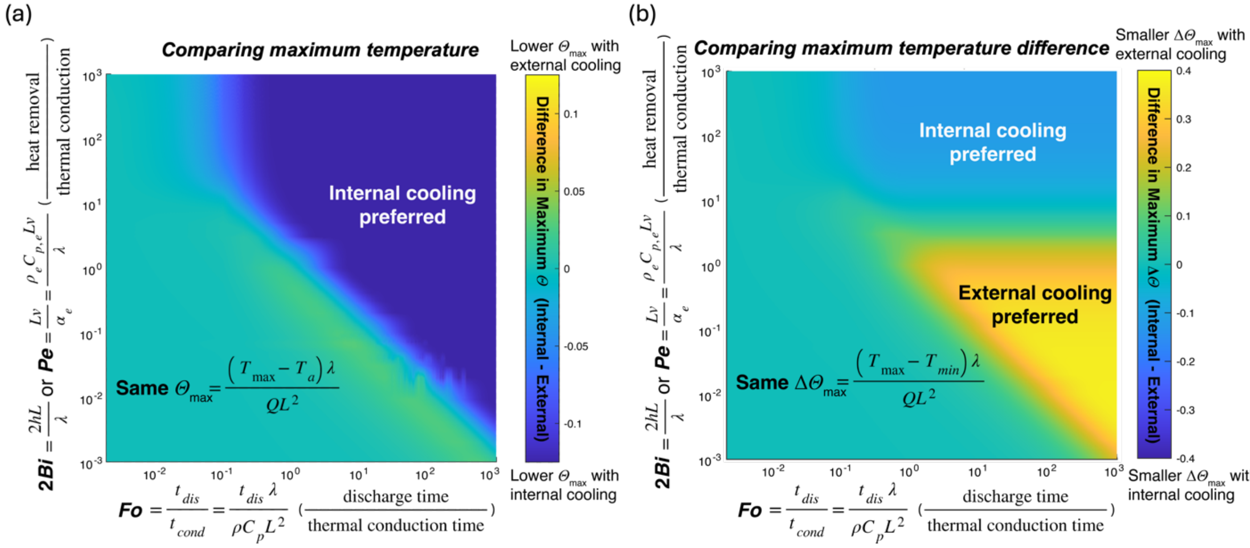

Figure IV-9: *Comparative analysis of external vs. internal cooling effects on (a) cell maximum temperature and (b) cell maximum temperature difference.*

4. *Conclusions*

This chapter builds on the mass and thermal transport discussions from **Chapters II** and **III**, focusing on transient electrolyte concentration and temperature developments, as well as temperature distribution within a cell stack. A new dimensionless group, *Fo*, is introduced, which compares the discharge timescale with the diffusion or thermal conduction timescale, and a large *Fo* suggests that the end-of-discharge can be approximated with the steady-state solution. For mass transport, the findings in **Chapter II** are validated through analytical examination of the governing equation for electrolyte mass transport. The discussion also covers the evolution of concentration over time in scenarios with both stagnant electrolyte and flowing electrolyte, which can be particularly relevant to shorter-duration applications, such as pulsed charge/discharge. For thermal transport, an analytical examination is conducted on temperature changes and variations within a cell stack using both external and internal cooling methods, followed by a comparison of their effectiveness. Due to the lack of access within the cell, the external cooling approach may not effectively reduce cell temperature variations and could, and in some cases, exacerbate them. In contrast, internal cooling directly influences temperature distribution, potentially minimizing variation at high flow rates. However, practical considerations, such as increased pumping power, may limit the desirability of high flow rates, as discussed in detail in **Chapter VI**. Despite these considerations, the convection battery-enabled internal cooling presents a promising avenue for effective thermal management with reduced temperature gradients, which is difficult to achieve using the current external thermal management approaches.

5. *List of Symbols*

Symbol	**Description**
A	Cell cross-sectional area
C_p	Heat capacity
$C_{p,e}$	Electrolyte heat capacity
c_{bulk}	Bulk electrolyte concentration
$c_e(x,t)$	Anion concentration in the electrolyte
c_{initial}	Initial electrolyte concentration
D_{eff}	Effective electrolyte diffusivity
F	Faraday constant
h	Cell convective heat transfer coefficient
I_{app}	Applied current density
L	Thickness
Q	Cell volumetric heat generation rate
T_{a}	Ambient temperature
T_{inlet}	Electrolyte inlet temperature
$T(x,t)$	Cell temperature

t_{combined}	Timescale for combined electrolyte diffusion and convection
t_{cond}	Timescale for thermal conduction
t_{convec}	Timescale for electrolyte convection
$t_{\mathrm{depletion}}$	Timescale for electromigration
t_{diff}	Timescale for electrolyte diffusion
t_{dis}	Timescale for discharge or charge
t_+	Li^+ transference number
v	Superficial velocity in the cell
ε	Porosity
λ	Thermal conductivity
ρ	Density
ρ_e	Electrolyte density

V. Extra Electrolyte Requirements

1. Introduction

In the preceding three chapters, the analysis relied on the assumption that the electrolyte storage tank was substantially larger than the cell itself. This configuration maintained constant electrolyte concentration and temperature inside the tank, thereby focusing the examination on transport phenomena within the cell. However, such a high tank-to-cell volume ratio may not be optimal at the system level, negatively impacting energy and power densities and incurring additional costs due to excess electrolyte. Optimizing the tank-to-cell volume ratio is crucial for balancing performance gains by electrolyte flow against these trade-offs. An alternative configuration using a recirculation loop, where the storage tank is replaced by a pipe, could offer further advantages, such as an increased surface area for heat transfer. Nevertheless, evaluating this design demands a comprehensive understanding of how the dimensions of the pipe affect the balance between performance enhancement and operational costs, including factors like pumping loss. This chapter aims to delve into these issues by examining the impact of extra electrolyte on performance enhancement through electrolyte convection, and how this is influenced by changes in the volume and shape of the extra electrolyte.

2. Model Description

In this study, numerical simulations were conducted utilizing COMSOL Multiphysics 6.1 with the Livelink interface to MATLAB R2023a. A 1D electrochemical and thermal coupled convection cell model (**Figure III-1**) based on the P2D (Pseudo-Two-Dimensional) framework was developed by integrating the Lithium-Ion Battery Module and the Heat Transfer Module within COMSOL Multiphysics. The lateral walls of the cell are assumed to be well-insulated while heat exchange with the environment only occurs through the current collectors at either end of the cell (axial). Hence, the cell temperature is radially uniform but spatial temperature gradients can exist in the axial direction (x-direction in **Figure III-1**). To accommodate electrolyte flow, convection terms are incorporated into the electrolyte mass transport and thermal transport governing equations. The detailed descriptions of the modifications made and the governing equations can be found in **Chapters II** and **III**.

In our prior studies, the electrolyte storage tank is assumed to be well-mixed (0D). This approach is implemented in this COMSOL-based model through the Global Ordinary Differential Equations (ODEs) and Differential Algebraic Equations (DAEs) interface. In the context of a recirculation loop, this assumption translates to an infinite backmixing scenario. Additionally, to investigate the impact of electrolyte mixing in the tank/recirculation loop on convection battery cell performance, another treatment of the extra electrolyte assuming it has a 1D pipe configuration is also implemented in the model. Eq. (V-1) shows the electrolyte mass transport equation inside the pipe under this treatment.

$$\frac{\partial c_{\mathrm{pipe}}(x,t)}{\partial t}=\frac{\partial}{\partial x}[D_e\frac{\partial c_{\mathrm{pipe}}(x,t)}{\partial x}]-v_{\mathrm{pipe}}\frac{\partial c_{\mathrm{pipe}}(x,t)}{\partial x} \tag{V-1}$$

Here, $c_{\mathrm{pipe}}(x,t)$ is the electrolyte concentration inside the pipe at position x and time t, D_e is the electrolyte diffusion coefficient, v_{pipe} is electrolyte superficial velocity inside the pipe and is related to the superficial velocity in the cell, v, by the continuity equation $A_{\mathrm{pipe}}v_{\mathrm{pipe}} = A_{\mathrm{cell}}v$ by assuming constant fluid density, where A_{pipe} and A_{cell} are the cross-sectional areas of the pipe and the battery cell, respectively. The temperature distribution inside the pipe can be described as follows:

$$\rho_e C_{p,e}\frac{\partial T_{\mathrm{pipe}}(x,t)}{\partial t}=\frac{\partial}{\partial x}[\lambda_e\frac{\partial T_{\mathrm{pipe}}(x,t)}{\partial x}]-\rho_e C_{p,e}v_{\mathrm{pipe}}\frac{\partial T_{\mathrm{pipe}}(x,t)}{\partial x}+\frac{S_{\mathrm{pipe}}h_{\mathrm{pipe}}}{V_{\mathrm{pipe}}}\left(T_{ambient}-T_{\mathrm{pipe}}(x,t)\right) \tag{V-2}$$

Here, ρ_e is the electrolyte density, $C_{p,e}$ is the electrolyte heat capacity, $T_{\text{pipe}}(x,t)$ is the electrolyte temperature inside the pipe at position x and time t, λ_e is the electrolyte thermal conductivity. The pipe with total volume V_{pipe} is assumed to exchange heat with its surroundings through its lateral surface via convective cooling, with total lateral surface area S_{pipe}, convective heat transfer coefficient h_{pipe}, and ambient temperature T_{ambient}. The pressure drop inside the pipe, ΔP_{pipe}, is calculated using Hagen–Poiseuille equation:

$$\Delta P_{\text{pipe}} = \frac{32\mu L_{\text{pipe}} v_{\text{pipe}}}{d_{\text{pipe}}^2} \tag{V-3}$$

Here, μ is the electrolyte viscosity, L_{pipe} is the length of the pipe, and d_{pipe} is the diameter of the pipe. To simplify the analysis, each cell is considered to have an individual recirculation loop. The pressure drop through the cell, ΔP_{cell}, is estimated using Kozeny-Carman equation[153]:

$$\Delta P_{\text{cell}} = \frac{180\mu L_{\text{cell}} v}{\Phi_s^{\,2} D_p^{\,2}} \frac{(1-\varepsilon)^2}{\varepsilon^3} \tag{V-4}$$

where μ is the electrolyte viscosity, L_{cell} is the cell total length, v is the superficial velocity in the cell, ε is the porosity, and Φ_s is the sphericity of the active material particles with diameter D_p. The pumping energy E_{pump} is then calculated as:

$$E_{\text{pump}} = Q \Delta P t_{\text{d}} \tag{V-5}$$

where Q is the volumetric flowrate, which is assumed to be constant through the cell and the pipe, and t_{d} is the duration of discharge.

The gravimetric energy density of a convection battery system is calculated by:

$$E_{\text{system}} = \frac{Q_A^{max} \cdot Accessed\% \cdot \overline{V} - \dfrac{E_{pump}}{\eta_{pump}}}{m_{system}} \tag{V-6}$$

Here, Q_A^{max} is the theoretical accessible capacity of the cell, $Accessed\%$ is the percentage of the theoretical capacity accessed, $\overline{V}$ is the average running voltage during operation, η_{pump} is the pump efficiency, and m_{system} is the total system mass.

Multiple lithium-ion battery chemistries are implemented in the model, with parameter values obtained from the COMSOL library, LiionDB, and comprehensive literature reviews.[157,158] Using the Lithium Cobalt Oxide (LCO)/graphite chemistry, the model is validated against our MATLAB-based LIONSIMBA+c. For this study, we opted for the NMC622/Graphite chemistry, given its commercial availability and prevalent use in electric vehicles, with the electrolyte being $LiPF_6$ in a 1:1 EC:DMC mixture. The parameters used for the simulations performed in this study are shown in **Table V-1**. All the simulations were performed for galvanostatic operation, with a state of charge (SoC) range of 99% to 0.9%, a lower voltage limit of 3 V, and an upper temperature limits of 52 °C (325 K) based on the typical operating conditions and safety cutoffs for LIBs.[149] The cell and extra electrolyte are assumed to have the same initial electrolyte concentration of 1 M and same initial temperature of 25 °C (298 K) throughout the domain. To accommodate the computational demands of this study, the MIT Supercloud was employed,[159] which offered enhanced computational power and efficiency.

Table V-1: *Simulation parameters used in this study.*

	Units	**Positive CC**	**Positive Electrode**	**Separator**	**Negative Electrode**	**Negative CC**
	-	Al	$LiNi_{0.6}Mn_{0.2}Co_{0.2}O_2$	-	$Li_{\theta}C_6$	Cu
$brugg$	-	-	2.5	2.5	2.5	-
C_p	J/kg/K	884	905	1617	966	387
$C_{p,e}$	1635 J/kg/K					
c_{initial}	mol/m^3	-	1000	1000	1000	-
$c_s^{\max}$	mol/m^3	-	47664	-	30555	-
D_i^s	m^2/s	-	5×10^{-14}	-	2×10^{-14}	-
$E_a^{D_i^s}$	J/mol	-	5000	-	5000	-
$E_a^{k_i}$	J/mol	-	5000	-	5000	-
F	96485 C/mol	-	-	-	-	-
k_i	$m^{2.5}/(mol^{0.5}s)$	-	1×10^{-11}	-	2×10^{-11}	-
L	m	1×10^{-5}	6.9×10^{-5}	2.5×10^{-5}	9×10^{-5}	1×10^{-5}
R	8.314 J/mol/K	-	-	-	-	-
R_p	m	-	5×10^{-6}	-	5×10^{-6}	-
ε	-	-	0.4	0.4	0.4	-
$\varepsilon_{\mathrm{filler}}$	-	-	0.0872	-	0.0326	-
$\Theta_{100\%}$	-	-	0.258	-	0.9	-
$\Theta_{0\%}$	-	-	0.917	-	0.192	-
λ	W/m/K	238	0.66	0.312	1.195	398
μ	5×10^{-3} Pa•s					
ρ	kg/m^3	2702	3060	1036	1832	8933
ρ_e	$1240\ kg/m^3$					
σ	S/m	3.55×10^{7}	10	-	100	5.96×10^{7}

3. Results and Discussion

3.1. Extra electrolyte volume analysis

3.1.1. Requirement to achieve mass transport enhancement

In this section, we examine the influence of the extra-electrolyte-to-cell volume ratio on cell performance under isothermal conditions, facilitated by a sufficiently large cell convective heat transfer coefficient (h_{cell} = 500 W/(m²*K)). This coefficient effectively minimizes temperature increase during cell discharge, allowing us to attribute performance improvements solely to enhanced electrolyte mass transport. This analysis assumes a well-mixed tank, although subsequent sections will explore the effects of mixing dynamics on performance.

Figure V-1a illustrates the augmentation of theoretical capacity accessed by electrolyte flow, in comparison to a cell with stagnant electrolyte, at a discharge rate of 5C. Under the specified rapid discharge conditions, the stagnant cell is hindered by diffusion-limited behavior, leading to a notable depletion of electrolyte salt in the positive electrode before the discharge cycle concludes. This limitation is mitigated by the introduction of electrolyte flow, which enhances electrolyte mass transport, as supported by our previous findings.[144] As illustrated in **Figure V-1a**, the volume of extra electrolyte influences the effectiveness of the flow in boosting cell performance. We incorporate the dimensionless group ξ_M formulated in our previous work, which compares the electromigrative flux against the combined diffusive and convective fluxes, to offer a deeper insight into our analysis. In scenarios where flowrates are inadequate to overcome electrolyte mass transport limitations ($\xi_M >> 1$), a larger extra-electrolyte-to-cell volume ratio ($>10^{-2}$) shows slight performance benefits. Notably, at intermediate flow rates ($\xi_M \sim 1$), we discern an optimal extra-electrolyte-to-cell volume ratio of about 0.1; ratios below this threshold reduce the flow's efficacy, while higher ratios further diminish its effectiveness. Conversely, at flow rates capable of eliminating electrolyte mass transport constraints ($\xi_M <1$), the additional electrolyte volume ceases to have a substantial impact on enhancing cell performance.

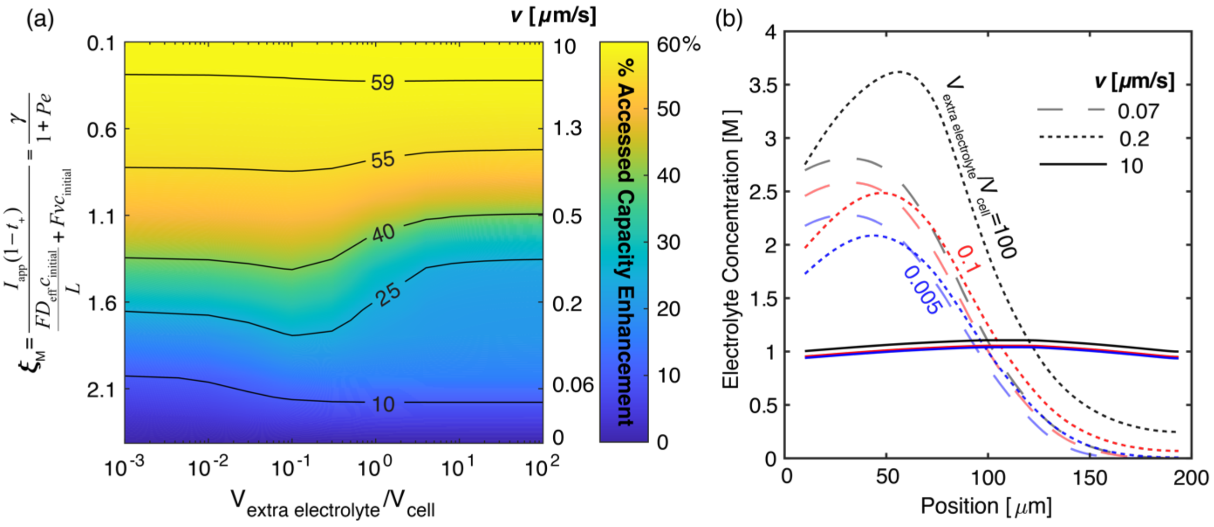

Figure V-1: *(a) Accessed capacity enhancement under 5C isothermal discharge by electrolyte flow of varying flowrates compared to a cell without stagnant electrolyte as a function of extra-electrolyte-to-cell volume ratio (b) Cell electrolyte concentration overlay for extra-electrolyte-to-cell ratios of 0.005 (blue), 0.1 (red), and 100 (black) at electrolyte flowrates of 0.07 µm/s (long-dashed lines), 0.2 µm/s (short-dashed lines), and 10 µm/s (solid lines). The tank concentration evolution with time can be found in* ***Figure V-6****.*

The findings depicted in **Figure V-1a** are further elucidated by examining the electrolyte concentration profiles shown in **Figure V-1b**, along with the concentration changes within the tank in **Figure V-6**. A substantial volume of extra electrolyte is more adept at buffering the impact of electrolyte depletion, thereby increasing the inlet electrolyte concentration to the cell and consequently leading to a heightened net concentration accumulation within the cell. For insufficient flowrates (ξ_M >> 1, long-dashed lines in **Figure V-1b**), a larger volume serves as a material source, increasing cell concentration and delaying electrolyte salt depletion (long-dashed lines). Nevertheless, the concentration accumulation is predominantly at the negative electrode, which limits the extent of performance enhancement. With increased flowrates (ξ_M ~ 1, short-dashed lines in **Figure V-1b**), more even distribution across the cell yields greater performance gains, but excessive concentration accumulation can impair cell performance due to reduced electrolyte conductivity, especially with an extra-electrolyte-to-cell volume ratio significantly above 0.1. At sufficient flowrates ($\xi_M \ll 1$, solid lines in **Figure V-1b**), a uniform electrolyte concentration within the cell renders the additional electrolyte volume inconsequential.

Figure V-1 highlights that, when the flowrate exceeds a certain threshold ($\xi_M < 1$), the contribution of increased electrolyte volume to performance improvement becomes negligible in terms of mass transport. In this scenario, the purpose of the electrolyte flow is merely to homogenize concentration, without the necessity for extra material input. However, up to a ratio of $V_{\text{extra electrolyte}}/V_{\text{cell}} \sim 0.5$ might be beneficial in boosting flow efficacy, potentially reducing required flowrate and mitigating startup effects. It is important to note that while these simulations focus on a single sandwich layer, the deduced flowrate remains applicable to larger cells with multiple layers, as it scales with electrode thickness rather than the cell dimension. In practical terms, this scenario underlines the potential gains achievable with minimal disruption to system design. Here, thermal management components remain unchanged, with flow benefits confined to the electrolyte mass transport enhancement and the accompanying reduced heat generation for eased thermal regulation requirement/safer operation. These benefits are achieved at the expense of the altered cell architecture to allow flow, additional requirements of extra electrolyte, necessary flow components (e.g., pumps, tubing), and the associated pumping losses.

3.1.2. Requirement to achieve thermal transport enhancement

In this section, we extend our analysis beyond the isothermal condition to assess how the extra-electrolyte-to-cell volume ratio influences the capability of electrolyte flow to regulate cell temperature. **Figure V-2a** delineates the enhancement in theoretical capacity enabled by electrolyte flow compared to a cell with stagnant electrolyte under a 5C discharge rate. For this scenario, the cell is modeled as insulated (h_{cell} = 0 W/(m^{2}K)), with thermal regulation achieved solely through heat removal by the flowing electrolyte. The well-mixed tank is designed with an aspect ratio (height/diameter) of 1.5 and an overall heat transfer coefficient (h_{tank}) of 100 W/(m^2K), indicative of either forced air convection or free liquid convection cooling methods.[154]

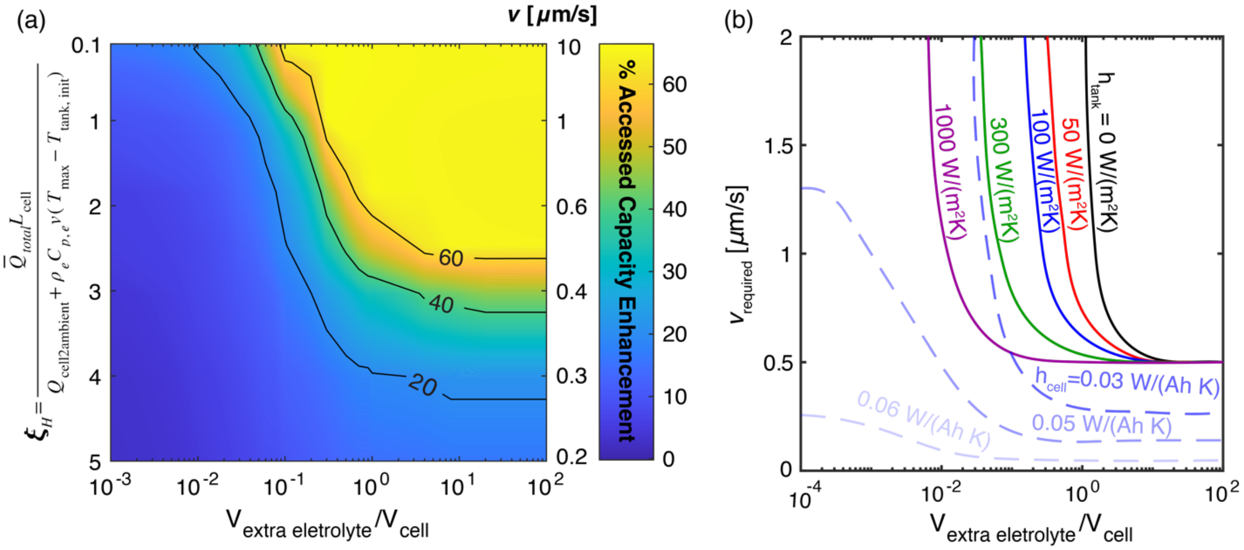

Figure V-2: *(a) Accessed capacity enhancement under 5C discharge by electrolyte flow of varying flowrates compared to a cell without stagnant electrolyte as a function of extra-electrolyte-to-cell volume ratio. The cell is insulated (h_{cell} = 0 W/(m^2K)), and the well-mixed tank has a height/diameter ratio of 1.5 and an overall heat transfer coefficient (h_{tank}) of 100 W/(m^2K) (b) Minimum flow velocity required to keep cell temperature below the safety threshold before the completion of discharge, plotted against the extra-electrolyte-to-cell volume ratio. This is depicted for varying h_{tank} values under an insulated cell condition(h_{cell} = 0 W/(m^2K), indicated by solid lines), and for increasing h_{cell} values while keeping h_{tank} constant at 100 W/(m^2K) (indicated by dashed lines).*

Under these conditions, the cell with stagnant electrolyte struggles with heat dissipation, reaching the safety temperature limit before the completion of discharge. In contrast, the introduction of electrolyte flow not only suppresses temperature escalation but also curtails heat generation by improving electrolyte mass transport, thereby extending cell runtime.[160] As depicted in **Figure V-2a**, in contrast to the isothermal case, the effectiveness of flow in temperature regulation is significantly influenced by the volume of extra electrolyte. The dimensionless group ξ_H formulated in our earlier work, which compares the heat generation to the sum of heat removal via ambient cooling and electrolyte convection, is incorporated in **Figure V-2a** to aid the analysis. The results suggest that a minimal volume of extra electrolyte diminishes the flow's ability to effectively regulate cell temperature, with a threshold below which effective thermal regulation is unattainable, regardless of the flow rate. Nevertheless, even with substantial extra electrolyte volume, an adequate flowrate (ξ_H ~1) remains crucial for effective temperature regulation.

A larger volume of extra electrolyte offers dual advantages: (1) enhanced heat storage capacity and (2) improved heat dissipation due to increased heat transfer surface area (with a fixed height/diameter ratio). These combined effects slow the temperature rise in the extra electrolyte, resulting in a cooler inlet electrolyte temperature to the cell and consequently improving the heat exchange efficiency between the cell and extra electrolyte. This leads to a lower requisite flow rate for effective thermal management. In scenarios where the extra electrolyte volume is minimal, the cell and tank's combined heat storage and dissipation capacities are insufficient to counterbalance the heat generation rate, causing the cell to reach the safety cutoff temperature regardless of flow rate. On the other hand, a significantly large extra electrolyte volume effectively maintains isothermal conditions, necessitating a flowrate that ensures the total heat removal rate of the cell matches its heat generation rate, i.e., $\xi_H < \sim 1$, to prevent the cell from reaching the safety cutoff temperature before end of discharge. Notably, unlike the flowrate needed for mass transport enhancement, which is dependent solely on electrode thickness, the flowrate required for thermal regulation scales with the cell dimension. For a cell comprising multiple sandwich layers, the flowrate inferred from **Figure V-2** should at least be scaled proportionally to the number of layers, and even higher if more uniform temperature distribution is desired.

Figure V-2a reveals a trade-off between the necessary velocity (i.e., pumping loss) and extra electrolyte volume (i.e., added weight and volume) for maximizing performance enhancement. This balance becomes more complex when factoring in the heat transfer efficiencies of both the tank and cell to their environment. **Figure V-2b** delineates this complexity by presenting the minimal flow velocity necessary to maintain cell temperature beneath the safety threshold prior to discharge completion. This is depicted as a function of the ratio of extra electrolyte volume to cell volume, across various h_{tank} while maintaining the insulated cell condition (h_{cell} = 0 W/(m^{2}K), represented by solid lines), and increasing h_{cell} with a constant h_{tank} of 100 W/(m^{2}K) (represented by dashed lines). The tank's heat dissipation ability to the environment affects the rate of temperature rise in the extra electrolyte, which, in turn, influences the effectiveness of a particular combination of flowrate and extra electrolyte volume on regulating the cell temperature. As the solid lines with increasing h_{tank} values suggest, superior heat dissipation by the tank lessens the need for higher flow rates and extra electrolyte volume. Likewise, the cell's inherent heat dissipation capability plays a crucial role in determining the required flow rate and extra electrolyte volume. When the cell's inherent heat dissipation capability is substantial enough to manage the cell temperature below the safety cutoff threshold, the scenario reverts to the previously discussed scenario where electrolyte flow mainly contributes to mass transport enhancement.

This scenario opens up the possibility for a significant redesign of existing lithium-ion battery systems by capitalizing on the electrolyte flow's capacity to regulate cell temperature. It suggests that internal thermal management, driven by electrolyte convection, could potentially replace the current external thermal management components. To enhance the tank's ability to dissipate heat (increasing h_{tank}), a strategy combining passive cooling with ambient air and active cooling by adapting the heat exchanger from modern liquid-based thermal management systems could be employed. This could render certain components, such as coolants and cooling plates, obsolete. However, this approach comes with trade-offs, such as considerable pumping losses at high flow rates, the need for more extra electrolyte and tubing, and possibly a larger pump to accommodate the increased demand for pumping power. Alternatively, retaining some level of external thermal management (i.e., increasing h_{cell}) could lessen the required flow velocity and the amount of extra electrolyte needed. This highlights the critical need for a thoughtful design approach that carefully weighs the trade-offs among flow velocity, the ratio of extra electrolyte to cell volume, and the choice between retaining or eliminating external thermal management components to arrive at an optimally configured system.

3.2. Extra electrolyte shape analysis

The previous analysis highlights the diminishing returns on mass transport enhancement from added electrolyte volume beyond a certain flow rate ($\xi_M < 1$), while the extra electrolyte volume and design have significant impact on the thermal regulation efficiency of the electrolyte flow. Enhanced thermal regulation can be achieved by improving the heat exchange capability of the extra electrolyte with its surroundings, either through a higher heat transfer coefficient (e.g., by incorporating a heat exchanger) as depicted in **Figure V-2b**, or by expanding the heat transfer surface area. For a tank with a fixed aspect ratio, enlarging the tank size enhances the heat transfer surface area and, consequently, the heat dissipation capability, as detailed in Section 3.1.2. Alternatively, when the tank volume is fixed, augmenting the aspect ratio can also increase the heat transfer area. In practical terms, an electrolyte tank with an exceedingly high aspect ratio resembles a recirculation pipe, making the well-mixed assumption inapplicable. Hence, a 1D pipe model is employed to assess the design impact of an electrolyte-filled recirculation pipe on cell performance, assuming a circular pipe for simplicity. **Figure V-3a** illustrates how altering the pipe's length-to-diameter ratio affects the efficacy of a 1.5 μm/s electrolyte flow in maintaining the cell temperature below critical levels during a 5C discharge, keeping the pipe volume constant at 30% of the cell volume and assuming a heat transfer coefficient of 100 W/(m^2K) for an insulated cell. As **Figure V-3a** shows, an increase in the length-to-diameter ratio of the pipe, while keeping its volume constant, leads to a slower rise in cell temperature due to a larger heat transfer area and the subsequently cooler inlet electrolyte temperatures. To examine mixing dynamics' effects, **Figure V-3a** also includes the temperature profiles for well-mixed tanks with equivalent volume and surface area (dashed lines). At a minimal length-to-diameter ratio of 0.01, the pipe functions similarly to a well-mixed tank, and their temperature profiles coincide. As the length-to-diameter ratio increases, thermal management efficiency via the recirculation pipe surpasses that of the well-mixed tank due to the development of temperature and concentration gradients within the pipe, enhancing the inlet electrolyte's concentration and cooling effect, thereby improving electrolyte flow's effectiveness. This suggests that the flow rates discussed in Section 3.1 are conservative, and a hybrid design incorporating both the storage tank and recirculation loop might offer intermediate performance between the solely well-mixed tank (dashed lines) and the exclusive recirculation loop (solid lines).

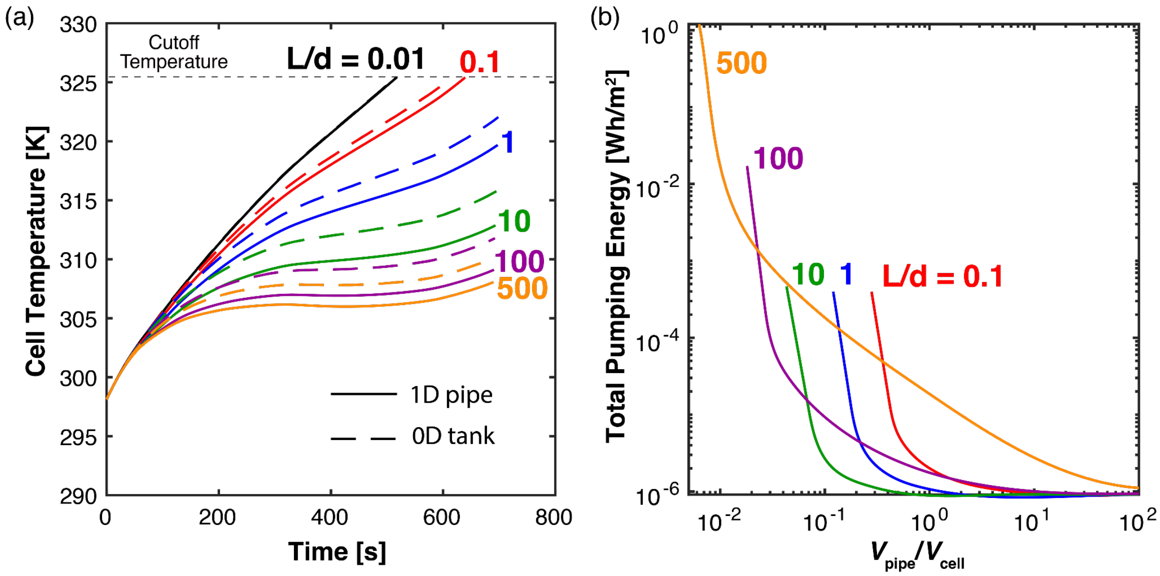

Figure V-3: *(a) Temperature profiles of cells with electrolyte recirculation pipes of varying length-to-diameter ratios, utilizing a fixed electrolyte volume at 30% of the cell's volume and a superficial velocity of 1.5 μm/s. The pipe has an overall heat transfer coefficient of 100 W/(m*^{2}*K). Dashed lines represent the temperature profiles under the well-mixed tank assumption with* h_{tank} *= 100 W/(m*^{2}*K), and the tank is matched in volume and surface area to the corresponding pipes. (b) Total pumping energy required for the* *cell and its recirculation pipes, plotted against varying pipe-to-cell volume ratios, with each line representing a different length-to-diameter ratio of the pipes. The energy increase enabled by electrolyte flow is 67 Wh/m*^{2}.

While a high length-to-diameter ratio is beneficial for thermal regulation due to increased heat transfer surface and reduced mixing, this advantage must be balanced against the system's overall pumping energy requirements. While reduced flow rates decrease pumping losses across the cell, elongated and narrower pipes may cause significant pressure drops, increasing the total pumping energy for both the cell and the pipe. This trade-off is depicted in **Figure V-3b**, examining the total pumping energy per unit cell cross-sectional area for various pipe volumes and length-to-diameter ratios, under the same conditions as **Figure V-3a**. Excessively high length-to-diameter ratios may be counterproductive due to the disproportionate pumping energy required for the pipe. With increasing pipe volume and length-to-diameter ratio, the minimum flow velocity required to keep the cell temperature below the safety threshold decreases. As the cell is kept unchanged, reduced velocity due to increased pipe volume and length-to-diameter ratio leads to lower pressure drops across the cell. For a specific pipe length-to-diameter ratio, enlarging the pipe volume significantly reduces the pipe's pressure drop initially, due to both the decreased required velocity and larger cross-sectional area, followed by a gradual decrease as the required velocity stabilizes. However, as the pipe's length-to-diameter ratio increases, the pressure drop for a given volume also increases, as the longer and narrower pipe's increased pressure drop outweighs the reduction from lower velocity. While the pipe's pressure drop is usually minor compared to the cell's, it becomes considerable at small volumes and high length-to-diameter ratios. Nonetheless, it's important to note that even the highest pumping energy is minimal compared to the overall energy enhancement of 67 Wh/m^2 achieved with electrolyte flow (32 Wh/m^2 without electrolyte flow and 99 Wh/m^2 with flow).

3.3. Practical design considerations

The previous sections discuss the impact of extra electrolyte on the mass and thermal transport benefits of electrolyte flow, as well as the complex interplay between extra electrolyte volume, electrolyte flowrate, and heat dissipation capability from the cell and the extra electrolyte to achieve effective thermal regulation. In this section, we aim to provide some insights into how these factors together play into the performance and cost of a convection battery system. We start by examining the impact of different design consideration on the gravimetric energy density of a convection system. A LIB system design in which the cells make up 85% of the total system weight (i.e., a cell to pack mass ratio of 0.85) excluding components necessary to enable electrolyte flow is selected as the basis of the analysis, which is representative of a system utilizing the emerging cell-to-pack design approach.[152] Compared to a system design using the traditional cell-module-pack design approach that has a cell to pack mass ratio of around 0.6, the balance of plant components in this system take up a smaller fraction, making the addition of components necessary to enable electrolyte flow (e.g., extra electrolyte, extra pump) have a larger impact, such representing a conservative estimation. In this baseline system, the coolant used for the liquid-based external thermal management is assumed to make up 5% of the system weight, and the rest 10% system weight consists of components such as battery management system (BMS), wiring, cooling plates, heat exchanger, and pump for the coolant. The system has a nominal energy density of 165 Wh/kg. Two potential convection battery system designs built upon the baseline system are considered. In the first system, the electrolyte flow only serves to provide mass transport enhancement, and the thermal regulation is achieved using the existing external thermal management components in the system (h_{cell} = 500 W/(m^2*K)). The minimum extra components required in this system to enable electrolyte flow include the extra electrolyte, its container (tubing and an optional storage tank), and an extra electrolyte pump (in addition to the existing coolant pump for the thermal management system). The electrolyte container is assumed to be 20% of the extra electrolyte weight. As discussed in Section 3.1.1, the flowrate needed to achieved mass transport only scales with electrode thickness and is in general ~ μm/s, leading to a required pump that adds negligible mass to the system (As an example, for a 77 kWh system, a pump with power output sufficient to provide 10 μm/s flow is well within 500 g, taking up less than 0.1% of the total system weight.) In the second system, the electrolyte flow is utilized to both enhance mass transport and regulate cell temperature. The coolant in the external thermal management system is eliminated from the baseline system, while other components remain unchanged. The coolant pump is assumed to be compatible with the electrolyte and is repurposed as the electrolyte pump. For this system, the minimum extra components to enable electrolyte are the extra electrolyte and the tubing, and the electrolyte storage tank is assumed to be not present in the system. The tubing is assumed to be made of plastic materials with a wall thickness of 0.3 mm, and has a heat transfer coefficient of 200 W/(m^{2}K) and a length-to-diameter ratio of 5 for a single sandwich layer. As discussed in Section 3.1.2, the flowrate needed for effective thermal management scales with the cell thickness rather than the electrode thickness, and a LIB cell stack such as a prismatic cell typically consists of numerous layers of the sandwich cell considered in the model for this work (**Figure III-1**). Simulating the temperature distribution in such a cell stack requires a more advanced model beyond the scope of this work, which is demonstrated in **Chapter VI**. For the purpose of this study, the velocity is scaled according to the dimensionless group ξ_H from the simulated single sandwich layer to a cell stack. A LIB cell stack consisting of 150 layers of the sandwich cell is assumed, leading to a total cell thickness of around 30 mm. Assuming a well-insulated cell (h_{cell} = 0 W/(m^{2}K)), the flowrate used for the single sandwich cell is scaled by 150 following ξ_H. To calculate the pumping loss in the pipe for this cell stack, the pipe is assumed to be scaled in length by 150 while the diameter remains unchanged, leading to the same $V_{\text{extra electrolyte}}/V_{\text{cell}}$ for the sandwich layer and the cell stack.

The actual gravimetric energy density for both system designs undergoing a 5C discharge is calculated using Eq. (V-6) assuming a pump efficiency of 50%. The results are shown in **Figure V-4**. For the system that only leverages the mass transport benefit of electrolyte flow, the total pumping energy is almost negligible for the ~μm/s, and the variation in energy density is mainly a result from the percentage of accessed capacity enhancement, as illustrated in **Figure V-1a**, and the added weight by the extra electrolyte. As **Figure V-4a** demonstrates, the system has the highest energy density at sufficient flowrate ($\xi_M < 1$) and with small extra electrolyte volume. This corresponds to the findings in Section 3.1.1 that extra electrolyte volume impact is minimal beyond a flowrate threshold but merely adds weight to the system. However, there is a practical limit to the minimum amount of extra electrolyte (e.g., it needs to complete the recirculation loop). As such, a system that only utilizes electrolyte flow for its mass transport benefits should focus on the design of an electrolyte manifold that minimizes extra electrolyte volume. For the system that uses electrolyte flow as thermal management in addition to mass transport enhancement, there exists an optimal intermediate extra electrolyte volume that yields the highest energy density as demonstrated in **Figure V-4b**. Note that due to the elimination of coolant in this system, the maximum achievable energy density is slightly larger than that of the system in **Figure V-4a**. An extra electrolyte volume smaller than the optimum will lead to insufficient thermal regulation, as discussed in Section 3.1.2, and potentially significant pumping loss in the pipe as discussed in Section 3.2. On the other hand, an extra electrolyte volume larger than the optimum adds significant weight to the system, negatively impacting the system energy density despite its superior thermal regulation capability. Note that the value for the optimal $V_{\text{extra electrolyte}}/V_{\text{cell}}$ depends on the heat dissipation capability of the cell and the pipe, as well as the cell operating condition, and should be optimized based on the application of the system.

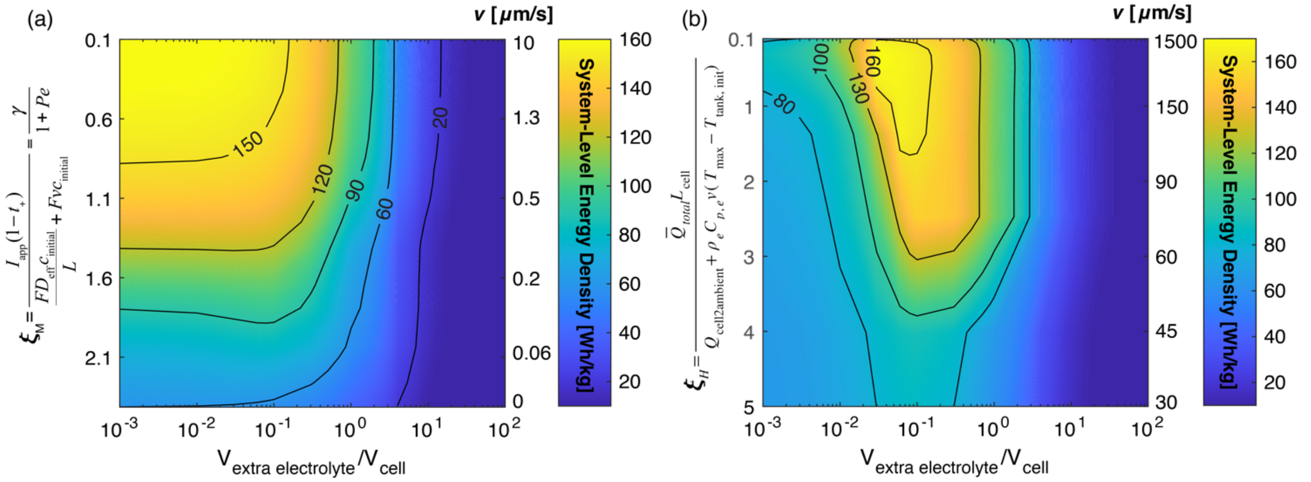

Figure V-4: *(a) Impact of extra electrolyte volume on the gravimetric energy density for a system designed to (a) solely utilize the mass transport benefit of electrolyte convection and (b) leverage both mass and thermal transport benefits of electrolyte flow. Note that the energy density value is based on the assumed system design in this work, and there are opportunities for improvement through system optimization.*

In addition to optimizing performance metrics such as energy density, development of a practical system relies on striking a balance between the benefits conferred and the associated additional cost. To effectively assess such costs, we employ a simplistic scheme wherein we price pump energy using electricity costs and convert them to an equivalent capital cost by discounting lifetime costs to the present. This assumes that the pump will draw power directly from the cell and therefore operates according to practical charging costs. These costs can then be directly compared to the capital cost associated with the extra electrolyte. We convert between costs on areal and energetic bases utilizing equivalent loadings and nominal capacities utilized in the above simulations, as is commonplace in the electrochemical storage literature. It is important to note that the capital cost of purchasing a pump was not included in these calculations, as the cost could vary widely depending on system scale, associated pump power, and required pump head.

Furthermore, it may be possible to utilize the existing pump infrastructure in the thermal management system, which would render this cost unnecessary.

As expected, such an analysis results in somewhat independent cost scaling–the pump cost remains unaffected by the extra electrolyte volume, and the extra electrolyte volume remains independent of the velocity and lifetime. Additionally, while the added electrolyte costs scale linearly with amount, pump costs have a more complicated cost scaling with both velocity and lifespan due to the square dependence in the pressure drop and discounting factors applied over the lifetime. Combining these plots in **Figure V-5** enables a proper comparison of the tradeoffs necessary for consideration in designing practical systems over lifetimes relevant to such systems. As such, we also extend velocities to more realistic values as highlighted in the discussion above.

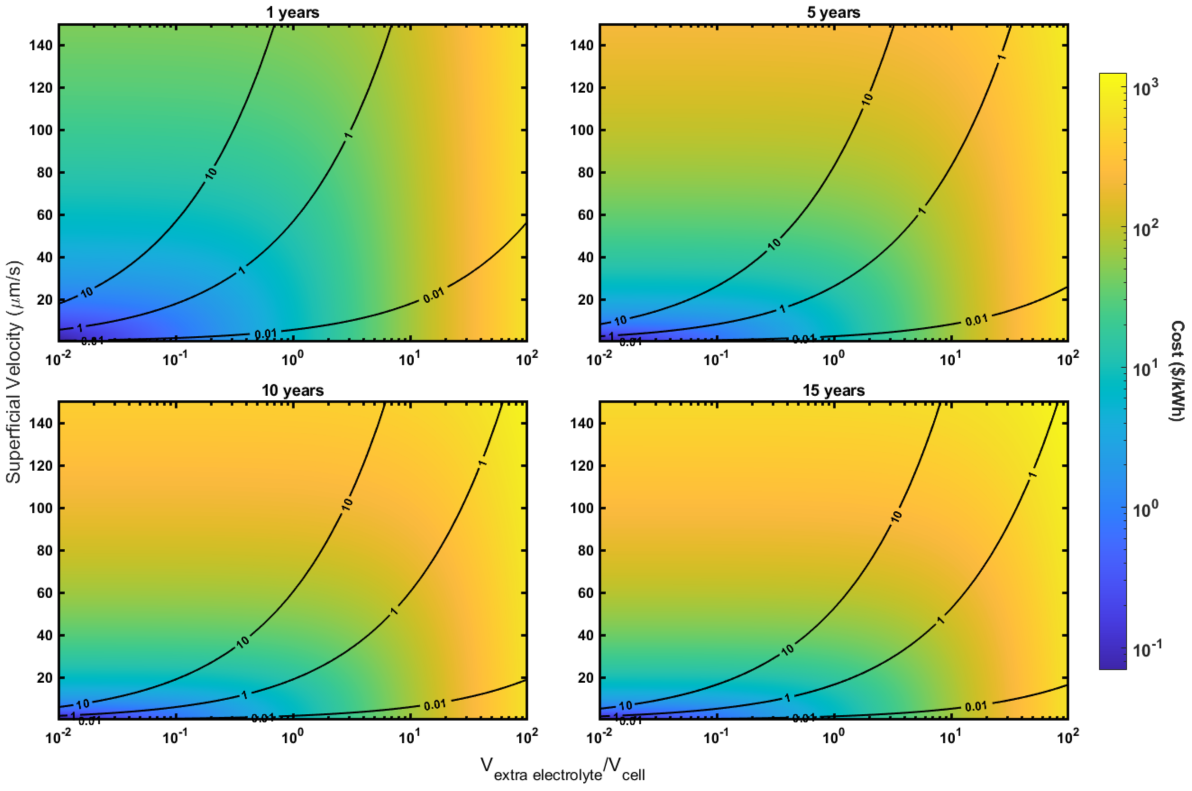

Figure V-5: *Total added cost of systems with electrolyte recirculation over a given lifetime. The pump is assumed to operate continuously over the associated lifespan at 50% efficiency. Solid lines represent the relative pump to added electrolyte costs of a given operating condition.*

To validate this analysis, we first note that when the velocity is zero, the cost of the added electrolyte is approximately $7/kWh, which aligns with values reported in the literature.[76,161] Examining the plot, we see that when the amount of extra electrolyte is greater than 10, the relative cost is high, such that even at high electrolyte velocities, the pump cost is minimal. As the amount of added electrolyte decreases, the pump cost is of greater significance, especially at high velocities and long system lifetimes. Still, we highlight that these costs are total lifetime costs. It is likely that in practical systems requiring system design decisions, such costs would be considered on an annualized basis, whereby increasing system lifetimes would actually reduce costs by spreading out the capital cost of the electrolyte over a longer period and by enabling discounting of future pump operating costs. For this reason, we also caution that the costs in the plot above should not necessarily be compared to current lithium-ion battery costs that are on the order of $100/kWh,[162] as operating costs of the thermal management system are typically not included in such values.

We highlight that this cost evaluation assumes that the pump is continuously operating, and that practical embodiments for many applications would not necessitate this. If this limitation were alleviated, the relative pumping cost would be substantially reduced. Further, we emphasize that this analysis only considers costs, as the benefits afforded by increased capacity under the extreme operating conditions would be application specific, and could manifest as premiums paid for electric vehicles or as extra electricity stored in grid-scale systems. Moreover, such benefits could include increased adoption rates of storage technologies, or the unlocking of applications in new areas, which would require detailed market analysis for potential market capture, all of which extend beyond the scope of this paper. We simply present this practical analysis as a means to assess and understand the design space for this technology, rather than for making actual decisions.

4. Conclusions

Previous studies show that a convection battery can improve cell performance through enhanced mass and thermal enhancement, but the requirements for the extra electrolyte to achieve such benefits have not been investigated. This work aims to fill this gap by examining the impact of extra electrolyte volume and design on the cell performance enhancement. Through simulating a single sandwich cell layer, it is demonstrated that to achieve the mass transport benefits, the extra electrolyte volume plays a minimum role beyond a flowrate threshold ($\xi_M < 1$), while if the electrolyte flow is also used for thermal regulation, tradeoffs exist between the required flowrate to effectively control the cell temperature, the extra electrolyte volume, and the incorporation of external thermal management. While utilizing thin and long piping for the extra electrolyte aids thermal regulation by enlarging heat transfer area and reducing mixing, pumping loss can become significant in pipes with a large length-to-diameter ratio and a small total volume. Finally, we synthesized the findings of this study by conducting practical analyses on the system energy density and the incremental costs associated with additional electrolyte and pumping. Note that the analyses are limited by the single sandwich layer cell model used in this study. Specifically, the temperature distribution is assumed to be uniform within the cell, and the thermal regulation will be effective with sufficient external cooling or internal cooling with a flowrate that satisfies $\xi_{\mathrm{H}} < 1$. This assumption is likely not applicable in a larger cell stack that has a non-uniform temperature distribution, resulting in a shorter run time due to the maximum temperature reaching the safety cutoff temperature despite sufficient external or internal cooling. Nevertheless, this work lays the groundwork and offers initial insights for exploration in convection battery system design. Building on this work, a comprehensive system design study utilizing an advanced model that considers the temperature distribution within a large cell stack is presented in **Chapter VI**.

5. *List of Symbols*

Symbol	**Description**
a	Particle surface area to volume
A_{cell}	Cell cross-sectional area
A_{pipe}	Pipe cross-sectional area
$Accessed\%$	Percentage of the theoretical capacity accessed
$brugg$	Bruggeman's coefficient
C_p	Heat capacity
$C_{p,e}$	Electrolyte heat capacity
c_{initial}	Initial electrolyte concentration
$c_{\mathrm{pipe}}(x,t)$	Electrolyte concentration in the pipe
$c_s^{\max}$	Maximum solid-phase concentration
D_e	Electrolyte diffusivity
D_{eff}	Effective electrolyte diffusivity
D_i^s	Solid-phase diffusivity
D_p	Active material particle diameter
d_{pipe}	Pipe diameter
$E_a^{D_i^s}$	Solid-phase diffusion temperature dependent activation energy

$E_a^{k_i}$	Reaction rate constant temperature dependent activation energy
E_{pump}	Total pumping energy
E_{system}	System gravimetric energy density
F	Faraday constant
h_{cell}	Cell convective heat transfer coefficient
h_{tank}	Tank convective heat transfer coefficient
h_{pipe}	Pipe convective heat transfer coefficient
I_{app}	Applied current density
k_i	Reaction rate constant
L	Thickness
L_{cell}	Total cell thickness
L_{pipe}	Pipe total length
m_{system}	Total system mass
ΔP_{cell}	Cell pressure drop
ΔP_{pipe}	Pipe pressure drop
Q	Electrolyte volumetric flowrate
Q_A^{max}	Theoretical areal capacity
R	Gas constant
R_p	Particle radius
S_{pipe}	Pipe total lateral surface area
T_{ambient}	Ambient temperature
$T_{\mathrm{pipe}}(x,t)$	Electrolyte temperature in the pipe
t_{d}	Duration of discharge
t_+	Li^+ transference number
$\bar{V}$	Average running voltage
V_{cell}	Cell total volume
$V_{\mathrm{extra\ electrolyte}}$	Extra electrolyte total volume
V_{pipe}	Pipe total volume
v	Superficial velocity in the cell
v_{pipe}	Superficial velocity in the pipe
ε	Porosity
$\varepsilon_{\mathrm{filler}}$	Filler fraction
η_{pump}	Pump efficiency
$\Theta_{100\%}$	Stoichiometry at 100% SoC
$\Theta_{0\%}$	Stoichiometry at 0% SoC
λ	Thermal conductivity
λ_e	Electrolyte thermal conductivity
μ	Electrolyte viscosity
ρ	Density
ρ_e	Electrolyte density
σ	Solid-phase conductivity
Φ_s	Active material particle sphericity

6. *Appendix: Tank concentration evolution*

Figure V-6 illustrates the change in concentration within the tank under the conditions for **Figure V-1b**. Adding a substantial amount of extra electrolyte can buffer against the depletion effects, resulting in a higher concentration of electrolyte entering the cell. Initially, increasing the flow of electrolyte causes a faster depletion within the tank due to a quicker material exchange with the electrolyte leaving the lithium-depleting electrode. However, as the flow rate increases, this depletion rate slows down because the concentration at the lithium-depleting electrode rises.

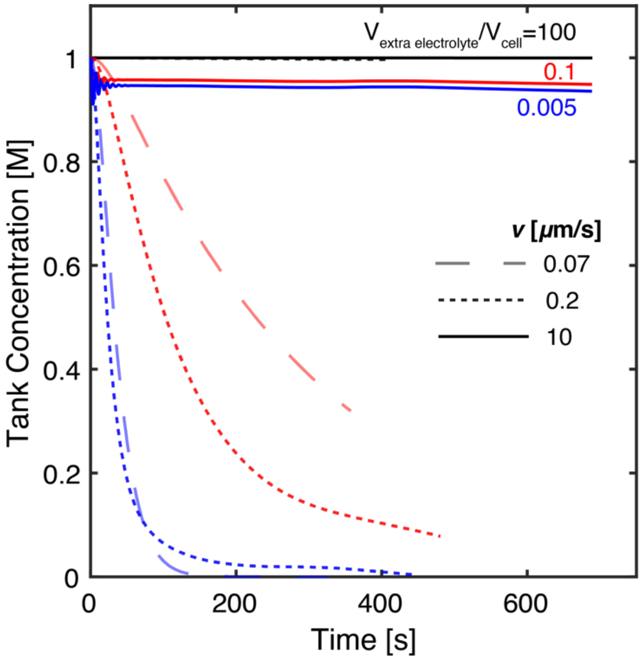

Figure V-6: *Concentration change within the tank under the conditions for* ***Figure V-1b****.*

VI. System Design and Potential Applications

1. Introduction

The previous chapters investigated the benefits of incorporating electrolyte convection into the LIB as well as the requirements of extra electrolyte in the system. In this final chapter, I aim to provide some insights into the prospective system designs and potential applications. While a full system optimization is beyond the scope of this thesis, the work serves as a starting point for future system design and applications, and points to future research directions needed for system optimization.

Currently there are two typical design approaches in scaling LIB cells into a battery pack for applications such as EVs. The traditional approach, known as the "Cell-Module-Pack", assembles a collection LIB cell into a battery module, and several modules are interconnected to form a battery pack. While the specific design varies, battery pack designed following this approach typically has a cell to pack gravimetric ratio of around 0.6, and a cell to pack volumetric ratio of around 0.4.[152] An emerging pack design trend is to skip the individual modules, directly integrating the cells into a battery pack, i.e., the "Cell-Pack" (CTP) approach. Compared to the traditional Cell-Module-Pack approach, the CTP approach leads to increased energy density due to reduced balance of plant components, leading to a cell to pack gravimetric ratio >0.8, and a cell to pack volumetric ratio of around 0.7.[152] Additionally, the cells in CTP designs are typically larger, leading to reduced manufacturing and integration cost. Some examples BYD's blade battery,[34] CATL's Qilin battery,[35] and Tesla's 4680 battery.[36]

CTP is likely to be the preferred approach to scale a single convection battery cell to a battery pack, as the internal thermal management offers the advantage of reduced thermal gradient inside larger cells, and the reduced cell number leads to simpler electrolyte manifold design. Among various possibilities, a preliminary conceptual design of a convection battery system using the CTP approach is presented, as discussed in Section 2. This design aims to minimally disrupt the current LIB architecture, particularly the Qilin Battery pack configuration.[163] To assess the cell performance within this framework, a COMSOL-based model that couples a 1D electrochemical model and a 2D heat transfer model was developed to simulate the electrochemical performance as well as temperature distribution of the prismatic cell. Furthermore, to quantify performance metrics such as system energy density and to facilitate comparisons with existing LIB systems, a system design model was formulated in line with the methodology employed by the BatPaC model, which is based on the cell-module-pack design,[164] incorporating assumptions derived from literature and online data on the cell-pack design. Two potential use cases of the convection battery system were subsequently investigated: fast charging and stationary energy storage.

2. A Conceptual Convection Battery System Design

A system design based on CATL's Qilin battery pack[163] is selected as the baseline system in this study, as shown in **Figure VI-1a**. This system consists of water/glycol-filled cooling plates located between arrays of prismatic cells. The cooling plates provide the dual function of thermal management structural support in the battery pack. A heat exchanger and a pump are included in the system to ensure the coolant reaches the desired temperature. A coolant reservoir can be optionally incorporated in the system to store the excessive coolant as the battery expands. The system also includes extra components not shown in the figure, such as the battery management system (BMS). **Figure VI-1b** shows a conceptual convection battery system design that aims to cause minimum disruption to the baseline system. In this design, each cell has an individual recirculation loop to ensure the electrolyte is maintained within its stability voltage window. The extra-electrolyte-filled circular tubing is embedded inside the cooling plate, with a diameter same as the cooling plate thickness. The system incorporates the same type of pump and heat exchanger as in the baseline system, although the weight and volume of these components could vary depending on specifications such as cooling capacity and pumping power requirements.

While the convection battery system largely resembles the baseline system, some differences exist. First, components such as the current collector need to be modified to permit flow, and the electrode design might need to be altered to balance performance and pumping requirements. Certain components need to be added to the cell, such as inlet/outlet connectors for the tubing, and a flow distributor might also be necessary to ensure uniform flow distribution. The tubing itself also adds extra weight to the system, although the contribution might not be significant as the tubing is likely to be made of plastic materials. There are also opportunities to eliminate certain components in the baseline system. For example, if the electrolyte flow can provide sufficient thermal management, the coolant can be eliminated, and the cooling plates might be replaced by cheaper or lighter components as they do not need to function as thermal management components.

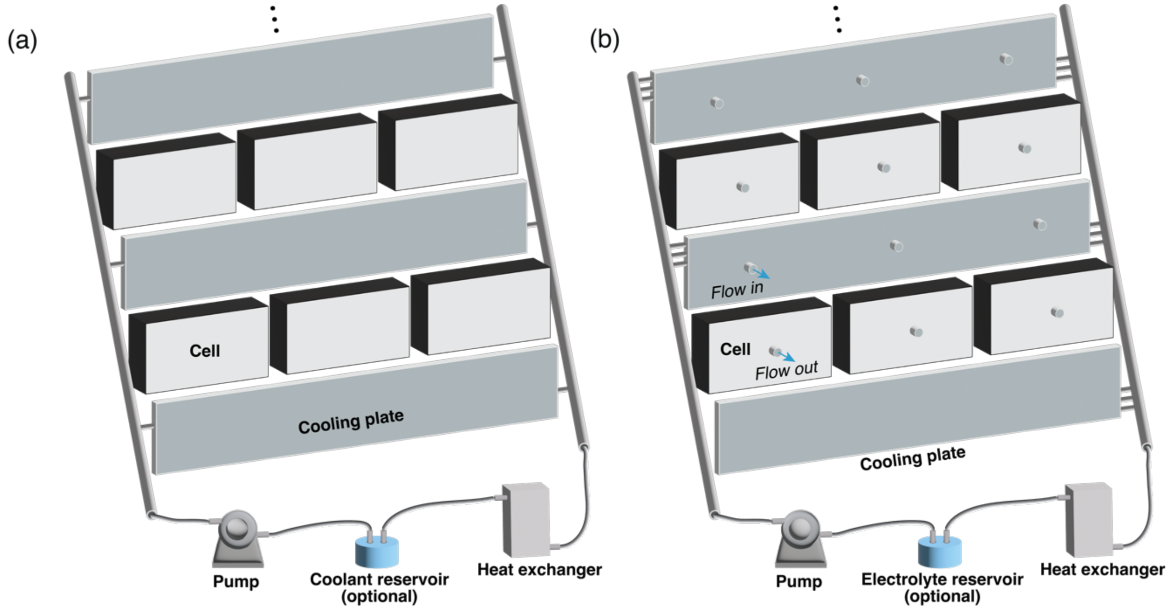

Figure VI-1: *(a) A baseline system design (no flow) based on CATL's Qilin battery pack. (b) A conceptual convection battery system design that aims to cause minimum disruption to the baseline system.*

3. Model Development

3.1. Thermal-electrochemical model

To predict the prismatic cell performance, a coupled thermal-electrochemical model is developed using COMSOL 6.1, as illustrated in **Figure VI-2**, which includes a 1D electrochemical sandwich layer model and a 2D heat transfer model. The 1D electrochemical sandwich layer model is the same as the ones used in prior chapters, and it is used to predict both the electrochemical performance of the cell and the heat generation rate within the sandwich layer as a function of position. The average heat generation is calculated and fed into the 2D heat transfer cell model, which is used to predict the temperature distribution inside the prismatic cell. The geometry of the 2D model represents the side profile of the prismatic cell, with cooling plates located at both left and right sides of the domain. The temperature distribution in the direction perpendicular to the 2D geometry is assumed to be constant, which is a reasonable assumption when the domain surface is insulated, and heat transfer only occurs through the boundaries. Both temperatures of the coolant entering the cooling plates and the electrolyte entering the cell are assumed to be at T_{inlet}, which implies that the heat exchanger in the system can provide sufficient cooling capacity. The coolant is also assumed to remain at constant temperature inside the cooling plate, which represents the best-case scenario of the external cooling, as in reality, the coolant temperature will increase as it goes through the cooling plate. The average temperature within the 2D model domain is calculated as serves as the operating temperature for the 1D electrochemical model. This treatment likely leads to an overestimation of the temperature gradient inside the cell, as in reality, the sandwich layers at colder places inside the cell will result in larger heat generation due to more sluggish kinetics and transport properties, thereby reducing the temperature gradient. As such, the temperature gradients predicted in this work represent the worst-case scenario.

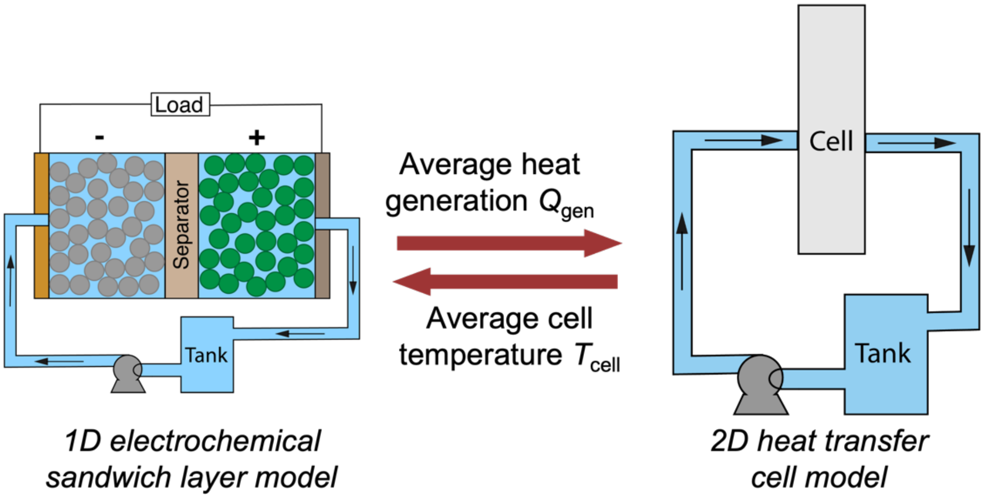

Figure VI-2: *Schematic of the thermal-electrochemical model.*

3.2. System design model

To assess the system-level performance such as energy and power densities, a system design model was developed, incorporating assumptions derived from BatPaC 5.1 package, literature, and online data on the Qilin Battery design. This model takes information such as runtime, energy and power output, and heat generation rate from the thermal-electrochemical model in Section 3.1 as inputs. The pumping power and energy calculations follow the same approach used in Section 2 of **Chapter V,** with the pressure drops through the electrolyte tubing and the cell estimated with Hagen-Poiseuille equation and Kozeny-Carman equation, respectively. For the enclosed cell in the baseline system, the cell casing is assumed to be aluminum, and the cell-level additional components beyond the casing, such as the terminal, spacer, and gasket, are assumed to take up 6% of the total cell mass. Unless otherwise specified, the convection battery cell adopts the same design as the cell in the baseline system, and the additional components necessary to enable electrolyte flow, such as the inlet/outlet connectors and flow distributor are assumed to take up 3% of the total cell mass. The cooling plates in both systems are assumed to be made of aluminum alloy, with the plate thickness 10% of the prismatic cell thickness, and a wall thickness of 0.5 mm. In the baseline system, the coolant is assumed to fill the entire cooling plate. In the convection battery system, the extra electrolyte tubing embedded in the cooling plate is assumed to be made of plastic and have the same diameter as the cooling plate thickness. Unless otherwise specified, the cooling system in both systems consisting of a heat exchanger, a pump, and valving is assumed to add 7 kg in mass and 2.8 L in volume to the system. The same type of pump with a pumping efficiency of 50% is assumed in both systems. The optional reservoir for coolant or the extra electrolyte is not included in this model. The additional components in the system, such as the BMS and wiring, are assumed to scale with the cell number, and adds 0.6 g per 1 Ah of cell capacity for each cell. For both systems, the total volume consists of the volumes of the cells, the cooling plates, and the cooling system. An additional 30% of the total cell volume is added to account for the additional system components.

4. Potential Application Demonstrations

Figure VI-3 shows a Ragone plot comparing system-level specific energy and power of a convection battery system and a typical LIB system (no flow). While the exact values might change based on different system designs, in general, the convection battery will provide higher specific power by eliminating electrolyte mass transport limitations. However, even with the potential to eliminate certain components such as the coolant and cooling plates, it is unlikely that the system will lead to significant system specific energy improvement for applications with low power requirement, as the current LIB system adopting CTP design already has a high cell-to-pack mass ratio 0.8-0.9. The system specific energy is ultimately constrained by the theoretical specific energy of the battery chemistries, which is typically 200-300 Wh/kg for Li-ion chemistries. This suggests that the convection battery system employing Li-ion chemistries is not suitable for applications with energy density requirements beyond Li-ion material limits, such as all-electric long-haul trucking[165] and all-electric commercial aircraft[27]. The most suitable applications for the convection battery system might be ones with energy density requirements within the Li-ion chemistry limits but will benefit from increased rate capability. Examples include EV fast charging, eVTOLs during takeoff and landing,[28,166] and hybrid vehicles.[167] Additionally, there are certain applications with requirements beyond specific power and energy, such as stationary energy storage applications, to which cost is the key consideration. The following sections examine how convection battery system can potentially provide value to two applications: fast charging and stationary energy storage.

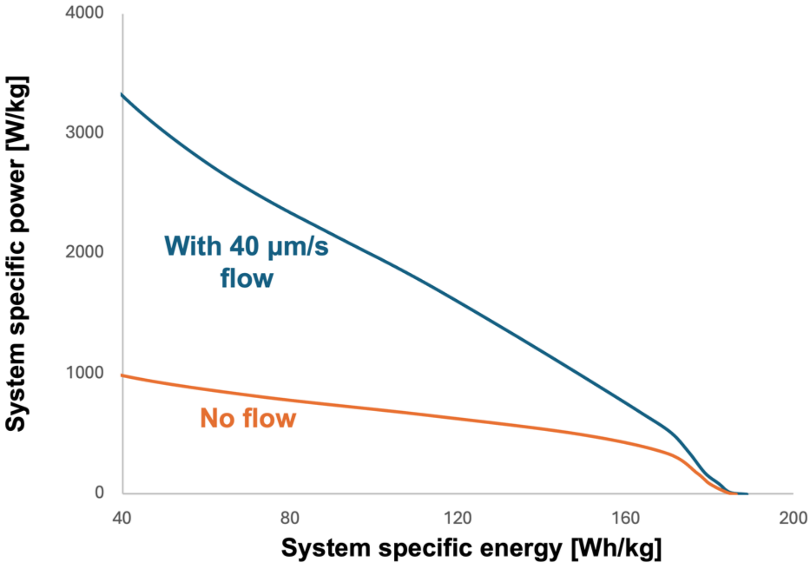

Figure VI-3: *A sample Ragone plot comparing the convection battery system and a typical LIB system (no flow).*

4.1. Fast charging

Fast charging is crucial to alleviating range anxiety and facilitates wider adoption of EVs. U.S. Advanced Battery Consortium sets goals of 80% charge in <15 mins.[26] Significant progress has been made by EV makers, with the best charging performance to 75% around 20 mins.[168] However, such improvement is typically accompanied with tradeoffs, such as through the use of thin electrodes, which scarifies energy density and increases cost. Additionally, fast charging under extreme conditions, such as cold weather in which transport properties are sluggish, presents significant challenge.[24] It is also critical to properly manage the large amount of heat generation accompanied by high rates to ensure safe operation, and the temperature variation should be minimized to prolong battery life. This section discusses the benefits and tradeoffs of using the convection battery for fast charging.

A typical LIB system (no flow) with the design shown in **Figure VI-1a** is selected as the baseline system. The cell utilizes NMC622/graphite chemistry with an N/P ratio of 1.1, and the electrolyte is $LiPF_6$ in a 1:1 EC:DMC mixture. The properties of the sandwich layer are summarized in **Table VI-1**. The prismatic cells have dimensions of 30 mm (thickness) x 200 mm (width) x 120 mm (height). The system consists of 216 cells in total, arranged by 6 cells per row and 36 rows in total. The cells are interconnected in a 108s2p configuration (108 cells in series and 2 series strings in parallel), resulting in the system with a nominal voltage of 396 V and a nominal capacity of 221 Ah. With a total nominal energy density of 87.5 kWh, the system has a gravimetric energy density of 182.4 Wh/kg (0.89 cell-to-system mass ratio), and a volumetric energy density of 396.8 Wh/L (0.71 cell-to-system volumetric ratio).

Table VI-1: *Simulation parameters used in this section.*

	Units	Positive CC	Positive Electrode	Separator	Negative Electrode	Negative CC
	-	Al	$LiNi_{0.6}Mn_{0.2}Co_{0.2}O_2$	-	$Li_\theta C_6$	Cu
$brugg$	-	-	2.5	2.5	2.5	-
C_p	J/kg/K	884	905	1617	966	387
$C_{p,e}$	1635 J/kg/K					
c_{initial}	mol/m^3	-	1000	1000	1000	-
$c_s^{\max}$	mol/m^3	-	47664	-	30555	-
D_i^s	m^2/s	-	5×10^{-14}	-	2×10^{-14}	-
$E_a^{D_i^s}$	J/mol	-	5000	-	5000	-
$E_a^{k_i}$	J/mol	-	5000	-	5000	-
F	96485 C/mol	-	-	-	-	-
k_i	m$^{2.5}$/(mol$^{0.5}$s)	-	1×10^{-11}	-	2×10^{-11}	-
L	m	1×10^{-5}	6.7×10^{-5}	2.5×10^{-5}	8×10^{-5}	1×10^{-5}
R	8.314 J/mol/K	-	-	-	-	-
R_p	m	-	5×10^{-6}	-	5×10^{-6}	-
ε	-	-	0.4	0.4	0.4	-
$\varepsilon_{\mathrm{filler}}$	-	-	0.0872	-	0.0326	-
$\Theta_{100\%}$	-	-	0.258	-	0.9	-
$\Theta_{0\%}$	-	-	0.917	-	0.127	-
λ	W/m/K	238	0.66	0.312	1.195	398
μ	5×10^{-3} Pa•s					
ρ	kg/m^3	2702	3060	1036	1832	8933
ρ_e	1240 kg/m^3					
σ	S/m	3.55×10^7	10	-	100	5.96×10^7

In this study, the constant current-constant voltage (CC-CV) charging protocol with a cutoff voltage of 4.2V is used. **Figure VI-4a** compares the charging time without electrolyte flow and with a 10 µm/s flow under isothermal conditions at 298.15K, which represents the charging performance achievable of a single cell without the complication of thermal transport limitations (e.g., under lab testing conditions). The charging rate during the CC period is varied, and the figure shows the total time that charges the cell from 10% to 80% capacity. As **Figure VI-4b** shows, a 10 µm/s flow significantly reduces charging times as a result of reduced overpotentials from overcoming mass transport limitations, as explained in **Chapter II**. The flowrate required to enhance mass transport only scales with the electrode thickness regardless of the cell dimension, leading to a total pumping power of 1.8 W to achieve 10 µm/s flow for the entire system. This leads to minimal pumping energy, and the pump required to provide the pumping power likely adds negligible weight to the entire system.

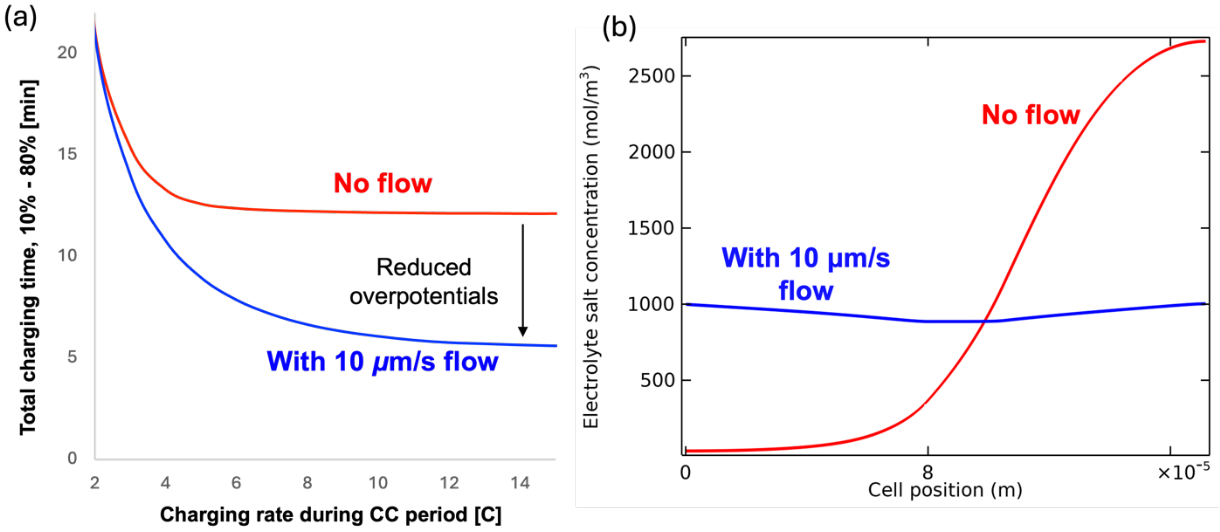

Figure VI-4: *(a) Total charging time under isothermal conditions (298.15 K) of the cell without flow and with 10 µm/s flow. CC-CV charging protocol with 4.2V cutoff voltage is used. Note that the charging time values will vary depending cell design and ambient temperature, but the overall trends still hold. (b) The electrolyte flow reduces charging speed by enabling a more uniform electrolyte concentration.*

In addition to the reduction in charging time, the enhanced mass transport by electrolyte flow potentially helps alleviate certain degradation mechanisms as well. The higher and more uniform electrolyte concentration in the anode leads to a smaller magnitude of lithium plating potential at the anode-separator interface (**Figure VI-5a**), suggesting reduced lithium plating, and the more uniform intercalation fraction within the electrode (**Figure VI-5b**) might reduce electrode cracking caused by mechanical stress. However, it should be noted that the electrolyte flow could potentially introduce new degradation pathways, which needs to be investigated experimentally in future work.

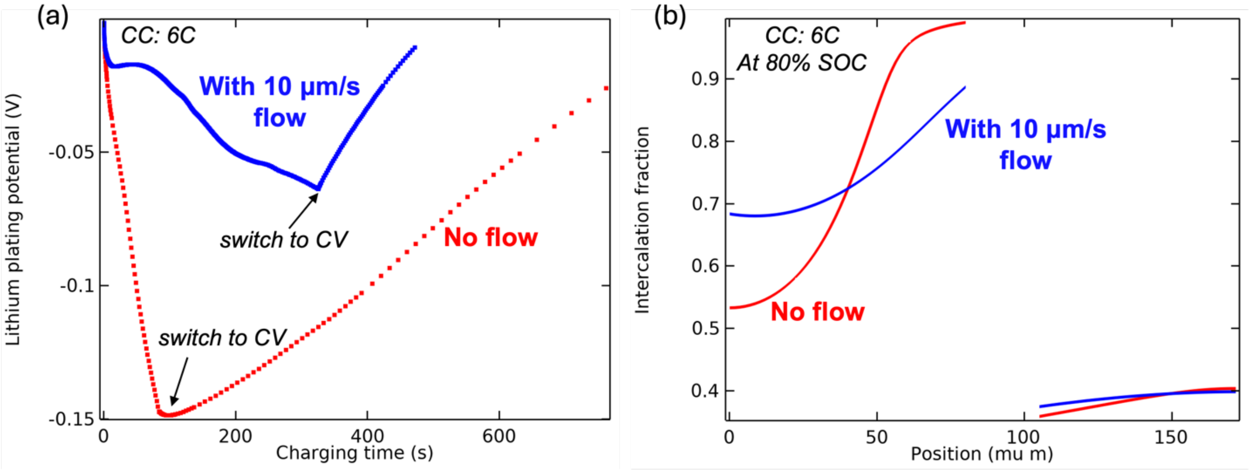

Figure VI-5: *The enhanced mass transport through 10 μm/s flow leads to (a) reduced lithium plating potential and (b) more uniform intercalation within the electrode.*

The isothermal charging speed can be considered as the best charging speed that can be achieved of a given sandwich cell design. In practice, the charging speed likely needs to be slowed due to thermal transport limitation within a larger cell stack. As shown in **Figure VI-6a**, for the 30 mm-thick cell considered in this work undergoing CC-CV charging with 6C during the CC period, the cell center will reach the safety cutoff temperature (325 K) despite high external cooling capacity (h_{cell} = 500 W/(m^{2}K), T_{coolant} = 288.15 K) applied at both sides. This is due to the small thermal conductivity of the cell, especially in the through-layer direction, leading to a large *Biot* number and a subsequently large temperature gradient within the cell. As shown in **Figure VI-6b**, the rate during the CC period needs to be slowed to 3.8 C to ensure the cell center does not reach the safety cutoff temperature during charging, and may need to be slowed even further to if a smaller temperature variation is desired for prolonged life.

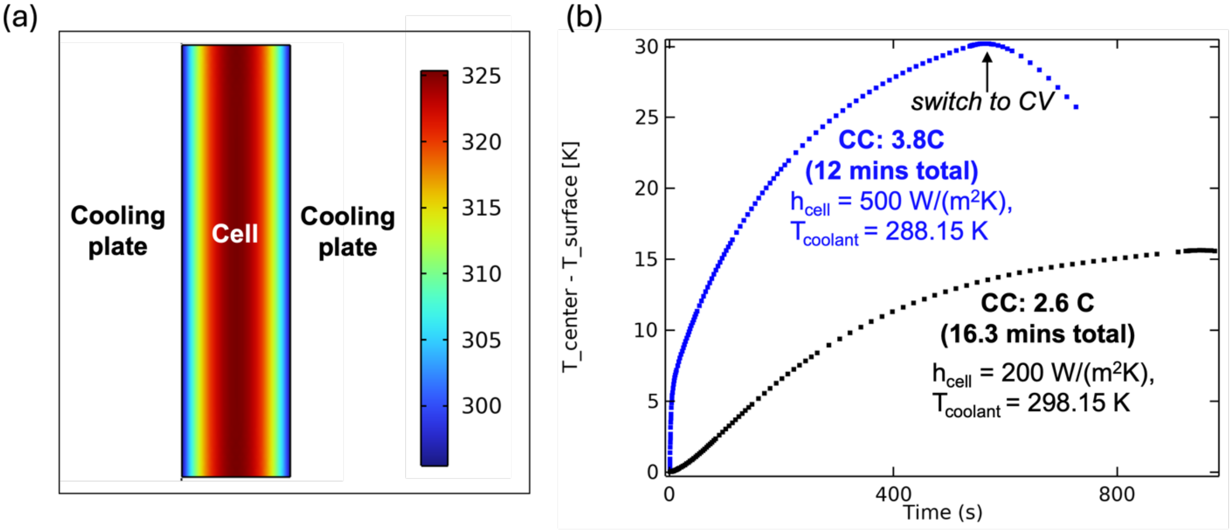

Figure VI-6: *(a) Temperature distribution at 142s within the cell undergoing CC (6C) – CV (4.2V) charge with external cooling (h_{cell} = 500 W/(m^2K), $T_{coolant}$ = 288.15 K). The cell is forced to stop due to the center reaching the safety cutoff temperature. (b) The maximum CC charging rates with external cooling to ensure the cell does not reach the safety cutoff temperature (blue), and the maximum temperature difference within the cell does no exceed 15K (black). Note that the coolant conditions are different, as the first case aims to maximize heat dissipation while the second case aims to minimize temperature difference.*

As discussed in **Chapter IV** Section 3, the external cooling approach is limited, especially with large dimension and high heat generation rate, due to a lack of control over the internal of the cell. In contrary, the internal cooling approach offers direct control over the cell temperature distribution, which is especially helpful in mitigating the thermal management challenge during fast charging, as shown in **Figure VI-7** for a CC (6C)-CV (4.2V) 10%-80% SoC charging session. The effectiveness of electrolyte flow in facilitating fast charging improves with flowrate, which in turn influences the system design. A flow of 5 µm/s, adequate to mitigate mass transport limitations, enhances cell temperature regulation, allowing the cell to achieve a higher capacity. This improvement primarily results from a lower rate of heat generation due to decreased overpotentials (**Table VI-2**). Given that the increase in heat dissipation from this modest flow rate is minimal, the need for external cooling capacity remains essential, leading to a reduced energy density (**Table VI-2**). When a higher flowrate of 140 µm/s is used, the entire charging session can be completed owing to effective thermal management, and external management system components such as the coolant are no longer needed in the system design. Further increase in the flowrate can more effectively reduce the cell temperature variation, which is desirable for reduced degradation within the cell.[122,169]

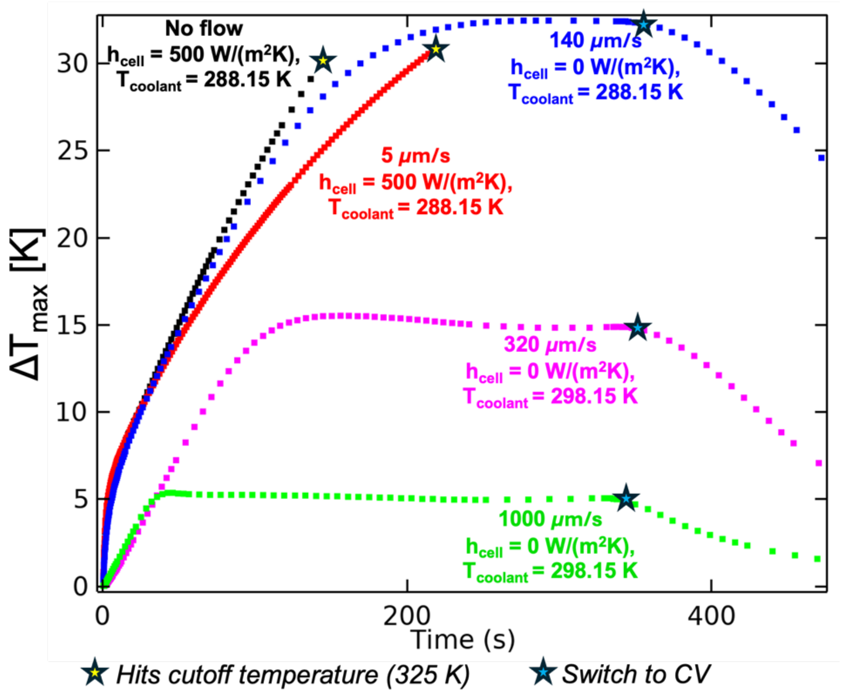

Figure VI-7: *Increasing electrolyte flowrate provides increasing thermal management benefits during fast charging. CC (6C) – CV (4.2V) is used, and the cell is charged from 10% to 80% capacity.*

While a high electrolyte flowrate can reduce charging time by effectively regulating cell temperature with minimum temperature variation—a feat difficult with current external thermal management systems—it comes with tradeoffs, such as increased pump energy requirements and pressure drops, as summarized in **Table VI-2**. Note that liquid-based external thermal management also requires pumping through the cooling plate, but the pumping loss is typically trivial compared to the pumping power associated with the internal thermal management. Since mass of the pump is proportional to its pumping power, a high flowrate might necessitate a heavier pump, reducing the system energy density. Alternatively, the pump could become so cumbersome that it is more practical to station it at the charging site, necessitating substantial upgrades to the charging infrastructure. Finally, an increased flowrate also elevates the potential for flow-induced degradation, suggesting a practical upper limit to flowrate that ensures a viable cell lifespan. This threshold warrants future experimental investigation.

Table VI-2: *The charging times and associated design and operating metrics at varying flowrates for a CC (6C) – CV (4.2V) 10%-80% charging session. For reference, the charging power of the system at 6C is 500 kW. * Includes an extra pump (0.5kg / 0.5L) for the electrolyte; ** Same pump as in the "no flow" system;*** A larger pump is used (adds 5kg / 2L); ****Assumes the heavy-duty pump is provided at the charging station.*

	No flow	**5 µm/s**	**140 µm/s**	**320 µm/s**	**1000 µm/s**
Charging time $T_{max} < T_{cutoff}$ *[mins] /* $\Delta T_{max} < 15K$ *[mins]*	12 / 16.3	9.2 / 14	7.9 / 12	6.1 / 7.8	5.6 / 5.6
External cooling needed	Yes	Yes	No	No	No
ΔP_{cell} *[bar]*	0	0.08	2.1	4.9	15
Total Pumping power [kW]	0	5e-4	0.36	1.9	18
6C Average heat generation [kW]	73	55	53	53	54
Nominal energy density Gravimetric [Wh/kg] / Volumetic [Wh/L]	182.4 / 396.8	175.5 / 395.9*	182.1 / 396.8**	180.2 / 393.2***	182.1 / 396.8****

To mitigate the adverse impacts of high flow, alternative cell and system design strategies should be explored. One example is to consider redesigning the electrode to make it more porous and thicker. As the pumping loss is closely related to the electrode porosity, as shown in **Figure VI-8a**, an increase in electrode porosity will lead to reduced pressure drop and pumping loss. While a more porous electrode will lead to reduced energy density, this can be mitigated by increasing the electrode thickness. Note that this electrode design is uniquely desirable to the convection battery system, as increasing electrode thickness leads to greater electrolyte mass transport resistance, resulting in a significant increase in total charging time when electrolyte flow is not present, as shown in **Figure VI-8b**. In contrary, in the presence of sufficient electrolyte flow to eliminate the mass transport limitation, this alternative design only slightly increases the total charging time a slightly larger ohmic resistance.

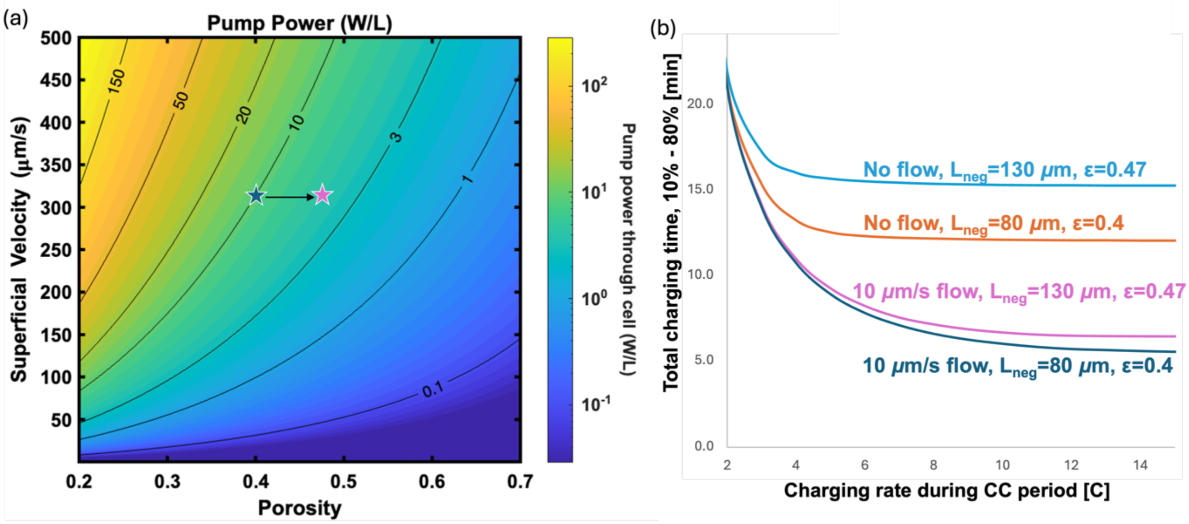

Figure VI-8: *(a) Pumping power as a function of porosity calculated using the Kozeny-Carman equation. (b) The comparison of isothermal charging times of the two electrode designs without flow and with a 10 μm/s to eliminate mass transport limitations.*

Table VI-3 compares the charging performance and system metrics of the baseline electrode design (80 μm thick anode with 0.4 porosity) and an alternative electrode design (130 μm thick anode with 0.47 porosity) for the CC (6C) – CV (4.2V) 10%-80% charging session. An electrolyte flowrate of 320 μm/s flow is used in both cases. The alternative electrode design leads to a slight increase in charging time and reduced energy densities, but the pressure drop through the cell and the total pumping power are significantly reduced.

Table VI-3: *The charging performance and metrics of systems with two different electrode designs. The electrolyte flowrate is 320 μm/s, and the charging protocol is CC (6C) – CV (4.2V) with the cell from 10% to 80% capacity.*

	L_{neg}**=80 μm, ε=0.4**	L_{neg}**=130 μm, ε=0.47**
Charging time $\Delta T_{max} < 15K$ *[mins]*	7.8	8.2
ΔP_{cell} *[bar]*	4.9	2.3
Total Pumping power [kW]	1.9	1.1
Nominal energy density Gravimetric [Wh/kg] / Volumetic [Wh/L]	180.2 / 393.2	178.9 / 375.5

4.2. Stationary energy storage

LIBs are increasingly employed for stationary energy storage, with applications ranging from second-long services such as frequency regulation to hours-long services such as peak shaving.[9,170] In contrast to the EV sector that prioritize battery performance metrics, for stationary storage, cost is the key consideration. This section presents some initial findings into the potential benefits of electrolyte convection for stationary storage applications. The simulations examine a cell utilizing LMO/graphite chemistry with an N/P ratio of 1.2, and the electrolyte is $LiPF_6$ in a 1:1 EC:DMC mixture. The properties of the sandwich layer are summarized in **Table VI-4**.

Table VI-4: *Simulation parameters used in this section.*

	Units	Positive CC	Positive Electrode	Separator	Negative Electrode	Negative CC
	-	Al	Spinel $LiMn_2O_4$	-	$Li_\theta C_6$	Cu
brugg	-	-	2.5	2.5	2.5	-
C_p	J/kg/K	884	914	1617	966	387
$C_{p,e}$	1635 J/kg/K					
c_{initial}	mol/m^3	-	1000	1000	1000	-
$c_s^{\max}$	mol/m^3	-	22860	-	30555	-
D_i^s	m^2/s	-	1×10^{-13}	-	2×10^{-14}	-
$E_a^{D_i^s}$	J/mol	-	5000	-	5000	-
$E_a^{k_i}$	J/mol	-	5000	-	5000	-
F	96485 C/mol	-	-	-	-	-
k_i	m$^{2.5}$/(mol$^{0.5}$s)	-	1×10^{-10}	-	2×10^{-11}	-
L	m	1×10^{-5}	Varying	2.5×10^{-5}	Varying	1×10^{-5}
R	8.314 J/mol/K	-	-	-	-	-
R_p	m	-	5×10^{-6}	-	5×10^{-6}	-
ε	-	-	0.4	0.4	0.4	-
$\varepsilon_{\text{filler}}$	-	-	0.0810	-	0.0326	-
$\Theta_{100\%}$	-	-	0.175	-	0.9	-
$\Theta_{0\%}$	-	-	0.95	-	0.192	-
λ	W/m/K	238	0.5	0.312	1.195	398
μ	5×10^{-3} Pa•s					
ρ	kg/m^3	2702	2876	1036	1832	8933
ρ_e	1240 kg/m^3					
σ	S/m	3.55×10^7	10	-	100	5.96×10^7

For short-duration services such as frequency regulation, the battery is swiftly charged and discharged for seconds to minutes to mitigate the mismatch between load and generation of the power grid. The depth of charge/discharge is in general very small, and the battery typically sits at a SoC near 50% to be prepared for fluctuations on either side.[9] For this scenario, a 10-second pulse test starting at SoC = 50% was performed using the COMSOL model to compare the maximum discharge rate without flow and with a 10 μm/s flow at varying electrode thicknesses. At this short duration of operation, cell temperature rise is minimum, and thermal transport enhancement by electrolyte flow is likely not required. As such, a 10 μm/s flow is used to solely provide the mass transport benefits. As **Figure VI-9a** shows, electrolyte flow will lead to a higher maximum discharge rate, but the improvement diminished with electrode thickness. The enhancement by electrolyte flow is limited because at the duration of ~ seconds, the electrolyte is unlikely to build up a significant concentration gradient, especially at lower rates with the thicker electrodes that are mainly constrained by the ohmic resistance. Nevertheless, the electrolyte flow could still lead to some enhancement in peak power, or given the same power requirement, a slightly thicker electrode could be used to potentially lead to a lower cost through reduced inactive material fraction and manufacturing cost.[171]

The benefits of electrolyte convection become more significant at longer-duration services, such as peak-shaving services that require a full discharge within hours starting at 100% SoC. **Figure VI-9b** shows the simulation results of the maximum allowable anode thickness to achieve full discharge for varying durations without flow and with a 10 μm/s flow. Similar to the previous case, a flowrate of ~10 μm/s that is sufficient to eliminate mass transport limitation is used, as thermal transport is unlikely to limit cell performance given the low C rates (0.1C to 2C). As **Figure VI-9b** demonstrates, the electrolyte convection leads to a significant increase in the maximum allowable electrode thickness, as mass transport limitation becomes significant with thick electrodes and long discharge time. Through the use of thick electrodes, the convection battery has the potential to reduce cost of longer-duration services by minimizing inactive components and manufacturing expenses.

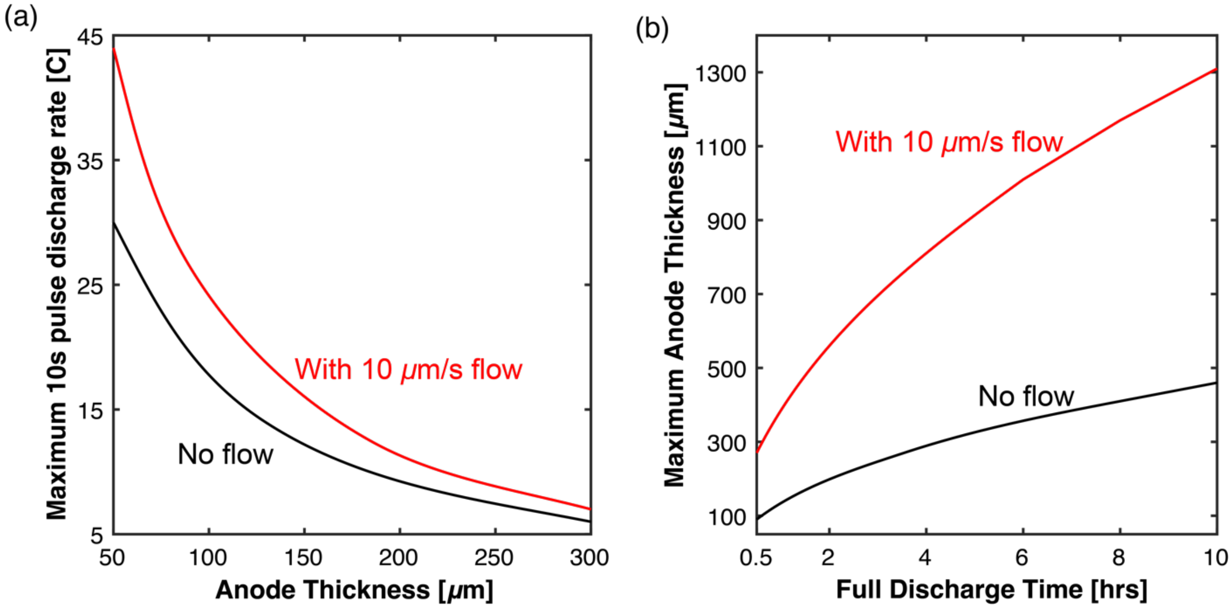

Figure VI-9: *(a) Maximum 10s pulse discharge rate as a function of anode thickness for cells without flow and with 10 μm/s flow. (b) Maximum anode thickness that can be used to achieve full discharge of varying durations for cells without flow and with 10 μm/s flow.*

Besides the performance-related benefits, there might be additional benefits and opportunities enabled by the open cell architecture of the convection battery design. For example, because of the potential safety issue, transportation of LIB has already been regulated,[23] and the convection battery might provide the opportunity for safer transportation and storage by separating the solid and liquid components when the system is not in use. Additionally, there is an emerging trend to facilitate circular use of the LIBs,[172] with most efforts surrounding LIB recycling and repurposing.[173,174,24] With the open cell architecture, the convection battery might provide the opportunity to rejuvenate the cell at the end of life. There might also be opportunities for maintenance and service throughout the battery life to extend its lifespan and reduce energy storage cost.

5. *Conclusions and Future Directions*

This chapter aims to provide some initial insights into the convection battery system design and its potential applications. While many designs are possible, the convection battery system will likely adopt the CTP design strategy for more simplified manifold design. A conceptual design based on a baseline system derived from the Qilin battery pack design was proposed, and a COMSOL-based thermo-electrochemical as well as a system design model were developed to enable comparison between the two systems. The system design model also serves as the foundation for techno-economic analyses in the future. While there are opportunities to eliminate certain components such as the coolant and cooling plates, a convection battery system is unlikely to lead to a significant improvement in energy density over the current LIB systems. Two applications that the convection battery might provide value in were investigated. The findings for each application are summarized below, and the future research directions are also discussed.

Fast charging: The convection battery has the potential to reduce charging time through enhanced electrolyte mass transport. By reducing heat generation and facilitating heat dissipation from within the battery cell, the convection battery could also address the key challenges with current external thermal management approaches, leading to more efficient and uniform temperature control. With increasing flowrates, there are increasing thermal management benefits, but tradeoffs such as increasing pumping power requirements, higher degradation risk, and decreased energy density also become more significant. To optimize the system design, a key parameter, namely the maximum allowed velocity, needs to be identified. Future studies could involve investigating flow-induced degradation mechanisms, obtaining experimental pressure drop measurement, and assessing impact of pressure drop on hardware requirements. While certain strategies could be adopted to mitigate the adverse effects, such as utilizing thicker and more porous electrodes, these strategies are typically accompanied by tradeoffs such as reduced energy density. It is thus important to understand the desired system performance & cost targets (e.g., industrial engagement) for system optimization. Additionally, for the more established sectors such as EVs, a convection battery system design should aim for minimum disruption to current Li-ion battery manufacturing infrastructure and processes.

There are additional considerations even if a convection battery can prove feasible to build with the predicted charging benefits in this work. In this study, it is assumed that the heat exchanger can provide enough cooling capacity for the coolant and/or extra electrolyte to reach the desired temperature. However, the cooling capacity of existing heat exchangers may not meet the requirement of high C rates.[175] Additionally, the pumping power required of the heat exchanger to provide the high cooling capacity may be forbiddingly high. For example, to provide 500 kW fast charging and assuming a 94% efficiency (i.e., 6% heat generation) as is typical with the current LIB technology,[175] 30 kW cooling capacity is required. If the cooling capacity were to be provided entirely through active cooling with the heat exchanger, which commonly has a coefficient of performance (cooling power/input power) of around 3, the input power required of the heat exchanger, typically in the form of pumping power, will be around 10 kW. In addition to the power consumption, such a cooling system will add significant weight and volume to the battery system. As such, maximizing passive cooling (i.e., use ambient air to move heat around) might be a critical design factor. Additionally, current charging station provides power up to ~350 kW,[176] hence charging infrastructure with higher power will be necessary to enable faster charging.

Stationary storage: Electrolyte flow has the potential to drive down cell cost through thicker electrodes, and the open cell architecture could enable new opportunities such as safer transport and maintenance. A techno-economic analysis is needed in the future to assess the cost benefits associated with these strategies. Additionally, due to the relatively high material cost of lithium-ion chemistries, there are more cost-effective chemistries (e.g., sodium-ion) that are developed for stationary storage applications. Exploring the advantages of electrolyte convection in systems employing these alternative chemistries could offer further insights. Lastly, the simulation work predicts that the convection battery could enable ~mm thick electrode for hour-long applications. This electrode thickness may not be achievable through current LIB electrode manufacturing methods, and a future research direction should therefore be to explore alternative approaches to fabricate thick electrodes.

6. List of Symbols

Symbol	**Description**
$brugg$	Bruggeman’s coefficient
C_p	Heat capacity
$C_{p,e}$	Electrolyte heat capacity
c_{initial}	Initial electrolyte concentration
c_s^{max}	Maximum solid-phase concentration
D_i^s	Solid-phase diffusivity
$E_a^{D_i^s}$	Solid-phase diffusion temperature dependent activation energy
$E_a^{k_i}$	Reaction rate constant temperature dependent activation energy
F	Faraday constant
h_{cell}	Cell convective heat transfer coefficient
k_i	Reaction rate constant
L	Thickness
ΔP_{cell}	Cell pressure drop
R	Gas constant
R_p	Particle radius
T_{coolant}	Electrolyte inlet temperature
ΔT_{max}	Maximum temperature difference within the cell
T_{inlet}	Electrolyte inlet temperature
v	Superficial velocity in the cell
ε	Porosity
$\varepsilon_{\mathrm{filler}}$	Filler fraction
$\Theta_{100\%}$	Stoichiometry at 100% SoC
$\Theta_{0\%}$	Stoichiometry at 0% SoC
λ	Thermal conductivity
λ_e	Electrolyte thermal conductivity
μ	Electrolyte viscosity

ρ	Density
ρ_e	Electrolyte density
σ	Solid-phase conductivity

VII. Summary and Outlook

The drive to broaden the application of state-of-the-art Lithium-Ion Battery (LIB) technology, with the goal of decarbonizing additional sectors, calls for improvements in LIB performance, especially in terms of high-energy and high-power capabilities. This thesis explores the potential advantages and opportunities arising from altering the cell architecture to incorporate electrolyte flow perpendicular to the electrodes, an approach referred to as the “convection battery”.

Despite previous demonstrations in literature and our laboratory of the potential benefits of electrolyte flow for cell performance, a comprehensive engineering analysis exploring electrolyte convection benefits and design considerations for such systems remains unexplored. This work aims to fill this gap by employing modeling and analytical tools for an in-depth examination of Li-ion convection battery technology, covering both fundamental and practical aspects. Throughout this thesis, I develop and utilize various simulation tools, ranging from a MATLAB-based 1D isothermal sandwich cell model to a COMSOL-based 2D model for analyzing the performance of large cell stacks, and a system design model to evaluate the performance metrics of a convection battery system. These tools have enabled me to demonstrate that integrating electrolyte convection within a LIB cell can significantly enhance mass and thermal transport, a crucial factor for high-demand applications such as fast charging and electric Vertical Takeoff and Landing (eVTOL) operations. Further, my analysis reveals that the additional electrolyte volume required for these benefits can be minimized with adequate flow rate and heat dissipation, confirming the practicality of the convection battery system. Finally, by proposing a potential system design and illustrating its utility in two distinct scenarios, I have endeavored to highlight the convection battery's unique value proposition and its capacity to broaden the applicability of current LIB technologies.

However, it is pivotal to recognize that this thesis represents an initial exploration into the convection battery concept, aiming to discern its feasibility for laboratory pursuit and to outline design guidelines for a convection battery cell and system. The anticipated performance enhancements posited in this thesis are contingent upon several assumptions that might encounter practical challenges, potentially leading to discrepancies between predicted and actual performance outcomes. These assumptions, elaborated upon in Section 4 of **Chapter I**, might necessitate significant research and engineering efforts to actualize. For instance, it is anticipated that current collectors will need alterations to allow for fluid permeability, and there might be a need to redesign electrode microstructures, moving away from the existing commercial LIB electrodes towards structures characterized by greater porosity and reduced tortuosity. Such alterations are imperative to facilitate electrolyte flow without incurring prohibitive pressure drops and pumping power at elevated flow rates. Furthermore, to ensure uniform flow distribution within the cell, the integration of additional components, such as a flow distributor, may become requisite.

In this body of work, estimates for pressure drop and pumping energy, derived via the Kozeny-Carman equation, require empirical validation and refinement through actual pressure drop measurements. Future modeling endeavors could further refine these assumptions and furnish performance predictions under scenarios where these assumptions are not upheld. For instance, a 3D model incorporating a detailed electrode microstructure could unveil the intricacies of flow dynamics and distribution within the electrode. Models accounting for non-uniform flow distribution might also shed light on performance deviations from the ideal.

The system design model, employed to evaluate the performance metrics of the hypothetical convection battery design, draws upon assumptions sourced from literature and the BatPaC model for LIBs. This model warrants refinement in future studies as more information about the convection battery system design emerges. The application demonstrations elucidated in **Chapter VI** are intended to provide preliminary insights into potential areas where the convection battery could find utility and add value. A systematic analysis is imperative in future endeavors to pinpoint the most apt applications for this technology.

Moreover, several critical facets not captured by the models in this thesis necessitate further investigation. For example, the lifetime of LIB technology, a pivotal aspect, presents challenges for analysis via simulation tools. While the convection battery concept, in theory, may mitigate certain degradation mechanisms, such as Li-plating, through enhanced electrolyte mass transport, it might also introduce novel degradation pathways, such as SEI shearing by flow. Empirical studies are thus warranted to probe the degradation behaviors and lifespan of convection batteries. Additionally, the exploration of chemistries beyond Li-ion, such as aqueous chemistries, could illuminate the potential of convection batteries in scenarios where Li-ion chemistry faces significant degradation hurdles.

The engineering of a convection battery system encompasses a multitude of design considerations. For instance, the design of the manifold must ensure uniform flow rates across all cells while minimizing shunt currents through the external electrolyte and manifold. A paramount engineering challenge lies in maintaining a leak-free system, given the potential hazards posed by the electrolyte used in LIBs, necessitating an air-free environment. This might involve minimizing connection ports within the system, considering the adoption of contactless pumps, and selecting materials compatible with the electrolyte solvent. Current LIB systems employ modular designs to guarantee that the failure of a single cell does not compromise overall system performance, facilitating the easy replacement of failed battery cells. Achieving a modular design that allows the safe swap of battery cells within a convection battery system may pose additional challenges and necessitate sophisticated engineering solutions.

The strategies devised to facilitate the convection battery system might entail increased costs. While cost considerations fall outside the scope of this thesis, a future techno-economic analysis is essential to ascertain the economic viability of convection battery technology. Such an analysis should also explore avenues for cost reduction, including maintenance and servicing of the cell. The system design model introduced in this thesis serves as an initial step toward this cost analysis.

In conclusion, this thesis establishes a foundation for the convection battery technology, highlighting its potential to improve the performance of current LIB systems and to venture into novel application domains. The trajectory of this technology is marked by a spectrum of challenges and possibilities. Moving from theoretical constructs to real-world implementations will demand concerted efforts in research, inventive engineering solutions, and collaborative engagement across various disciplines. The anticipated benefits and opportunities highlighted in this thesis make such endeavors a worthy pursuit.

VIII. References

(1) U.S. Energy Information Administration. *Monthly Energy Review*; 2017.

(2) Committee on Prospering in the Global Economy of the 21st Century: An Agenda for American Science and Technology; National Academy of Sciences; National Academy of Engineering; Institute of Medicine (U.S.). *Rising above the Gathering Storm Energizing and Employing America for a Brighter Economic Future.*; National Academies Press: Washington, 2007.

(3) U.S. Energy Information Administration. *Annual Energy Outlook 2015*; 2015.

(4) *A History of Atmospheric CO_2 and Its Effects on Plants, Animals, and Ecosystems*; Ehleringer, J. R., Cerling, T. E., Dearing, M. D., Eds.; Ecological studies; Springer: New York, NY, USA, 2005.

(5) Li, M.; Lu, J.; Chen, Z.; Amine, K. 30 Years of Lithium-Ion Batteries. *Adv. Mater.* **2018**, *30* (33), 1800561. https://doi.org/10.1002/adma.201800561.

(6) Zubi, G.; Dufo-López, R.; Carvalho, M.; Pasaoglu, G. The Lithium-Ion Battery: State of the Art and Future Perspectives. *Renew. Sustain. Energy Rev.* **2018**, *89*, 292–308. https://doi.org/10.1016/j.rser.2018.03.002.

(7) Dahn, J.; Ehrlich, G. M. Chapter 26. Lithium-Ion Batteries. In *Linden's Handbook of Batteries*; McGraw-Hill Professional, 2010; p 26.1-26.79.

(8) Doughty, D. H. Chapter 27. Rechargeable Lithium Metal Batteries (Ambient Temperature). In *Linden's Handbook of Batteries*; McGraw-Hill Professional, 2010; p 27.1-27.28.

(9) Hesse, H. C.; Schimpe, M.; Kucevic, D.; Jossen, A. Lithium-Ion Battery Storage for the Grid—A Review of Stationary Battery Storage System Design Tailored for Applications in Modern Power Grids. *Energies* **2017**, *10* (12), 2107. https://doi.org/10.3390/en10122107.

(10) Lawder, M. T.; Suthar, B.; Northrop, P. W. C.; De, S.; Hoff, C. M.; Leitermann, O.; Crow, M. L.; Santhanagopalan, S.; Subramanian, V. R. Battery Energy Storage System (BESS) and Battery Management System (BMS) for Grid-Scale Applications. *Proc. IEEE* **2014**, *102* (6), 1014–1030. https://doi.org/10.1109/JPROC.2014.2317451.

(11) Frost & Sullivan, S. S. *Global Li-ion Battery Materials Market, Forecast to 2026*; MF51-39; Frost & Sullivan, 2020; pp 29–31.

(12) *Report - What we do -SNE Research.* https://www.sneresearch.com//en/business/report_view/43/page/30? (accessed 2024-04-12).

(13) Mizushima, K.; Jones, P. C.; Wiseman, P. J.; Goodenough, J. B. LixCoO2 ($0<x\leqslant1$): A New Cathode Material for Batteries of High Energy Density. *Solid State Ion.* **1981**, *3–4*, 171–174. https://doi.org/10.1016/0167-2738(81)90077-1.

(14) Manthiram, A. A Reflection on Lithium-Ion Battery Cathode Chemistry. *Nat. Commun.* **2020**, *11* (1), 1550. https://doi.org/10.1038/s41467-020-15355-0.

(15) Armand, M.; Axmann, P.; Bresser, D.; Copley, M.; Edström, K.; Ekberg, C.; Guyomard, D.; Lestriez, B.; Novák, P.; Petranikova, M.; Porcher, W.; Trabesinger, S.; Wohlfahrt-

Mehrens, M.; Zhang, H. Lithium-Ion Batteries – Current State of the Art and Anticipated Developments. *J. Power Sources* **2020**, *479*, 228708. https://doi.org/10.1016/j.jpowsour.2020.228708.

(16) Ding, Y.; Cano, Z. P.; Yu, A.; Lu, J.; Chen, Z. Automotive Li-Ion Batteries: Current Status and Future Perspectives. *Electrochem. Energy Rev.* **2019**, *2* (1), 1–28. https://doi.org/10.1007/s41918-018-0022-z.

(17) Ziegler, M. S.; Trancik, J. E. Re-Examining Rates of Lithium-Ion Battery Technology Improvement and Cost Decline. *Energy Environ. Sci.* **2021**, *14* (4), 1635–1651. https://doi.org/10.1039/D0EE02681F.

(18) *Lithium Batteries: Markets and Materials: FCB028E | BCC Research*. https://www-bccresearch-com.libproxy.mit.edu/market-research/fuel-cell-and-battery-technologies/lithium-batteries-markets-materials-fcb028e.html (accessed 2020-12-01).

(19) Sanders, M. Lithium-Ion Battery Raw Material Supply and Demand 2016 – 2025. **2016**, 40.

(20) Pillot, C. Current Status and Future Trends for the Lithium-Ion Battery Market. *Power Tools* **2019**, 25.

(21) *Battery Pack Prices Fall As Market Ramps Up With Market Average At $156/kWh In 2019*. BloombergNEF. https://about.bnef.com/blog/battery-pack-prices-fall-as-market-ramps-up-with-market-average-at-156-kwh-in-2019/ (accessed 2020-12-01).

(22) https://www.alliedmarketresearch.com, A. M. R. *Lithium-ion Battery Market Size & Share | Industry Growth Analysis - 2032*. Allied Market Research. https://www.alliedmarketresearch.com/lithium-ion-battery-market (accessed 2024-04-12).

(23) Safety Risk Assessment, 1st Edition. **2016**, 19.

(24) *Tesla Drivers in Chicago Confront a Harsh Foe: Cold Weather - The New York Times*. https://www.nytimes.com/2024/01/17/business/tesla-charging-chicago-cold-weather.html?partner=slack&smid=sl-share (accessed 2024-01-22).

(25) Ahmed, S.; Bloom, I.; Jansen, A. N.; Tanim, T.; Dufek, E. J.; Pesaran, A.; Burnham, A.; Carlson, R. B.; Dias, F.; Hardy, K.; Keyser, M.; Kreuzer, C.; Markel, A.; Meintz, A.; Michelbacher, C.; Mohanpurkar, M.; Nelson, P. A.; Robertson, D. C.; Scoffield, D.; Shirk, M.; Stephens, T.; Vijayagopal, R.; Zhang, J. Enabling Fast Charging – A Battery Technology Gap Assessment. *J. Power Sources* **2017**, *367*, 250–262. https://doi.org/10.1016/j.jpowsour.2017.06.055.

(26) *USCAR: Energy Storage System Goals*. https://www.uscar.org/guest/article_view.php?articles_id=85 (accessed 2020-04-17).

(27) Bills, A.; Sripad, S.; Fredericks, W. L.; Singh, M.; Viswanathan, V. Performance Metrics Required of Next-Generation Batteries to Electrify Commercial Aircraft. *ACS Energy Lett.* **2020**, *5* (2), 663–668. https://doi.org/10.1021/acsenergylett.9b02574.

(28) Fredericks, W. L.; Sripad, S.; Bower, G. C.; Viswanathan, V. Performance Metrics Required of Next-Generation Batteries to Electrify Vertical Takeoff and Landing (VTOL) Aircraft. *ACS Energy Lett.* **2018**, *3* (12), 2989–2994. https://doi.org/10.1021/acsenergylett.8b02195.

(29) Manthiram, A. An Outlook on Lithium Ion Battery Technology. *ACS Cent. Sci.* **2017**, *3* (10), 1063–1069. https://doi.org/10.1021/acscentsci.7b00288.

(30) Kim, T.; Song, W.; Son, D.-Y.; Ono, L. K.; Qi, Y. Lithium-Ion Batteries: Outlook on Present, Future, and Hybridized Technologies. *J. Mater. Chem. A* **2019**, *7* (7), 2942–2964. https://doi.org/10.1039/C8TA10513H.

(31) Yi, T.-F.; Wei, T.-T.; Li, Y.; He, Y.-B.; Wang, Z.-B. Efforts on Enhancing the Li-Ion Diffusion Coefficient and Electronic Conductivity of Titanate-Based Anode Materials for Advanced Li-Ion Batteries. *Energy Storage Mater.* **2020**, *26*, 165–197. https://doi.org/10.1016/j.ensm.2019.12.042.

(32) Hannan, M. A.; Al-Shetwi, AliQ.; Begum, R. A.; Young, S. E.; Hoque, M. M.; Ker, P.; Mansur, M.; Alzaareer, K. The Value of Thermal Management Control Strategies for Battery Energy Storage in Grid Decarbonization: Issues and Recommendations. *J. Clean. Prod.* **2020**, *276*, 124223. https://doi.org/10.1016/j.jclepro.2020.124223.

(33) Lawder, M. T.; Suthar, B.; Northrop, P. W. C.; De, S.; Hoff, C. M.; Leitermann, O.; Crow, M. L.; Santhanagopalan, S.; Subramanian, V. R. Battery Energy Storage System (BESS) and Battery Management System (BMS) for Grid-Scale Applications. *Proc. IEEE* **2014**, *102* (6), 1014–1030. https://doi.org/10.1109/JPROC.2014.2317451.

(34) *BYD's New Blade Battery Set to Redefine EV Safety Standards - Technological Innovations for a Better Life | BYD USA*. https://en.byd.com/. https://en.byd.com/news/byds-new-blade-battery-set-to-redefine-ev-safety-standards/ (accessed 2024-01-22).

(35) *CATL launches CTP 3.0 battery "Qilin," achieves the highest integration level in the world*. https://www.catl.com/en/news/958.html (accessed 2024-01-22).

(36) Hawkins, A. J. *Tesla announces "tabless" battery cells that will improve range of its electric cars*. The Verge. https://www.theverge.com/2020/9/22/21449238/tesla-electric-car-battery-tabless-cells-day-elon-musk (accessed 2024-01-22).

(37) Hannan, M. A.; Al-Shetwi, AliQ.; Begum, R. A.; Young, S. E.; Hoque, M. M.; Ker, P.; Mansur, M.; Alzaareer, K. The Value of Thermal Management Control Strategies for Battery Energy Storage in Grid Decarbonization: Issues and Recommendations. *J. Clean. Prod.* **2020**, *276*, 124223. https://doi.org/10.1016/j.jclepro.2020.124223.

(38) Suppes, G. J.; Sawyer, B. D.; Gordon, M. J. High-Energy Density Flow Battery Validation. *AIChE J.* **2011**, *57* (7), 1961–1967. https://doi.org/10.1002/aic.12390.

(39) Gordon, M.; Suppes, G. Li-Ion Battery Performance in a Convection Cell Configuration. *AIChE J.* **2013**, *59* (5), 1774–1779. https://doi.org/10.1002/aic.13950.

(40) Gordon, M.; Suppes, G. Convection Battery-Modeling, Insight, and Review. *AIChE J.* **2013**, *59* (8), 2833–2842. https://doi.org/10.1002/aic.14080.

(41) Kim, S. U.; Monroe, C. W. Increasing the Rate Capability of Batteries with Electrolyte Flow. *Appl. Energy* **2013**, *103*, 207–211. https://doi.org/10.1016/j.apenergy.2012.09.028.

(42) Carney, T. J.; Brushett, F. R. Electrodes Comprising Composite Mixtures and Related Devices and Methods. US20190348669A1, November 14, 2019. https://patents.google.com/patent/US20190348669A1/en (accessed 2020-10-01).

(43) Torchio, M.; Magni, L.; Gopaluni, R. B.; Braatz, R. D.; Raimondo, D. M. LIONSIMBA: A Matlab Framework Based on a Finite Volume Model Suitable for Li-Ion Battery Design, Simulation, and Control. *J. Electrochem. Soc.* **2016**, *163* (7), A1192–A1205. https://doi.org/10.1149/2.0291607jes.

(44) Newman, J.; Tiedemann, W. Porous-Electrode Theory with Battery Applications. *AIChE J.* **1975**, *21* (1), 25–41. https://doi.org/10.1002/aic.690210103.

(45) Romero, V. C. E.; Llano, K.; Calvo, E. J. Electrochemical Extraction of Lithium by Ion Insertion from Natural Brine Using a Flow-by Reactor: Possibilities and Limitations. *Electrochem. Commun.* **2021**, *125*, 106980. https://doi.org/10.1016/j.elecom.2021.106980.

(46) Palagonia, M. S.; Brogioli, D.; La Mantia, F. Lithium Recovery from Diluted Brine by Means of Electrochemical Ion Exchange in a Flow-through-Electrodes Cell. *Desalination* **2020**, *475*, 114192. https://doi.org/10.1016/j.desal.2019.114192.

(47) Romero, V. C. E.; Putrino, D. S.; Tagliazucchi, M.; Flexer, V.; Calvo, E. J. Sustainable Electrochemical Extraction of Lithium from Natural Brine: Part II. Flow Reactor. *J. Electrochem. Soc.* **2021**, *168* (2), 020518. https://doi.org/10.1149/1945-7111/abde81.

(48) Romero, V. C. E.; Putrino, D. S.; Tagliazucchi, M.; Flexer, V.; Calvo, E. J. Electrochemical Flow Reactor for Selective Extraction of Lithium Chloride from Natural Brines. *J. Electrochem. Soc.* **2020**, *167* (12), 120522. https://doi.org/10.1149/1945-7111/abace8.

(49) Palagonia, M. S.; Brogioli, D.; Mantia, F. L. Influence of Hydrodynamics on the Lithium Recovery Efficiency in an Electrochemical Ion Pumping Separation Process. *J. Electrochem. Soc.* **2017**, *164* (14), E586–E595. https://doi.org/10.1149/2.1531714jes.

(50) Liu, M.-Q.; Li, H.-M.; Le, Z.-Y.; Zhao, J.-F.; Chang, L.-M.; Fang, L.; Hou, M.-Q.; Wang, H.-R.; Xu, T.-H.; Nie, P. Porous Current Collector Enables Carbon Superior Electrochemical Performance for K-Ion Capacitors. *Rare Met.* **2023**, *42* (1), 134–145. https://doi.org/10.1007/s12598-022-02111-0.

(51) Chen, J.; Wang, Y.; Li, S.; Chen, H.; Qiao, X.; Zhao, J.; Ma, Y.; Alshareef, H. N. Porous Metal Current Collectors for Alkali Metal Batteries. *Adv. Sci.* **2023**, *10* (1), 2205695. https://doi.org/10.1002/advs.202205695.

(52) Aiken, C. P.; Kowalski, N.; Fitzner, R. C.; Trussler, S.; Harlow, J. E.; Butler, E. J.; Dahn, J. R. Tracking Electrolyte Motion in Cylindrical Li-Ion Cells Using Moment of Inertia Measurements. *J. Electrochem. Soc.* **2023**, *170* (4), 040529. https://doi.org/10.1149/1945-7111/acce72.

(53) Nazer, N. S.; Strobl, M.; Kaestner, A.; Vie, P. J. S.; Yartys, V. A. Operando Neutron Imaging Study of a Commercial Li-Ion Battery at Variable Charge-Discharge Current Densities. *Electrochimica Acta* **2022**, *427*, 140793. https://doi.org/10.1016/j.electacta.2022.140793.

(54) Mühlbauer, M. J.; Dolotko, O.; Hofmann, M.; Ehrenberg, H.; Senyshyn, A. Effect of Fatigue/Ageing on the Lithium Distribution in Cylinder-Type Li-Ion Batteries. *J. Power Sources* **2017**, *348*, 145–149. https://doi.org/10.1016/j.jpowsour.2017.02.077.

(55) Orbay, M.; Leistenschneider, D.; Leibing, C.; Balducci, A. A Novel Strategy to Enable Effective Use of Dioxolane-Based Electrolytes in Lithium-Ion Batteries. *ChemElectroChem* **2023**, *10* (13), e202300171. https://doi.org/10.1002/celc.202300171.

(56) Carman, P. C. Fluid Flow through Granular Beds. *Chem. Eng. Res. Des.* **1997**, *75*, S32–S48. https://doi.org/10.1016/S0263-8762(97)80003-2.

(57) Coulson, J. M.; Richardson, J. F. *Chemical Engineering. 2: Particle Technology and Separation Processes*, 5. ed., repr.; Butterworth Heinemann: Amsterdam, 2010.

(58) Forchheimer, P. *Hydraulik*, 3 Aufl.; B.G. Teubner: Leipzig, 1930.

(59) Kruczek, B. Carman–Kozeny Equation. In *Encyclopedia of Membranes*; Drioli, E., Giorno, L., Eds.; Springer: Berlin, Heidelberg, 2015; pp 1–3. https://doi.org/10.1007/978-3-642-40872-4_1995-1.

(60) Holzer, L.; Marmet, P.; Fingerle, M.; Wiegmann, A.; Neumann, M.; Schmidt, V. *Tortuosity and Microstructure Effects in Porous Media: Classical Theories, Empirical Data and Modern Methods*; Springer Series in Materials Science; Springer International Publishing: Cham, 2023; Vol. 333. https://doi.org/10.1007/978-3-031-30477-4.

(61) Holzer, L.; Marmet, P.; Fingerle, M.; Wiegmann, A.; Neumann, M.; Schmidt, V. Review of Theories and a New Classification of Tortuosity Types. In *Tortuosity and Microstructure Effects in Porous Media: Classical Theories, Empirical Data and Modern Methods*; Holzer, L., Marmet, P., Fingerle, M., Wiegmann, A., Neumann, M., Schmidt, V., Eds.; Springer International Publishing: Cham, 2023; pp 7–50. https://doi.org/10.1007/978-3-031-30477-4_2.

(62) Yang, C.; R. Teixeira, A.; Shi, Y.; C. Born, S.; Lin, H.; Song, Y. L.; Martin, B.; Schenkel, B.; Lachegurabi, M. P.; F. Jensen, K. Catalytic Hydrogenation of N -4-Nitrophenyl Nicotinamide in a Micro-Packed Bed Reactor. *Green Chem.* **2018**, *20* (4), 886–893. https://doi.org/10.1039/C7GC03469E.

(63) Zhu, J.; Luo, H.; Li, W.; Gao, T.; Xia, Y.; Wierzbicki, T. Mechanism of Strengthening of Battery Resistance under Dynamic Loading. *Int. J. Impact Eng.* **2019**, *131*, 78–84. https://doi.org/10.1016/j.ijimpeng.2019.05.003.

(64) Beuse, T.; Fingerle, M.; Wagner, C.; Winter, M.; Börner, M. Comprehensive Insights into the Porosity of Lithium-Ion Battery Electrodes: A Comparative Study on Positive Electrodes Based on LiNi0.6Mn0.2Co0.2O2 (NMC622). *Batteries* **2021**, *7* (4), 70. https://doi.org/10.3390/batteries7040070.

(65) Wan, C. T.-C.; Jacquemond, R. R.; Chiang, Y.-M.; Nijmeijer, K.; Brushett, F. R.; Forner-Cuenca, A. Non-Solvent Induced Phase Separation Enables Designer Redox Flow Battery Electrodes. *Adv. Mater.* **2021**, *33* (16), 2006716. https://doi.org/10.1002/adma.202006716.

(66) Billaud, J.; Bouville, F.; Magrini, T.; Villevieille, C.; Studart, A. R. Magnetically Aligned Graphite Electrodes for High-Rate Performance Li-Ion Batteries. *Nat. Energy* **2016**, *1* (8), 1–6. https://doi.org/10.1038/nenergy.2016.97.

(67) Delattre, B.; Amin, R.; Sander, J.; Coninck, J. D.; Tomsia, A. P.; Chiang, Y.-M. Impact of Pore Tortuosity on Electrode Kinetics in Lithium Battery Electrodes: Study in Directionally

Freeze-Cast LiNi0.8Co0.15Al0.05O2 (NCA). *J. Electrochem. Soc.* **2018**, *165* (2), A388–A395. https://doi.org/10.1149/2.1321802jes.

(68) Huang, Z.; Mu, A.; Wu, L.; Wang, H. Vanadium Redox Flow Batteries: Flow Field Design and Flow Rate Optimization. *J. Energy Storage* **2022**, *45*, 103526. https://doi.org/10.1016/j.est.2021.103526.

(69) Kumar, S.; Jayanti, S. Effect of Flow Field on the Performance of an All-Vanadium Redox Flow Battery. *J. Power Sources* **2016**, *307*, 782–787. https://doi.org/10.1016/j.jpowsour.2016.01.048.

(70) Xu, Q.; Zhao, T. S.; Leung, P. K. Numerical Investigations of Flow Field Designs for Vanadium Redox Flow Batteries. *Appl. Energy* **2013**, *105*, 47–56. https://doi.org/10.1016/j.apenergy.2012.12.041.

(71) Jespers, S.; Deridder, S.; Desmet, G. A Microfluidic Distributor Combining Minimal Volume, Minimal Dispersion and Minimal Sensitivity to Clogging. *J. Chromatogr. A* **2018**, *1537*, 75–82. https://doi.org/10.1016/j.chroma.2018.01.029.

(72) Park, Y.-J.; Yu, T.; Yim, S.-J.; You, D.; Kim, D.-P. A 3D-Printed Flow Distributor with Uniform Flow Rate Control for Multi-Stacked Microfluidic Systems. *Lab. Chip* **2018**, *18* (8), 1250–1258. https://doi.org/10.1039/C8LC00004B.

(73) Vangelooven, J.; Desmet, G. Computer Aided Design Optimisation of Microfluidic Flow Distributors. *J. Chromatogr. A* **2010**, *1217* (43), 6724–6732. https://doi.org/10.1016/j.chroma.2010.05.032.

(74) Blomgren, G. E. The Development and Future of Lithium Ion Batteries. *J. Electrochem. Soc.* **2017**, *164* (1), A5019–A5025. https://doi.org/10.1149/2.0251701jes.

(75) Nykvist, B.; Nilsson, M. Rapidly Falling Costs of Battery Packs for Electric Vehicles. *Nat. Clim. Change* **2015**, *5* (4), 329–332. https://doi.org/10.1038/nclimate2564.

(76) Schmuch, R.; Wagner, R.; Hörpel, G.; Placke, T.; Winter, M. Performance and Cost of Materials for Lithium-Based Rechargeable Automotive Batteries. *Nat. Energy* **2018**, *3* (4), 267–278. https://doi.org/10.1038/s41560-018-0107-2.

(77) Luo, X.; Wang, J.; Dooner, M.; Clarke, J. Overview of Current Development in Electrical Energy Storage Technologies and the Application Potential in Power System Operation. *Appl. Energy* **2015**, *137*, 511–536. https://doi.org/10.1016/j.apenergy.2014.09.081.

(78) Gallagher, K. G.; Trask, S. E.; Bauer, C.; Woehrle, T.; Lux, S. F.; Tschech, M.; Lamp, P.; Polzin, B. J.; Ha, S.; Long, B.; Wu, Q.; Lu, W.; Dees, D. W.; Jansen, A. N. Optimizing Areal Capacities through Understanding the Limitations of Lithium-Ion Electrodes. *J. Electrochem. Soc.* **2016**, *163* (2), A138–A149. https://doi.org/10.1149/2.0321602jes.

(79) Colclasure, A. M.; Dunlop, A. R.; Trask, S. E.; Polzin, B. J.; Jansen, A. N.; Smith, K. Requirements for Enabling Extreme Fast Charging of High Energy Density Li-Ion Cells While Avoiding Lithium Plating. *J. Electrochem. Soc.* **2019**, *166* (8), A1412. https://doi.org/10.1149/2.0451908jes.

(80) Malifarge, S.; Delobel, B.; Delacourt, C. Experimental and Modeling Analysis of Graphite Electrodes with Various Thicknesses and Porosities for High-Energy-Density Li-Ion

Batteries. *J. Electrochem. Soc.* **2018**, *165* (7), A1275–A1287. https://doi.org/10.1149/2.0301807jes.

(81) Patry, G.; Romagny, A.; Martinet, S.; Froelich, D. Cost Modeling of Lithium-Ion Battery Cells for Automotive Applications. *Energy Sci. Eng.* **2015**, *3* (1), 71–82. https://doi.org/10.1002/ese3.47.

(82) Videa, M.; Xu, W.; Geil, B.; Marzke, R.; Angell, C. A. High Li + Self-Diffusivity and Transport Number in Novel Electrolyte Solutions. *J. Electrochem. Soc.* **2001**, *148* (12), A1352. https://doi.org/10.1149/1.1415030.

(83) Logan, E. R.; Tonita, E. M.; Gering, K. L.; Li, J.; Ma, X.; Beaulieu, L. Y.; Dahn, J. R. A Study of the Physical Properties of Li-Ion Battery Electrolytes Containing Esters. *J. Electrochem. Soc.* **2018**, *165* (2), A21. https://doi.org/10.1149/2.0271802jes.

(84) Du, Z.; Wood, D. L.; Belharouak, I. Enabling Fast Charging of High Energy Density Li-Ion Cells with High Lithium Ion Transport Electrolytes. *Electrochem. Commun.* **2019**, *103*, 109–113. https://doi.org/10.1016/j.elecom.2019.04.013.

(85) Kim, D. S.; Kim, Y. E.; Kim, H. Improved Fast Charging Capability of Graphite Anodes via Amorphous Al2O3 Coating for High Power Lithium Ion Batteries. *J. Power Sources* **2019**, *422*, 18–24. https://doi.org/10.1016/j.jpowsour.2019.03.027.

(86) Yuan, T.; Yu, X.; Cai, R.; Zhou, Y.; Shao, Z. Synthesis of Pristine and Carbon-Coated Li4Ti5O12 and Their Low-Temperature Electrochemical Performance. *J. Power Sources* **2010**, *195* (15), 4997–5004. https://doi.org/10.1016/j.jpowsour.2010.02.020.

(87) Tian, B.; Xiang, H.; Zhang, L.; Li, Z.; Wang, H. Niobium Doped Lithium Titanate as a High Rate Anode Material for Li-Ion Batteries. *Electrochimica Acta* **2010**, *55* (19), 5453–5458. https://doi.org/10.1016/j.electacta.2010.04.068.

(88) Li, W.; Song, B.; Manthiram, A. High-Voltage Positive Electrode Materials for Lithium-Ion Batteries. *Chem. Soc. Rev.* **2017**, *46* (10), 3006–3059. https://doi.org/10.1039/C6CS00875E.

(89) Xu, C.; Xu, B.; Gu, Y.; Xiong, Z.; Sun, J.; Zhao, X. S. Graphene-Based Electrodes for Electrochemical Energy Storage. *Energy Environ. Sci.* **2013**, *6* (5), 1388–1414. https://doi.org/10.1039/C3EE23870A.

(90) Sander, J. S.; Erb, R. M.; Li, L.; Gurijala, A.; Chiang, Y.-M. High-Performance Battery Electrodes via Magnetic Templating. *Nat. Energy* **2016**, *1* (8). https://doi.org/10.1038/nenergy.2016.99.

(91) Huang, C.; Grant, P. S. Coral-like Directional Porosity Lithium Ion Battery Cathodes by Ice Templating. *J. Mater. Chem. A* **2018**, *6* (30), 14689–14699. https://doi.org/10.1039/C8TA05049J.

(92) Zhao, W.; Luo, G.; Wang, C.-Y. Effect of Tab Design on Large-Format Li-Ion Cell Performance. *J. Power Sources* **2014**, *257*, 70–79. https://doi.org/10.1016/j.jpowsour.2013.12.146.

(93) Campbell, I. D.; Gopalakrishnan, K.; Marinescu, M.; Torchio, M.; Offer, G. J.; Raimondo, D. Optimising Lithium-Ion Cell Design for Plug-in Hybrid and Battery Electric Vehicles. *J. Energy Storage* **2019**, *22*, 228–238. https://doi.org/10.1016/j.est.2019.01.006.

(94) Yang, X.-G.; Zhang, G.; Ge, S.; Wang, C.-Y. Fast Charging of Lithium-Ion Batteries at All Temperatures. *Proc. Natl. Acad. Sci.* **2018**, *115* (28), 7266–7271. https://doi.org/10.1073/pnas.1807115115.

(95) Dornbusch, D. A.; Hilton, R.; Lohman, S. D.; Suppes, G. J. Experimental Validation of the Elimination of Dendrite Short-Circuit Failure in Secondary Lithium-Metal Convection Cell Batteries. *J. Electrochem. Soc.* **2015**, *162* (3), A262–A268. https://doi.org/10.1149/2.0021503jes.

(96) Ramadesigan, V.; Northrop, P. W. C.; De, S.; Santhanagopalan, S.; Braatz, R. D.; Subramanian, V. R. Modeling and Simulation of Lithium-Ion Batteries from a Systems Engineering Perspective. *J. Electrochem. Soc.* **2012**, *159* (3), R31. https://doi.org/10.1149/2.018203jes.

(97) Krewer, U.; Röder, F.; Harinath, E.; Braatz, R. D.; Bedürftig, B.; Findeisen, R. Review—Dynamic Models of Li-Ion Batteries for Diagnosis and Operation: A Review and Perspective. *J. Electrochem. Soc.* **2018**, *165* (16), A3656. https://doi.org/10.1149/2.1061814jes.

(98) Franco, A. A.; Rucci, A.; Brandell, D.; Frayret, C.; Gaberscek, M.; Jankowski, P.; Johansson, P. Boosting Rechargeable Batteries R&D by Multiscale Modeling: Myth or Reality? *Chem. Rev.* **2019**, *119* (7), 4569–4627. https://doi.org/10.1021/acs.chemrev.8b00239.

(99) Doyle, C. M. Design and Simulation of Lithium Rechargeable Batteries. PhD thesis, University of California, Berkeley, 1995. https://doi.org/10.2172/203473.

(100) *Fortran Programs for the Simulation of Electrochemical Systems*. http://www.cchem.berkeley.edu/jsngrp/fortran.html (accessed 2018-06-06).

(101) *Batteries and Fuel Cells Software - Fuel Cell and Battery Modeling*. https://www.comsol.com/batteries-and-fuel-cells-module (accessed 2020-06-03).

(102) *Battery Design Studio*. http://www.batdesign.com/batterydesign.html (accessed 2020-06-03).

(103) Cai, L.; White, R. E. Mathematical Modeling of a Lithium Ion Battery with Thermal Effects in COMSOL Inc. Multiphysics (MP) Software. *J. Power Sources* **2011**, *196* (14), 5985–5989. https://doi.org/10.1016/j.jpowsour.2011.03.017.

(104) Hindmarsh, A. C.; Brown, P. N.; Grant, K. E.; Lee, S. L.; Serban, R.; Shumaker, D. E.; Woodward, C. S. SUNDIALS: Suite of Nonlinear and Differential/Algebraic Equation Solvers. *ACM Trans Math Softw* **2005**, *31* (3), 363–396. https://doi.org/10.1145/1089014.1089020.

(105) T.K. Sherwood; Pigford, R. L.; Wilke, C. R. *Mass Transfer*; Chemical engineering series; McGraw-Hill, 1975.

(106) Doyle, M. Comparison of Modeling Predictions with Experimental Data from Plastic Lithium Ion Cells. *J. Electrochem. Soc.* **1996**, *143* (6), 1890. https://doi.org/10.1149/1.1836921.

(107) Newman, J. S.; Thomas-Alyea, K. E. *Electrochemical Systems*; Hoboken, N.J. : J. Wiley, c2004., 2004.

(108) Versteeg, H. K.; Malalasekera, W. *An Introduction to Computational Fluid Dynamics: The Finite Volume Method*, 2nd ed.; Pearson Education Ltd: Harlow, England ; New York, 2007.

(109) Valo̸en, L. O.; Reimers, J. N. Transport Properties of LiPF[Sub 6]-Based Li-Ion Battery Electrolytes. *J. Electrochem. Soc.* **2005**, *152* (5), A882. https://doi.org/10.1149/1.1872737.

(110) Subramanian, V. R.; Diwakar, V. D.; Tapriyal, D. Efficient Macro-Micro Scale Coupled Modeling of Batteries. *J. Electrochem. Soc.* **2005**, *152* (10), A2002–A2008. https://doi.org/10.1149/1.2032427.

(111) Torchio, M.; Magni, L.; Gopaluni, R. B.; Braatz, R. D.; Raimondo, D. M. LIONSIMBA: A Matlab Framework Based on a Finite Volume Model Suitable for Li-Ion Battery Design, Simulation, and Control. *J. Electrochem. Soc.* **2016**, *163* (7), A1192–A1205. https://doi.org/10.1149/2.0291607jes.

(112) Fuller, T. F.; Doyle, M.; Newman, J. Simulation and Optimization of the Dual Lithium Ion Insertion Cell. *J. Electrochem. Soc.* **1994**, *141* (1), 1. https://doi.org/10.1149/1.2054684.

(113) Marquis, S. G.; Sulzer, V.; Timms, R.; Please, C. P.; Chapman, S. J. An Asymptotic Derivation of a Single Particle Model with Electrolyte. *J. Electrochem. Soc.* **2019**, *166* (15), A3693. https://doi.org/10.1149/2.0341915jes.

(114) Jiang, F.; Peng, P. Elucidating the Performance Limitations of Lithium-Ion Batteries Due to Species and Charge Transport through Five Characteristic Parameters. *Sci. Rep.* **2016**, *6* (1). https://doi.org/10.1038/srep32639.

(115) Masias, A.; Marcicki, J.; Paxton, W. A. Opportunities and Challenges of Lithium Ion Batteries in Automotive Applications. *ACS Energy Lett.* **2021**, 621–630. https://doi.org/10.1021/acsenergylett.0c02584.

(116) Choi, D.; Shamim, N.; Crawford, A.; Huang, Q.; Vartanian, C. K.; Viswanathan, V. V.; Paiss, M. D.; Alam, M. J. E.; Reed, D. M.; Sprenkle, V. L. Li-Ion Battery Technology for Grid Application. *J. Power Sources* **2021**, *511*, 230419. https://doi.org/10.1016/j.jpowsour.2021.230419.

(117) Tomaszewska, A.; Chu, Z.; Feng, X.; O'Kane, S.; Liu, X.; Chen, J.; Ji, C.; Endler, E.; Li, R.; Liu, L.; Li, Y.; Zheng, S.; Vetterlein, S.; Gao, M.; Du, J.; Parkes, M.; Ouyang, M.; Marinescu, M.; Offer, G.; Wu, B. Lithium-Ion Battery Fast Charging: A Review. *eTransportation* **2019**, *1*, 100011. https://doi.org/10.1016/j.etran.2019.100011.

(118) Olabi, A. G.; Maghrabie, H. M.; Adhari, O. H. K.; Sayed, E. T.; Yousef, B. A. A.; Salameh, T.; Kamil, M.; Abdelkareem, M. A. Battery Thermal Management Systems: Recent Progress and Challenges. *Int. J. Thermofluids* **2022**, *15*, 100171. https://doi.org/10.1016/j.ijft.2022.100171.

(119) Wu, W.; Wang, S.; Wu, W.; Chen, K.; Hong, S.; Lai, Y. A Critical Review of Battery Thermal Performance and Liquid Based Battery Thermal Management. *Energy Convers. Manag.* **2019**, *182*, 262–281. https://doi.org/10.1016/j.enconman.2018.12.051.

(120) Ji, Y.; Zhang, Y.; Wang, C.-Y. Li-Ion Cell Operation at Low Temperatures. *J. Electrochem. Soc.* **2013**, *160* (4), A636. https://doi.org/10.1149/2.047304jes.

(121) Storch, M.; Fath, J. P.; Sieg, J.; Vrankovic, D.; Krupp, C.; Spier, B.; Riedel, R. Temperature and Lithium Concentration Gradient Caused Inhomogeneous Plating in Large-Format

Lithium-Ion Cells. *J. Energy Storage* **2021**, *41*, 102887. https://doi.org/10.1016/j.est.2021.102887.

(122) Liu, X.; Ai, W.; Naylor Marlow, M.; Patel, Y.; Wu, B. The Effect of Cell-to-Cell Variations and Thermal Gradients on the Performance and Degradation of Lithium-Ion Battery Packs. *Appl. Energy* **2019**, *248*, 489–499. https://doi.org/10.1016/j.apenergy.2019.04.108.

(123) Yang, N.; Zhang, X.; Shang, B.; Li, G. Unbalanced Discharging and Aging Due to Temperature Differences among the Cells in a Lithium-Ion Battery Pack with Parallel Combination. *J. Power Sources* **2016**, *306*, 733–741. https://doi.org/10.1016/j.jpowsour.2015.12.079.

(124) Zichen, W.; Changqing, D. A Comprehensive Review on Thermal Management Systems for Power Lithium-Ion Batteries. *Renew. Sustain. Energy Rev.* **2021**, *139*, 110685. https://doi.org/10.1016/j.rser.2020.110685.

(125) Tete, P. R.; Gupta, M. M.; Joshi, S. S. Developments in Battery Thermal Management Systems for Electric Vehicles: A Technical Review. *J. Energy Storage* **2021**, *35*, 102255. https://doi.org/10.1016/j.est.2021.102255.

(126) Sharma, D. K.; Prabhakar, A. A Review on Air Cooled and Air Centric Hybrid Thermal Management Techniques for Li-Ion Battery Packs in Electric Vehicles. *J. Energy Storage* **2021**, *41*, 102885. https://doi.org/10.1016/j.est.2021.102885.

(127) Zhao, G.; Wang, X.; Negnevitsky, M.; Zhang, H. A Review of Air-Cooling Battery Thermal Management Systems for Electric and Hybrid Electric Vehicles. *J. Power Sources* **2021**, *501*, 230001. https://doi.org/10.1016/j.jpowsour.2021.230001.

(128) Han, T.; Khalighi, B.; Yen, E. C.; Kaushik, S. Li-Ion Battery Pack Thermal Management: Liquid Versus Air Cooling. *J. Therm. Sci. Eng. Appl.* **2019**, *11* (2), 021009. https://doi.org/10.1115/1.4041595.

(129) Kalaf, O.; Solyali, D.; Asmael, M.; Zeeshan, Q.; Safaei, B.; Askir, A. Experimental and Simulation Study of Liquid Coolant Battery Thermal Management System for Electric Vehicles: A Review. *Int. J. Energy Res.* **2021**, *45* (5), 6495–6517. https://doi.org/10.1002/er.6268.

(130) Roe, C.; Feng, X.; White, G.; Li, R.; Wang, H.; Rui, X.; Li, C.; Zhang, F.; Null, V.; Parkes, M.; Patel, Y.; Wang, Y.; Wang, H.; Ouyang, M.; Offer, G.; Wu, B. Immersion Cooling for Lithium-Ion Batteries – A Review. *J. Power Sources* **2022**, *525*, 231094. https://doi.org/10.1016/j.jpowsour.2022.231094.

(131) Dubey, P.; Pulugundla, G.; Srouji, A. K. Direct Comparison of Immersion and Cold-Plate Based Cooling for Automotive Li-Ion Battery Modules. *Energies* **2021**, *14* (5), 1259. https://doi.org/10.3390/en14051259.

(132) Shen, Z.-G.; Chen, S.; Liu, X.; Chen, B. A Review on Thermal Management Performance Enhancement of Phase Change Materials for Vehicle Lithium-Ion Batteries. *Renew. Sustain. Energy Rev.* **2021**, *148*, 111301. https://doi.org/10.1016/j.rser.2021.111301.

(133) Zhang, J.; Shao, D.; Jiang, L.; Zhang, G.; Wu, H.; Day, R.; Jiang, W. Advanced Thermal Management System Driven by Phase Change Materials for Power Lithium-Ion Batteries:

A Review. *Renew. Sustain. Energy Rev.* **2022**, *159*, 112207. https://doi.org/10.1016/j.rser.2022.112207.

(134) Ping, P.; Zhang, Y.; Kong, D.; Du, J. Investigation on Battery Thermal Management System Combining Phase Changed Material and Liquid Cooling Considering Non-Uniform Heat Generation of Battery. *J. Energy Storage* **2021**, *36*, 102448. https://doi.org/10.1016/j.est.2021.102448.

(135) Hu, X.; Zheng, Y.; Howey, D. A.; Perez, H.; Foley, A.; Pecht, M. Battery Warm-up Methodologies at Subzero Temperatures for Automotive Applications: Recent Advances and Perspectives. *Prog. Energy Combust. Sci.* **2020**, *77*, 100806. https://doi.org/10.1016/j.pecs.2019.100806.

(136) Ji, Y.; Wang, C. Y. Heating Strategies for Li-Ion Batteries Operated from Subzero Temperatures. *Electrochimica Acta* **2013**, *107*, 664–674. https://doi.org/10.1016/j.electacta.2013.03.147.

(137) Bandhauer, T. M.; Garimella, S. Passive, Internal Thermal Management System for Batteries Using Microscale Liquid–Vapor Phase Change. *Appl. Therm. Eng.* **2013**, *61* (2), 756–769. https://doi.org/10.1016/j.applthermaleng.2013.08.004.

(138) Bandhauer, T.; Garimella, S.; Fuller, T. F. Electrochemical-Thermal Modeling to Evaluate Battery Thermal Management Strategies: II. Edge and Internal Cooling. *J. Electrochem. Soc.* **2014**, *162* (1), A137. https://doi.org/10.1149/2.0581501jes.

(139) Mohammadian, S. K.; He, Y.-L.; Zhang, Y. Internal Cooling of a Lithium-Ion Battery Using Electrolyte as Coolant through Microchannels Embedded inside the Electrodes. *J. Power Sources* **2015**, *293*, 458–466. https://doi.org/10.1016/j.jpowsour.2015.05.055.

(140) Sievers, M.; Sievers, U.; Mao, S. S. Thermal Modelling of New Li-Ion Cell Design Modifications. *Forsch. Im Ingenieurwesen* **2010**, *74* (4), 215–231. https://doi.org/10.1007/s10010-010-0127-y.

(141) Shah, K.; Jain, A. Modeling of Steady-State and Transient Thermal Performance of a Li-Ion Cell with an Axial Fluidic Channel for Cooling. *Int. J. Energy Res.* **2015**, *39* (4), 573–584. https://doi.org/10.1002/er.3274.

(142) Shah, K.; McKee, C.; Chalise, D.; Jain, A. Experimental and Numerical Investigation of Core Cooling of Li-Ion Cells Using Heat Pipes. *Energy* **2016**, *113*, 852–860. https://doi.org/10.1016/j.energy.2016.07.076.

(143) Choi, K. W.; Yao, N. P. Heat Transfer in Lead-Acid Batteries Designed for Electric-Vehicle Propulsion Application. *J. Electrochem. Soc.* **1979**, *126* (8), 1321–1328. https://doi.org/10.1149/1.2129270.

(144) Gao, W.; Orella, M. J.; Carney, T. J.; Román-Leshkov, Y.; Drake, J.; Brushett, F. R. Understanding the Impact of Convective Transport on Intercalation Batteries Through Dimensional Analysis. *J. Electrochem. Soc.* **2020**, *167* (14), 140551. https://doi.org/10.1149/1945-7111/abbce3.

(145) Gu, W. B.; Wang, C. Y. Thermal-Electrochemical Modeling of Battery Systems. *J. Electrochem. Soc.* **2000**, *147* (8), 2910. https://doi.org/10.1149/1.1393625.

(146) Abada, S.; Marlair, G.; Lecocq, A.; Petit, M.; Sauvant-Moynot, V.; Huet, F. Safety Focused Modeling of Lithium-Ion Batteries: A Review. *J. Power Sources* **2016**, *306*, 178–192. https://doi.org/10.1016/j.jpowsour.2015.11.100.

(147) Srinivasan, V.; Wang, C. Y. Analysis of Electrochemical and Thermal Behavior of Li-Ion Cells. *J. Electrochem. Soc.* **2002**, *150* (1), A98. https://doi.org/10.1149/1.1526512.

(148) Chen, S. C.; Wan, C. C.; Wang, Y. Y. Thermal Analysis of Lithium-Ion Batteries. *J. Power Sources* **2005**, *140* (1), 111–124. https://doi.org/10.1016/j.jpowsour.2004.05.064.

(149) No, A. *Research and Development of High-Power and High-Energy Electrochemical Storage Devices*; United States Advanced Batter Consortium, LLC, Southfield, MI (United States), 2014. https://doi.org/10.2172/1160224.

(150) Zhang, C.; Huang, J.; Sun, W.; Xu, X.; Li, Y. Research on the Influence of Liquid on Heat Dissipation and Heating Characteristics of Lithium-Ion Battery Thermal Management System. *World Electr. Veh. J.* **2022**, *13* (4), 68. https://doi.org/10.3390/wevj13040068.

(151) Yang, X.-G.; Liu, T.; Gao, Y.; Ge, S.; Leng, Y.; Wang, D.; Wang, C.-Y. Asymmetric Temperature Modulation for Extreme Fast Charging of Lithium-Ion Batteries. *Joule* **2019**, *3* (12), 3002–3019. https://doi.org/10.1016/j.joule.2019.09.021.

(152) Yang, X.-G.; Liu, T.; Wang, C.-Y. Thermally Modulated Lithium Iron Phosphate Batteries for Mass-Market Electric Vehicles. *Nat. Energy* **2021**, 1–10. https://doi.org/10.1038/s41560-020-00757-7.

(153) Carman, P. C. Fluid Flow through Granular Beds. *Chem. Eng. Res. Des.* **1997**, *75*, S32–S48. https://doi.org/10.1016/S0263-8762(97)80003-2.

(154) Edge, E.; LLC, E. E. *Convective Heat Transfer Coefficients Table Chart*. https://www.engineersedge.com/heat_transfer/convective_heat_transfer_coefficients__13378.htm (accessed 2023-01-19).

(155) Li, S.; Zhang, C.; Zhao, Y.; Offer, G. J.; Marinescu, M. Effect of Thermal Gradients on Inhomogeneous Degradation in Lithium-Ion Batteries. *Commun. Eng.* **2023**, *2* (1), 1–14. https://doi.org/10.1038/s44172-023-00124-w.

(156) Guo, Z. Y.; Tao, W. Q.; Shah, R. K. The Field Synergy (Coordination) Principle and Its Applications in Enhancing Single Phase Convective Heat Transfer. *Int. J. Heat Mass Transf.* **2005**, *48* (9), 1797–1807. https://doi.org/10.1016/j.ijheatmasstransfer.2004.11.007.

(157) Wang, A. A.; O'Kane, S. E. J.; Brosa Planella, F.; Houx, J. L.; O'Regan, K.; Zyskin, M.; Edge, J.; Monroe, C. W.; Cooper, S. J.; Howey, D. A.; Kendrick, E.; Foster, J. M. Review of Parameterisation and a Novel Database (LiionDB) for Continuum Li-Ion Battery Models. *Prog. Energy* **2022**, *4* (3), 032004. https://doi.org/10.1088/2516-1083/ac692c.

(158) Steinhardt, M.; Barreras, J. V.; Ruan, H.; Wu, B.; Offer, G. J.; Jossen, A. Meta-Analysis of Experimental Results for Heat Capacity and Thermal Conductivity in Lithium-Ion Batteries: A Critical Review. *J. Power Sources* **2022**, *522*, 230829. https://doi.org/10.1016/j.jpowsour.2021.230829.

(159) Reuther, A.; Kepner, J.; Byun, C.; Samsi, S.; Arcand, W.; Bestor, D.; Bergeron, B.; Gadepally, V.; Houle, M.; Hubbell, M.; Jones, M.; Klein, A.; Milechin, L.; Mullen, J.; Prout, A.; Rosa, A.; Yee, C.; Michaleas, P. Interactive Supercomputing on 40,000 Cores for

Machine Learning and Data Analysis. In *2018 IEEE High Performance extreme Computing Conference (HPEC)*; 2018; pp 1–6. https://doi.org/10.1109/HPEC.2018.8547629.

(160) Gao, W.; Drake, J.; Brushett, F. R. Modeling the Impact of Electrolyte Flow on Heat Management in a Li-Ion Convection Cell. *J. Electrochem. Soc.* **2023**, *170* (9), 090508. https://doi.org/10.1149/1945-7111/aceab4.

(161) Wentker, M.; Greenwood, M.; Leker, J. A Bottom-Up Approach to Lithium-Ion Battery Cost Modeling with a Focus on Cathode Active Materials. *Energies* **2019**, *12* (3), 504. https://doi.org/10.3390/en12030504.

(162) Frith, J. T.; Lacey, M. J.; Ulissi, U. A Non-Academic Perspective on the Future of Lithium-Based Batteries. *Nat. Commun.* **2023**, *14* (1), 420. https://doi.org/10.1038/s41467-023-35933-2.

(163) *Report: CATL's New Qilin Battery Enters Series Production*. InsideEVs. https://insideevs.com/news/658474/report-catl-qilin-battery-series-production/ (accessed 2024-03-18).

(164) *BatPaC: Battery Manufacturing Cost Estimation | Argonne National Laboratory*. /tcp/batpac-battery-manufacturing-cost-estimation (accessed 2019-10-24).

(165) Sripad, S.; Viswanathan, V. Performance Metrics Required of Next-Generation Batteries to Make a Practical Electric Semi Truck. *ACS Energy Lett.* **2017**, *2* (7), 1669–1673. https://doi.org/10.1021/acsenergylett.7b00432.

(166) Yang, X.-G.; Liu, T.; Ge, S.; Rountree, E.; Wang, C.-Y. Challenges and Key Requirements of Batteries for Electric Vertical Takeoff and Landing Aircraft. *Joule* **2021**, S2542435121002051. https://doi.org/10.1016/j.joule.2021.05.001.

(167) *EUCAR*. EUCAR. https://www.eucar.be/ (accessed 2024-03-29).

(168) *The 10 Fastest-Charging EVs We Tested in 2023*. MotorTrend. https://www.motortrend.com/features/fastest-charging-evs/ (accessed 2024-03-29).

(169) Carter, R.; Kingston, T. A.; Atkinson, R. W.; Parmananda, M.; Dubarry, M.; Fear, C.; Mukherjee, P. P.; Love, C. T. Directionality of Thermal Gradients in Lithium-Ion Batteries Dictates Diverging Degradation Modes. *Cell Rep. Phys. Sci.* **2021**, *2* (3), 100351. https://doi.org/10.1016/j.xcrp.2021.100351.

(170) Twitchell, J.; DeSomber, K.; Bhatnagar, D. Defining Long Duration Energy Storage. *J. Energy Storage* **2023**, *60*, 105787. https://doi.org/10.1016/j.est.2022.105787.

(171) Ciez, R. E.; Steingart, D. Asymptotic Cost Analysis of Intercalation Lithium-Ion Systems for Multi-Hour Duration Energy Storage. *Joule* **2020**, *4* (3), 597–614. https://doi.org/10.1016/j.joule.2020.01.007.

(172) *CIRCULAR | arpa-e.energy.gov*. http://arpa-e.energy.gov/technologies/programs/circular (accessed 2024-03-30).

(173) Liu, C.; Lin, J.; Cao, H.; Zhang, Y.; Sun, Z. Recycling of Spent Lithium-Ion Batteries in View of Lithium Recovery: A Critical Review. *J. Clean. Prod.* **2019**, *228*, 801–813. https://doi.org/10.1016/j.jclepro.2019.04.304.

(174) Zhang, X.; Li, L.; Fan, E.; Xue, Q.; Bian, Y.; Wu, F.; Chen, R. Toward Sustainable and Systematic Recycling of Spent Rechargeable Batteries. *Chem. Soc. Rev.* **2018**, *47* (19), 7239–7302. https://doi.org/10.1039/C8CS00297E.

(175) Keyser, M.; Pesaran, A.; Li, Q.; Santhanagopalan, S.; Smith, K.; Wood, E.; Ahmed, S.; Bloom, I.; Dufek, E.; Shirk, M.; Meintz, A.; Kreuzer, C.; Michelbacher, C.; Burnham, A.; Stephens, T.; Francfort, J.; Carlson, B.; Zhang, J.; Vijayagopal, R.; Hardy, K.; Dias, F.; Mohanpurkar, M.; Scoffield, D.; Jansen, A. N.; Tanim, T.; Markel, A. Enabling Fast Charging – Battery Thermal Considerations. *J. Power Sources* **2017**, *367*, 228–236. https://doi.org/10.1016/j.jpowsour.2017.07.009.

(176) *350 kW V4 Tesla Supercharger Emerges In Planning Documents*. InsideEVs. https://insideevs.com/news/679445/350kw-v4-tesla-supercharger/ (accessed 2024-05-07).

IX. Permissions

Chapter I, Section 1 was adapted from work written for *The Future of Energy Storage* report published by the MIT Energy Initiative. **Chapter II** was adapted from work previously published by IOP Publishing on behalf of the *Journal of the Electrochemical Society*: Gao, W., Orella, M. J., Carney, T. J., Román-Leshkov, Y., Drake, J., & Brushett, F. R. (2020). Understanding the Impact of Convective Transport on Intercalation Batteries Through Dimensional Analysis. *Journal of The Electrochemical Society*, *167*(14), 140551. **Chapter III** was adapted from work previously published by IOP Publishing on behalf of the *Journal of the Electrochemical Society*: Gao, W., Drake, J., & Brushett, F. R. (2023). Modeling the Impact of Electrolyte Flow on Heat Management in a Li-Ion Convection Cell. *Journal of The Electrochemical Society*, *170*(9), 090508. **Chapter V** is in preparation for submission to the *Journal of Power Sources*. **Chapter VI** is in preparation for submission to an undetermined journal.